Solar wind and interplanetary magnetic field effects in the magnetosphere-ionosphere system

A Thesis Submitted to the
College of Graduate Studies and Research
in Partial Fulfillment of the Requirements
for the degree of Doctor of Philosophy
in the Department of Physics and Engineering Physics
University of Saskatchewan
Saskatoon

By
Kateryna Yakymenko

Permission to Use

In presenting this thesis in partial fulfilment of the requirements for a Postgraduate degree from the University of Saskatchewan, I agree that the Libraries of this University may make it freely available for inspection. I further agree that permission for copying of this thesis in any manner, in whole or in part, for scholarly purposes may be granted by the professor or professors who supervised my thesis work or, in their absence, by the Head of the Department or the Dean of the College in which my thesis work was done. It is understood that any copying or publication or use of this thesis or parts thereof for financial gain shall not be allowed without my written permission. It is also understood that due recognition shall be given to me and to the University of Saskatchewan in any scholarly use which may be made of any material in my thesis.

Requests for permission to copy or to make other use of material in this thesis in whole or part should be addressed to:

Head of the Department of Physics and Engineering Physics
116 Science Place
University of Saskatchewan
Saskatoon, Saskatchewan
Canada
S7N 5E2

Abstract

The research presented in this thesis investigates several effects in the magnetosphere-ionosphere system related to specific solar wind and interplanetary magnetic field drivers. For the southward Interplanetary Magnetic Field (IMF) when the coupling between the solar wind and the magnetosphere is efficient, the energy accumulation in the magnetotail is often interrupted by a spontaneous energy release into various parts of the magnetosphere-ionosphere system through a substorm process. When the IMF turns northward, the dayside reconnection is inefficient and the lobe reconnection becomes important. Onset of sunward flows in the dayside portion of the polar cap ionosphere is one effect related to this process. Another phenomenon under northward IMF is the occurrence of auroral arcs at very high latitudes. This thesis is focused of these three phenomena: substorms, dayside sunward plasma flows and the onset of polar cap arcs.

First, the relationship between the substorm occurrence and the solar wind driving is statistically investigated. Four independent lists of substorm events are considered. The events in these lists are inferred from jumps in the SuperMAG AL index for 1979–2015, from electron injections into geosynchronous orbit for 1989–2007, from positive bay events in 1982–2012, and from ground-based magnetometer data with the SOPHIE algorithm for 1981–2015. Additionally, a well-known list of substorms identified from IMAGE and Polar satellite imagery is considered. The different lists are investigated and the two lists with the most robust substorm onsets are chosen for further study. Substorm occurrence rates and substorm recurrence-time distributions are examined as functions of the phase of the solar cycle, the season of the year, the Russell-McPherron favorability, the type of solar wind plasma at Earth, the geomagnetic-activity level, and as functions of various solar and solar wind properties. Three populations of substorm occurrences are seen: (1) quasiperiodically occurring substorms with recurrence times of 24 hr, (2) randomly occurring substorms with recurrence times of about 6–15 hr, and (3) long intervals where no substorms occur. A working model is suggested where (1) the period of periodic substorms is set by the magnetosphere with variations in the actual recurrence times caused by the need for a solar wind driving interval to occur, (2) the mesoscale structure of the solar wind magnetic field triggers the oc-

currence of the random substorms, and (3) the large-scale structure of the solar wind plasma is responsible for the long intervals where no substorms occur. Statistically, the recurrence time of periodically occurring substorms is slightly shorter when the ram pressure of the solar wind is high, when the magnetic field strength of the solar wind is strong, when the Mach number of the solar wind is low, and when the polar-cap potential saturation parameter is high.

Second, SuperDARN radar data are used to investigate polar cap ionospheric flows under strongly dominant northward IMF. By considering line-of-sight velocities from SuperDARN radars looking in the meridional direction, it is shown that the near-noon flow is predominantly sunward in summer. The sunward velocity increases with intensification of the flow driver (the reverse convection electric field); the effect is stronger in summer and in the Southern hemisphere. Statistical patterns of the sunward flows along the noon-midnight meridian clearly indicate seasonal differences in the intensity and flow direction. Simultaneous SuperDARN convection maps in both hemispheres, averaged over periods of approximately two hours, show that sunward flows are faster in the summer hemisphere. In addition to this, while the sunward flows are aligned with the midnight-noon line in a winter hemisphere, they are oriented toward earlier magnetic local hours in a summer hemisphere.

Finally, data from the SuperDARN radars and DMSP and Swarm satellite are used to investigate plasma flows around polar cap arcs. Two cases of arcs, that are just detached from the auroral oval, are considered — one in the morning sector and one in the evening sector. It is shown that polar cap arcs introduce mesoscale structuring of the global convection pattern in the polar cap, and clear flow shears occur. The shears are interpreted as a superposition of the background plasma flow and relatively narrow channels of plasma flow intrinsically related to the polar cap arcs. PolarDARN radar observations at close ranges consistently indicate sunward flows collocating with the arcs. This result is additionally supported by DMSP satellite observations. According to the SuperDARN data, the detached arcs are preceded in time by the flow of the plasma from the auroral oval to the polar cap. It is hypothesised that such inflows are indicators that the formation of polar cap arcs is related to instability processes in the plasma sheet.

Acknowledgements

First of all, I would like to express my sincere gratitude and appreciation to my supervisor, Professor Alexandre Koustov (Sasha). First time our paths crossed when he, knowing nothing about me, agreed to help me with my Master thesis; this was a hard time for me, and Sasha's help and attitude played a key role in my successful graduation. After that he invited me to the University of Saskatchewan to work with him as a PhD student. During these years he was always very patient with me, which sometimes can be a challenging task. He gave me lots of freedom, I never was forced to work on something that I did not find interesting. Sasha always encouraged me to participate in conferences and summer schools, gave me lots of valuable advice about my future career and life. It was great to work with him and I learnt a lot from this experience. For all this, I am greatly indebted to him.

Thank you to many faculty members, researchers and staff I met at the University of Saskatchewan, especially to Drs. Andrei Smolyakov and Rainer Dick.

For the opportunity to participate in the CaNoRock PhD Summer School and the great experience I had during the School, I express my gratitude to Drs. David Knudsen, Kathryn McWilliams, Jøran Moen, Lasse Clausen and many others.

I am also most grateful for the LANL Vela Fellowship I received in 2016 which allowed me to spend entire summer at the Los Alamos National Laboratory as a participant of the LANL Space Weather Summer School. The time turned out to be crucial to my future career. My thanks go to all the people involved: to my supervisor for introducing to me this opportunity and giving me a lot of practical and moral support with application and travel; to the director of the Summer School Dr. Misa Cowee for the great organization; to Dr. Reiner Friedel for making this Fellowship possible and for brewing for us the best beer ever; to Drs.Vania Jordanova, Peter Gary, Mick Denton, Ari Li, Humberto Godinez, Richard Schirato and others who shared their time to introduce all the different research that is going on in the lab, their lectures were amazing and very motivating; to my husband who drove me across the U.S. and participated in the School with me even though space weather is not exactly his field of study. My special and separate gratitude is for my summer school mentor, Dr. Joe Borovsky. He is an incredible researcher and a unique person. His energy

and passion for work are inspiring. Joe was very generous with his time and experience, I was greatly enriched by our work together. Part of this thesis is the result of this work.

I am extremely grateful for the financial support which I received from the Department of Physics and Engineering Physics and Gerhard Herzberg Fund.

SuperDARN is a collection of radars funded by National Scientific Agencies of Australia, Canada, China, France, Japan, South Africa, United Kingdom, and United States of America. A free access to all SuperDARN data is higly appeciated. We thank particularly the Canadian Foundation for Innovation, NSERC and Canadian Space Agency who funded installation and operation of the PolarDARN radars. For the ground magnetometer data we gratefully acknowledge: Intermagnet; USGS, Jeffrey J. Love; CARISMA, PI Ian Mann; CANMOS; The S-RAMP Database, PI K. Yumoto and Dr. K. Shiokawa; The SPIDR database; AARI, PI Oleg Troshichev; The MACCS program, PI M. Engebretson, Geomagnetism Unit of the Geological Survey of Canada; GIMA; MEASURE, UCLA IGPP and Florida Institute of Technology; SAMBA, PI Eftyhia Zesta; 210 Chain, PI K. Yumoto; SAMNET, PI Farideh Honary; The institutes who maintain the IMAGE magnetometer array, PI Eija Tanskanen; AUTUMN, PI Martin Connors; DTU Space, PI Dr. Juergen Matzka; South Pole and McMurdo Magnetometer, PI's Louis J. Lanzarotti and Alan T. Weatherwax; ICESTAR; RAPIDMAG; PENGUIn; British Artarctic Survey; McMac, PI Dr. Peter Chi; BGS, PI Dr. Susan Macmillan; Pushkov Institute of Terrestrial Magnetism, Ionosphere and Radio Wave Propagation (IZMIRAN); GFZ, PI Dr. Juergen Matzka; MFGI, PI B. Heilig; IGFPAS, PI J. Reda; University of LAquila, PI M. Vellante; EMMA, MFGI PI B. Heilig, IGFPAS, J. Reda, University of L'Aquila, PI M. Vellante; Geoscience Australia, PI Marina Costelloe; BCMT, PI V. Lesur and A. Chambodut; Antarctic 40-degree magnetic meridian chain, PI R. Clauer; SuperMAG, PI Jesper W. Gjerloev. We acknowledge use of NASA/GSFC's Space Physics Data Facility's OMNIWeb service, and OMNI data. We thank Xianging Chu for supplying the MPB index and Tom Cayton for supplying the SOPA energetic-electron fits.

Thank you to my dear parents for their infinite love and many sacrifices they made for the sake of our future and to my sister for always being there for me. I cannot express how grateful I am for having such an amazing family.

My special thanks are to my beloved husband (concurrently best friend and soul mate) for

making me much happier person than I am used to be. His loving care and encouragement helped me keeping going with the thesis when the temptation to give up was especially strong.

Contents

List of Tables

List of Figures

List of Abbreviations

AACGM	Altitude-Adjusted Geomagnetic
CLY	Clyde River
CME	Coronal Mass Ejection
CRB	Convection Reversal Boundary
DCE	Dome-C East
DMSP	Defense Meteorological Satellite Program
DNL	Distant Neutral Line
EUV	Extreme Ultraviolet
HF	High Frequency
IDM	Ion Drift Meter
IGRF	International Geomagnetic Reference Field
IMF	Interplanetary Magnetic Field
INV	Inuvik
GDI	Gradient Drift Instability
GSM	Geocentric Solar Magnetospheric
FAC	Field-Aligned Current
FoV	Field of View
LANL	Los Alamos National Laboratory
LLBL	Low-Latitude Boundary Layer
l-o-s	line-of-sight
MCM	McMurdo
MLAT	Magnetic Latitude
MLT	Magnetic Local Time
MPB	Midlatitude Positive Bay
NENL	Near-Earth Neutral Line
OMTI	Optical Mesosphere Thermosphere Imager
PolarDARN	Polar Dual Auroral Radar Network
RB	Resolute Bay
RKN	Rankin Inlet
SCW	Substorm Current Wedge
SAPS	Sub-Auroral Polarization Stream
SOPA	Synchronous Orbit Particle Analyzer
SSM	Special Sensor Magnetometer
SuperDARN	Super Dual Auroral Radar Network
TII	Thermal Ion Imager
ULF	Ultra Low Frequency
UT	Universal Time

Chapter 1

Introduction

1.1 Sun-Earth environment

The importance of space weather becomes more and more widely recognised by people and governments [*Jonas and McCarron*, 2016]. According to the definition of space weather given by the European Space Weather Portal (`http://www.spaceweather.eu/en/glossary`), *"Space weather is the physical and phenomenological state of natural space environments. The associated discipline aims, through observation, monitoring, analysis and modelling, at understanding and predicting the state of the sun, the interplanetary and planetary environments, and the solar and non-solar driven perturbations that affect them; and also at forecasting and nowcasting the possible impacts on biological and technological systems."* Extreme space weather events can have detrimental effects on technological systems as well as human health and safety. For example, coronal mass ejections, among other effects, perturb the geomagnetic field, thus inducing electric currents in conductors on Earth (e.g., power transmission grids, cables, pipelines) which can cause power blackout and equipment damage. Geomagnetic storms and substorms also result in energization of radiation belts, which can severely damage spacecraft electronics and interfere with incoming and outgoing signals. During geomagnetic storms, perturbations of electron density in the ionosphere cause GPS errors. Solar flares can disrupt HF radio communication. There are many other space weather effects including particles and radiation effects in space, changes of low-altitude spacecraft orbits, etc. To be prepared for space weather events, we need to understand how different parts of the Sun-Earth system are related to each other and how processes in these different parts affect each other. This Chapter is a brief overview of key elements and processes in the Sun-Earth environment.

1.1.1 The solar wind and interplanetary magnetic field

The Sun is the main driver of space weather. The upper atmosphere of the Sun (corona) is continuously releasing some of its plasma into interplanetary space. Such outward plasma flow is called the solar wind. The induction equation for the solar wind plasma [e.g., *Treumann and Baumjohann*, 1997]:

$$\frac{\partial \mathbf{B}}{\partial t} = \nabla \times (\mathbf{v} \times \mathbf{B}) + \eta \nabla^2 \mathbf{B} \tag{1.1}$$

where $\mathbf{B}$ is the solar wind magnetic field, $\mathbf{v}$ is the solar wind plasma velocity, $\eta = 1/(\mu_0 \sigma)$ is the magnetic diffusivity, μ_0 is the permeability of free space, and σ is the plasma conductivity.

Equation 1.1 describes the evolution of the magnetic field in time. The first term on the right-hand side of the equation, called "convective term", describes changes of the magnetic field due to the plasma motion perpendicular to the magnetic field. The second term on the right, "diffusive term", describes diffusion of the magnetic field. The ratio of the convective term to the diffusive term is the magnetic Reynolds number:

$$R_m = \frac{L_0 v_0}{\eta} = \mu_0 \sigma L_0 v_0 \tag{1.2}$$

where v_0 is the characteristic speed and L_0 is the characteristic length scale of plasma. For the solar wind plasma anywhere except in close proximity to intense current sheets, $R_m >> 1$. Thus, the induction equation for the solar wind can be written as

$$\frac{\partial \mathbf{B}}{\partial t} = \nabla \times (\mathbf{v} \times \mathbf{B}) \tag{1.3}$$

which means that the electric field in the solar wind plasma should satisfy

$$\mathbf{E} = -\mathbf{v} \times \mathbf{B} \tag{1.4}$$

Equation 1.4 holds when $\sigma \to \infty$. It follows from Equation 1.3 that the magnetic field flux passing through any closed surface S which moves with the plasma, does not change in time. Indeed, the change of the magnetic field flux through the moving surface S can be written

as [*Spitzer*, 1962]

$$\frac{d\Phi}{dt} = \int\limits_S \left[\frac{\partial \mathbf{B}}{\partial t} - \nabla \times (\mathbf{v} \times \mathbf{B})\right] \cdot \mathbf{n} dS \tag{1.5}$$

Thus,

$$d\Phi/dt = 0 \tag{1.6}$$

This is the mathematical formulation of the frozen-flux (Alfvén) theorem which states that in a perfectly conducting plasma, magnetic field lines move with the plasma ("frozen" into the plasma).

The frozen-in condition means that as the solar wind leaves the Sun it carries along some of the solar magnetic field. This magnetic field is called the *interplanetary magnetic field (IMF)*. Electric conductivity at the base of the solar corona is very high and, therefore, the end of an IMF field line connected to the Sun rotates with the Sun, the other end is dragged radially outward by the solar wind. As a result, the IMF follows a spiral pattern known as the Parker spiral. The IMF at the heliospheric colatitude θ and radial distance r from the Sun is given by [e.g., *Brekke*, 2013]

$$B_r = B_0 \frac{r_0^2}{r^2} \tag{1.7a}$$

$$B_\theta = 0 \tag{1.7b}$$

$$B_\phi = -B_0 \frac{r_0^2 \Omega}{r v_r} \tag{1.7c}$$

where r_0 is the distance from the center of the Sun at which plasma leaves the solar atmosphere, B_0 is the strength of the magnetic field at this distance, Ω is the angular velocity of the Sun. At the distance of the Earth's orbit (1 AU) the direction of the IMF forms an angle of $\sim 45^\circ$ with the radial direction. Beyond 15 AU the angle is almost 90°. Equations 1.7a-1.7c are an approximation and in reality the IMF fluctuates about the Parker spiral configuration.

The direction of the IMF at the distance of Earth's orbit is a very important parameter in space physics and it is most often defined in the so-called *geocentric solar magnetospheric*

Table 1.1: Solar wind parameters at 1 AU from the 1963-2012 OMNI data set. Reproduced from *Borovsky* [2016].

Symbol	Median Value	5th Percentile	95th Percentile	Quantity
n_{sw}	5.3 cm^{-3}	1.9 cm^{-3}	17.1 cm^{-3}	Solar wind plasma density
v_{sw}	414 km/s	309 km/s	643 km/s	Solar wind bulk speed
B_{sw}	5.6 nT	2.7 nT	12.1 nT	IMF magnetic field strength
T_{ion}	7.0 eV	1.6 eV	26.5 eV	Plasma ion temperature
θ_{clock}	90°	15.6°	164.1°	IMF clock angle
M_A	8.0	4.0	15.9	Alfvén Mach number in the plasma
τ_{age}	100 hr	65 hr	135 hr	Plasma travel time from the Sun

(GSM) coordinate system. In this coordinate system the X axis points from the center of the Earth toward the Sun, the Y axis is perpendicular to the terrestrial magnetic dipole and the Z axis completes the right-hand coordinate system such that the positive Z is oriented in the same sense as the northern magnetic pole. The direction of the IMF in this coordinate system is usually given by a parameter called the clock angle:

$$\theta_{clock} = \cos^{-1}\left(\frac{B_Z}{\sqrt{B_y^2 + B_z^2}}\right) \tag{1.8}$$

$\theta_{clock} = 0°$ when the IMF is purely northward and $\theta_{clock} = 180°$ when the IMF is purely southward. Figure 1.1a is the distribution of the hourly averaged IMF clock angle θ_{clock}. The figure was obtained by binning 351,592 hourly averages of the IMF clock angle into 35 bins. The data for the solar wind magnetic field were obtained from the OMNI data set [*King and Papitashvili*, 2005]. The OMNI data set contains measurements of the solar wind magnetic field and plasma parameters assembled from a number of spacecrafts and propagated to the Earth's bow shock nose. The data are available at `https://omniweb.gsfc.nasa.gov`. The distribution peaks for θ_{clock} between $87.4° - 92.6°$ (see also Table 1.1 which gives the median clock angle of 90°). Green shaded area in Figure 1.1a highlights the distribution tail where $\theta_{clock} < 30°$. This corresponds to a criterion we use to select events in Chapter 4. Only about 9% of all observations correspond to this domain.

If we similarly define an angle α between the IMF B_x and IMF B_y components, the resulting distribution is plotted in Figure 1.1b. Here $\alpha = 0$ when the IMF is purely sunward and $\alpha = 180$ when the IMF is purely antisunward. The distribution peaks between 41.1°−

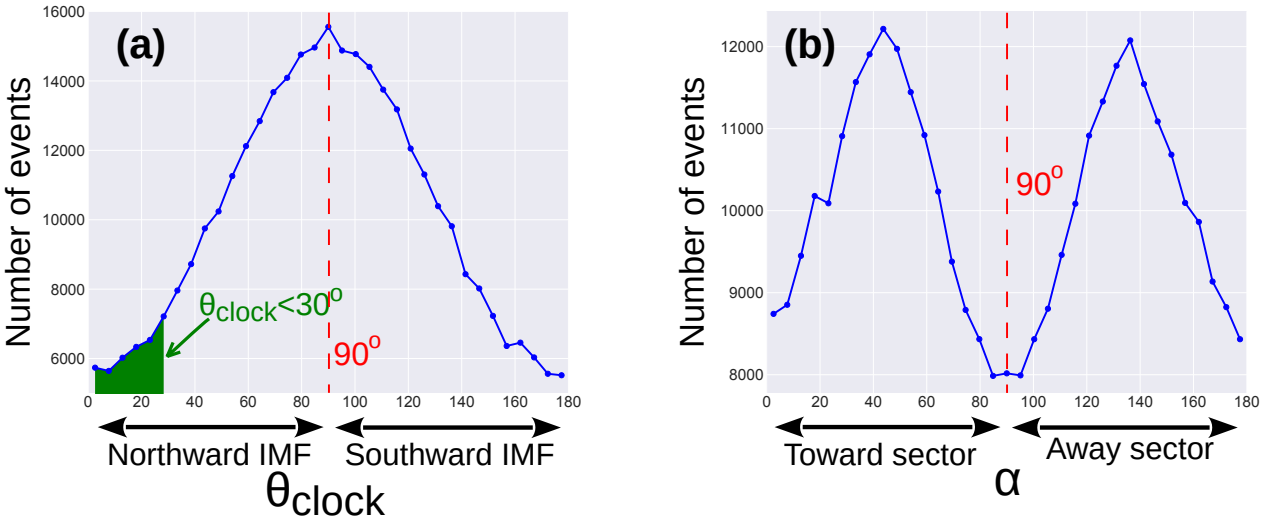

Figure 1.1: (a) The IMF clock angle and (b) angle between GSM B_x and B_y components of the IMF binned for 351,592 hourly averages for observations from 1963 to 2017. The data are from the OMNI data set.

46.3° and 133.7° − 138.9°. Therefore, on average, the IMF follows the Parker spiral. Note that $\alpha < 90°$ corresponds to the situation when the IMF roughly points toward the Sun and $\alpha > 90°$ when the IMF points away from the Sun. It has been found since early observations of the IMF that there is a sector structure in this field [*Ness and Wilcox*, 1965] such that the Earth is located either in a sector where the IMF is directed toward the Sun (in a so-called "toward" magnetic sector) or in a sector where the IMF is directed away from the Sun (in an "away" magnetic sector). Changes of the sector structure are associated with the solar rotation; the Earth encounters 2–4 sector reversals during one full rotation of the Sun about its axis.

Since the solar wind plasma is attached to the IMF and the Earth's plasma to the Earth's magnetic field, these plasmas cannot easily mix. Consequently, the terrestrial magnetic field is confined to a magnetic cavity called the *magnetosphere*. The solar wind deforms the dipole-like Earth's magnetic field to reach a pressure equilibrium. As a result, the magnetosphere is compressed and confined on the dayside extending to about $10R_E$ (R_E is the Earth's radius) and stretched into a long tail called the *magnetotail* on the nightside. The magnetotail extends far from the Earth, well beyond the lunar orbit. The solar wind is supersonic and superalfvenic (Table 1.1); as a consequence, a standing shock called *bow shock* forms, which slows, compresses and heats the solar wind plasma. Region of the shocked plasma downstream

of the bow shock is called the *magnetosheath*. The boundary separating solar wind plasma and the IMF from magnetosphere is called magnetopause. Magnetic field changes sharply across the magnetopause, therefore, according to the Ampèr's law, electric currents flow along the magnetopause.

1.1.2 Solar wind-magnetosphere coupling

In the mechanism outlined in the previous section, there is no connection between the solar wind and the magnetosphere; such a model is called a "closed magnetosphere". Exchange of the energy and momentum in the closed magnetosphere is possible through viscous interaction [*Axford and Hines*, 1961] which results in antisunward plasma motion at the flanks of the magnetosphere and sunward return flow in the inner magnetosphere. In reality, however, the magnetosphere is almost never closed, and it is widely accepted that the main process responsible for the solar wind-magnetosphere coupling is magnetic reconnection [*Dungey*, 1961; *Cowley*, 2013]. Magnetic reconnection takes place when the frozen-in condition breaks down and the second term on the right-hand side of Equation 1.1 becomes important. Magnetic field lines from different magnetic regions diffuse toward each other, break and reconnect into a different topology. *Dungey* [1961] was the first who suggested that magnetic reconnection at the nose of the magnetopause drives the convection in the magnetosphere. The process is shown schematically in Figure 1.2a. Here the magnetosphere is shown in the GSM coordinate system in the $X - Z$ plane as observed from the dusk side. The IMF in Figure 1.2a is purely southward and thus antiparallel to the terrestrial magnetic field lines at the subsolar point. In such circumstances reconnection is possible in this region (red dot "I") and magnetic field lines previously connected with both ends to the Earth ("closed" magnetic field lines) merge with the IMF field lines (line labelled 1 in Figure 1.2a). Such magnetic field lines become "open" in the sense This sequencend in connected to the Earth and the other is connected to the solar wind. The newly reconnected magnetic field lines are then dragged by the solar wind in the antisunward direction (positions 2-5). In the magnetotail northern and southern open magnetic field lines reconnect again at a second reconnection site (red dot "II") called distant neutral line (DNL), typically located about 100 R_E downtail from the Earth. Thus merged magnetic field lines (labelled by number 6 in Figure 1.2a) then move toward

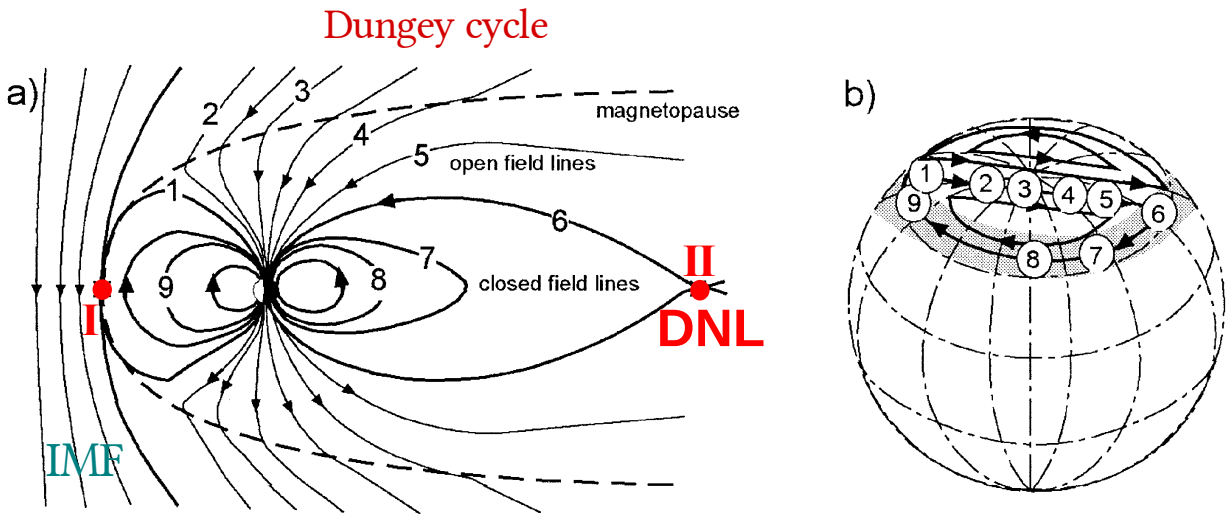

Figure 1.2: A sketch showing (a) reconnection and convection of magnetic field lines in a Dungey cycle for purely southward IMF; different numbers show sequential positions of the convecting magnetic field lines. (b) Motion of the ionospheric footprints of the convecting with the Dungey cycle magnetic field lines. From *Kivelson and Russell* [1995].

the Earth into the dipolar region of the magnetosphere (positions 7,8) and around the Earth back to the dayside magnetosphere (position 9) where the magnetic field lines will eventually reconnect with the solar wind again. This sequence (1-9) is called Dungey cycle. The ionospheric footprints of the magnetic field lines that move with the Dungey cycle, move in the same direction (Figure 1.2b). This corresponds to plasma convection in high-latitude ionosphere: antisunward plasma flow across the polar cap (positions 1-5) and sunward flow at lower latitudes (positions 6-9). The resulting pattern consists of two convection cells as shown in Figure 1.2b [*Heppner and Maynard*, 1987; *Cowley and Lockwood*, 1992].

When the IMF B_z turns positive, the solar wind magnetic field lines and the Earth's magnetic field lines at the subsolar point become parallel. Despite some indications that the dayside low-latitude reconnection can take place even for positive IMF B_z [e.g., *Scurry et al.*, 1994; *Phan et al.*, 1996; *Fuselier et al.*, 1997], the efficiency of such reconnection is very low and it continues only for large enough IMF clock angle ($\theta_{clock} > 45°$). However, the magnetosphere usually does not become closed even for very small IMF clock angles. It is believed that the reconnection can occur at high latitudes in the tail lobes, poleward of the cusps. The idea of the high-latitude lobe reconnection was first proposed by *Dungey* [1963].

There are many possible scenarios for the lobe reconnection [e.g., *Russell*, 1972; *Cowley*, 1981; *Cowley*, 1983; *Song and Russell*, 1992; *Lockwood and Moen*, 1999; *Watanabe et al.*, 2010]. The most popular scenario is schematically shown in Figure 1.3. In this scenario, tail magnetic field lines are open (lines labelled 1 and 2) and reconnection takes place only in one hemisphere. Reconnection occurs between interplanetary magnetic field lines i and opened previously during a period of southward IMF lobe magnetic field lines o at X. Note that in this situation no new open flux is generated, rather reconfiguration of old open flux occurs such that magnetic field line 2 transforms into magnetic field line 3, which then stirred by the solar wind [*Reiff*, 1982] around dusk and dawn flanks (positions 4,5) and returned back to the reconnection site by magnetic tension. The ionospheric footprints of these magnetic field lines move in sunward direction at the highest latitudes of the dayside polar cap (positions 1-3 in Figure 1.3b) and then return in antisunward direction at lower latitudes in the polar cap (positions 4-6). Emerging convection pattern consists of two small convection cells L in the polar cap and two viscous cells V [*Axford and Hines*, 1961] in the auroral zone.

An important issue of the solar wind-magnetosphere coupling is quantification of the process. Many driver functions that describe efficiency of the solar wind-magnetosphere reconnection have been proposed [e.g., *Rostoker et al.*, 1972; *Gonzalez and Mozer*, 1974; *Kan and Lee*, 1979; *Wygant et al.*, 1983; *Perreault and Akasofu*, 1978; *Vasyliunas et al.*, 1982; *Newell et al.*, 2007; *Borovsky and Birn*, 2014]. One of the most commonly used reconnection functions is the east-west component of the solar wind motional electric field $E_y = -v_{sw}B_z$, where v_{sw} is the solar wind velocity [*Gonzalez and Mozer*, 1974]. Although there is correlation between E_y and geomagnetic activity, the correlation coefficient is not very high. For example, Figure 1.4a examines correlation between auroral electrojet index AE (see Section 1.3.2) and the east-west component of the interplanetary electric field. The correlation coefficient between $-v_{sw}B_z$ and AE is +0.575 [*Borovsky*, 2016]. Various combinations of v_{sw}, θ_{clock}, and the IMF magnetic field B (or transverse to the Earth-Sun direction component $B_T = \sqrt{B_z^2 + B_y^2}$) were constructed. Among them the Newell "universal coupling function"

$$d\Phi_{MP}/dt = v_{sw}^{4/3} B_T^{2/3} \sin^{8/3}(\theta_{clock}/2) \tag{1.9}$$

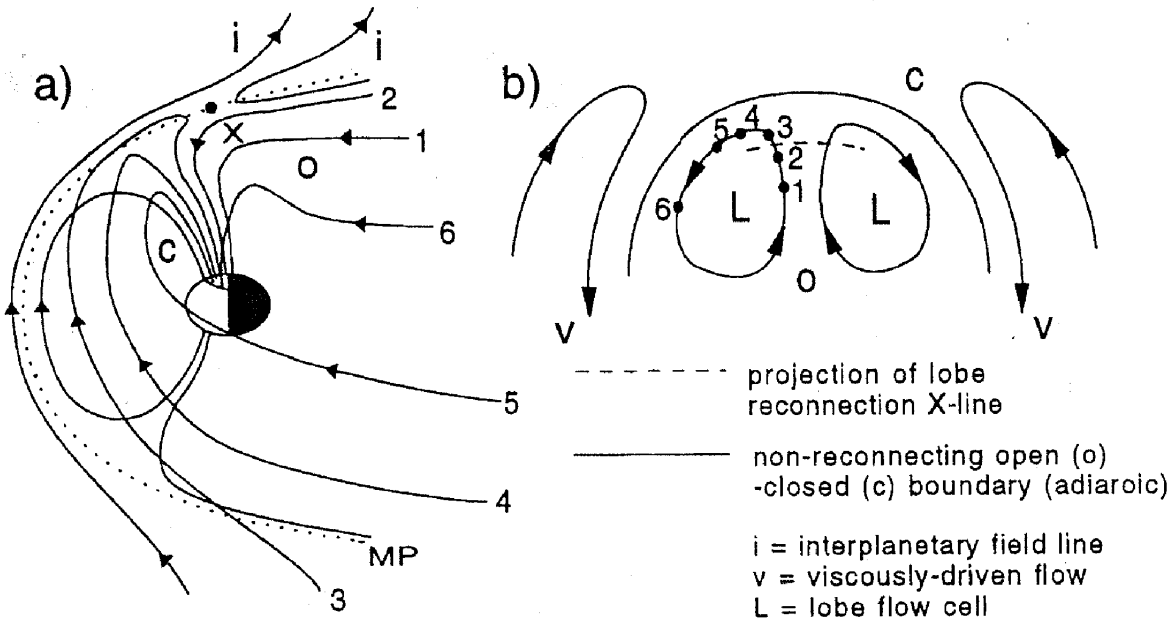

Figure 1.3: Schematics showing (a) reconnection and convection of magnetic field lines for northward IMF B_z; different numbers show sequential positions of the convecting magnetic field lines. (b) Motion of the ionospheric footprints of the convecting magnetic field lines. From *Lockwood and Moen* [1999].

shows the best correlation with various geomagnetic activity indices [*Newell et al.*, 2007]. Indeed, Figure 1.4 shows that $d\Phi_{MP}/dt$ correlates much better with AE comparing to E_y (correlation coefficient for $d\Phi_{MP}/dt$ is +0.775). *Borovsky and Birn* [2014] derived a new reconnection function R_{quick} based on a more realistic assumption that the solar wind-magnetosphere coupling is controlled by local parameters of the magnetosheath plasma rather than solar wind parameters in front of the bow shock. The R_{quick} in MKS units is:

$$R_{quick} = 2.04\mu_0^{1/2} m_p^{1/2} n_{sw}^{1/2} v_{sw}^2 \sin^2(\theta_{clock}/2) M_A^{-1.35} [1 + 680 M_A^{-3.30}]^{-1/4} \qquad (1.10)$$

where n_{sw} is the solar wind proton number density, v_{sw} is the solar wind velocity, θ_{clock} is the IMF clock angle with respect to the Earth's magnetic dipole, and $M_A = v_{sw}/v_A$ is the solar wind Alfvén Mach number, with $v_A = B_{sw}/(4\pi m_p n_{sw})^{1/2}$ being the Alfvén speed in the upstream solar wind, m_p is the proton mass. R_{quick} has even better correlation with geomagnetic activity as seen from Table 1 of *Borovsky and Birn* [2014].

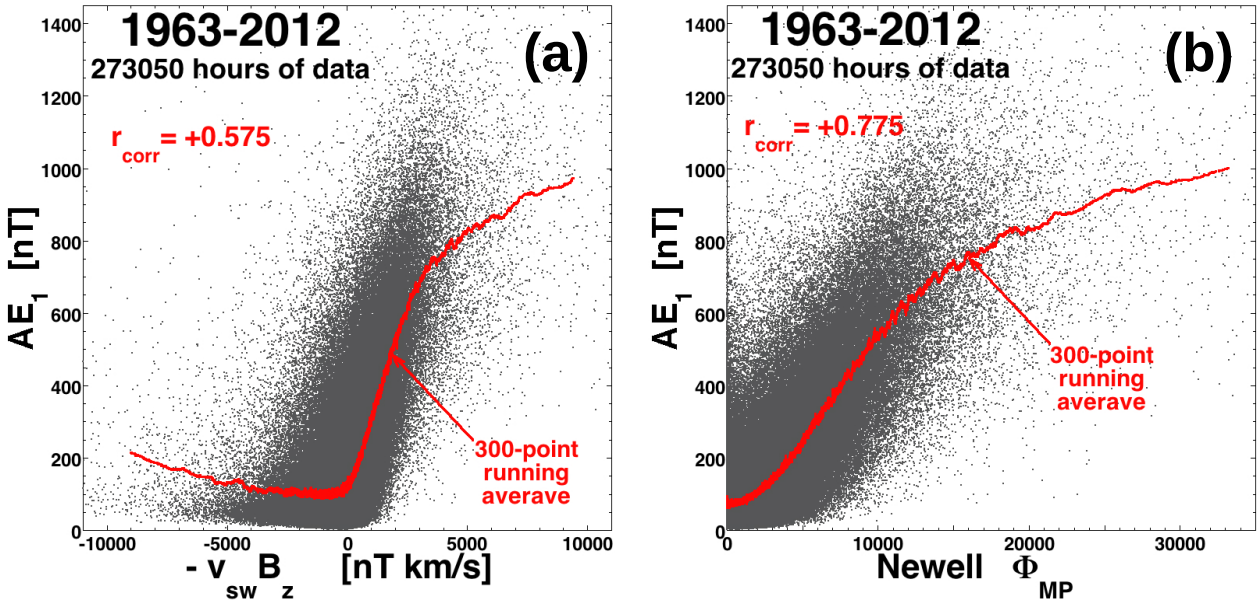

Figure 1.4: Hourly values of the auroral electrojet index AE plotted as functions of (a) measured value of $-v_{sw}B_z$ in the solar wind; (b) universal coupling function Φ_{MP} of *Newell et al.* [2007]. The gray points are the individual hourly values and the red points are 300-point running averages of the black points. From *Borovsky* [2016].

Much less attention has been paid to coupling functions quantifying the solar wind-lobe reconnection which occurs for northward IMF. *Wilder et al.* [2008] proposed an equation for an energy coupling function E_{RC} representing coupling at high-latitude lobe:

$$E_{RC} = VB_T \cos^4\theta \tag{1.11}$$

where V is $-Vx$ component of the solar wind velocity. The formula was successfully used by the authors to study saturation effect of the reverse convection potentials in the dayside polar cap.

1.1.3 The magnetosphere

A schematic representation of the Earth's magnetosphere is shown in Figure 1.5. The key magnetospheric regions and current systems are the following:

- *Low-Latitude Boundary Layer (LLBL)* is a region of plasma of the solar wind origin which penetrates from the magnetosheath inside the magnetosphere on the dawn and

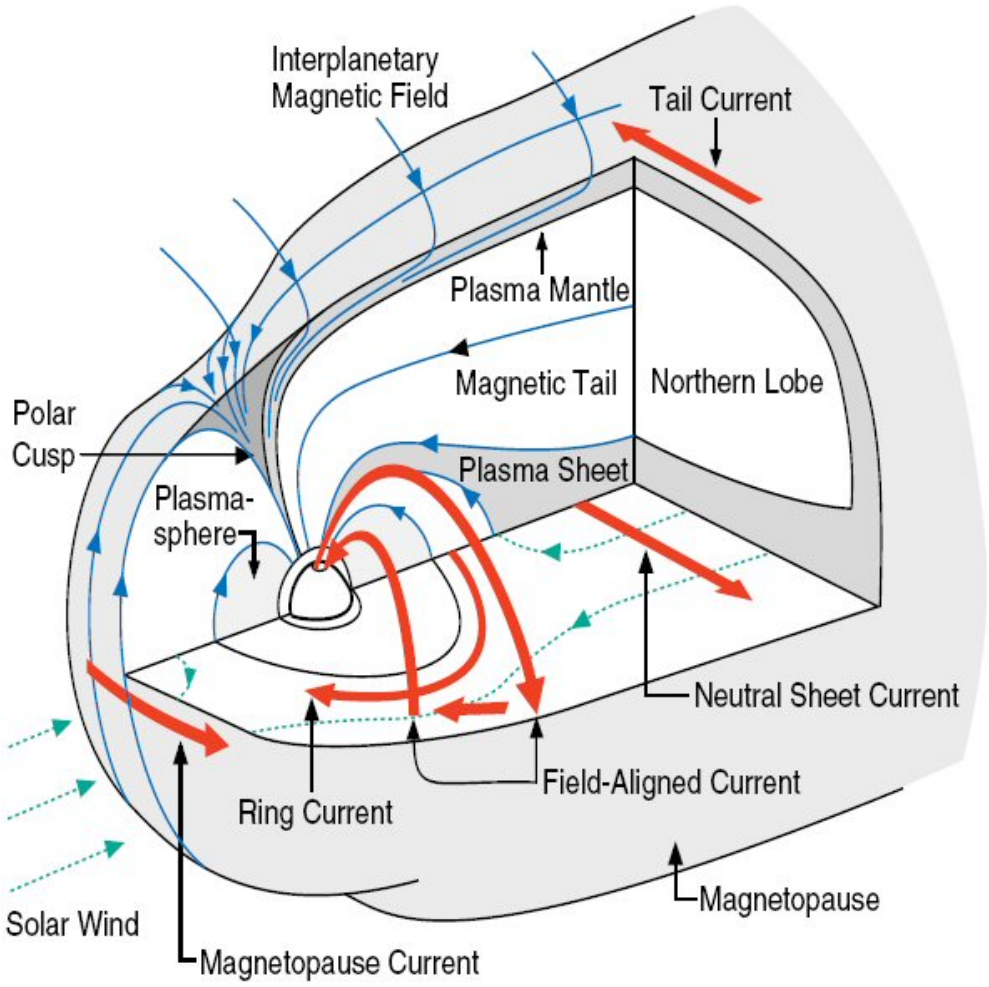

Figure 1.5: Cut away model of the terrestrial magnetosphere showing the plasma regions, magnetic field lines, electric currents and plasma flows. From *Russell* [2004].

dusk sides. Plasma in the LLBL is less dense and more hot than in the adjacent magnetosheath and it flows antisunward.

- *Cusps* are locations that separate regions where magnetic field lines from the Earth are directed sunward and magnetic field lines that are directed tailward. Cusp's ionospheric footprint is centered on local noon typically near 77° geomagnetic latitude, extending 2–3 hours in longitude and $\sim 1°$ in latitude. Plasma from the solar wind has direct access to the ionosphere through the cusps.

- *Lobes.* Magnetospheric regions occupied by magnetic field lines connected to the Earth's Southern and Northern polar caps. These are regions of very low plasma β ($\sim 3 \cdot 10^{-3}$)

cold rarefied (~ 0.01 cm^{-3}) plasma.

- *Plasma Sheet* is a magnetospheric region of a hot (several keV) low-density (~ 0.3 cm^{-3}) plasma that forms a flat sheet in the equatorial plane of the magnetotail. It is about 10 Earth's radii thick and $20 - 30$ R_E in the dawn-dusk direction. In the middle of the plasma sheet magnetic field is very low and thus the region is called *neutral sheet*. Magnetic field here reverses its direction from sunward north of the sheet to antisunward south of the sheet, consequently, a *cross-tail current* is flowing here from dawn to dusk.

- *Plasma Sheet Boundary Layer (PSBL)* is a transition layer from almost empty cold tail lobes to more dense hot plasma sheet; it is characterized by field-aligned beams of electrons and ions.

- *Plasmasphere* is a region of cold (~ 1 eV), dense ($10^0 - 10^3$ cm^{-3}) plasma of ionospheric origin in the inner magnetosphere. The outer boundary of the plasmasphere (*plasmapause*) is determined by a drop in plasma density by order of magnitude. Motion of charged particles here is controlled by the Earth's magnetic field and thus magnetospheric plasma co-rotates with the Earth.

- *Van Allen Radiation Belts* are regions occupied by high-energy charged particles trapped in the dipolar region of the magnetosphere (co-locating with the plasmasphere). The inner radiation belt (from about 1.1 to 3.3 R_E) is populated by highly energetic protons (with energies up to 100 MeV) and energetic electrons (~ 0.1 MeV). Outer radiation belt (3–9 R_E) consists mostly of energetic electrons with energies up to 10 MeV. The outer radiation belt is highly dynamic and variable depending on geomagnetic activity. A third radiation belt has been discovered in 2012 from Van Allen Probes observations. This radiation belt was temporarily observed during September 2012 at distances of $\sim 3 - 3.5$ R_E [*Baker et al.*, 2013].

- *Ring Current* is a large-scale current flowing in the inner magnetosphere at distances of about 3-7 R_E overlapping with the outer radiation belt. Charged particles in this region move with gradient-curvature drift with electrons moving eastward and ions moving westward thus producing a current circling the Earth.

- *Field-Aligned Currents (FACs)* are several sheets of currents that flow along magnetic field lines between the magnetosphere and high-latitude ionosphere. FACs play a key role in the magnetosphere-ionosphere coupling and will be discussed in Section 1.2.2.

1.2 Magnetosphere-ionosphere coupling

In the collisionless plasma dominating the magnetosphere, the parallel electric fields (electric fields aligned with magnetic field lines) give rise to motion of charged particles in such a direction that potential difference will decrease and the parallel electric field will short out. This means that there are no potential drops along magnetic field lines in the magnetosphere and magnetic field lines are equipotentials. Thus the distribution of the electric field in the magnetosphere maps along magnetic field lines into the ionosphere and vise versa. This way electrodynamic processes in the magnetosphere and ionosphere are coupled together causing exchange of energy and momentum between the two regions. This coupling is the reason for the ionospheric convection driven by magnetospheric convection described in Section 1.1.2. The coupling is also important for magnetospheric substorms, generation of aurora, flow of FACs, etc.

1.2.1 The ionosphere

The ionosphere is a region of the Earth's upper atmosphere where the number of free electrons and ions is significant enough to affect the propagation of radio waves. The main source of ionization in the ionosphere is the solar UV radiation and X-rays. Ionization of the high-latitude ionosphere is also affected significantly by energetic particle precipitation from the magnetosphere. The ionosphere starts at an altitude of about 50 km and extends to more than 1000 km. It is customary to subdivide the ionosphere into layers or, more correctly, regions called D, E, and F regions. The D region extends from $\sim$ 50 km to $\sim$ 90 km, its typical electron densities are low, of the order of $10^2 - 10^3$ cm^{-3}, during daytime and the region almost vanishes at night. Although plasma density in the D region is low, it affects radio waves significantly because radiowave absorption is very strong in this region. The E region lies at altitudes between about 90 and 140 km. Variations of plasma density

in the E region approximately follow the Chapman model [*Chapman*, 1931] with diurnal maximum at local noon (maximum of about 10^5 cm^{-3} at $\sim$ 120 km) and seasonal maximum in summer. At night the E layer becomes very weakly ionized. The upper, F layer, extends from $\sim$ 150 km to $\sim$ 600 km; the plasma densities are the highest in this region, typically of order of 10^6 cm^{-3} around 250 km altitude. In the *F2* and upper F regions transport processes become important in the distribution of the plasma density.

Unlike solar wind and magnetospheric plasma, plasma in the ionosphere is cold, dense, and collisional. Collisions occur mainly between charged particles and neutrals such that the motion of the charged particles is affected differently by electromagnetic forces. The ionospheric medium becomes non-isotropic which makes the ionospheric conductivity to be a tensor quantity [*Kivelson and Russell*, 1995]:

$$\overline{\overline{\sigma}} = \begin{pmatrix} \sigma_P & \sigma_H & 0 \\ -\sigma_H & \sigma_P & 0 \\ 0 & 0 & \sigma_\parallel \end{pmatrix} \tag{1.12}$$

where

$$\sigma_P = \frac{n_e e^2}{m_e} \left(\frac{\nu_{en}}{\nu_{en}^2 + \Omega_e^2} + \frac{m_e}{m_i} \frac{\nu_{in}}{\nu_{in}^2 + \Omega_i^2} \right) \tag{1.13}$$

$$\sigma_H = \frac{n_e e^2}{m_e} \left(\frac{\Omega_e}{\nu_{en}^2 + \Omega_e^2} - \frac{m_e}{m_i} \frac{\Omega_i}{\nu_{in}^2 + \Omega_i^2} \right) \tag{1.14}$$

$$\sigma_\parallel = \frac{n_e e^2}{m_e} \left(\frac{1}{\nu_{en}} + \frac{m_e}{m_i} \frac{1}{\nu_{in}} \right) \tag{1.15}$$

where $\nu_{en}(\nu_{in})$ is the electron (ion) collision frequency with neutrals, $\Omega_e(\Omega_i)$ is the electron (ion) gyrofrequency, n_e is the electron number density, e is the elementary charge, σ_P is the Pedersen conductivity, i.e. the conductivity in the direction perpendicular to the magnetic field and parallel to the electric field, σ_H is the Hall conductivity, i.e. the conductivity perpendicular to both the electric and magnetic fields, $\sigma_\parallel$ is the parallel conductivity, i.e. the conductivity along magnetic field lines; the parallel conductivity is conductivity of plasma in the absence of magnetic field.

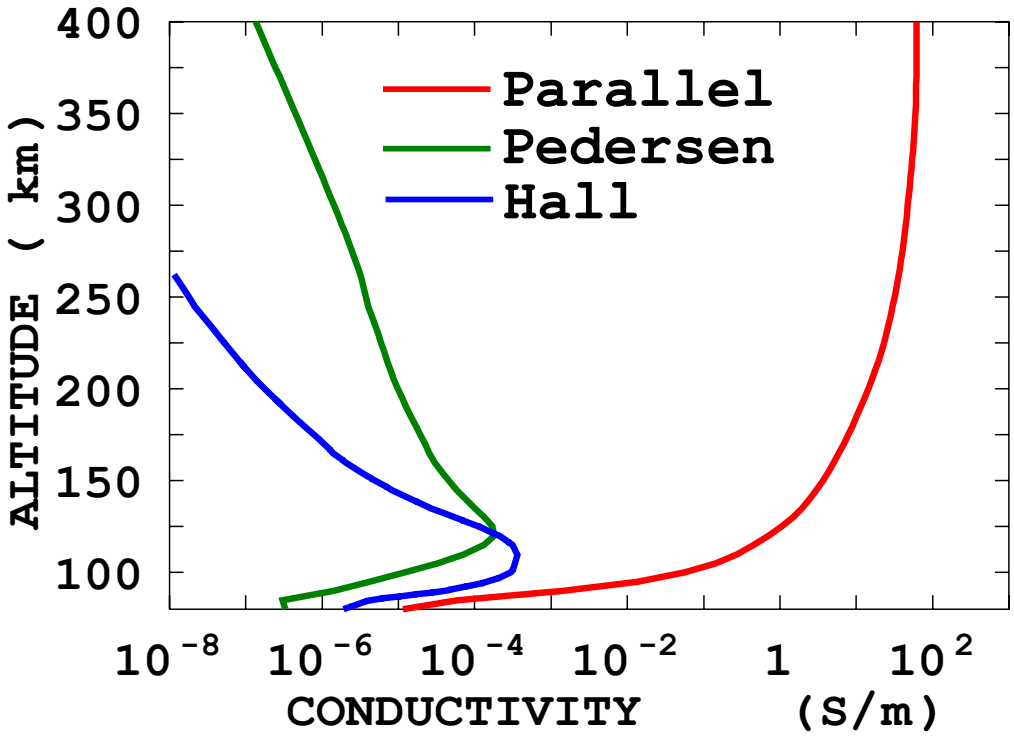

Figure 1.6: An example of modelled altitude profile of the ionospheric conductivity over Saskatoon on 28 April 2017. The data for the plot were obtained Equations 1.13-1.15 using model ionospheric (from the IRI model [*Bilitza*, 2001]) and atmospheric (from the NRLMSISE-00 model [*Picone et al.*, 2002]) parameters and equations for collision frequencies of charged ionospheric particles with neutrals from *Banks and Kockarts* [2013].

The ionospheric Ohm's law then can be written as

$$\mathbf{j} = \sigma_P \mathbf{E}_\perp - \sigma_H \left(\frac{\mathbf{E}_\perp \times \mathbf{B}}{B} \right) + \sigma_\parallel \mathbf{E}_\parallel \tag{1.16}$$

Thus currents in the ionosphere have three components: parallel to the electric field and perpendicular to the magnetic field (Pedersen current), in the $\mathbf{E} \times \mathbf{B}$ direction (Hall current), and parallel to the magnetic field (FAC).

The ionospheric conductivity varies with location, local time, season, and solar activity. In Figure 1.6 altitude variations of modelled parallel (red line), Pedersen (green line), and Hall (blue line) conductivities are shown for Saskatoon location on 28 April 2017. It is seen that the parallel conductivity is much larger than the Hall and Pedersen conductivities. The Pedersen and Hall conductivities are low in the F region, and thus currents there are very

low. This is because in the F region electron and ion gyrofrequencies are much higher than their respective collision frequency with neutrals ($\Omega_i >> \nu_{in}$, $\Omega_e >> \nu_{en}$), thus their motion is controlled mainly by magnetic field: both species move with $\mathbf{E} \times \mathbf{B}$ drift (note particularly low Hall conductivity in the F region). Both Hall and Pedersen conductivities peak in the E region at altitudes between about 100 and 150 km, this region is called the *dynamo region*. The strong currents in the dynamo region are due to the fact that while motion of electrons here is still controlled by the magnetic field ($\Omega_e >> \nu_{en}$), ion gyrofrequency becomes smaller than ion-neutral collision frequency ($\Omega_i < \nu_{in}$). Ions no longer $\mathbf{E} \times \mathbf{B}$ drift and move partly along the electric field; this motion contributes to the Pedersen current. The Hall current in the dynamo region is carried by electrons.

1.2.2 Field-aligned and convection currents

Ring-like regions of the ionosphere centered on the Northern and Southern geomagnetic poles and magnetically connected to the plasma sheet and plasma sheet boundary layer are called the *auroral ovals*. Charged particles from the plasma sheet precipitate along magnetic field lines into the auroral ionosphere, significantly increasing its conductivity. The increased conductivity, together with the electric fields of magnetospheric origin, result in two intense currents flowing inside the auroral ovals from noon toward midnight (Figure 1.7a); these currents are called *convective electrojets*. The eastward electrojet flows in the afternoon sector and westward electrojet flows in the morning and midnight sector. The eastward and westward electrojets are Hall currents which are fed by FACs flowing into the ionosphere around noon; the electrojets leave the auroral oval in the midnight sector.

Figure 1.7b shows the electric field pattern in the auroral oval. The electric fields are directed poleward in the afternoon and evening sectors and equatorward in the midnight and morning sectors. The auroral electric fields are associated with Pedersen currents in the ionospheric dynamo region. The currents are roughly oriented in the noon-south direction (Figure 1.7c) and serve as the major contribution to the closure of FACs. FACs play a fundamental role in coupling between the magnetosphere and auroral ionosphere. If a flow disturbance arises on one end of a magnetic flux tube, FAC must develop in order to transfer the changes to the entire flux tube. Two main large-scale systems of FACs flowing between

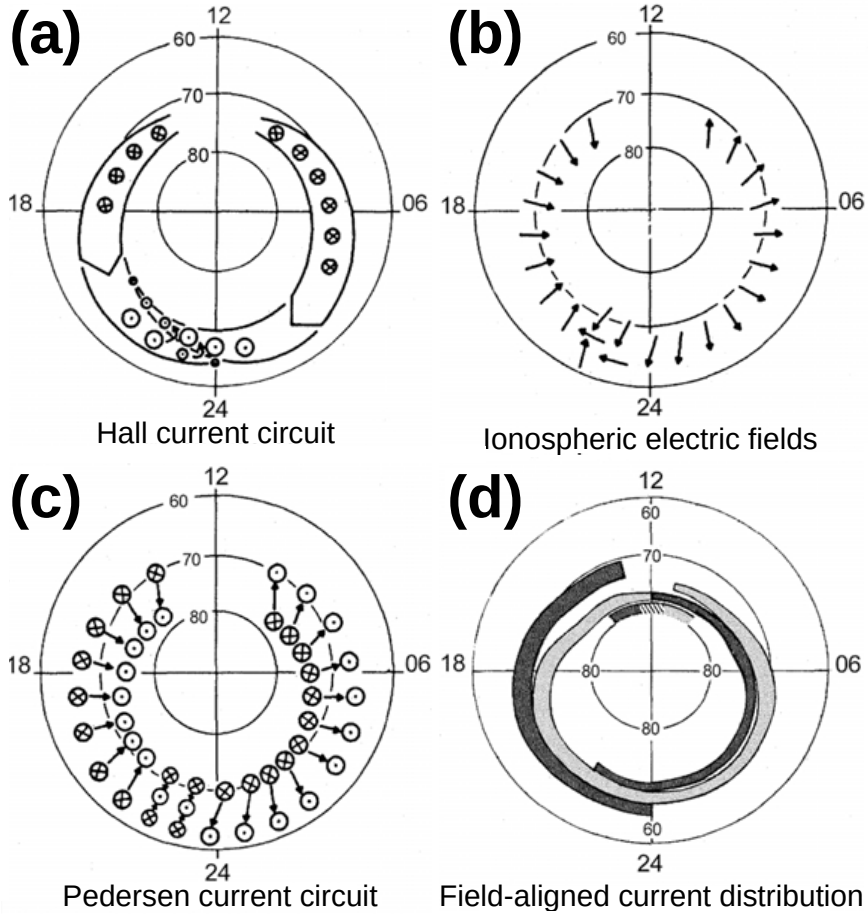

Figure 1.7: Currents and electric fields in the ionosphere. (a) Auroral electrojets (Hall currents) and associated FACs; (b) distribution of perpendicular electric fields in the auroral oval; (c) Pedersen currents and associated FACs. Panels (a)-(c) from *Baumjohann and Treumann* [1996]. (d) Statistical pattern of FAC distribution, dark regions indicate downward FACs, light grey regions – upward FACs (from *Iijima and Potemra* [1976]).

the magnetosphere and ionosphere are Region 1 and Region 2 currents. Figure 1.7d shows statistical distribution of FACs as determined by *Iijima and Potemra* [1976]. The downward (upward) portions of the currents are shown by dark (light grey) colors. Region 1 currents originate from the LLBL and enter the ionosphere at the poleward edge of the auroral oval. Region 1 currents flow downward into the ionosphere in the morning sector and upward back to the magnetosphere in the evening sector. Region 2 FACs originate in the inner magnetosphere and enter the ionosphere at the equatorward side of the auroral oval. They

are directed opposite to the Region 1 currents and thus flow into the ionosphere at the dusk and out of the ionosphere at the dawn.

1.2.3 The aurora

Aurora occurs mainly within the auroral oval where magnetospheric charged particles precipitate along the magnetic field lines from the plasma sheet and plasma sheet boundary layer into the ionosphere. Ionospheric regions poleward to the auroral ovals, *polar caps*, are normally void of auroral precipitation because they are magnetically connected to magnetotail lobes, where plasma is cold and very rarefied. When the charged particles (mainly electrons, but proton aurora is also observed at lower latitudes) hit the Earth's upper atmosphere, they excite the atmospheric atoms and molecules. Subsequent de-excitation of the atoms and molecules produces visual aurorae. The color of the aurora depends on the energy of precipitating particles and type and electrical state of the atmospheric atoms and molecules that are being excited. The most frequently observed aurora, green aurora, is produced by excitation of atomic oxygen at altitudes of 100-250 km. At higher altitudes excited atomic oxygen produces red emission. Red auroral glow is also produced at low altitudes of about 100 km by molecular nitrogen.

Two broad classes of auroral precipitation are called *diffuse* and *discrete* aurora. The equatorward part of the auroral oval is made up of diffuse aurora. Diffuse aurora is relatively uniform featureless glow caused by charged particles of ~ 1 keV originating from the inner plasma sheet. The most intense diffuse aurora is observed in the post-midnight sector. At higher latitudes, in the region of upward FACs, the discrete aurorae are often observed. The discrete aurora or auroral arc is a band of optical emission caused by highly energetic electrons originating in the plasma sheet boundary layer. Auroral arcs are narrow in the north-south direction (< 100 km) and can extend over several thousand kilometers in the east-west direction. The auroral arcs are caused by high-energy (of several keV) precipitating electrons that originate in the plasma sheet boundary layer. The electrons are accelerated by an upward parallel electric field [*Reiff et al.*, 1988; *McFadden et al.*, 1999], however it is not clear how the parallel electric field can be maintained in the collisionless magnetospheric plasma. Occurrence of auroral arcs within the auroral oval correlates with southward component of

the interplanetary magnetic field (IMF) and disturbed geomagnetic conditions.

1.3 Substorms

As discussed in Section 1.1.2, magnetic flux, opened on the frontside magnetosphere by a process of reconnection, is then transported by the solar wind in antisunward direction and laid down in the magnetotail. In the magnetotail, the flux reconnects again at the DNL and convects back to the dayside magnetosphere. During periods of strong solar wind-magnetosphere coupling, which is usually associated with southward IMF, rates of the dayside reconnection become larger than rates of the nightside reconnection. As a result, magnetic flux accumulates in the tail. The accumulation of magnetic energy defines the first of the three phases of the substorm, the *growth* phase. During the growth phase, diameter of the magnetotail increases, consequently, the size of the polar cap increases and auroral oval moves to lower latitudes. The increase of the magnetic field in the magnetotail lobes is accompanied by thinning of the plasma sheet and enhancement of the cross-tail current. The latter leads to stretching of tail lobe magnetic field lines as schematically shown in the top panel of Figure 1.8. The growth phase lasts typically around 1 hour.

As more and more energy is deposited in the magnetotail, the tail becomes unstable and eventually the energy is released explosively into the entire magnetosphere-ionosphere system. This phase is called *expansion phase* and the beginning of the phase is called substorm onset. Although the exact mechanism that triggers substorm onset is not yet a fully resolved question, it is widely accepted that the key event is the formation of an X-type neutral line, the near-Earth neutral line (NENL) [*McPherron et al.*, 1973a], in the near-Earth plasma sheet (10-20 R_E). Reconnection at the NENL results in distinct topological changes of the magnetotail. After the reconnection, two sets of closed magnetic field lines are formed. Earthward of the NENL, previously stretched magnetic field lines return to a more dipolar configuration, this process is called *dipolarization*. Downtail of the reconnection site, between NENL and DNL, forms a large bubble of plasma called plasmoid [*Hones et al.*, 1986] as sketched in the middle panel of Figure 1.8. The magnetic field of the plasmoid is disconnected

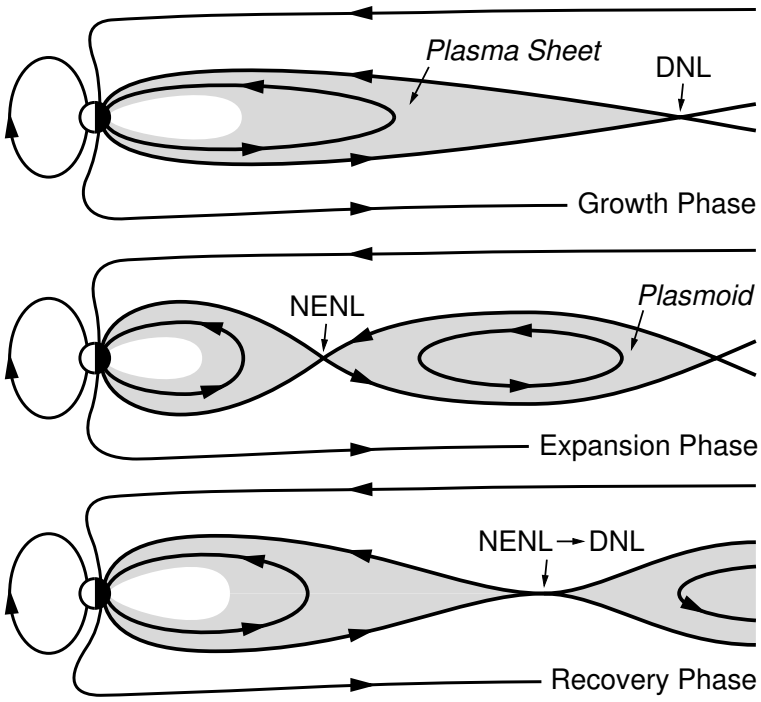

Figure 1.8: Reconfiguration of the magnetotail during the three substorm phases. From *Baumjohann and Treumann* [1996].

from both the Earth and the solar wind; after the disconnection, the plasmoid moves in antisunward direction and eventually leaves the magnetosphere. The expansion phase lasts 10–60 min. During the final phase of the substorm, *recovery* phase, magnetosphere returns to its quiet state. NENL moves tailward (Figure 1.8, bottom panel), plasma sheet recovers. The recovery phase lasts 30 min to 3 hours.

The substorm onset manifests itself in a number of mangetospheric and ionospheric phenomena. The dipolarization results in an injection of energetic particles (tens of keV) into the outer radiation belt such that satellites located at the geosynchronous orbit start to detect increased fluxes of electrons and ions. During the expansion phase the near-Earth part of the cross-tail current disrupts [e.g., *Fairfield and Ness*, 1970] and diverges into the ionosphere. As a result, a new current system called the substorm current wedge (SCW) forms [*McPherron et al.*, 1973a]. As shown in Figure 1.9, the SCW consists of two sheets of FACs, downward FAC to the east of the central meridian and upward FAC to the west from the central meridian. The FACs are closed in the ionosphere by a westward electrojet. The SCW perturbs the geomagnetic field in the auroral oval and at midlatitudes producing

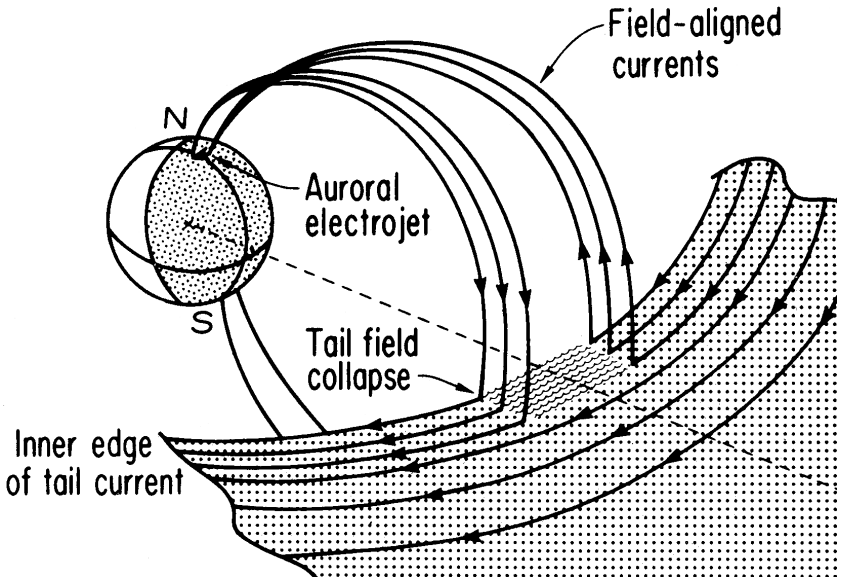

Figure 1.9: A sketch showing substorm current wedge. From *McPherron et al.* [1973a].

distinct signatures in the ground-based magnetometer records. Fluctuations in the SCW lead to ULF-range magnetic perturbations called Pi 2 pulsations. Perhaps the most prominent ionospheric manifestation of the magnetospheric substorm is the auroral breakup, or sudden brightening and disruption of an auroral arc in the midnight sector.

1.3.1 Auroral substorm

First morphological description of the auroral substorm was given by *Akasofu* [1964]. During the growth phase a system of discrete arcs, typically in the premidnight auroral oval, move equatorward. The onset of the auroral substorm begins when one of the most equatorward arcs brightens suddenly and breaks into separate features. The onset is often called the auroral breakup. In Figure 1.10a the auroral oval is shown just before a substorm breakup. In the next frame (b) first signs of the auroral breakup are seen in the auroral oval at ∼21–22 MLT. After the breakup, the brightening expands poleward and westward. In Figure 1.10 this expansion is seen in frames c-f. This expanding bright region of auroral activity is called auroral bulge. The bulge intensification and expansion is not continuous and evolves as a series of pulse-like intensifications. Although it is not seen from rather poor resolution in

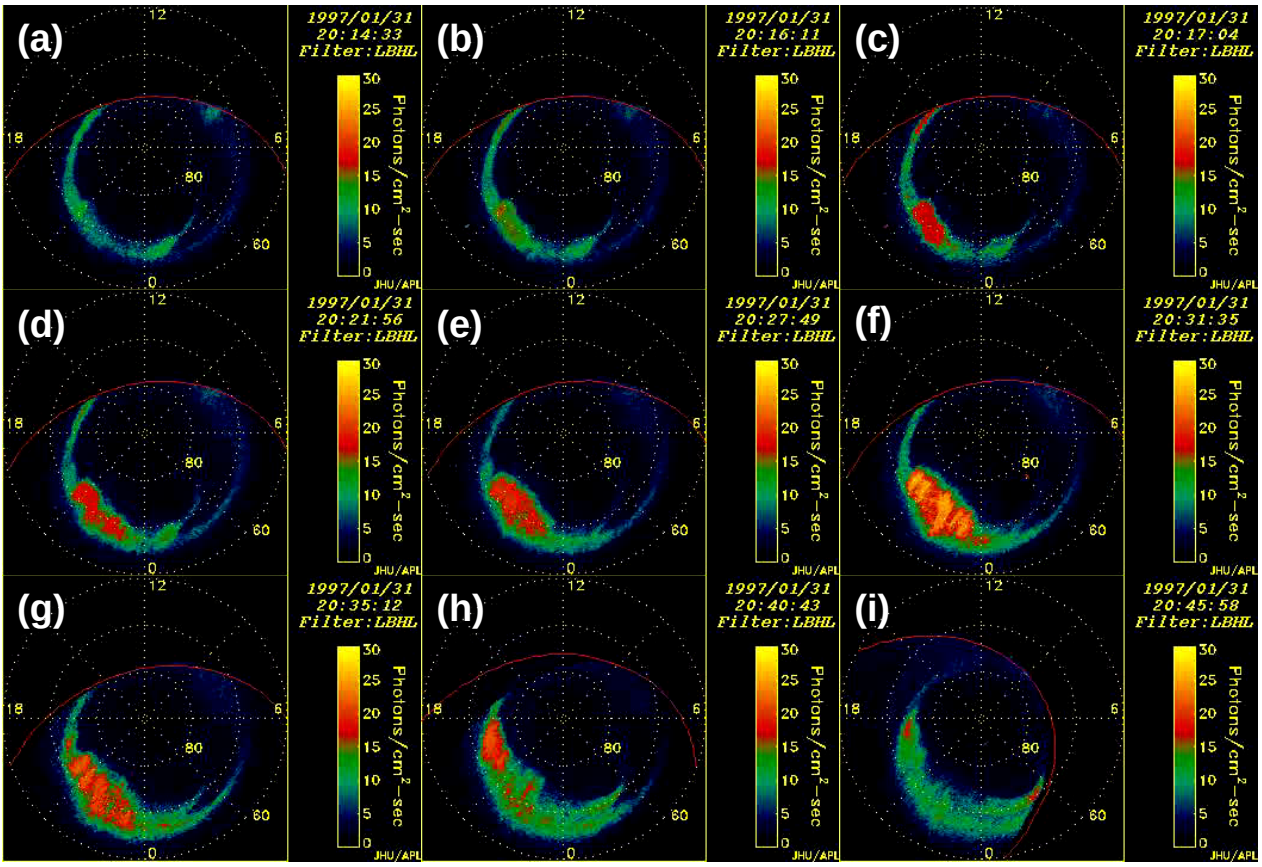

Figure 1.10: Sequence of images of the Norther auroral oval demonstrating development of an auroral substorm. The images were taken with the UVI instrument onboard of the NASA Polar satellite on 31 January 1997. The images are shown in the MLT-MLAT coordinate system.

Figure 1.10, the auroral bulge consists of various rapidly changing forms: folded discrete arcs, spirals, fragments of arcs, pulsating patches, etc. At the northwestern part of the auroral bulge eventually develops a sharply curved auroral band that travels westward. This band is called westward travelling surge. Occasionally, longitudinally confined north-south oriented auroral structures sporadically occur within the bulge [*Rostoker et al.*, 1987]. These finger-like structures also named auroral streamers can be distinguished in Figure 1.10f. The auroral streamers typically occur at the beginning of the recovery phase. The recovery phase begins when the substorm auroral bulge reaches its highest latitude and starts to retreat equatorward and dim (Figure 1.10g-h). Eastward propagating wave-like auroral structures called omega bands tend to develop during the recovery phase. Often during recovery phase a "double oval" forms [*Elphinstone and Hearn*, 1993], consisting of two regions of activity,

the main oval and another oval locating poleward of the normal oval, separated by a dark region. A real substorm may depart from the given above schematics and there are events that can be misidentified as substorms (e.g., pseudobreakups). During geomagnetically active times the midnight auroral oval is very active and dynamic so it is difficult to tell where one substorm ends and another begins. In addition, every substorm is unique, this all makes it challenging at times to identify a substorm from a single data set.

1.3.2 Ground magnetic perturbations

For general assessment of magnetic activity, planetary magnetic index Kp was introduced [e.g., *Kivelson and Russell*, 1995]. It is a measure of magnetic disturbance derived from a set (13) of magnetometers located at subauroral latitudes. The strength of the westward and eastward auroral electrojets can be estimated by measuring magnetic effects of the currents on the ground. Analysis of magnetic field data from auroral magnetometer stations can be an extensive task. To simplify this analysis, special indices were devised to provide a measure of electrojet activity. These indices were introduced by *Davis and Sugiura* [1966] and called the auroral electrojet indices AU, AL, and AE. The auroral electrojet indices are derived from a number (typically 10–13) of ground-based magnetometer stations distributed in local time along the typical auroral oval latitude region in the Northern hemisphere. The horizontal component H of the geomagnetic field is recorded by each station. Next, a baseline is subtracted from all the measurements. The baseline is determined each month for each station as the average H value measured by each station on the five international quietest days. Then for each UT time the largest and smallest values of the data obtained from all the stations are defined as AU and AL indices, respectively. Basically, the AU (AL) index is the upper (lower) envelope of the superposed component H measured by each station with the baseline subtracted off. The AE index is defined as the difference AU-AL. The negative H perturbations (measured by the AL index) correspond to the westward electrojet and the positive perturbations (measured by the AU index) – to the eastward electrojet.

As was discussed earlier, the SCW closes in the ionosphere by a westward electrojet flowing in the midnight portion of the auroral oval. Thus, during a substorm, the westward electrojet increases and the AL index drops to more negative values. Figure 1.11 shows

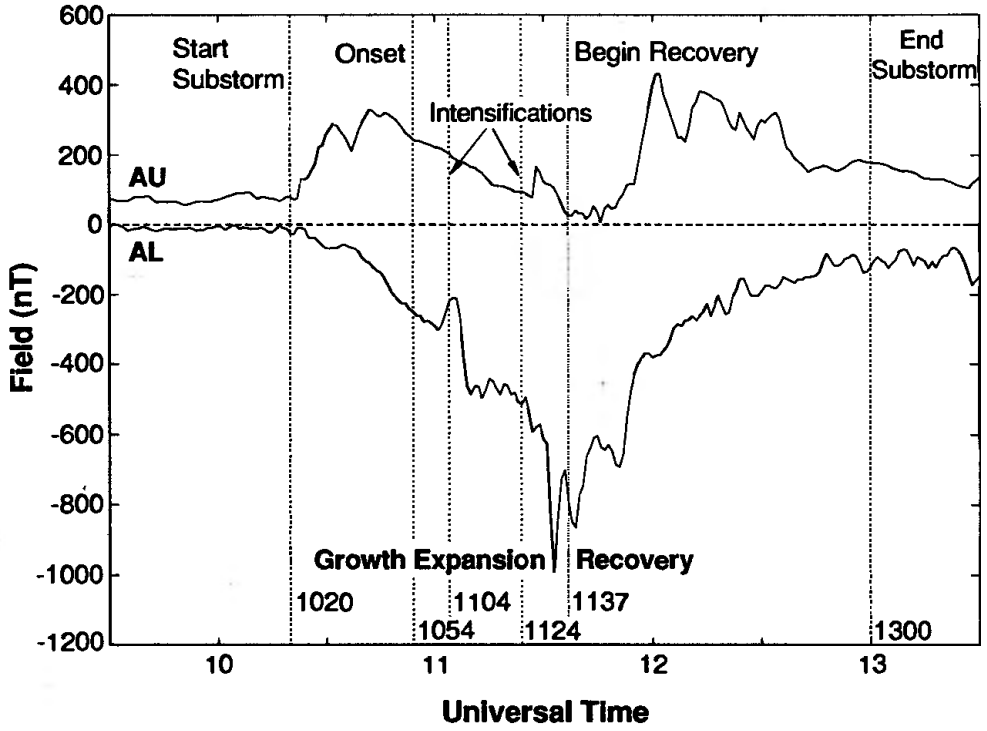

Figure 1.11: Variations of the AU and AL indices during a well-studied substorm. The three substorm phases and their start and end moments are labelled in the figure. From [*Kivelson and Russell*, 1995].

variations of the AU and AL indices during a substorm. AL index decreases up to -1000 nT during the growth phase. The substorm onset is usually defined by the time when the slope of the AL index increases suddenly. After the AL index reaches a minimum value, it begins to grow back to its pre-substorm values. This corresponds to the recovery phase. Note that sharp negative excursions are observed not only at the onset time, but also several times during the expansion phase and even during the recovery phase. These negative excursions are called substorm intensifications and should be distinguished from the onset. The growth phase in the time records of the AL index is marked by a slow decrease of the AL index. The growth phase is usually seen in isolated substorms but can be difficult to distinguish during substorms that closely follow each other. The negative excursion of the AL index associated with the expansion phase is also called negative bay. The negative bay is one of the manifestations of the magnetospheric substorm. The AU index does not show a distinctive pattern of changes associated with the substorm.

In contrast to the auroral zone, variations in the H component at midlatitudes show a positive excursion, or positive bay [*McPherron et al.*, 1973b]. These perturbations are caused by the FAC sheets of the SCW. The FACs disturb geomagnetic field at midlatitudes such that perturbation of the east component is asymmetric about the central meridian of the SCW with largest amplitudes at the locations of the FACs; the north-south perturbation is symmetric about the central meridian with the largest values along the central meridian. Analysis of the midlatitude perturbations allow us to determine the location of the SCW-associated FACs and estimate the strength of the currents. It is also possible to infer substorm onset from the midlatitude magnetic records. Similarly to the auroral electrojet indices, attempts were made to devise a midlatitude positive bay index. Different implementations of this index are discussed in *McPherron and Chu* [2017].

1.3.3 Substorm injections

Substorm injections are sharp and dramatic enhancements of particle fluxes in the inner magnetosphere. Substorm injections are often observed at geosynchronous orbit ($\sim 6.6\ R_E$) in association with substorms and they are considered to be one of the most reliable indicators of substorm onset [e.g., *Reeves et al.*, 1996]. Both electrons and ions with typical energies in the range of tens to hundreds keV are injected during substorms. When fluxes at all energies are enhanced simultaneously, it is referred to as a dispersionless injection. The region in the inner magnetosphere where dispersionless injections are observed is referred to as injection region. Typical extent of the injection region is several local time hours in the premidnight sector [e.g., *Reeves et al.*, 1991]. There is also a small azimuthal separation between electron and ion injection region with electrons being offset eastward relatively to ions [*Birn et al.*, 1997; *Thomsen et al.*, 2001]. Dispersionless injections commence at radial distances of about $6.6 - 9\ R_E$ and then expand radially earthward and tailward [*Spanswick et al.*, 2010]. The question of what exactly initiates substorm injections is not fully understood.

Figure 1.12a illustrates a typical dispersionless substorm injection. Four LANL geostationary satellites were operating during a substorm event on 29 August 2014. Figure 1.12c shows schematically positions of the satellites at the time of the substorm onset. The geosynchronous orbit is shown as a red circle, labels on the circle are local time hours. Pink shaded

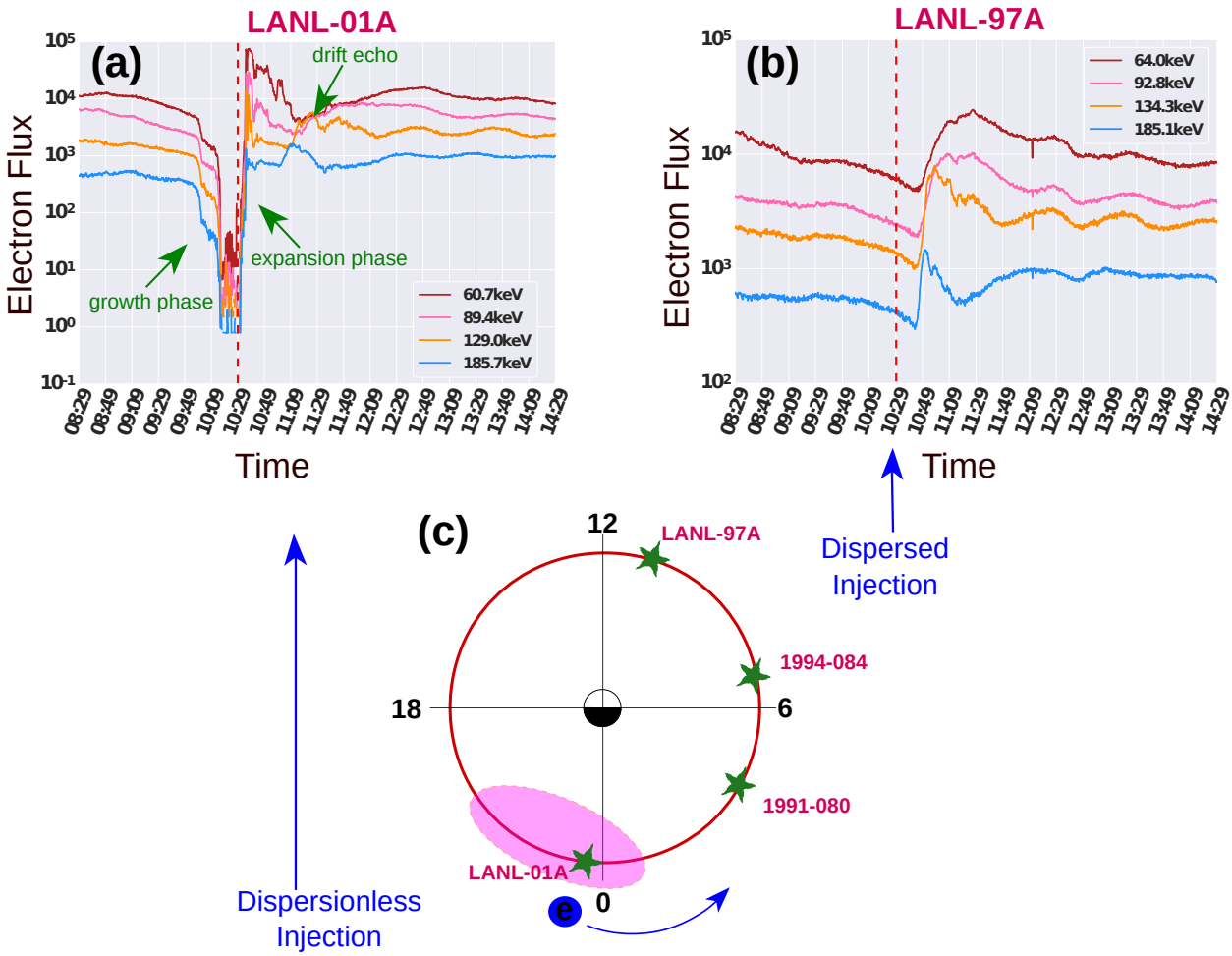

Figure 1.12: Energetic particle injections associated with a substorm observed at 10:29 UT on 29 August 2014 with LANL geostationary satellites. (a) A dispersionless injection detected by LANL-01 satellite; (b) a dispersed injection detected by LANL-97A satellite about 15 min later; (c) local time locations of the LANL satellites at the time of the substorm.

area shows typical location and extend of the injection region. At the substorm onset one of the satellites, LANL-01A, was located inside the injection region. Variations of electron fluxes measured by this satellite are shown in Figure 1.12a. Vertical red dashed line marks time of the onset. Lines of different colors represent variations of fluxes detected by different energy channels. Before the substorm onset, electron fluxes were decreasing during a 2-hour interval, this decrease is associated with the substorm growth phase. At the substorm onset, electron fluxes of all energies start to rise simultaneously (dispersionless injection). Fluxes increase sharply by several orders of magnitude during the expansion phase. After energetic

electrons and ions are injected into geosynchronous orbit, they start to move around the Earth with gradient-curvature drift: electrons move eastward and ions – westward. Because the velocity of the drift depends on particle energy, more energetic particles will be detected by the satellites located outside of the injection region before less energetic particles. This is demonstrated in Figure 1.12b where variations of electron fluxes are shown as measured by the LANL-97A satellite. First of all, one can see that increase of fluxes happens with some delay relatively to the substorm onset. This is because the satellite was located about 12 local hours away from the injection region. It is also seen that the injection of the 185-keV electrons was detected several minutes before the injection of the 64-keV electrons. Such injection is called dispersed injection. Another dispersed injection can be seen in Figure 1.12a about 40 min after the dispersionless injection. In this case the electrons from the first injection travelled all the way around the Earth and were detected by the same satellite again. Such events are known as drift echo events [e.g., *Belian et al.*, 1978; *Lanzerotti et al.*, 1971].

1.4 Objectives and thesis outline

The magnetosphere-ionosphere system responds to the solar wind driving in a variety of ways. The goal of this thesis is to investigate some of the aspects of this response. During periods of southward IMF (the IMF B_z^- conditions), the main process by which the magnetosphere redistributes energy from the solar wind into entire magnetosphere-ionosphere system is via magnetospheric substorms. Substorms occur intermittently and it is not clear how to predict occurrence of the next substorm. It has been hypothesised that the substorm cycle is in essence a simple process and the complexity and apparent randomness of substorm occurrence is caused by the complexity of the solar wind driving [*Freeman and Morley*, 2004]. It is not known, however, what are the solar wind parameters that determine occurrence of substorms. Thus it is important to understand how substorm occurrence rates react to changes in the solar wind. The first objective of this thesis is to make a detailed investigation of the substorm occurrence rates and recurrence times. Specifically, we aim to achieve the following goals :

- to create a reliable list of substorms. To meet this goal we explore and critically analyze various data sets and algorithms used for identification of substorms.

- to mathematically analyze the distribution of recurrence times of substorms;
- to determine if there is a periodicity in the driving of the magnetosphere corresponding to the most probable periodicity in the substorm occurrence;
- to investigate how substorm occurrence rates vary with the solar cycle, type of solar wind plasma and season and estimate role of the Russel-McPherron effect [*Russell and McPherron*, 1973] in the seasonal variations;
- to investigate how distribution of substorm recurrence changes with substorm amplitude, geomagnetic activity, and solar wind conditions.

When the IMF B_z turns northward (the IMF B_z^+ conditions) and stays northward for an extended period of time, substorms become vanishingly infrequent. However, coupling between the solar wind and the magnetosphere still takes place. As was discussed in Section 1.1.2 the coupling results in a high-latitude convection pattern different from the standard two-cell convection pattern. For these conditions plasma in the dayside portion of the polar cap is expected to flow in sunward direction along the noon-midnight meridian. The second objective of this thesis is to investigate these high-latitude sunward flows under strongly dominated IMF B_z conditions. Up until recently, the SuperDARN data deep in the polar cap were limited but recent installation of additional radars in the Northern and Southern hemispheres provides opportunities to look into this issue. The main questions we want to answer for this research are the following:

- What are typical speeds and directions of the sunward flows for $B_z^+ >> |B_y|$ while the standard SuperDARN data analysis techniques are employed?
- What are seasonal variations of PolarDARN line-of-sight (l-o-s) velocities along the noon-midnight meridian?
- What are interhemispheric differences in high-latitude convection patterns for strongly northward IMF conditions?

Another IMF B_z^+-related phenomenon in the polar cap is polar cap auroral arcs. Since the electrodynamics in the ionosphere is intimately coupled to the electrodynamical processes in

the magnetosphere (Section 1.2), the detailed picture of polar cap arc-associated convection can help us understand some of the magnetospheric processes related to the solar wind driving for northward IMF conditions. The third objective of this thesis is to conduct a multi-instrumental study of the electrodynamics of polar cap arcs. More specifically we want to address the following questions:

- How do polar cap arcs respond to changes in the IMF?
- What are the ionospheric plasma flows in the vicinity of polar cap arcs?
- How flows around polar cap arcs are related to global high-latitude convection?
- What is the time evolution of convection pattern associated with polar cap arcs?

The thesis is organized as follows. Chapter 2 gives a description of the instrumentation used to study ionospheric plasma convection (SuperDARN radars, instruments onboard of DMSP and Swarm satellites), to detect polar cap arcs (Resolute Bay all-sky camera), and to identify substorm injections (LANL satellites). Chapter 3 first presents an investigation of various substorm lists created from various data sets. The most reliable lists of substorms are determined and used for a detailed statistical study of the substorm occurrence rates, recurrence times and their relation to the solar wind driving. In Chapter 4 statistical variations of l-o-s velocities measured by the PolarDARN radars are analyzed for two years of observations. Next, in order to better describe interhemispheric differences of high-latitude plasma convection for strongly dominated IMF B_z^+, simultaneous average convection maps in Southern and Northern hemispheres are compared for a collection of events. Chapter 5 presents a detailed investigation of two individual cases of polar cap auroral activity over Resolute Bay. Special attention is payed to studying various aspects of plasma convection associated with polar cap arcs. In Chapter 6 conclusions are drawn and suggestions for future research, inspired by the thesis, are discussed.

Chapter 2

Instrumentation

2.1 SuperDARN HF radars

SuperDARN (Super Dual Auroral Radar Network) is a network of ground-based, coherent, high-frequency (HF, 8-20 MHz) radars for studying the Earth's upper atmosphere and ionosphere [*Greenwald et al.*, 1995; *Chisham et al.*, 2007]. As can be seen from Figure 2.1, fields of view (FoV) of the SuperDARN radars cover a large part of the sub-auroral (StormDARN), auroral, and polar (PolarDARN) ionosphere in both hemispheres. The whole list of existing radars with coordinates of their locations, and their boresight directions can be found at VT SuperDARN web-site. The main mission of the SuperDARN is to continuously monitor plasma convection in the ionosphere. For this, the network was designed in such a way that FoV of different radars overlap (Figure 2.1). When a common volume of the ionospheric plasma is observed by different radars from different directions, the line-of-sight (l-o-s) Doppler velocity measurements from the radars can be combined to derive full velocity vector.

Currently the network consists of 36 nearly-identical radars; each radar utilizes the same software and provides identical data products. A SuperDARN radar consists of two parallel arrays of antennas: 16 electronically phased antennas comprising a main array and additional 4 antennas comprising a secondary (interferometer) array. The latter is used to calculate the elevation angle of arriving signal by calculating phase difference between signals received by the main and secondary arrays [*André et al.*, 1998]. The antennas in the main array are steered in 16 beam directions. The beams are separated in azimuth by $\sim 3.24^\circ$ covering a total FoV of 52°. Range resolution along each beam is determined by the pulse length of transmitted signal. In the standard operating mode the pulse length is 300 μs corresponding

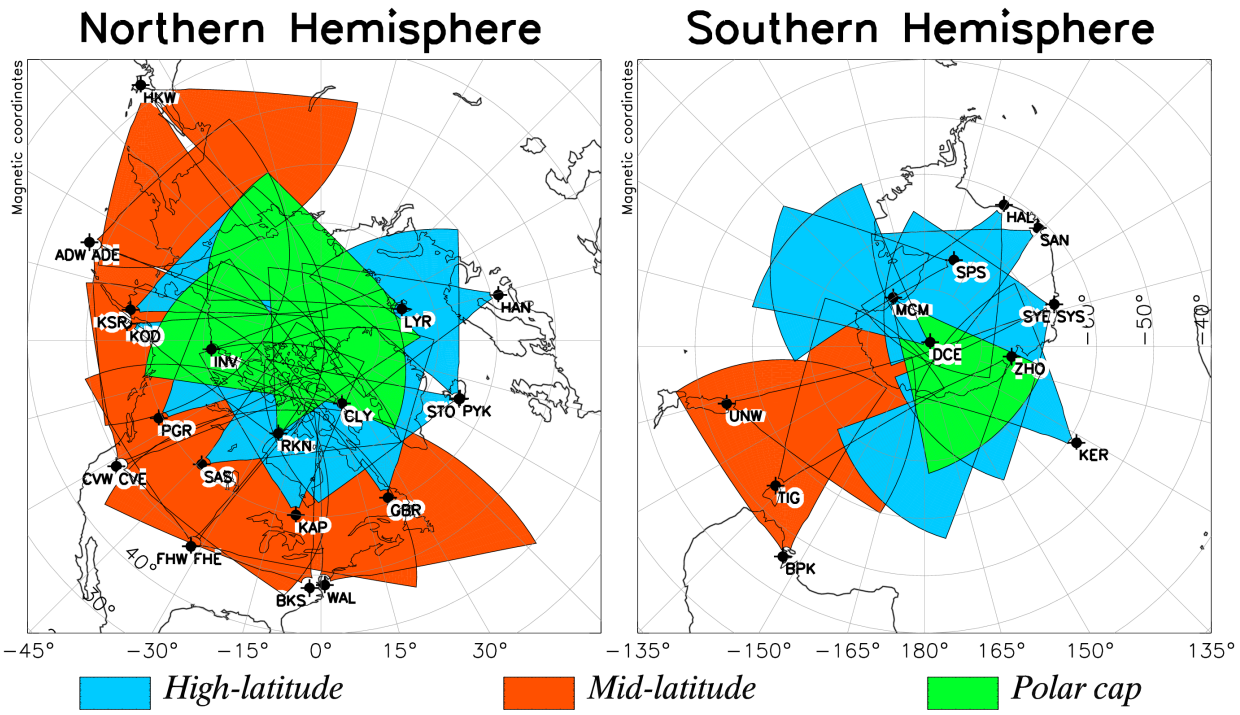

Figure 2.1: SuperDARN FoV in the Northern (left panel) and Southern (right panel) hemispheres. PolarDARN radars (green) are of particular interest in the context of this thesis. The maps are plotted in the AACGM magnetic coordinate system. From VT SuperDARN web-site.

to a resolution of 45 km. Typically there are 75 range gates along each beam with the first gate starting at a distance of 180 km from the radar location. A full scan through all 16 beams lasts 1 or 2 minutes, with a dwell time of 3 or 7 seconds for each position, respectively. Apart from the standard operation mode, or normal mode, part of the time the SuperDARN radars operate in various special modes.

2.1.1 Principle of coherent scattering

A coherent radar receives reflected radio waves (echoes) from a scattering region of interest when there are regular spatial variations of plasma density inside the volume. Together with the spatial coherence, the scattering medium must exhibit some degree of temporal coherence, i.e., does not change much between successive radio signals [*Hargreaves*, 1992].

When a transmitted signal encounters a periodic electron density fluctuation (plasma wave) with wavelength equal to half of the radar wavelength, the reflected back signal will interfere constructively thus increasing power of the backscattered signal. The constructive interference and temporal coherence of scattering structures allow the SuperDARN radars to use relatively low-power signals (< 10 kW).

SuperDARN radars receive signals from small-scale ionospheric irregularities with the wavelength of order of 10 m. These irregularities are typically aligned along magnetic field lines. In order to receive a signal scattered back to the radar, incident signal must fall perpendicularly on the scattering plasma structure, i.e., the radar wave vector must be orthogonal to the direction of geomagnetic field. At high latitudes geomagnetic field lines are nearly vertical and thus radio waves propagating along straight lines cannot be scattered back to the radar. At HF frequencies, a signal experiences a refraction that causes it to bend. If the refraction is sufficiently strong, the signal can eventually reach orthogonality with magnetic field lines. Ionospheric refraction depends on the plasma density, which can vary significantly depending on local time, season, level of geomagnetic activity, etc. Thus propagation conditions are subject to change. One of the solutions to mitigate these changes is to operate radars over an extended frequency range. High refraction can also bend radio wave to the point when the wave is reflected from the ionosphere toward the ground and then scattered back to the ionosphere before returning to the radar. This type of backscatter is called *ground scatter*.

2.1.2 Gradient drift instability

The majority of SuperDARN backscattered signal returns from F-region irregularities. These irregularities move with the surrounding plasma which in the F region $\mathbf{E} \times \mathbf{B}$ drifts (Section 1.2.1). Thus, Doppler velocity of SuperDARN echo allows measurements of plasma convection speed.

It is believed that the main mechanism responsible for the excitation of F-region irregularities is the gradient drift instability (GDI) [*Tsunoda*, 1988; *Fejer and Kelley*, 1980]. For generation of the GDI, a gradient in plasma density ∇N must exist in the crossed electric and magnetic fields. For high-latitude F-region ionosphere, the gradient perpendicular to

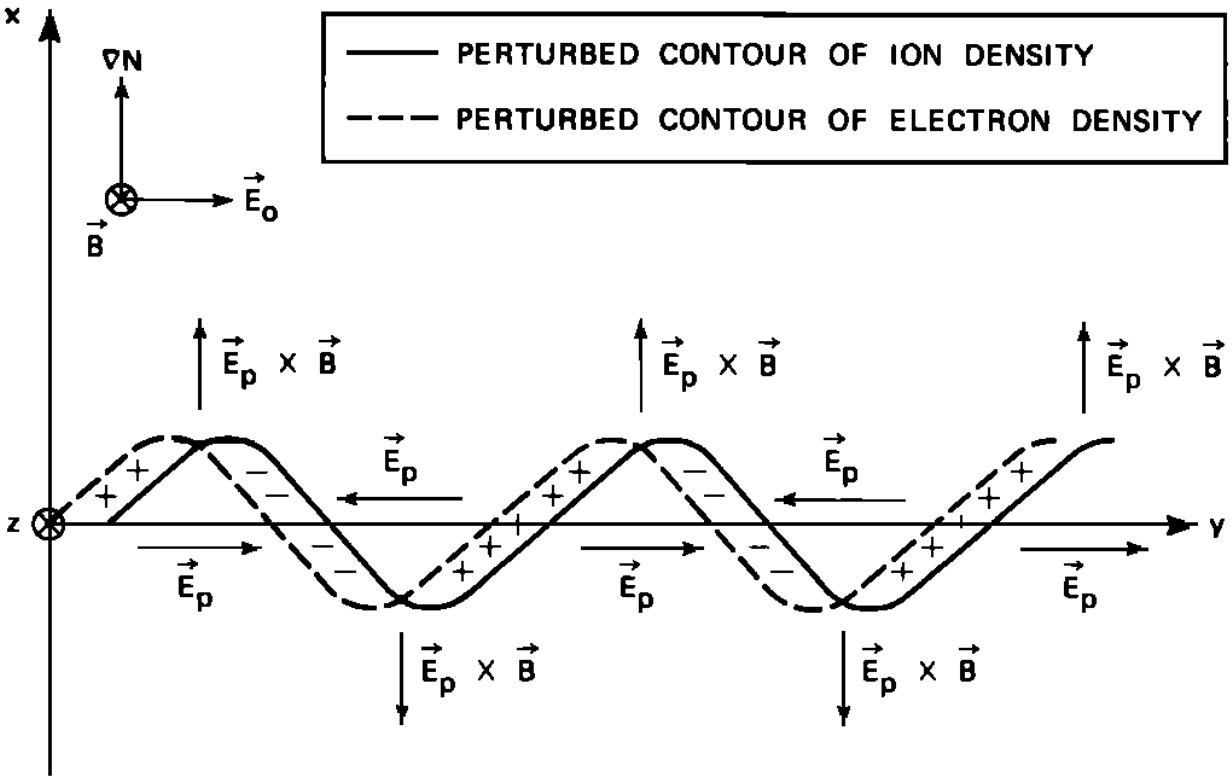

Figure 2.2: A schematic representation of the mechanism of the GDI. Shown is the geometry that leads to the maximal growth rate of the instability. From *Tsunoda* [1988].

both the electric and magnetic fields has the most destabilizing effect on plasma. The mechanism of excitation of the GDI is schematically shown in Figure 2.2. The electric field $\mathbf{E_0}$ is perpendicular to the plasma gradient ∇N and background magnetic field $\mathbf{B}$. Consider a sinusoidal perturbation in the x direction. In the F region, both electrons and ions have the same Hall drift velocity while there is a relative Pedersen drift between ions and electrons. Ions move in the direction of the electric field E_0 thus creating charge separation. This separation produces a polarization electric field $\mathbf{E_p}$. As a result the plasma starts to $\mathbf{E_p} \times \mathbf{B}$ drift such that regions of less (more) dense plasma move into regions with higher (lower) plasma density. Hence the amplitude of initial perturbation increases and plasma becomes unstable. For the three-dimensional case, where wave vector of the perturbation $\mathbf{k} = k_x\hat{\mathbf{x}} + k_y\hat{\mathbf{y}} + k_z\hat{\mathbf{z}}$, with the perpendicular component to the magnetic field $\mathbf{k}_\perp = \sin\alpha k_\perp\hat{\mathbf{x}} + \cos\alpha k_\perp\hat{\mathbf{y}}$, $\mathbf{E_0} = E_0\sin\beta\hat{\mathbf{x}} + E_0\cos\beta\hat{\mathbf{y}}$, the general equation for the growth

rate of the GDI in the linear approximation reads [*Keskinen and Ossakow*, 1982]:

$$\gamma = \frac{-\cos\alpha \dfrac{\nu_{ei}}{\Omega_e}\dfrac{1}{L}\left(\dfrac{\nu_{in}}{\Omega_i}\dfrac{E_0}{B}\cos(\alpha-\beta) - \dfrac{k_z}{k_y}V_d\right)}{\dfrac{k_z^2}{k_y^2} + \dfrac{\nu_{in}}{\Omega_i}\dfrac{\nu_{ei}}{\Omega_e}} - D_\perp k_y^2 - D_\parallel k_z \tag{2.1}$$

where $D_\perp = \dfrac{\nu_{ei}}{|\Omega_e|\Omega_i}c_s^2$ and $D_\parallel = \dfrac{c_s^2}{\nu_{in}}\left(1 + \dfrac{\dfrac{\nu_{in}}{\Omega_i}}{\dfrac{\nu_{ei}\nu_{in}}{|\Omega_e|\Omega_i} + \dfrac{k_\parallel^2}{k_y^2}}\right)$ are diffusion coefficients perpendicular to the magnetic field and along the magnetic field, respectively, $c_s = \sqrt{\dfrac{k_B(T_e+T_i)}{m_i}}$ is the ion-acoustic speed , $L^{-1} = (1/n_0)(\partial n_0/\partial y)$ is the plasma density scale length, n_0 is the background plasma density, ν_{ei} and ν_{in} are the electron-ion and ion-neutral collision frequencies, respectively, Ω_i (Ω_e) is the ion (electron) gyrofrequency, V_d is the electron-ion differential velocity in the direction of the magnetic field.

For the situation in Figure 2.2 when the electric field $\mathbf{E_0}$ is perpendicular to the density gradient and the wave propagating along the y-axis (i.e., $\beta = 0^\circ$ and $\alpha = 0^\circ$ or $\alpha = 180^\circ$), Equation 2.1 becomes:

$$\gamma = \frac{-\dfrac{\nu_{ei}}{\Omega_e}\dfrac{1}{L}\left(\dfrac{\nu_{in}}{\Omega_i}\dfrac{E_0}{B} - \theta V_d\right)}{\theta^2 + \dfrac{\nu_{ei}\nu_{in}}{\Omega_e\Omega_i}} - D_\perp k_y^2 - D_\parallel k_z \tag{2.2}$$

where $\theta \equiv \dfrac{k_z}{k_y}$. Solving $\left.\dfrac{\partial\gamma}{\partial\theta}\right|_{\theta=\theta_{max}} = 0$ for θ, the growth rate is maximum when

$$\theta_{max} = \frac{\nu_{in}}{\Omega_i}\frac{E_0}{BV_d} \pm \sqrt{\left(\frac{E_0}{BV_d}\right)^2\left(\frac{\nu_{in}}{\Omega_i}\right)^2 + \frac{\nu_{ei}\nu_{in}}{\Omega_e\Omega_i}} \tag{2.3}$$

To estimate θ_{max} for typical high-latitude F-region ionosphere, *Keskinen and Ossakow* [1982] used parameters $\nu_{in}/\Omega_i \approx 10^{-4}$, $\nu_{ei}/\Omega_e \approx 10^{-4}$, $E_0 \approx 10$ mV/m, $B \approx 5\times10^{-3}$ T, $n_0 = 10^{11}$ m^{-3} and $j_\parallel = 1$ μA/m^2 and obtained $|\theta_{max}| = 10^{-4}$. This means that the growth rate maximizes when $k_z << k_x$, i.e., the GDI excites irregularities which are strongly field-aligned. Therefore,

the maximum growth rate

$$\gamma = \frac{E_0}{BL} = \frac{V_{\mathbf{E}\times\mathbf{B}}}{L} \tag{2.4}$$

where $V_{\mathbf{E}\times\mathbf{B}}$ is the $\mathbf{E}\times\mathbf{B}$ (Hall) drift velocity. It follows from Equation 2.4 that the higher electric fields and density gradients result in higher growth rate. The growth rate is greater than 0 when the density gradient points in the direction of the $\mathbf{E}\times\mathbf{B}$ drift and $\gamma < 0$ when it is in the opposite direction. This means that if there is a density structure immersed in plasma with some background electric field, the GDI will operate only on one side of the structure.

2.1.3 SuperDARN FIT technique

Three main parameters obtained with the SuperDARN radars are Doppler velocity, spectral width, and echo power. The Doppler velocity is the l-o-s component of the convection velocity. The l-o-s velocities from different radars can be combined to obtain large-scale convection maps. There are several approaches to this [*Cerisier and Senior*, 1994; *Ruohoniemi and Baker*, 1998; *Amm et al.*, 2010; *Fiori et al.*, 2010], however, the most commonly used technique to derive large-scale convection maps is the FIT, or Map Potential Technique by *Ruohoniemi and Baker* [1998].

For the FIT technique the ground scatter, as well as data with error estimates exceeding 200 m/s, are excluded from the analysis. For each l-o-s velocity measurement at time t_k and location (b, g) in the radar beam/gate coordinates, median filtering is applied. Weighted medians are computed for all the measurements in the 3×3 region of beam/gate cells centered at (b, g) for three consecutive scans centered at t_k. If number of velocity values from the previous step is low, no value is assigned for the cell (b, g) at the t_k.

After the spatio-temporal filtering, the data are mapped from the beam/gate coordinate system to the Altitude Adjusted Corrected Geomagnetic (AACGM) [*Baker and Wing*, 1989; *Gustafsson et al.*, 1992] coordinate system. Next, the filtered data combined into grid cells of equal area. The grid is chosen such that each cell has 1° width in latitudinal dimension, corresponding to $\sim$ 111 km, and $\sim$ 111 km in longitudinal dimension. If there are less than 25% of all the possible measurements in a given cell, all the l-o-s velocity measurements in

the cell are disregarded, otherwise, the average l-o-s velocity is selected. This way velocities from different radars are defined on the common grid; such gridded velocities are used next to produce convection maps.

To obtain vector velocities from the gridded velocities, the vector velocities are first expressed through coefficient of expansion of electrostatic potential. Namely, the electrostatic potential can be written as the solution of the Laplace's equation in spherical coordinates [*Fiori et al.*, 2010]:

$$\Phi(\theta,\phi) = \sum_{k=0}^{k_{max}} \sum_{m=0}^{k} \left[A_{km}\cos(m\phi) + B_{km}\sin(m\phi)\right] P_k^m(\cos\theta) \tag{2.5}$$

where P_k^m are the associated Legendre functions, k_{max} is the maximum degree, θ and ϕ are the geomagnetic colatitude and longitude, respectively, A_{km} and B_{km} are constant coefficients. The electric field and convection velocity can be expressed through the electrostatic potential through the equations

$$\mathbf{E} = -\nabla\Phi, \qquad \mathbf{v} = -\frac{\nabla\Phi \times \mathbf{B}}{B^2} \tag{2.6}$$

Now, the coefficients A_{km} and B_{km} can be found by minimizing the expression [*Ruohoniemi and Baker*, 1998]:

$$\chi^2 = \sum_{i=1}^{N} \frac{1}{\sigma_i^2}\left[\mathbf{v_i}\cdot\hat{\mathbf{k}}_\mathbf{i} - W_i^2\right] \tag{2.7}$$

where W_i and σ_i are the gridded velocity and its uncertainty at the grid cell i, $\mathbf{v_i}$ is the vector velocity at the grid cell obtained from Equation 2.6, and $\hat{\mathbf{k}}_\mathbf{i}$ is the direction of the beam associated with the l-o-s velocity W_i.

For the grid cells where there is no l-o-s velocity measurements, values from a statistical model are used [*Ruohoniemi and Greenwald*, 1996]. This way the distribution of electrostatic potential and plasma convection can be found for high-latitude ionosphere (the lower latitude convection boundary is specified along the Heppner-Maynard boundary [*Heppner and Maynard*, 1987; *Shepherd and Ruohoniemi*, 2000]). An example of the convection map obtained with the Map Potential technique is shown in Figure 2.3. The map was generated for 7:20–7:22 UT on 18 January 2002 using the Ruohoniemi and Greenwald 1996 statistical model [*Ruohoniemi and Greenwald*, 1996] for $4 < B_t < 6$ nT. The black solid (dashed) lines

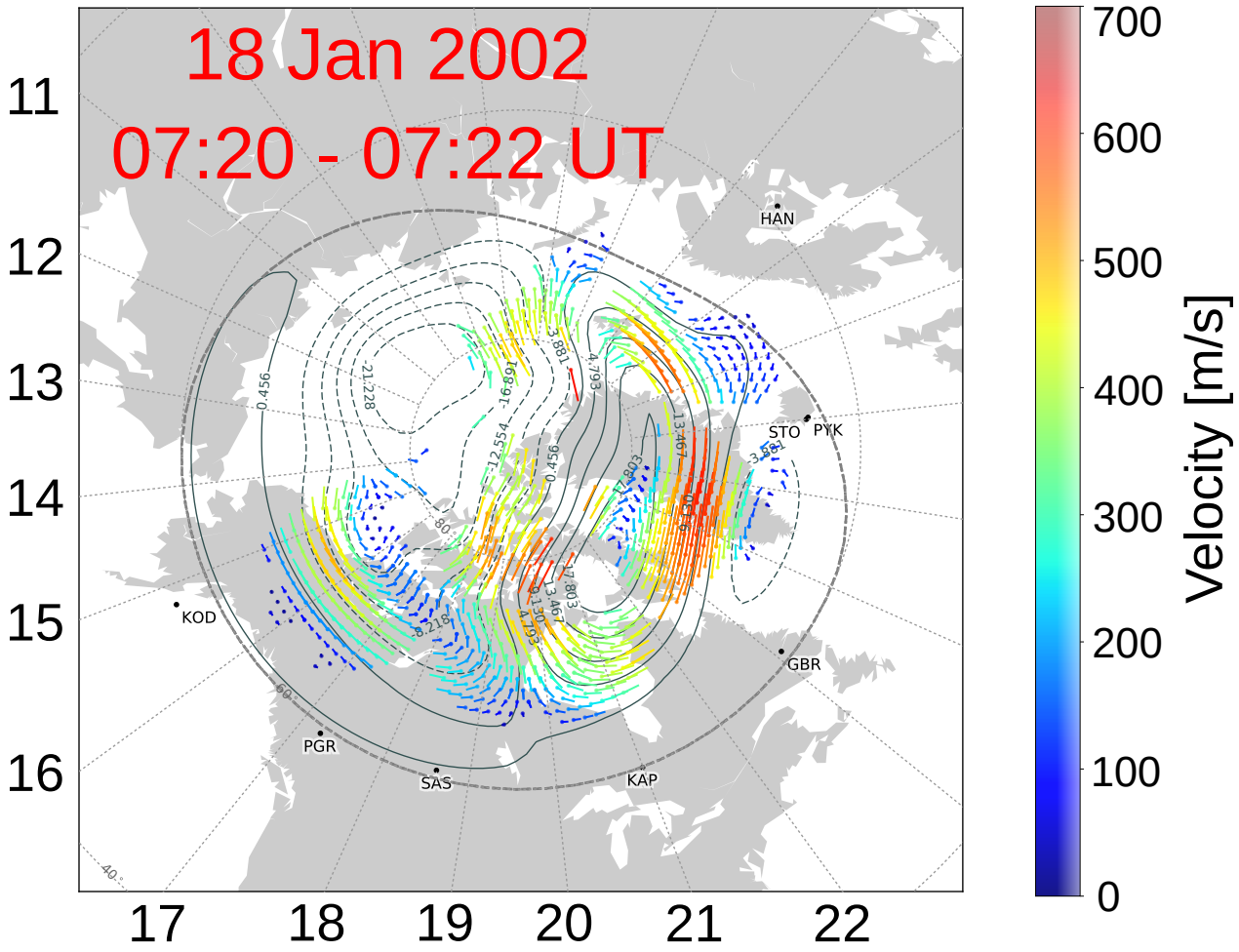

Figure 2.3: A map of high-latitude ionospheric convection in the Northern hemisphere for 7:20–7:22 UT on 18 January 2002. The plot is produced using the FIT technique and the Ruohoniemi and Greenwald 1996 statistical model [*Ruohoniemi and Greenwald*, 1996]. The map is shown in the MLT-MLAT coordinate system.

represent contours of constant negative (positive) electrostatic potential. The cross polar cap potential, i.e., the difference between the highest and the lowest electrostatic potentials, equals 47 kV for this map. The vectors of plasma flow at each grid cell where the gridded velocity data were available are color-coded according to the colorbar shown at the right of the plot. Total number of the velocity vectors in the map is 938. Data from eight SuperDARN radars (shown on the map by black dots) were used to produce the map. The thick grey dashed line represents the Heppner-Maynard boundary. The GSM IMF B_z during the two-minute time interval was ~ -3.6 nT and IMF $B_y \approx 3.9$ nT. Two cells with antisunward flow across the polar cap can be clearly distinguished within the map as is expected for the B_z^-

IMF conditions.

2.2 Optical Mesosphere Thermosphere Imager at Resolute Bay

The all-sky camera has been used in the aurora research for many years. It was first introduced by Gartlein and Elvey in about 1950 [*Elvey et al.*, 1955; *Akasofu*, 1974]; during the International Geophysical Year (1957-1958) a network of more than 100 all-sky cameras was set up to study the aurora. This led to the inception of two key concepts in the space physics research: the auroral oval [*Khorosheva*, 1967; *Akasofu*, 1968; *Feldstein*, 1969] and auroral substorm [*Akasofu*, 1964]. All-sky cameras significantly evolved since the early studies and they remain an important instrument in substorm and auroral research [*Syrjäsuo et al.*, 1998; *Mende et al.*, 1999; *Donovan et al.*, 2003; *Mende et al.*, 2009]. In this dissertation, an Optical Mesosphere Thermosphere Imager (OMTI) all-sky camera at Resolute Bay (RB) is used to study auroral forms in the polar cap. The location of the camera (74.73° N and 265.07° E geographic coordinated; 82.9° AACGM latitude) is convenient for the research as it allows to observe night sky deep in the polar cap and in conjunction with the PolarDARN radars.

The OMTI instrument was developed by the Solar-Terrestrial Environment Laboratory, Nagoya University in 1997 in order to study the dynamics and chemistry of upper atmosphere through night airglow emission [*Shiokawa et al.*, 1999, 2009]. OMTIs consist of a Fabry-Perot interferometer, three all-sky cameras, three meridian scanning photometers and a Spectral Airglow Temperature Imager. Of particular interest to aurora research is the all-sky camera instrument, capable of producing 2-dimensional airglow patterns. It is schematically shown in Figure 2.4a. The fish-eye lens has a FoV of 180°, the rotating filter wheel contains several filters to measure airglow at various wavelengths. Table 2.1 lists the filters and their characteristics. Light Passed through the lens is focused on the cooled-CCD detector. The operation of the camera is fully automated by a personal computer.

Two of the brightest auroral emission lines occur at 557.7 and 630.0 nm. The green line emission (557.7 nm) occur due to the transition of an electron from the ^1S excited state to the ^1D state of atomic oxygen. The most important process for the excitation of the $O(^1S)$

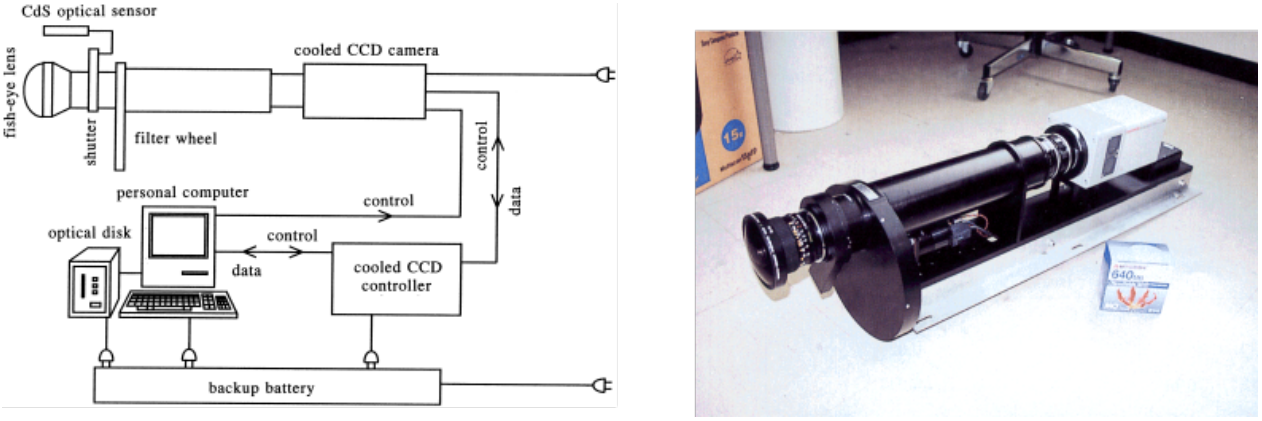

Figure 2.4: Schematic diagram (left) and an image (right) of the OMTI all-sky camera. From *Shiokawa et al.* [1999].

state is through energetic particle impact *Shiokawa and Fukunishi* [1990]:

$$O(^3P) + e \longrightarrow O(^1S) + e' \tag{2.8}$$

followed by

$$O(^1S) \longrightarrow O(^1D) + h\nu \qquad (557.7 \text{ nm}) \tag{2.9}$$

Shiokawa and Fukunishi [1990] also demonstrated that the peak of the 557.7 nm-emission occurs at $\sim$ 200 km for soft electron precipitation and at $\sim$ 120 km for hard precipitation. The mean lifetime of the excited state $O(^3P_2)$ is relatively long ($\sim$ 1 s).

The red line emission (630 nm) emitted by atomic oxygen in its transition from ^1D state to the ground state $^3P_2$. There are several sources of $O(^1D)$ [*Solomon et al.*, 1988], the most important two are electron impact excitation:

$$O(^3P_2) + e \longrightarrow O(^1D) + e' \tag{2.10}$$

and dissociative recombination of O_2^+:

$$O_2^+ + e \longrightarrow O + O(^1D) \tag{2.11}$$

Table 2.1: Filter details: typical exposure times, bandwidth and sensitivity of the RB OMTI all-sky camera.

Emission	Wavelength (nm)	Bandwidth (nm)	Exposure (s)	Sensitivity (count/R/s)
OI	557.7	1.90	30	0.082
OI	630.0	1.87	30	0.100
OH	720–910	190	2	—
OI	777.4	1.86	45	0.080
Na	589.3	1.82	30	0.109
background	572.5	1.64	30	0.092

followed by

$$O(^1D) \longrightarrow O(^3P) + h\nu \tag{2.12}$$

Radiative lifetime of $O(^1D)$ is 107 s. Red-line emission mainly originates at F-region altitudes. All the auroral images in this thesis were obtained by mapping data of 630-nm emission on a horizontal plane by assuming that the emission originates at altitude of 250 km.

2.3 DMSP instruments

The Defense Meteorological Satellite Program (DMSP) is a constellation of satellites launched to provide information on the Earth's environment and terrestrial weather. Each satellite is in circular (apogee/perigee = 848 ± 22 km), sun-synchronous, near-polar (inclination = $98.8^\circ \pm 0.15^\circ$) orbit [*Rich and Hairston*, 1994]. The satellites move at about 7.45 km/s with the orbital period of 101 minute. The DMSP mission started in 1960s and is active to the present day. Each satellite carries various sensors and instruments; of particular interest to this research are the precipitating particle spectrometer, the fluxgate magnetometer, and the thermal plasma monitor [*Greenspan et al.*, 1986].

Special Sensor Precipitating Plasma Monitor (SSJ/5) is a sensor to measure precipitating electrons and ions in 19 energy channels logarithmically spaced from 30 eV to 30 keV [*Schumaker et al.*, 1988]. The dwell time of the SSJ/5 detector is 50 ms and complete electron and ion spectra are produced every second. The FoV of the detector is a 4° by 90° fan for electrons and ions extending from zenith to horizon. The FoV of SSJ/5 is much broader

comparing to that of its predecessor, SSJ/4, allowing measurements of particle pitch angle. The main objective of the instrument is to identify boundaries of the auroral oval. In the thesis, measurements from SSJ/5 onboard of the DMSP F16 and F17 satellites are used to identify inverted-V precipitating electrons inside the polar cap.

Special Sensors–Ions, Electron, and Scintillation thermal plasma analysis package (SSIES) is a suite of instruments for measuring various plasma parameters, including a Retarding Potential Analyzer (RPA), an Ion Drift meter (IDM), a scintillation meter, and a Langmuir probe. The IDM measures the vertical and horizontal cross-track components of plasma drift [*Rich and Hairston*, 1994]. The IDM is a Faraday cup facing the direction of the satellite's motion. On the front of the cup is a negatively charged grid to prevent electrons from entering the detector. The aperture of the IDM is square and the circular collector plate behind it is divided into four separate plates. If the ion drift has a cross-track component, more ions will hit one plate than the other. This imbalance will be reflected in the current difference flowing between different plates. From the difference of the currents, the angle of arrival of ions to the collector plates can be determined. Horizontal and vertical ion drifts can be obtained from the horizontal and vertical angles of arrival if apparent ion drift velocity along the track is known. The apparent ion drift velocity along the track is the satellite velocity plus the component of plasma drift along the track. The latter can be taken from the RPA measurements. If the RPA along-track ion velocities are not available, the component of plasma drift along the track is set to zero. This results in an error of $\pm 8\%$ or less [*Rich and Hairston*, 1994].

Fluxgate magnetometer (SSM) [*Rich*, 1984] measures the strength and direction of the total Earth's magnetic field at the satellite location. The SSM performs the magnetic field measurements within the range of $\pm 64,000$ nT with a resolution of 12 nT per axis at a rate of 20 samples per second. By subtracting a model magnetic field (for example, IGRF), measurements of magnetic disturbances produced by currents can be obtained.

2.4 Swarm Electric Field Instrument

Swarm is a mission dedicated to survey the Earth's magnetic field and its temporal evolution. The three Swarm satellites (Alpha, Bravo, and Charlie) were launched in November 2013 into near-polar circular orbit. The Swarm constellation eventually reached a configuration where Swarm A and C satellites are flying at an altitude of approximately 465 km separated by $\sim 1.4^{\circ}$ in longitude and by 170 s along the orbit. The Swarm B is flying at an altitude of about 530 km, the longitudinal separation of the Swarm B from the lower pair is increasing by $\sim 20^{\circ}$ per year. The configuration aims to separate external (ionospheric and magnetospheric currents) and internal (geodynamo processes in the outer core, lithospheric magnetisation, currents in the mantle, etc.) contributions to the total magnetic field. All the Swarm satellites are identical and carry identical sets of instruments for high-precision and high-resolution measurements of the geomagnetic field and separation of various field sources [*Friis-Christensen et al.*, 2008]. The instruments include a vector magnetometer, a scalar magnetometer, an accelerometer, and an Electric Field Instrument (EFI).

The EFI consists of two Thermal Ion Imagers (TIIs) on the ram face of the satellite and two Langmuir probes beneath the TIIs. The TII is a relatively new technique to measure ion drifts [*Knudsen et al.*, 2003, 2017] capable of producing three-dimensional measurements of plasma flow velocities. Ions enter the TII sensor through a narrow aperture as shown in Figure 2.5, upper panel. A potential difference maintained between two hemispheric grids deflects the incoming ions toward the detector. Ions that have smaller kinetic energy per charge are deflected more toward the center of the detector, while ions with higher energy per charge hit the detector farther from the center. Images of ion distribution are then recorded on a CCD detector. From the two-dimensional ion distribution images, ion drift velocity, ion temperature and density can be derived. The two TII sensors are orthogonal to each other thus providing a three-dimensional ion distribution function.

An example of images from the TIIs onboard of the Swarm A are shown in the bottom panel of Figure 2.5 [*Knudsen et al.*, 2017]. The bright spot in each image corresponds to the distribution of O^{+} ions; to the right of it is a dim ring corresponding to ions with lower ram energy. The former is analysed to derive ion drift velocity. The TII images are collected at

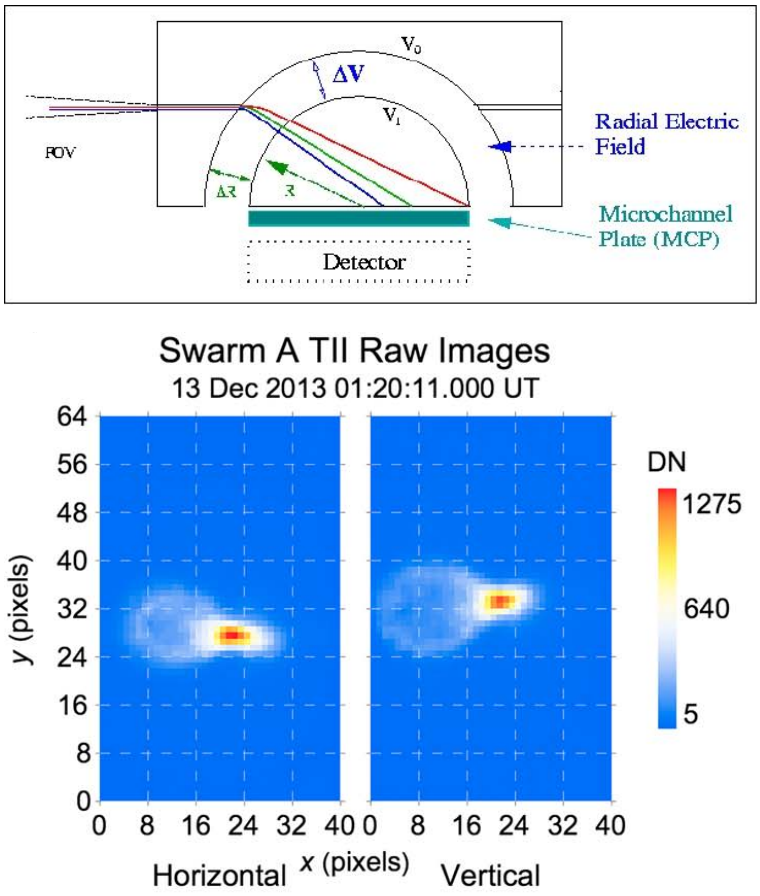

Figure 2.5: Schematic representation of the TII focusing system (top). Image by Dr. Johnathan Burchill. Raw images from horizontal and vertical TII sensors of the Swarm A on 13 December 2013 at 01:20:11 UT. From *Knudsen et al.* [2017].

a rate of 16 s^{-1}. Initial data preprocessing happens on board, including averaging of eight images from each sensor every half a second. Further data processing happens on the ground to produce three-dimensional ion drifts at a rate of 2 s^{-1}.

2.5 LANL GEO SOPA instrument

Los Alamos National Laboratory (LANL) geostationary satellites provide charged particle measurements from 1 eV to several MeV. Geostationary orbit is a circular geosynchronous orbit, lying in the Earth's equatorial plane at radial distances of about 42,164 km from the center of the Earth. The geostationary orbit is located in a region between the inner and

outer magnetosphere; the environment here is very dynamic and rapidly changing thus this region presents a particular interest to space weather research. Depending on the level of geomagnetic activity and solar wind conditions, LANL satellites can sample plasma from different magnetospheric regions. Since 1989, at least 3 LANL GEO satellites conduct measurements at a given time (see, for example, Figure 1.12c from Section 1.3.3) thus providing simultaneous multipoint observations of plasma environment at the geostationary orbit. Each LANL GEO satellite is equipped with a Magnetospheric Plasma Analyzer (MPA), a Synchronous Orbit Particle Analyzer (SOPA), and an Energy Spectrometer for Particles (ESP). The MPA instrument [*McComas et al.*, 1993] measures the three-dimensional plasma electron and ion distributions with energies between $\sim$ 1 eV and $\sim$ 40 keV. The SOPA instrument [*Belian et al.*, 1992] provides measurements of the electron distributions from 10 channels from $\sim$ 40 keV to more than 1.5 MeV and ion distribution from 12 channels between $\sim$ 50 keV and $\sim$ 8 MeV. The ESP measures particles fluxes in six electron channels from 0.7 to 10 MeV and three ion channels from 20 to 100 MeV.

Only measurements from the SOPA instrument are considered in this thesis. The SOPA instrument consists of three detector telescopes arranged at angles of 30°, 90°, and 120° to the satellite's spin axis directed toward the center of the Earth. Each telescope has a very thin front detector (4 μm) and very thick (3000 μm) back detector. Only small percentage of electrons deposit their energy on the thin detector and thus this detector counts ions. The thick detector counts electrons. The particle counts are converted then to fluxes using flux conversion factors [*Cayton and Tuszewski*, 2005] obtained from Monte Carlo simulations. The SOPA instrument provides data with 10-s resolution.

Chapter 3

Solar wind drivers of substorm processes

Despite decades of research on the nature of substorms with ground-based and space-born measurements including the recent dedicated space science mission THEMIS [*Angelopoulos*, 2008], the major process/trigger of the substorm and its location in space remains largely undetermined. Debates are also with respect to the extent the solar wind driving controls the onsets.

One of the difficulties in the substorm research is the historical dilemma arising from the lack of a universal definition of a substorm: the definition is unsettled both as to the defining signatures of a substorm [e.g., Akasofu,1968, 1979; Rostoker et al., 1980] and as to the critical amplitude of the event [e.g., *Akasofu*, 1968, 1979; *Rostoker et al.*, 1980]. As a result, many substorms identified from specific set of observations could be simply auroral activations. In this Chapter we first investigate several lists of substorm events obtained from various data sets: the SML index, the MPB index, geosynchronous energetic-electron measurements, and optical auroral observations. The goal of this investigation is to assess to what extent the lists are contaminated by activations and identify the most reliable lists.

Two of the lists are used to study statistical properties of substorm occurrence rates, substorm recurrence times and their connections to the structure of the solar wind. The study will not touch the substorm "triggering" by northward turnings of the solar wind magnetic field at rotational discontinuities [e.g., *Rostoker*, 1983; *Mcpherron et al.*, 1986; *Lyons et al.*, 1997; *Hsu and McPherron*, 2002, 2009; *Freeman and Morley*, 2009], but rather focus on the role of intervals of enhanced solar wind driving of the magnetosphere. Some results from this Chapter have been published in *Borovsky and Yakymenko* [2017].

3.1 Introduction

The analysis of the waiting times (recurrence times) Δt between the sequential substorm onsets (with the onsets determined by ion and electron injections into the geosynchronous orbit) found indications that substorms occur in two fashions, with distinct populations of randomly occurring substorms and periodically occurring substorms [*Borovsky et al.*, 1993]. Information-theoretic statistics were used to examine the recurrence times Δt between substorm onsets (with the onsets determined by particle injections and by jumps in the AL index) to verify that substorms do occur in a periodic fashion with a period of 2–4 hr [*Prichard et al.*, 1996]. It was speculated [*Borovsky et al.*, 1993; *Belian et al.*, 1994] that periodic substorms occur during time intervals when the solar wind driving of the magnetosphere is quasi-continuous while randomly occurring substorms are associated with randomly occurring intervals of enhanced solar wind driving of the magnetosphere.

Substorms and substorm occurrence rates are important to understand. A substorm results in a morphological transition of the magnetosphere, changing the magnetic field configuration of the near-Earth magnetotail [*McPherron et al.*, 1973a] and ejecting a portion of the magnetotail plasma downtail [*Hones*, 1977]. A substorm produces a substantial energy transfer from the magnetotail to the ionosphere [*Baumjohann and Kamide*, 1984] and to magnetospheric plasma populations [*Baumjohann et al.*, 1991]. Substorm occurrence is important for the evolution of the outer electron radiation belt: (1) substorm-injected electrons are probably the seed population for the radiation belt [*McDiarmid and Burrows*, 1965; *Friedel et al.*, 2002], (2) plasma waves in the dipolar magnetosphere that are driven by the injected-particle populations may resonantly energize radiation-belt electrons to relativistic energies [*Meredith et al.*, 2001; *He et al.*, 2014], and (3) the induction electric fields of repeated substorms may directly energize radiation-belt electrons as they drift across the nightside of the dipole during substorm expansion phases [*Kim et al.*, 2000; *Fok et al.*, 2001; *Dai et al.*, 2014]. Under special circumstances substorms can also directly produce MeV electrons and protons [*Ingraham et al.*, 2001; *Borovsky et al.*, 2016]. Substorm injections may also produce ULF waves in the dipolar magnetosphere [*Southwood*, 1976; *Anderson et al.*, 1990; *Zolotukhina et al.*, 2008], and substorm injections have been suspected to produce

outward transport of the plasmaspheric plasma [*Spiro et al.*, 1981; *Borovsky et al.*, 2014]. Among the population of periodically occurring substorms, a subset of "global sawtooth oscillations" was found [*Borovsky*, 2004; *Henderson*, 2004; *Henderson et al.*, 2006a,b; *Cai et al.*, 2006, 2011]. Whereas typical substorms involve a stretching and sudden dipolarization of the nightside magnetic field, global sawtooth oscillations involve sudden morphological changes in the dayside and the nightside magnetosphere and sudden changes in dayside currents. In this Chapter, global sawtooth oscillations will not be separated from periodic substorms.

Two outstanding questions about the occurrence of substorms are the following: (1) What does in the solar wind trigger the occurrence of random magnetospheric substorms and of periodic magnetospheric substorms? (2) What are the factors that determine the $\sim$ 3 hr periodicity for the recurrence of many substorms?

In general, the substorm occurrence rate is not well studied, particularly the rate versus the strength of the solar wind driving, the rate versus the type of solar wind plasma, the rate through the phases of the solar cycle, or the rate in the various phases of the different types of geomagnetic storms. Substorms are known to be associated with intervals of southward interplanetary magnetic field (IMF) [*Fairfield and Cahill Jr*, 1966; *Caan et al.*, 1978; *Morley and Freeman*, 2007; *Wild et al.*, 2009; *Newell and Gjerloev*, 2011]. Studies of the occurrence rates of substorms are limited to investigation of the rates as a function of the solar cycle [*Borovsky and Nemzek*, 1994; *Nevanlinna and Pulkkinen*, 1998; *Tanskanen*, 2009; *Tanskanen et al.*, 2011; *Chu et al.*, 2015], as a function of the season of the year [*Tanskanen*, 2009; *Tanskanen et al.*, 2011; *Guo et al.*, 2014], and as a function of the phase of the geomagnetic storms [*Lee and Min*, 2002; *Tanskanen et al.*, 2005].

Substorm-recurrence studies have focused mainly on the periodicity of global sawtooth oscillations, but the criteria discerning global oscillations from ordinary periodic substorms were often not rigorously enforced in the event selections. Hence, some of those global-sawtooth-oscillation studies pertain to periodic substorms in general. The recurrence studies focused on determining the periodicity [*Prichard et al.*, 1996; *Cai and Clauer*, 2009; *Huang et al.*, 2003a,b], on examining the solar wind role in the periodicity [e.g., *Belian et al.*, 1994; *Huang et al.*, 2003a, 2004, 2005; *Lavraud and Borovsky*, 2008; *Partamies et al.*, 2009], and on determining what physically causes the $\sim$ 3 hr periodicity of the magnetosphere [*Belian*

et al., 1994; *Freeman and Morley*, 2004; *Brambles et al.*, 2011, 2013; *Ouellette et al.*, 2013; *Welling et al.*, 2015].

3.2 Data sets and event selection

As was discussed in Section 1.3, substorm onset is associated with the formation of a substorm current wedge (SCW), a current system which develops as a result of the reduction and diversion of magnetospheric cross-tail current [*Birn and Hesse*, 2014; *Kepko et al.*, 2015]. The SCW disturbs the geomagnetic field and its signatures could be identified from magnetometer records. For this study we create 3 lists of substorm onsets from ground-based magnetic data from both the auroral oval and the midlatitude regions. The forth list of substorms examined in this Chapter is based on another ionospheric manifestation of a substorm – auroral breakup – the sudden brightening and poleward expansion of the aurora near midnight. Finally, specific morphological changes in particle characteristics at geosynchronous orbit allow us to create a fifth list of substorm onsets.

3.2.1 Auroral electrojet events (SOPHIE events and SML events)

The strength of auroral electrojet activity is traditionally characterized by the auroral electroject indices AU and AL. Substorm onset is marked by an abrupt decrease ("negative bay") in the time records of the AL index (Section 1.3.2); the decrease is a consequence of an intensification of the westward electrojet due to the contribution from the horizontal part of the SCW. The AL index is derived from a limited number of magnetometer stations that have an uneven MLT distribution and are located along a specific MLAT. The limited spatial coverage might result in incorrect estimation of substorm onset times and underestimation of substorm occurrence rates when used in statistical studies. An alternative to the AL index is the so-called SuperMAG AL (SML) index. The difference between SML and AL index is in number of stations used and in methods for establishing baseline. For this study we use the SML index database from 1979 to 2015 available at `http://supermag.jhuapl.edu/indices/`. Detailed description of the data and data processing techniques used in the derivation of the SML index is given by *Gjerloev* [2012] and *Newell and Gjerloev* [2011].

No generally accepted method exists to identify substorm events from the auroral electrojet indices and different criteria were used in various studies [e.g., *Newell and Gjerloev*, 2011; *Tanskanen et al.*, 2002; *Semenov et al.*, 2015; *Forsyth et al.*, 2015]. To create a collection of auroral electrojet substorm events, we tested various criteria; from visual examination of the events selected by the different algorithms, we chose two algorithms that in our (subjective) opinion were least prone to confuse noise-like oscillations in data with substorm signatures.

The first list of substorm onsets from the SML index was obtained with the use of the SOPHIE algorithm proposed recently by *Forsyth et al.* [2015]. The main idea of the algorithm is to divide data into intervals of "expansion phase", "recovery phase", and "possible growth phase" according to the value of the derivative dSML/dt of the SML index after it is smoothed with a low-pass filter. The intervals are subsequently modified by a number of corrections and then preliminary substorm onsets are identified as times when expansion phases start. The times of the preliminary onsets are further corrected with the unfiltered SML data by looking for a point where the derivative of the unfiltered data exceeds the expansion phase threshold (for details see *Forsyth et al.* [2015]). The expansion phase threshold is a percentile of dSML/dt< 0 and can be chosen arbitrary, resulting in more or less strict criterion on the sharpness of a decrease of the SML. For the present study we adopted 75% percentile for the expansion phase threshold. $103,905$ events were identified by the SOPHIE-75% algorithm for the period from January 1981 to December 2015.

Another scheme was chosen to select robust events in the SML index (these will be called SML events). The criterion used to find onset times is similar to the 100 nT-in-10 min criterion used by *Prichard et al.* [1996] to select substorm onset times in the 1 min resolution AL index or the 80 nT-in-15 min criterion used by *Tanskanen* [2009] for their IL index. The present scheme locates regions where the SML index decreases by at least 150 nT in 15 min, then locates potential onset times within those time intervals where the 2 min decrease of SML is more than 10 nT (which is a slope of more than -150 nT in 15 min). Then, for each potential onset time, the time integral of the magnitude of the SML index for the 45 min after the onset time is compared with the time integral of the magnitude of the SML index for the 45 min prior to the onset time: if the "after" integral is less than 1.5 times the "before" integral, that onset time is rejected as not representing the onset of a substantial change

in geomagnetic activity. (This integral test is designed to eliminate reactivations from the onset list, and the integral test should also eliminate pseudobreakups that are not followed by actual substorms.) The first surviving onset time in each interval where SML decreases 150 nT or more in 15 min is taken to be the onset of the substorm. Finally, if a 150 nT-in-15 min interval occurs within 15 min of a prior 150 nT-in-15 min interval, the second interval is voided and the onset time in that second interval is not used. To some degree, this eliminates multiple onsets being counted as separate substorms. In this robust-event scheme, the minimum time between substorm onsets in the 1979–2015 SML data set is 26 min. The total number of 28,464 events was selected by the algorithm covering interval from 1979 to 2016.

3.2.2 Midlatitude positive bay events

The FACs of the SCW current system are known to have an effect on midlatitude ground-based magnetometer records [*Chu et al.*, 2014]. The downward part of the FAC results in westward magnetic perturbations eastward of the central meridian and eastward perturbations westward of the central meridian, while both FACs of the SCW create northward perturbation along the central meridian. *Chu et al.* [2015] used this property to develop the so-called midlatitude positive bay (MPB) index. The authors defined the MPB index as the moving variance (measured in nT^2) in changes of the northward and eastward component of magnetic field at midlatitude. Magnetic field measurements from 41 midlatitude stations in both hemispheres were used to create a database of the MPB index covering 31 years of observations (from 1982 to 2012). We used the database to create a list of "positive bay" events that are believed to be signatures of substorms. To identify a positive bay event from the data we used the threshold of 25 nT^2 proposed by *Chu et al.* [2015] and for the onset time, we used time of the maximum of the second derivative of the MPB index. The data were initially smoothed to eliminate high-frequency oscillations in the same way as the SML index was smoothed in the SOPHIE algorithm. Unlike *Chu et al.* [2015], we did not restrict our database to isolated events only; our aim was to examine the whole set of positive bay events. The reason for this is that during disturbed time intervals, substorms are rarely isolated and often multiple onsets and intensifications are observed. We also did not exclude

any close in time events and did not use any criteria other than the 25 nT^2 threshold rule. As a result, we obtained a very large database of 121,541 events (in comparison, the list of isolated events by *Chu et al.* [2015] consists of 40,562 events).

3.2.3 Optical auroral substorm events

The optical substorm onset database used in this study consists of two well-known lists: the IMAGE list [*Frey et al.*, 2004; *Frey and Mende*, 2006] and the Polar list [*Liou*, 2010]. Both lists are based on global auroral observations from satellites. The Polar list consists of auroral breakups identified from images taken with the UVI imager on board of the Polar satellite. The list covers Polar observations between 1996 and 2000 when the geometry of the Polar orbit allowed good conditions for observations of the Northern auroral oval. In total, 2003 auroral substorms were identified during this period. The list is extended by an additional 536 events of auroral substorms identified in the Southern Hemisphere in 2007. The IMAGE list was acquired from the FUV camera observations on the IMAGE satellite. The database covers events from 2000 to 2006, resulting in 4193 auroral breakups that occurred in the Northern and Southern Hemispheres. Both lists were created using similar algorithms based on visual examination of images, however the events in the IMAGE list require auroral breakups to be separated by at least 30 min from each other, while events in the Polar list ask only for 10-min separation.

3.2.4 Electron injection events

The injection of energetic electrons detected at geosynchronous orbit is temporally associated with the onset of a substorm [e.g., *Kamide and McIlwain*, 1974; *Yeoman et al.*, 1994; *Weygand et al.*, 2008] and is simultaneous with the dipolarization process in the nightside magnetosphere at geosynchronous orbit [*Lezniak et al.*, 1968; *DeForest and McIlwain*, 1971; *Sauvaud and Winckler*, 1980; *Birn et al.*, 1998]. An automated method to identify substorm electron injections into geosynchronous orbit was developed based on the observation that the specific entropy $S = T/n^{2/3}$ [*Borovsky and Cayton*, 2011] of the hot-electron population at geosynchronous orbit decreases significantly when a fresh injection of electrons occurs.

This entropy decrease is seen as a simultaneous increase of the hot-electron number density and decrease of the hot-electron temperature (hardness of the energy spectrum). When there are no new injections, the population of substorm-injected electrons at geosynchronous orbit ages and the specific entropy of the population steadily increases with time. During this aging, the number density of the electrons decreases with time and the mean energy of the electrons increases with time; this is consistent with less-energetic electrons being lost from geosynchronous orbit at a higher rate leaving a population of more-energetic electrons.

Multispacecraft measurements of energetic electrons from the SOPA (Synchronous Orbit Particle Analyzer) instruments [*Cayton and Belian*, 2007] in geosynchronous orbit are used to determine the specific entropy of the substorm-injected electron population. Specifically, density-temperature fits to the SOPA electron counting rates for the substorm-injected population are used [*Cayton et al.*, 1989; *Cayton and Belian*, 2007; *Denton et al.*, 2010]. The spin-averaged counting rates for each electron energy channel are modeled as linear combinations of two relativistic-Maxwellian components plus a non-electron background contribution; minimizing the squared deviations between the observed and model counting rates summed over 10 electron channels yields the best-fit two-Maxwellian spectra (see *Cayton and Belian* [2007] for full details). The relativistic bi-Maxwellian fitting describes two populations of electrons: a "soft" population of electrons with a temperature of $\sim$ 30 keV and a "hard" population of electrons with a temperature of $\sim$ 150 keV [*Cayton et al.*, 1989; *Denton et al.*, 2010]. The "soft" population (which is used here) is the suprathermal tail of the electron plasma sheet whose appearance at geosynchronous orbit is associated with substorm injections [*Lezniak et al.*, 1968; *Cayton et al.*, 1989; *Birn et al.*, 1998, 2000]. The "hard" component is the outer electron radiation belt [*Cayton et al.*, 1989; *Belian et al.*, 1996; *Denton et al.*, 2010]. Density-temperature fits to the electron count rates are made every 10 seconds for every spacecraft carrying a SOPA detector; from these 10-s-resolution fits median values of the temperature and median values of the density are calculated every 30 min on each spacecraft and these 30-min-resolution median densities n and median temperatures T are utilized to calculate a specific entropy $S = T/n^{2/3}$ with a 30-min resolution for each operating spacecraft. To determine the occurrence of an electron injection at geosynchronous orbit, the minimum value of the quantity $\log_e(S)$ is calculated every 30 min for all of the spacecraft

operating at that time; when this multisatelite-minimum value of $\log_e(S)$ decreases by 1.0 or more during an hour, an injection is declared. $\log_e(S)$ decreasing by a factor of 1.0 is equivalent to $\log_{10}(S)$ decreasing by a factor of 0.434 or S decreasing by a multiplicative factor of $e^{-1} = 0.368$. Sometimes the specific entropy continues to decrease for two or more subsequent half-hour intervals. (This could be owed to times wherein a sudden decrease in S was captured in the half-hour-resolution medians, or it could be owed to multiple injections during a substorm expansive phase.) If two subsequent half-hour intervals meet the criteria for declaration of an injection, the occurrence of the injection is taken to occur in the first of the two intervals. Hence, in this electron-injection identification scheme, the time between substorm injections is 60 min at the minimum.

Note that the time at which a substorm is detected by using the entropy method depends on the local time positions of the geosynchronous spacecraft at the time of the actual substorm onset. If no satellite is present in the vicinity of local midnight, then the freshly injected electrons must drift toward dawn and then into the dayside until a satellite is encountered. Hence, the substorm-onset times determined from the SOPA injections are systematically delayed by about 0-0.5 hr from the substorm onsets determined by the SML index. The total number of 16,025 electron-injection events was selected by the algorithm covering interval from 1989 to 2007.

3.2.5 Example of data and event selection

An example of SML and MPB data for one day of observations, 15 July 2007, and the results of the event selection for this day are shown in Figure 3.1. Geomagnetic activity changed throughout the day from moderately active conditions ($Kp = 4+$) at the beginning of the day to quiet ($Kp = 1+$) in the second part of the day and thus the event demonstrates the way the indices vary from moderately disturbed to quiet conditions. The top panel in Figure 3.1 shows variations of the SML index where the green solid line represents the low-pass-filtered data used in the SOPHIE algorithm. A number of substorm-like disturbances closely follow each other in the first half of the day, while the SML does not change much in the second part of the day with only one small intensification at $\sim$ 19:00 UT. The MPB index (square root of the MPB index will be used throughout the study) overall shows similar behaviour

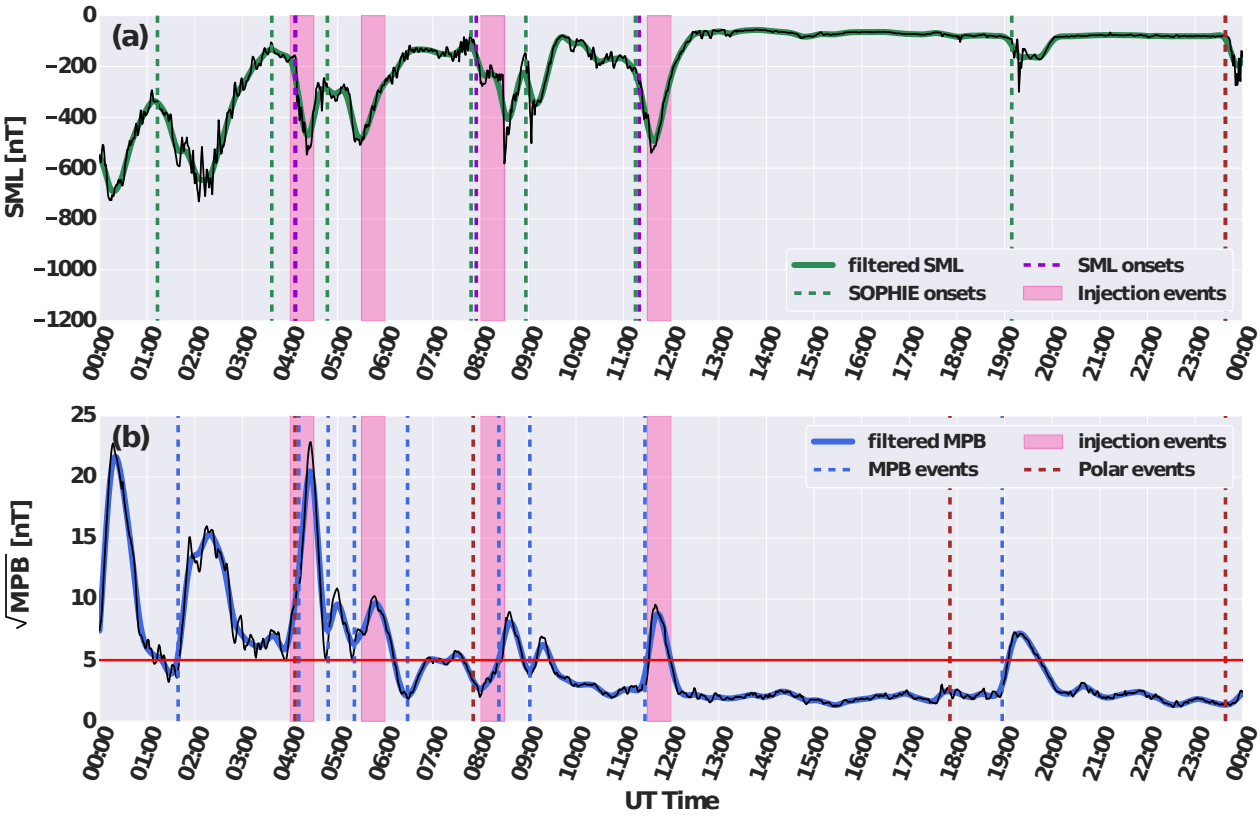

Figure 3.1: Example of data and event selection for 15 July 2007: (a) Variations of the SML index are plotted in black, green line is filtered with 30-min low-pass filter SML index. Vertical dashed green lines are onsets identified by SOPHIE algorithm, purple vertical lines are events identified by the 150 nT-in-15 min algorithm; (b) variations of the 30-min low-pass filtered MPB index (blue line) overplotted on top of unfiltered MPB index (black line). Pink stripes show time intervals of electron injection events; brown lines mark substorm onsets identified from Polar UVI.

with many positive bays during the first half of the day and one single bay at $\sim$ 19:00 UT in the second half of the day.

The number of positive bays in the MPB index is larger than the number of negative bays in the SML index. For example, the clear recovery phase in the SML data started at $\sim$5:30 UT is followed by an interval of quiet phase with a new activation at about 8:00 UT. At the same time, the MPB index recovered from $\sim$5:30 UT to $\sim$6:00 UT and then a new positive bay started developing during the time when SML was quiet. The situation with a positive bay in the MPB data during time of growth or recovering phase of the SML index is observed frequently during intervals of disturbed geomagnetic conditions. Since data from a very dense network of stations is utilized in the creation of the SML index, it is unlikely that

the SML misses a SCW activation. Our interpretation is that the MPB index is sensitive to subauroral polarization streams (SAPS) — fast westward flows in the ionosphere that are commonly observed equatorward of the main auroral oval in the midnight sector during moderately to strongly disturbed conditions [*Foster and Vo*, 2002; *Koustov et al.*, 2008]. SAPS lie in a region of FAC [*Foster and Vo*, 2002] which we believe might result in magnetic field perturbations at midlatitudes. Comparison of several SAPS events in the literature with the MPB index variation seem to confirm this hypothesis, but more detailed statistical investigation is required.

Dashed lines in Figure 3.1 indicate times for 5 types of events (identified as substorm onsets): green lines are SOPHIE events, purple lines are the 150 nT-in-15 min events (subsequently the events will be referred to as simply "SML events"), brown lines are Polar onsets, blue lines are MPB events, and pink bands represent the time intervals of the injection events. 9 MPB events, 7 SOPHIE events, 3 SML events, 4 Polar events, and 4 injection events were identified for the day. All but two events in the MPB data are accompanied by auroral electrojet negative bay disturbances at approximately the same time. Particle injection events tend to appear later in time compared with auroral disturbances. This can be explained by the fact that no time correction was made when energetic electrons were observed with a satellite located in a local time sector away from midnight: it can take up to $30 - 40$ min for the "soft" electron population to drift from the nightside to the dayside and thus measurements from a satellite located away from the injection region will detect to substorm onsets later in time.

The SML events are preceded by intervals of growth phase, indicating that this type of events is unlikely to be intensifications of a recently started substorm. Two of the Polar onsets observed during the disturbed interval coincide well with positive and negative bays, while the Polar auroral substorm at ∼18:00 UT is followed by a magnetic perturbation but one hour later. We note that Polar observations during this time were made in the Southern hemisphere while the magnetometer data come primarily from the Northern Hemisphere. The considered event of 15 July 2007 was in the middle of winter in the Southern hemisphere and summer in the Northern hemisphere. If the Polar event at 18:00 UT was a true breakup, the above observation implies interhemispheric asymmetry of the ionospheric manifestations

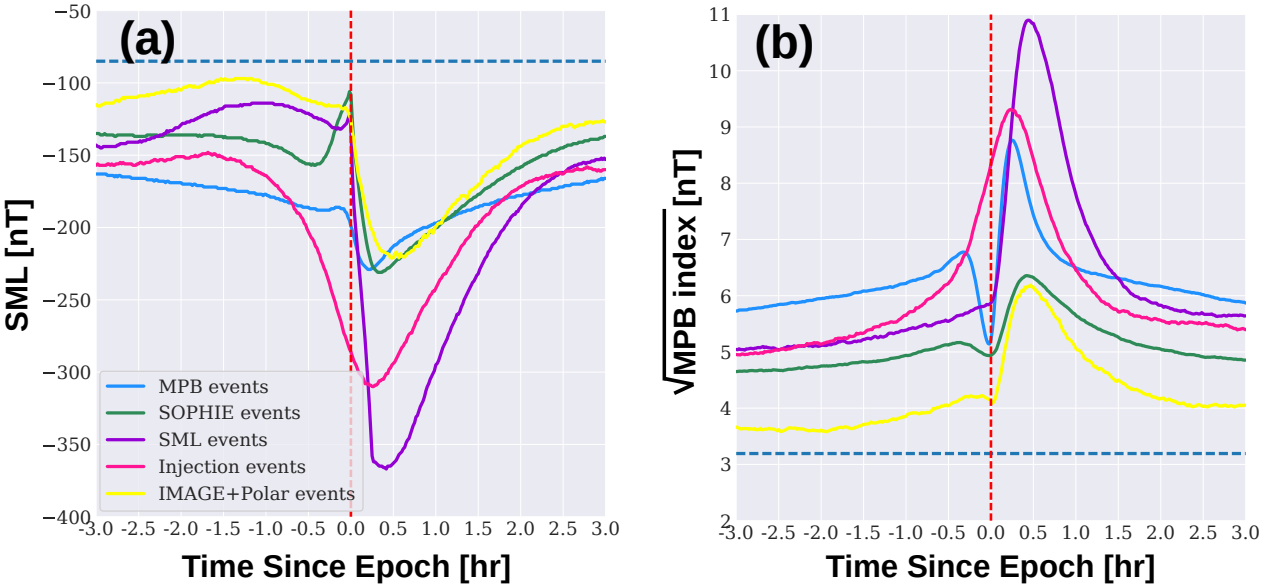

Figure 3.2: Superposed (a) SML and (b) MPB index centered on five types of events (see legend). Horizontal blue dashed lines shows median SML and MPB values for all years of observations.

of substorms.

3.3 Comparison of events

In Figure 3.2 the superposed medians of (a) SML and (b) MPB index are plotted for a 3-hr window where the zero epoch times are taken to be five types of substorm events described in the previous Section. The negative bay centered on the SML events (purple curve in Figure 3.2a) has the largest amplitude: the "median" SML for these SML events drops from ~ -130 nT to ~ -360 nT in a short time and then recovers over about 2 hours. The second largest amplitude of SML comes from the centering on injection events. Taking into account that injection events have only 30-min resolution and additional ambiguity exists in the time of events for satellites in different LT sectors, the median SML of injection events is smoothed over time and, therefore, underestimated. The three other types of events have much smaller SML amplitudes. The superposed curve for optical events (yellow curve) starts from very quiet conditions and have relatively small drop. Note that auroral breakups without "clear" onset were excluded from the IMAGE and Polar lists; this condition might have biased

the list toward quiet-time events and away from disturbed periods (especially storm-time conditions) when identification of auroral breakup becomes highly ambiguous. Clear growth phase signatures are seen for about an hour before optical and SML events. The SML index centered on MPB events (blue curve in Figure 3.2a) has the most elevated values prior to the onset and the smallest negative bay. This implies that the majority of MPB events start during already disturbed conditions and are intensifications of an ongoing event. Note that the SML index for SOPHIE events has an additional negative excursion followed by a peak just before the event. This feature was noticed earlier [e.g., *Forsyth et al.*, 2015] and explained by presence of events with multiple onsets and intensifications. We explored this by looking at superposed SML centered on events that were specially selected by requiring a 2 hr absence of other events prior to the event. The resulting curve (not shown here) showed no signs of this additional peak.

Variations of the MPB index centered on the five sets of events (Figure 3.2b) yields similar results: the positive bay is largest for SML events followed by injection events. The MPB index centered on MPB events has an additional maximum about 20 min prior to onset time (similar to the behavior of the SML index on SML events) which disappears when only isolated events considered. All the events except the IMAGE + Polar events have elevated background values. Note the small amplitude of the positive bay of the IMAGE+Polar substorms. As these events are one of the most reliable signatures of substorm onsets, this result implies that substorms can be accompanied by relatively small magnetic perturbations.

In Figure 3.3 the distribution of recurrence times (waiting times) is plotted for four sets of events: MPB events (blue curve), SOPHIE events (green curve), SML events (purple curve), and injection events (pink curve). The recurrence time Δt is defined as the time interval between the occurrence of subsequent substorm onsets. Note that in Figure 3.3 the recurrence times for optical events are not studied: without an available record of when the optical instrumentation was able to detect substorm onsets, it cannot be verified that no substorms occurred during the Δt time interval calculated between subsequent substorms in the optical-event list. Note that the recurrence-time distributions of MPB events and SOPHIE events (see also Figure 3c of *Forsyth et al.* [2015]) are very different from the recurrence-time distributions of SML events and injection events. Finer-resolution binning

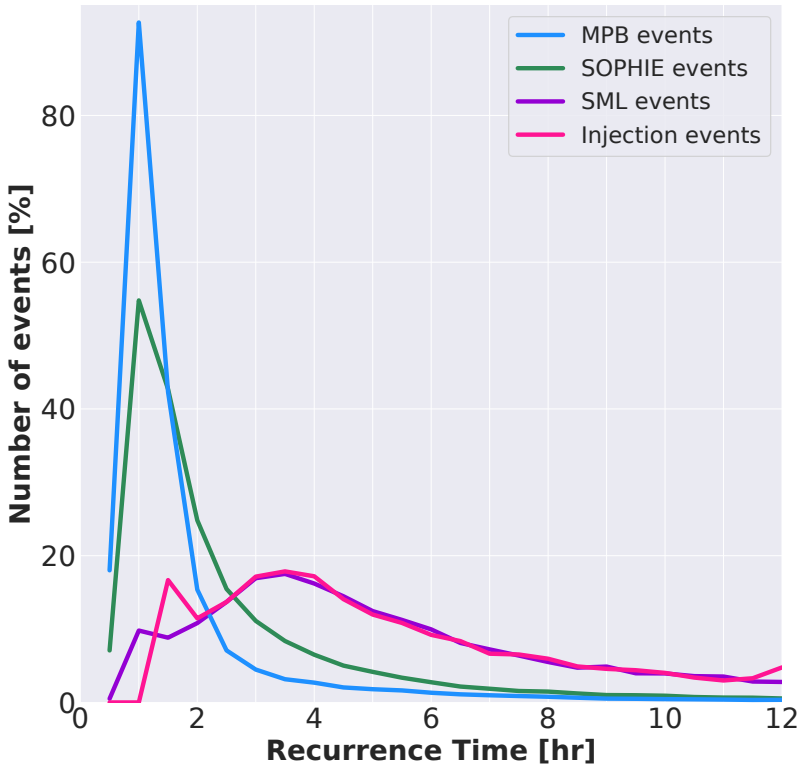

Figure 3.3: Substorm recurrence times Δt for events in four different data sets.

of the Δt values finds that the recurrence-time distributions of MPB and SOPHIE events both peak at about 45 min whereas the recurrence-time distributions of SML and injection events both peak at about 3 hr. Clearly, MPB events and SOPHIE events are different events from SML events and injection events. An interpretation used in this study is that (1) SML events and injection events are substorm onsets (where a substorm onset is the beginning of an interval of enhanced geomagnetic activity) and (2) MPB and SOPHIE events are dominantly substorm activations (where a substorm activation is an increase in geomagnetic activity during an ongoing interval of enhanced geomagnetic activity). (See also the discussion in *Forsyth et al.* [2015] about the nature of the SOPHIE events.) In other words, SML events and injection events are substorm onsets and MPB events and SOPHIE events are dominated by enhancements during ongoing substorms. Note in Figure 3.3 that the distribution of Δt values for injection events is picking up some substorm activations (peak at about 1 hr for the pink curve) in addition to the substorm onsets (peaking at about 3 hr). In Table 3.1 the minimum Δt value and median Δt value for the distributions of Figure 3.3 are listed. Note

Table 3.1: Properties of the substorm recurrence time Δt for events in four different data sets.

	MPB Events	SOPHIE Events	SML Events	Injection events
Minimum Δt	6 min	12 min	26 min	60 min
Median Δt	0.94 hr	1.5 hr	5.4 hr	5.0 hr
Average occurrence rate	10.7 per day	8.4 per day	2.2 per day	2.7 per day

that there are Δt values as low as 6 min and 12 min, respectively, for the MPB and SOPHIE events.

In Table 3.1 the average substorm occurrence rates are listed for the SOPHIE, MPB, SML, and injection evnts. Note that the occurrence rates of SOPHIE events and MPB events are much greater than the occurrence rates of SML events and injection events. With an average of 8.4 events per day for SOPHIE and 10.7 per day for MPB it is clear that these events are dominantly substorm activations. The occurrence rates of SML events (2.2 per day) and injection events (2.7 per day) are consistent with substorm occurrence rates in the literature: *Borovsky et al.* [1993] found 4.2 per day, *Prichard et al.* [1996] found 4.6 per day, *Tanskanen et al.* [2005, 2011] found 1.424 for 11 hours of observations per day (~ 3.1 per day).

In Figure 3.4 the substorm occurrence rate for the four sets of events is plotted as a function of Kp. As expected, all of the occurrence rates increase with the Kp index. At low Kp the occurrence rates of the MPB events (blue), the SML events (purple), and the injection events (pink) show a threshold effect where very few substorms occur when Kp is less than 1+. The occurrence rate of SOPHIE events (green curve) does not show clear threshold effect; the occurrence rate of SOPHIE events increases almost linearly with Kp. The occurrence rate of MPB events, on the other hand, increases much faster with Kp than that of SOPHIE: for quiet geomagnetic conditions, the number of MPB events is smaller than the number of SOPHIE events; however, as conditions become more disturbed, the number of MPB events increases rapidly. This supports our earlier hypothesis that MPB events include events associated with SAPS. SML and injection events reach a plateau of about 5 and 6 events per day, respectively, after $Kp > 4o$. SOPHIE events do not show such saturation effect and grow in number steadily with Kp to very high rates. Occurrence of MPB events grows slower after $Kp > 4o$ to even larger values (more than one event per hour) for high

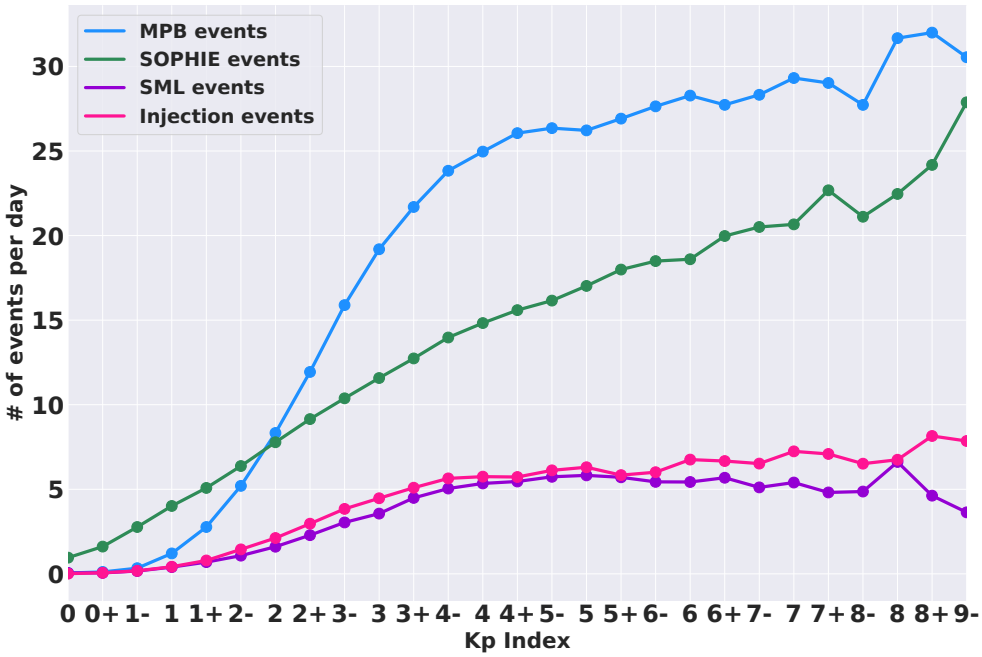

Figure 3.4: Occurrence rate of four types of events (see legend) depending on the level of geomagnetic activity.

Kp. Figure 3.4 supports again that SOPHIE and MPB events are different from SML and injection types of events. Additionally, MPB and SOPHIE event differ from each other.

Forsyth et al. [2015] recognised the problem of SOPHIE events contamination by intensifications and pseudobreakups. Their solution is to impose a requirement for a growth phase interval just before a substorm event. Our analysis (not shown here), however, demonstrated that this condition results in a loss of many substorms during disturbed intervals: when geomagnetic conditions are disturbed, substorms follow each other without an apparent growth phase.

3.4 Substorm-like signatures associated with interplanetary shocks

A substorm manifests itself in a number of mangetospheric and ionospheric phenomena and as was demonstrated earlier substorm signatures are seen in various data sets. Here we will show that these signatures do not necessary mean a substorm onset and care should be taken

in calling an event a substorm especially in case studies.

For this study 47 intervals between interplanetary shocks travelling ahead of coronal mass ejections (CMEs) and the ejecta plasma of CMEs were considered. Plasma that resides between an interplanetary shock and ejecta is called CME-sheath plasma. The CME-sheath is an interval of shocked, compressed ambient solar wind. The shock-sheath intervals are found by examining the ACE and OMNI data to find intervals where ejecta plasma drives geomagnetic activity. Interplanetary shocks ahead of the ejecta are located with 64-s resolution ACE data; these shocks can be found on the ACE list of "Disturbances and Transients" at `http://www.ssg.sr.unh.edu/mag/ace/ACElists/obslist.html#shocks`. The time of arrival of each shock at Earth is determined by inspecting the 1-min-resolution SYM-H index and marking times when SYM-H undergoes a sudden positive perturbation. The sheath plasma behind each shock is taken to commence in time with the shock and to terminate in time when the leading edge of the ejecta plasma arrives. Many of the collected intervals of ejecta are magnetic clouds in the *Lepping et al.* [2005] cloud collection. In this manner 47 shock-sheath events were obtained in the years 1998–2006.

Reaction of MPB and SML indices on the shock and sheath is shown in Figure 3.5a where superposed median indices centered on the time of the interplanetary shock arrival at Earth are plotted for a 3-hr window. The SML index drops by more than 200 nT in less than 10 min. MPB also jumps to a very large values within a matter of minutes. Changes in the both indices centered on the sheath shock are more abrupt than changes of the indices around any of the events shown in Figure 3.2. Note also very large amplitude of the $\sqrt{\text{MPB}}$ index: it reaches values above 18 nT, while $\sqrt{\text{MPB}}$ is below 14 nT for any of the events in Figure 3.2. After the sheath's arrival at Earth, the indices become very perturbed as can be seen in the right part of the Figure 3.5a.

In Figure 3.5b the change in the substorm occurrence rate from before the shock (when the Earth is in the unshocked ambient solar wind) to after the shock (when the Earth is in the compressed CME-sheath plasma) is seen. The statistics is poor so the numbers quoted are very approximate. The rate of MPB events (blue curve) increases from about 0.25 events per 30 min to about 0.5 events per 30 min (a rate change from about 12 per day to about 24 per day) and the rate of SML events (green curve) changes from about 0.2 per 30 min to

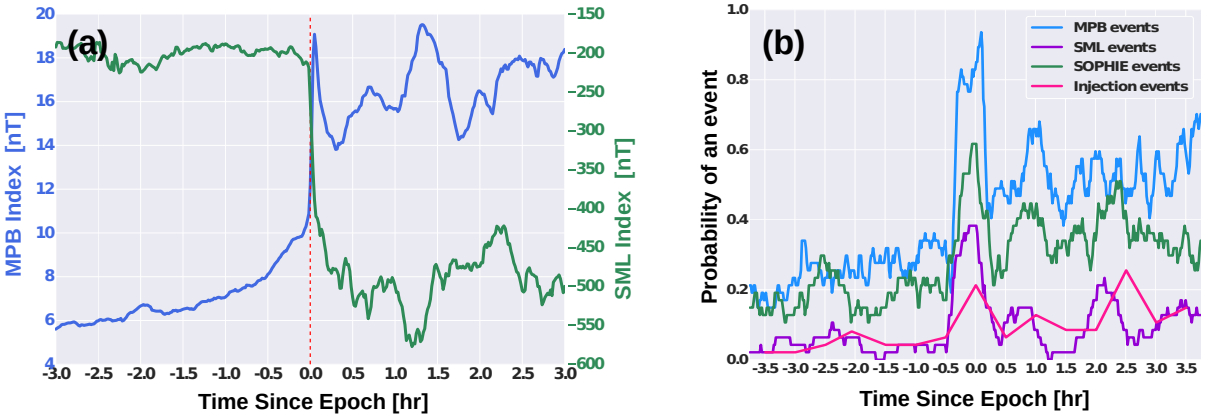

Figure 3.5: (a) Superposed MPB index (left axis) and SML index (right axis). (b) Superposed moving probability to detect an event in a 30-min interval. Zero epoch time for each plot is the time of the interplanetary shock arrival at Earth.

about 0.3 per 30 min (from about 9.6 per day to about 14.4 per day). In Figure 3.5b SML events increase from about 0.05 per 30 min to about 0.1 per 30 min (2.4 per day to 4.8 per day) and injection event increase from about 0.08 per 30 min to about 0.12 per 30 min (2.3 per day to about 3.8 per day). One interesting feature of Figure 3.5 is elevated probability of a substorm immediately upon arrival of the sheath at Earth. Changes in the MPB and SML indices upon arrival of the shock at Earth (Figure 3.5a) would be undoubtedly identified as prominent substorm onset by SOPHIE, SML, and MPB algorithms. We argue, however, that more time needs to pass since the sheath's initial arrival to produce a substorm. Indeed, a sustained period of increased driving is needed for a substorm to occur [*Newell and Liou*, 2011]. The changes in the indices most probably are caused by a compression of the magnetosphere. We investigated this question deeper by looking at the reaction of the energetic-particle population at geosynchronous orbit.

In Figure 3.6 superposed electron fluxes from the three lowest energy channels of the LANL SOPA instrument are centered on the time of the shock arrival at Earth (panels a and b) and on the occurrence times of SML events (panels c and d). We considered separately changes in the fluxes as detected by satellites located at the time of an event in the midnight-to-dawn (23 to 5 LT) and in the noon-to-dusk (10 to 20 LT) sectors. When reaction of the fluxes in the noon LT sector was analysed, care was taken to exclude times when

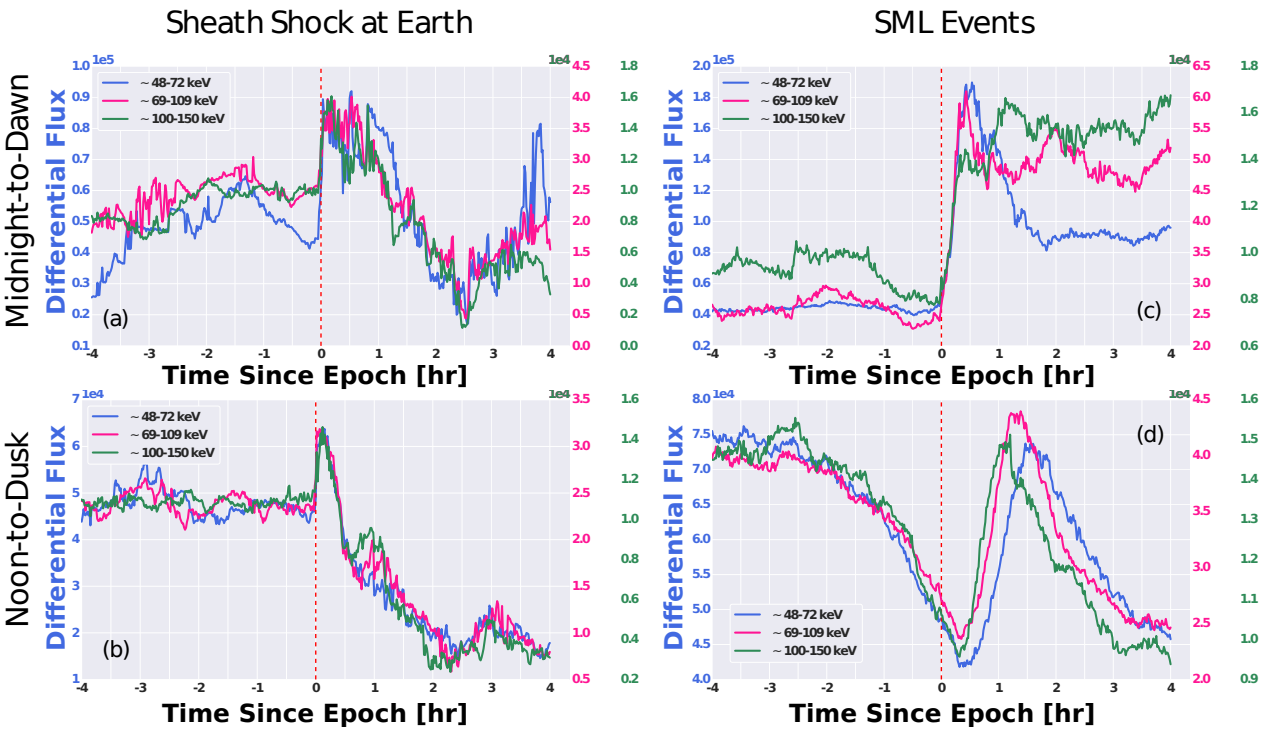

Figure 3.6: Superposed electron fluxes from low-energy channels (see legend) of the LANL SOPA instrument. Panels (a) and (b) correspond to the shock at Earth zero epoch time, panels (c) and (d) – to the onset time of SML events. Observations divided into "midnight-to-dawn" (23-5 LT sector) and "noon-to- dusk"(10-20 LT sector) groups depending on the position of satellite at the time of event.

geosynchronous satellites left the magnetosphere and entered the magnetosheath as determined by examining plasma data from the same spacecraft. Considered SML events span time interval from September 1989 to September 1993. Note the differences between reaction of the fluxes on the shock at Earth and SML events. First of all, as seen from Figure 3.6 (panels a and b), changes in the fluxes centered on the shock happen simultaneously in both LT sectors. For SML substorm events, in contrast, fluxes begin to rise at the zero epoch time in the midnight-to-dawn LT sector (Figure 3.6c) and show up to 30 min delay in the noon-to-dusk LT sector. This is expected as substorm-associated electron injections occur close to the midnight sector and then electrons drift eastward, so satellites located in the noon-to-dusk sector will detect changes in fluxes later in time than satellites in the midnight-to-dawn sector. Another important difference is that changes in fluxes associated with the SML events happen nearly simultaneously when observed with satellites in the midnight-to-

dawn sector (panel c) and electron fluxes show dispersion when observed in the noon-to-dusk sector. This is expected as lower-energy electrons have lower drift velocities and require more time for them to drift away from the injection region. Increases of electron fluxes centered on the shock at Earth events, on the other hand, are dispersionless in both LT sectors. Note also that jumps of fluxes at the time of the shock at Earth are more sharp than jumps of fluxes at the time of SML events. All these observations support the argument that changes in the SML and MPB index at time of the shock at Earth are not caused by the occurrence of a substorm.

3.5 Substorm recurrence-time distributions

In Section 3.3 we arrived to a conclusion that the most robust substorm events are those determined by jumps in the SML index (SML events) and substorm onsets determined by electron injections into geosynchronous orbit. In Figure 3.7a the distribution of recurrence times is plotted for SML events in the years 1979–2015 (blue curve) and for substorm injections into geosynchronous orbit in the years 1989–2007 (red curve). The recurrence-time distributions for electron injections and for SML events are similar to each other. The recurrence-time distributions in Figure 3.7a are similar to substorm recurrence-time distributions found in previous studies [e.g., *Borovsky et al.*, 1993; *Prichard et al.*, 1996, Figures 3,4 and Figure 1, respectively], where it was found that the distributions are composed of a quasi-Gaussian population centered on about 3 hr and an exponential distribution at larger Δt values. Owing to the larger data statistics used in the present study, the distributions in Figure 3.7 extend to much larger values of Δt than prior distributions did.

In Figure 3.7b the SML recurrence-time distribution from Figure 3.7a is mathematically analyzed. The distribution from the SML data is plotted in black. For recurrence times 30 hr$< \Delta t <$165 hr the black curve is fit by an exponential function

$$\text{fit1} = 0.328 \exp(-\Delta t/31.4\,\text{h}) \tag{3.1}$$

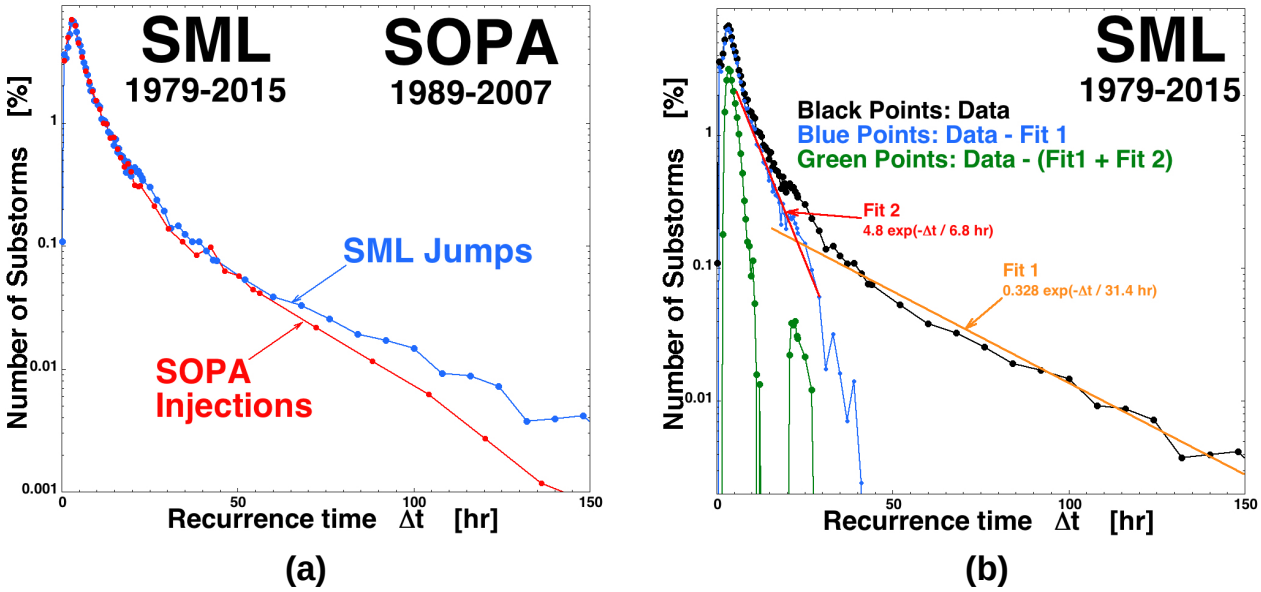

Figure 3.7: (a) The recurrence-time distributions of substorm onsets for 28,464 substorms identified with jumps in the SML index in 1979–2015 (blue) and for 16,025 substorms identified with electron injections into geosynchronous orbit in 1989–2007 (red). (b) The distribution for the SML events is mathematically analyzed into three populations.

This exponential fit is plotted as the orange curve in Figure 3.7b. Subtracting fit1 off of the black curve for all values of Δt, the blue curve results. For recurrence times 8 hr$< \Delta t <$24 hr the blue curve is fit by the exponential function

$$\text{fit2} = 4.84 \exp(-\Delta t/6.76 \text{ h}) \tag{3.2}$$

which is plotted as the red curve in Figure 3.7b. The green curve in Figure 3.7b is the blue curve with fit2 subtracted off for all values of Δt. Hence, the green curve in Figure 3.7b is the recurrence-time distribution (black) with the two exponential fits subtracted off. A similar analysis was performed in *Borovsky et al.* [1993], wherein a single exponential function was subtracted off of the recurrence-time distribution and the quasi-Gaussian residual (i.e., the green curve) was interpreted to be recurrence times for a population of quasiperiodically occurring substorms. The information-theoretic analysis of *Prichard et al.* [1996] confirmed that interpretation. In *Borovsky et al.* [1993] it was noted that an exponential distribution of recurrence times is consistent with random occurrence of substorms following a Poisson

process wherein the probability of substorm occurrence is independent of the past record of occurrence [*International Telegraph, and Telephone Corporation*, 1979].

The following interpretation is made for the residual distribution (green curve) and the two exponential fits of Figure 3.7b. (1) The residual waiting-time distribution (green curve) represents the recurrence of substorms in a periodic fashion with a substorm-recurrence period of 2–4 hr. (2) The exponential distribution (fit2) of recurrence times of expression (2) represents the occurrence of substorms associated with random occurrences of solar wind intervals capable of driving the magnetosphere sufficiently to create a substorm; we will look for evidence that the time scale of 6.8 hr of this fit is associated with the mesoscale magnetic structure of the solar wind. (3) The exponential distribution (fit1) of recurrence times of expression (1) represents the durations of intervals of the solar wind wherein it is probable that the driving of the magnetosphere is too weak to produce a substorm; we will look for evidence that the 34.5 hr time scale of this fit is associated with the large-scale structure of the solar wind plasma.

Figure 3.8 demonstrates some aspects of the periodic occurrence of substorms versus the random occurrence of substorms. In Figure 3.8 (top) the solar wind velocity is plotted for 20 days in the spring of the year 2005; two high-speed streams are contained in the 20 day interval. In Figure 3.8 (bottom) the solar wind driver function R_{quick} is plotted (black). R_{quick} is derived by *Borovsky and Birn* [2014] to represent the reconnection rate (in units of mV/m) at the nose of the magnetosphere based on the Cassak-Shay equation [*Cassak and Shay*, 2007] for the reconnection rate between two collisionless magnetized plasmas (the magnetosphere and the magnetosheath). R_{quick} is given by Equation 1.10. The formula for R_{quick} can be separated into two parts:

$$R_{quick} = R_{q0} \sin^2(\theta_{clock}/2) \tag{3.3a}$$

$$R_{q0} = 2.04 \mu_0^{1/2} m_p^{1/2} n_{sw}^{1/2} v_{sw}^2 M_A^{-1.35} [1 + 680 M_A^{-3.30}]^{-1/4} \tag{3.3b}$$

where m_p is the mass of a proton, R_{q0} represents the portion of R_{quick} that is associated with the structure of the solar wind plasma (n_{sw}, B_{sw}, and v_{sw}), and $\sin^2(\theta_{clock}/2)$ is the portion of R_{quick} that is associated with the magnetic field-vector structure of the solar wind. In

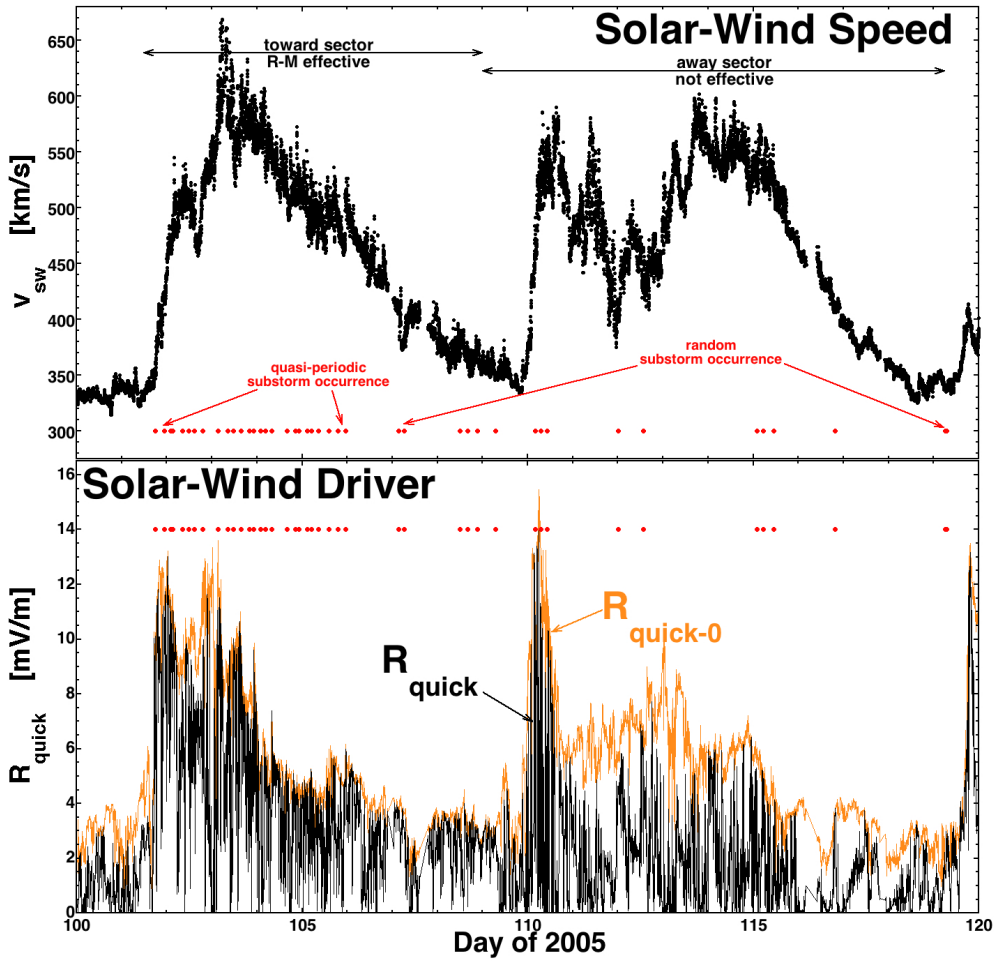

Figure 3.8: For 20 days in the spring of 2005 the occurrence of substorms (red dots) is examined in comparison with (top) the speed of the solar wind and (bottom) the strength of solar wind driving of the magnetosphere.

Figure 3.8 (bottom) R_{q0} is plotted in blue for the 20 days. In both panels of Figure 3.8 the occurrence times of substorm onsets as determined by jumps in the SML index are indicated by red dots. As indicated in Figure 3.8 (top) there is an interval wherein substorms occur in a quasiperiodic fashion (days 102–105) and an interval wherein substorms occur in a random fashion (days 107–118). In Figure 3.8 (top) an interval wherein the IMF sector is in a toward orientation and an interval wherein it is in an away sector are indicated. According to the Russell-McPherron effect [*Russell and McPherron*, 1973], the solar wind tends to be more geoeffective in the spring season when the IMF is in a toward sector and tends to be not geoeffective in the spring season when the IMF is in an away sector. This is reflected in

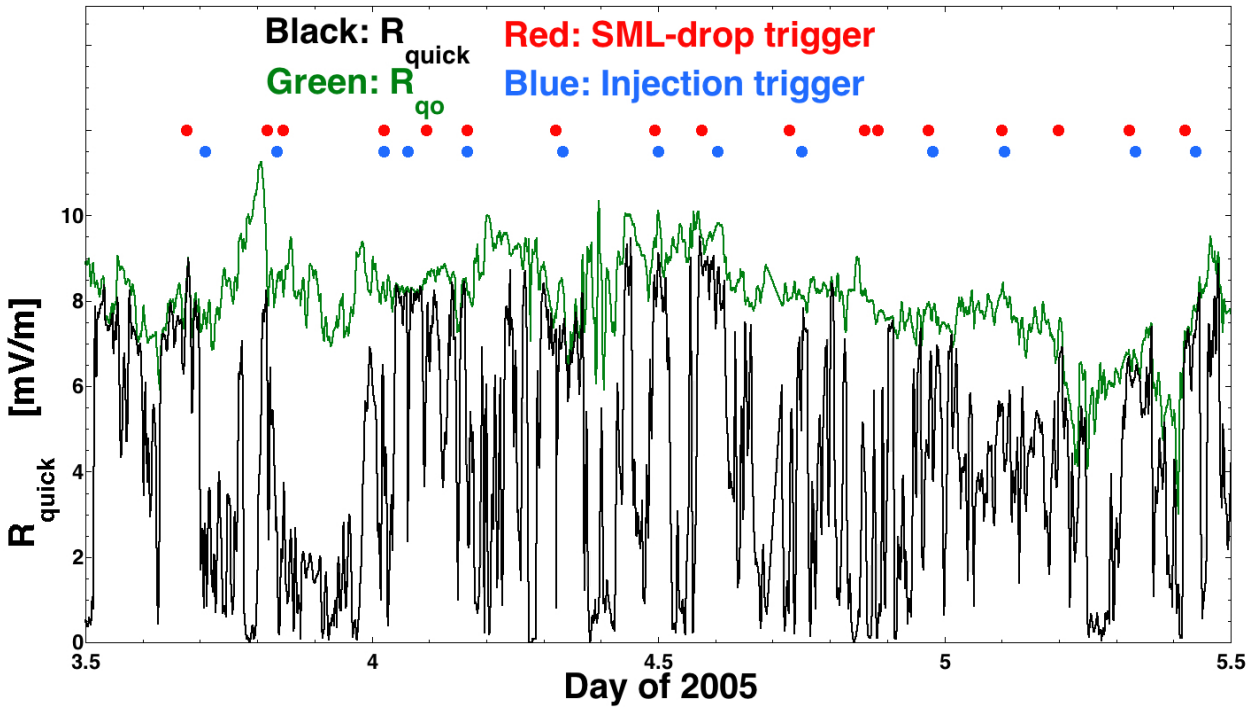

Figure 3.9: The occurrence of quasiperiodic substorms (red and blue dots) is compared with the driving of the magnetosphere by the solar wind (black curve) for 2 days in 2005.

Figure 3.8 (bottom) wherein R_{quick} (black) is larger in the first high-speed stream (toward sector) than it is in the second high-speed stream (away sector). In Figure 3.8 the periodic substorms are occurring when the solar wind driver (i.e. R_{quick}) is high for a sustained interval and the substorms are randomly occurring when the solar wind driving is weaker.

Note that the same conclusions as those from Figure 3.8 result if another solar wind driver such as the Newell function $v_{sw}^{4/3} B_{\perp}^{2/3} \sin^{8/3}(\theta_{clock}/2)$ [*Newell et al.*, 2007] is used, with that function separated into a plasma term $v_{sw}^{4/3} B_{\perp}^{2/3}$ and a magnetic-clock-angle term $\sin^{8/3}(\theta_{clock}/2)$.

Figure 3.9 focuses on an interval of quasiperiodic substorm occurrence in the year 2005. Two days are displayed. The solar wind driving function R_{quick} is plotted in black, and the plasma component R_{q0} of R_{quick} is plotted in green. The occurrence times of substorms as determined by jumps in the SML index are indicated in red, and the occurrence times of substorms as determined by electron injections are indicated in blue. Note that injection times are delayed by 0–30 min owing to the local-time positions of spacecraft in geosynchronous

orbit at the time of the actual substorm onset. In Figure 3.9 R_{quick} is highly time varying compared with R_{q0}: this is because of rapid variations in $\sin^2(\theta_{clock}/2)$ (expressions (3.3a) and (3.3b)) that are owed to rapid variations in θ_{clock}, the direction of the solar wind magnetic field. The rapid time variations in R_{quick} are caused by the mesoscale spatial structure of the solar wind magnetic field being advected past the Earth producing rapid changes in θ_{clock}. Note that the variations in R_{quick} occur more rapidly than the recurrence times between the substorm onsets.

In Figure 3.10 the superposed-epoch average of the solar wind driver function R_{quick} is plotted as a function of time where the zero epoch (trigger) is the occurrence time of substorm onset as determined by the jumps in the SML index. The substorm onsets are separated into two groups: random substorms (where the time since the prior substorm is 6 hr or more) and periodic substorms (where the time since the prior substorm is between 2 and 4 hr). In Figure 3.10 (top) the superposed average of R_{quick} is plotted in blue for the group of periodic substorms and the superposed average of R_{quick} is plotted in red for the group of random substorms. Both curves in Figure 3.10 (top) indicate that substorm onset is associated with an interval of enhanced solar wind driving prior to the onset [e.g., *Fairfield and Cahill Jr*, 1966; *Caan et al.*, 1977, 1978; *Morley and Freeman*, 2007; *Wild et al.*, 2009] (and see in particular the superposed-epoch analysis of *Newell and Gjerloev* [2011]). In Figure 3.10 (middle) the plasma portion R_{q0} of R_{quick} is plotted for the two sets of triggers: note that the substorm onset occurrence is not associated with a variation in the solar wind plasma properties. In Figure 3.10 (bottom) the superposed average of the IMF clock angle θ_{clock} is plotted for the two sets of triggers: both the periodically occurring (blue) and the randomly occurring (red) substorms are temporally associated with an increase in the IMF clock angle θ_{clock} at the time of the substorm onset. Note that for the red curve (randomly occurring substorms) in Figure 3.10 (bottom) that θ_{clock} is on average less than 90° (northward IMF) in the interval prior to the occurrence of the substorm, whereas for the blue curve (periodically occurring substorms) θ_{clock} is on average greater than 90° (southward) in the interval before the substorm occurs. This agrees with the idea that random substorms tend to occur during intervals of weaker driving and that periodic substorms occur during intervals of stronger driving (Figure 3.8). The two curves plotting R_{q0} in Figure 3.10 (middle) are consistent with

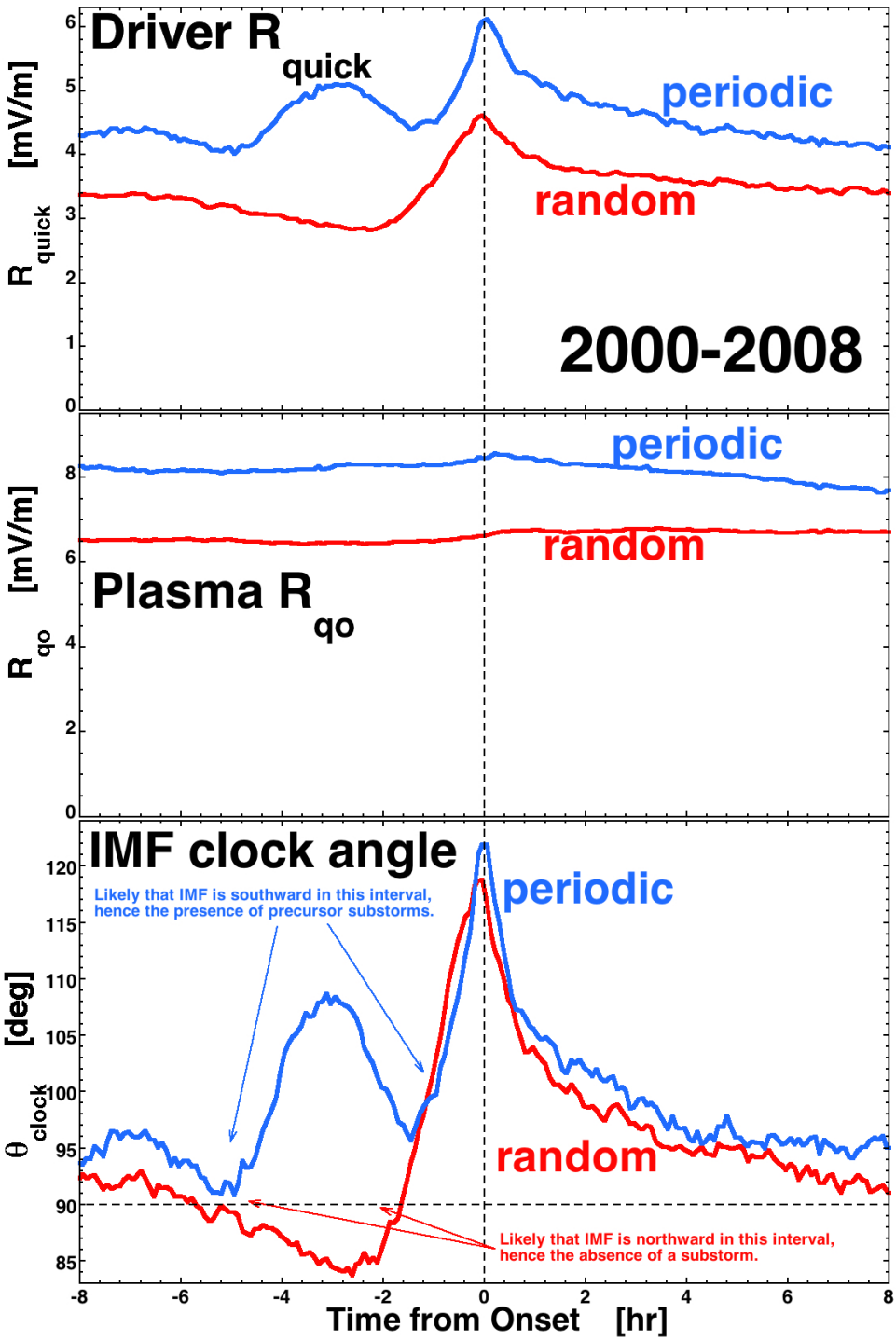

Figure 3.10: (top) The superposed average of the solar wind driver R_{quick}, (middle) the plasma portion R_{q0} of R_{quick}, and (bottom) the clock angle of the IMF centered on the times of substorm onsets as determined by the jumps in the SML index in 2000–2008. The substorms are separated into two populations: periodic (blue curves) and random (red curves).

this idea. Note in the blue curves for periodic substorms in Figure 3.10 (top and bottom)that there is an indication of enhanced driving 2–4 hr prior to the occurrence of the substorm at the zero epoch: this indicates that the prior substorms (which occurred by definition 2–4 hr earlier) are also associated with an interval of enhanced driving (caused by an interval of more southward IMF clock angle). This plot raises the question: is the $\sim$ 3 hr periodicity of substorm occurrence caused by an $\sim$ 3 hr periodicity in the solar wind producing a 3 hr periodicity in the driving of the magnetosphere or is it caused by an inherent property of the magnetosphere-ionosphere system?

To investigate whether there is an $\sim$ 3 hr periodicity in the driving of the magnetosphere by the solar wind, Figure 3.11 explores some time scales in the solar wind time series at Earth. Using 5 min averages of the advected solar wind magnetic field from the OMNI database [*King and Papitashvili*, 2005], the clock angle θ_{clock} of the IMF is calculated at Earth as a function of time for the 9 years (2000–2008). The zero crossings of the time series [e.g., *Ylvisaker*, 1965; *Sreenivasan et al.*, 1983] are determined wherein the clock angle θ_{clock} crosses from less than 90° (northward) to greater than 90° (southward) and the time intervals Δt between the zero crossings are calculated. The waiting-time distribution for the zero crossings for the 5 min averaged θ_{clock} is plotted in red in Figure 3.11. The 5 min resolution values of θ_{clock} are time averaged to 15 min, the zero crossings in the 15 min time series are located, and the waiting-time distribution of the 15 min averaged θ_{clock} values is plotted as the blue curve in Figure 3.11. The process is repeated for 30 min averages of θ_{clock} and for 60 min averages of θ_{clock}, and the waiting-time distributions for the zero crossings are plotted in green and purple, respectively, in Figure 3.11. The red curve in Figure 3.11 represents the occurrence distribution of times between the onsets of intervals of driving that are 5 min or more in length. Similarly, the blue curve in Figure 3.11 represents the occurrence distribution of waiting times between the onsets of driving intervals that are 15 min in length; the green curve represents the occurrence distribution of waiting times between the onsets of driving intervals that are 30 min in length, and the purple curve represents the occurrence distribution of waiting times between the onsets of solar wind driving intervals that are 60 min in length. In Figure 3.11 there is no indication of an $\sim$ 3 hr periodicity in the occurrence of driving intervals in the solar wind. If R_{q0} of the solar wind is strong, southward IMF

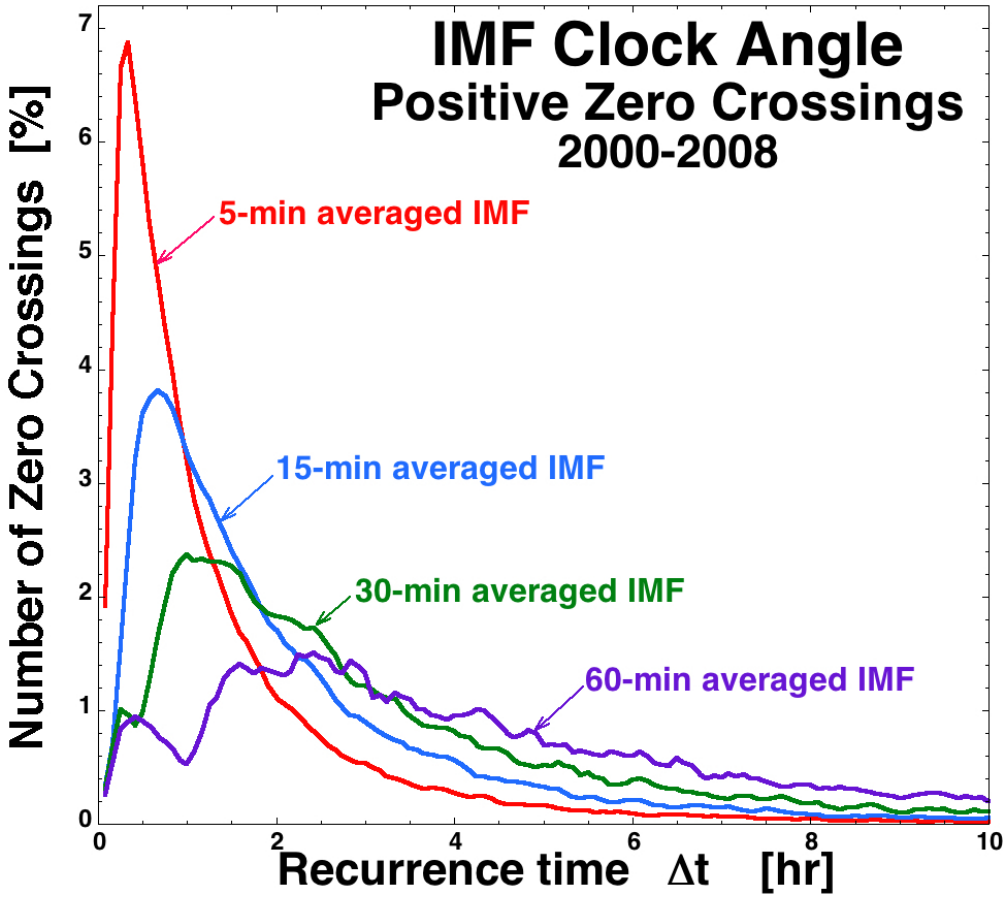

Figure 3.11: The waiting-time distributions for crossings of the IMF clock angle through 90° going southward. Each colored curve uses a different time averaging of the 5 min resolution OMNI data set.

intervals occur more frequently than 3 hr and intervals of enhanced driving will occur more frequently than the $\sim$ 3 hr periodicity of substorm occurrence (Figure 3.9). A working model of the occurrence of periodic substorms is that the periodicity of substorm occurrence is 2–4 hr because of some inherent property of the magnetosphere-ionosphere system and that a substorm will occur after this "magnetospheric" interval when the next available solar wind-driving interval occurs. Hence, the variability of the recurrence period is caused by the added waiting time for a solar wind-driving interval.

Solar wind time scales associated with the random occurrence of substorms are examined in Figure 3.12. The clock-angle zero-crossing waiting-time distributions plotted in Figure 3.11 are actually well fit by exponential distributions. In Figure 3.12a the 60 min averaged

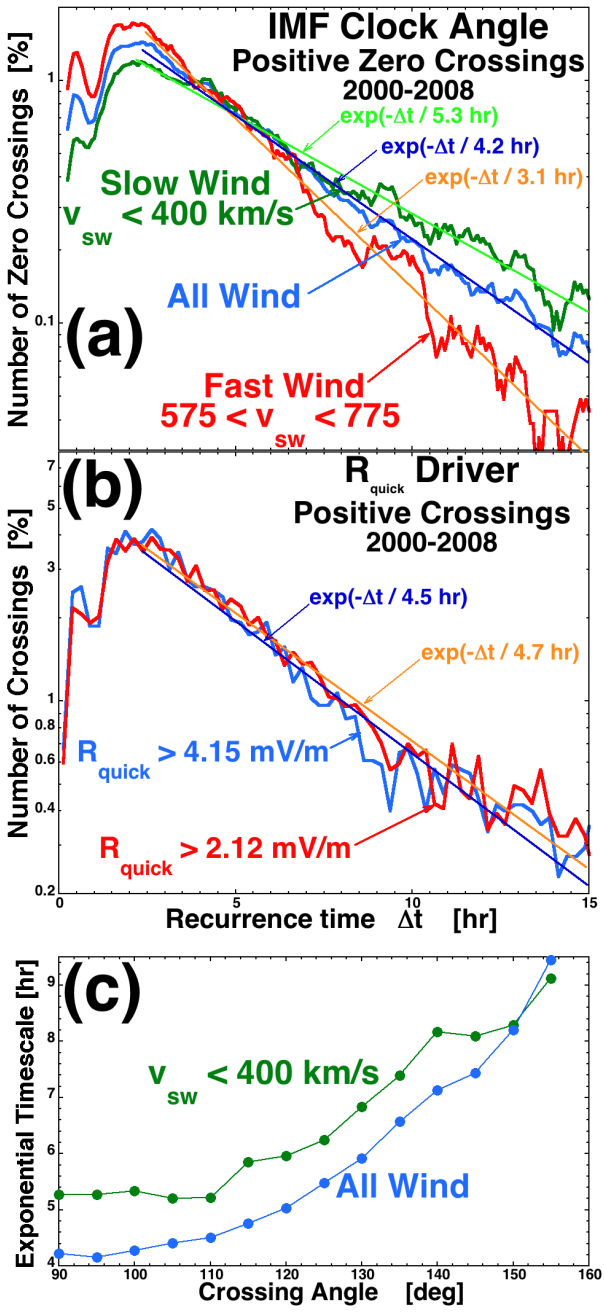

Figure 3.12: (a) For 60 min averages of the 5 min resolution OMNI data set, the waiting times for the 90° crossings of the IMF clock angle are binned: the blue curve is for all solar wind, the green curve is for slow solar wind ($v_{sw} < 400$ km/s), and the red curve is for fast solar wind (v_{sw} in the range of 575–775 km/s). Exponential fits to the three curves are shown. (b) For 60 min averages of the 5 min resolution OMNI data set, the waiting times for positive crossings of two values of the driver function R_{quick} are binned: the blue curve is for crossings of $R_{quick} = 4.15$ mV/m, and the red curve is for crossings of $R_{quick} = 2.12$ mV/m. Exponential fits to the two curves are shown. (c) The exponential fit parameters to the clock-angle waiting-time distributions are shown for the all solar wind (blue) and for the slow solar wind (green) as the crossing angle is varied from 90° to 155°.

distribution from Figure 3.11 is replotted (blue curve) logarithmically and fit with an exponential function $\exp(-\Delta t/4.2\text{ h})$. Hence, the 60 min average of the magnetic field vector of the solar wind has random southward crossings (through $\theta_{clock} = 90°$) randomly with a characteristic time scale of 4.2 hr between subsequent crossings. The solar wind zero-crossing waiting times are separately collected for intervals of typical slow wind ($v_{sw} < 400$ km/s) and for intervals of typical fast wind ($v_{sw} = 575 - 775$ km/s), and those distributions are plotted in green and red, respectively, in Figure 3.12a. The time scales of magnetic structure at Earth are shorter in the red curve of the fast wind (coronal-hole plasma) than they are in the green curve of the slow wind; the mesoscale magnetic structures of the slow wind are larger than the structures of the fast wind [*Borovsky*, 2008], and the slow wind advects the structures past the Earth at a slower rate. The slow-wind waiting-time distribution is fit by $\exp(-\Delta t/5.3\text{ h})$, and the fast-wind waiting-time distribution is fit by $\exp(-\Delta t/3.1\text{ h})$. Similarly, in Figure 3.12b the waiting-time distributions for crossings of the magnetospheric driver function R_{quick} are plotted and fitted. The red curve is the distribution of waiting times for the hourly average of R_{quick} to exceed 2.12 mV/m (which is the median value of R_{quick}), and the blue curve is the distribution of waiting times for the hourly average of R_{quick} to exceed 4.15 mV/m (which is the 75% quartile of R_{quick}). The exponential fit distributions for R_{quick} waiting times in Figure 3.12b yield similar waiting times as the southward crossings through $\theta_{clock} = 90°$ in Figure 3.12a. The fits in Figure 3.12a are for crossings southward across $\theta_{clock} = 90°$. If the zero line for the zero crossings is taken at larger values of θ_{clock} (i.e., more southward values), the waiting times are longer and the distribution has a different characteristic time scale. In Figure 3.12c the exponential fitting of the top plot is repeated for zero-crossing waiting-time distributions where the crossing angle is varied from $\theta_{clock} = 90°$ to $\theta_{clock} = 155°$. For intervals with the more southward IMF (greater θ_{clock}), the characteristic time of the exponential fit to the waiting-time distribution increases. The characteristic time scale of the exponential waiting-time distribution of substorms onsets (6.8 hr in Figure 3.7) is in the vicinity of the characteristic time scales of the exponential waiting-time distributions of solar wind-driving intervals in Figure 3.12c, particularly for slow solar wind where the randomly occurring substorms are prominent. Hence, the statistics support the picture articulated by *Morley and Freeman* [2007], wherein the randomly occurring substorms are

associated with randomly occurring intervals of good solar wind driving (associated with randomly occurring intervals of the direction of the solar wind magnetic field at Earth).

3.6 Solar cycle and seasonal variation in substorm occurrence

In Figure 3.13a the substorm occurrence rates (in unit of substorms per day) as determined from jumps in the SML index (red curve) and as determined from electron injections (blue curve) are plotted as a function of time for the years 1979 to 2015. Each point is the average value for a calendar year. In Figure 3.13c the monthly sunspot number is plotted. The substorm occurrence rate varies from year to year, and the two measures of substorm occurrence track each other fairly well. As is known [*Nevanlinna and Pulkkinen*, 1998; *Tanskanen*, 2009; *Tanskanen et al.*, 2011], the substorm occurrence rate is greatest in the declining phase of the solar cycle. During the declining phases of the solar cycle equatorward extensions of coronal holes on the Sun can have geometries that result in long-lived high-speed coronal-hole-origin plasma at Earth [*McAllister et al.*, 1996]; early in the declining phase (near solar maximum) high-speed ejecta can also enhance the early phases of high-speed-stream-driven storms. Note that the substorm occurrence rate was very low in the year 2009, which was an interval of exceptionally weak solar wind [*Smith et al.*, 2013; *Zerbo and Richardson*, 2015]. Note that the SML index for 1979 and 1980 had a sparsity of stations, which may account for the low substorm occurrence rates registered for those years in the red curve. In a 1 year running average of the fraction of time four different types of solar wind plasma are at Earth, as determined by the *Xu and Borovsky* [2015] solar wind categorization scheme applied to the OMNI solar wind data set (Figure 3.13b).

In Table 3.2 the substorm-occurrence rates as determined by jumps in SML and by electron injections are collected for the four phases of the solar cycle. (Note that the SML substorms and the injection substorms have different ranges of years, as seen in Figure 3.13.) Rates are given in units of substorms per year and substorms per day. The bottom line of Table 3.2 displays the substorm-occurrence rates for all phases of the solar cycle.

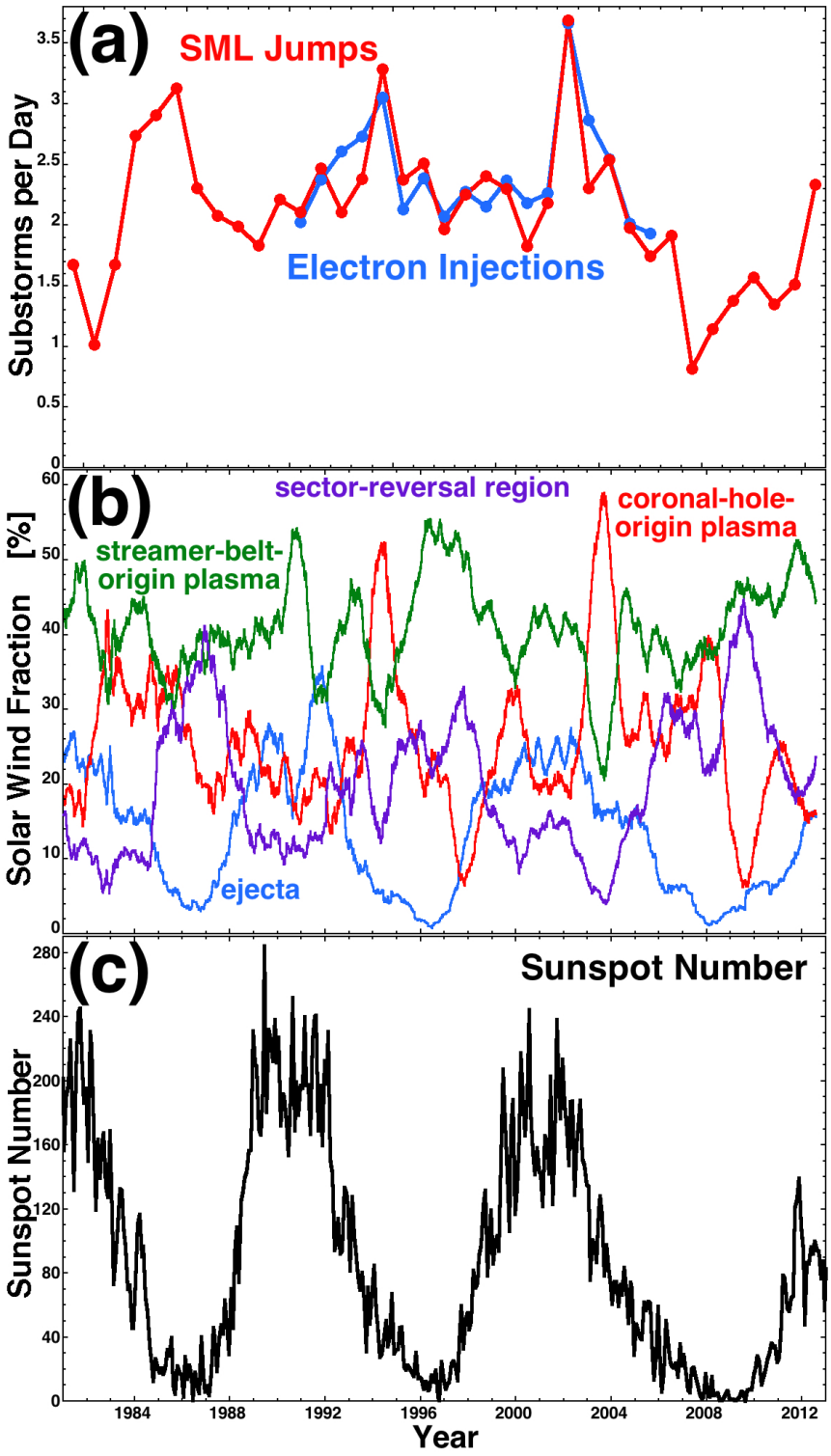

Figure 3.13: (a) The substorm occurrence rate (substorms per day) as a function of time for three solar cycles; the red curve is for substorms determined by jumps in the SML index, and the blue curve is for substorms determined by electron injections. (b) A 1-year running average of the fraction of time of four different types of solar wind at Earth, as determined from the parameters of the OMNI solar wind data set. (c) The monthly sunspot number.

Table 3.2: Substorm-occurrence rates for the various phases of the solar cycle.

	SML Events per Year	SML Events per Day	Injections per Year	Injections per Day
Solar maximum	723	1.99	842	2.31
Declining phase	1014	2.78	1028	2.81
Solar minimum	688	1.88	779	2.13
Ascending phase	641	1.85	809	2.22
All times	769	2.11	886	2.43

In Figure 3.14 the recurrence-time distributions for substorms as determined by jumps in the SML index are plotted for the four seasons of the solar cycle. In Figure 3.14 (left) the area under each curve is the number of substorms per year (cf. Table 3.2), and in Figure 3.14 (right) the areas under the four curves are all equal (the areas each being 100%). The declining phase of the solar cycle exhibits increased rates of substorm occurrence (cf. Table 3.2): the blue curve in Figure 3.14 (left) indicates that much of this increase in occurrence during the declining phase is an increase in the occurrence of periodic substorms centered on $\Delta t \sim 3$ hr. The blue curve in Figure 3.14 (left) also exhibits an increase in the rate of randomly occurring substorms with Δt greater than about 7 hr. In Figure 3.14 (right) it is seen that the fraction of substorms that are periodic ($\Delta t = 2 - 4$ hr) is higher for the declining phase and that the fraction of substorms that are random ($\Delta t >\sim 7$ hr) is smaller. Both panels of Figure 3.14 indicate that the distributions of substorm recurrence times Δt are similar to each other in the other three phases (solar maximum, solar minimum, and the ascending phase) of the solar cycle.

In Figure 3.15 the substorm occurrence rate (number of substorms per day) is plotted as a function of the equinoctial season of the year. In the plot winter is the approximately 91 daylong interval centered about the winter solstice (from day 309 to 34), spring is the approximately 91 daylong interval centered about the spring equinox (from day 34 to 126), summer is the approximately 91 daylong interval centered about the summer solstice (from day 126 to 218), and fall is the approximately 91 daylong interval centered about the fall equinox (from day 218 to 309). The substorm occurrence rate derived from jumps in the SML index is plotted in orange, and the occurrence rate as determined by electron injections is plotted in green. (The values of these two curves are collected in Table 3.3.) The occurrence

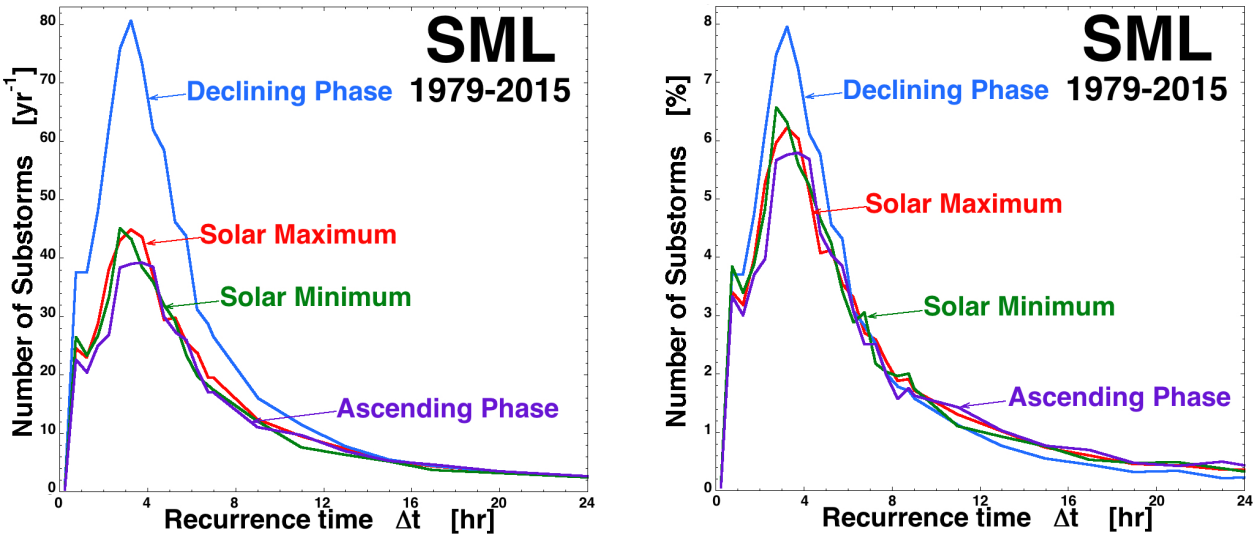

Figure 3.14: The recurrence-time distributions for substorms as determined by jumps in the SML index in 1979–2015 are plotted for the four phases of the solar cycle. (left) The area under each curve is the number of substorms per year, which differs for the different phases of the solar cycle (cf. Table 3.2). (right) The areas under the curves are all the same.

rates when the solar wind velocity is greater than 500 km/s are plotted in red and blue for SML events and injection events, respectively. Examining the orange and green curves in Figure 3.15, it is seen that the rate of substorm occurrence is slightly less in summer then it is in the other three seasons. This summer deficit has been noted before [e.g., *Borovsky and Nemzek*, 1994; *Tanskanen*, 2009; *Tanskanen et al.*, 2011; *Guo et al.*, 2014]. Note that *Tanskanen* [2009] and *Tanskanen et al.* [2011], using the IMAGE magnetometer chain in Scandinavia to identify substorms, found that the summer occurrence rate was only about half of the winter occurrence rate: the summer depletion found here using SML jumps and

Table 3.3: Substorm-occurrence rates (in units of substorms per day) are collected for the seasons of the year and for toward and away magnetic sectors of the solar wind.

	Toward Sectors		Away Sectors		All Data	
	SML Events	Injections	SML Events	Injections	SML Events	Injections
Winter	1.91	1.97	2.36	2.76	2.23	2.37
Spring	2.67	2.92	1.97	2.18	2.42	2.66
Summer	1.61	2.18	1.52	2.07	1.61	2.13
Fall	1.80	1.94	2.40	2.71	2.27	2.47

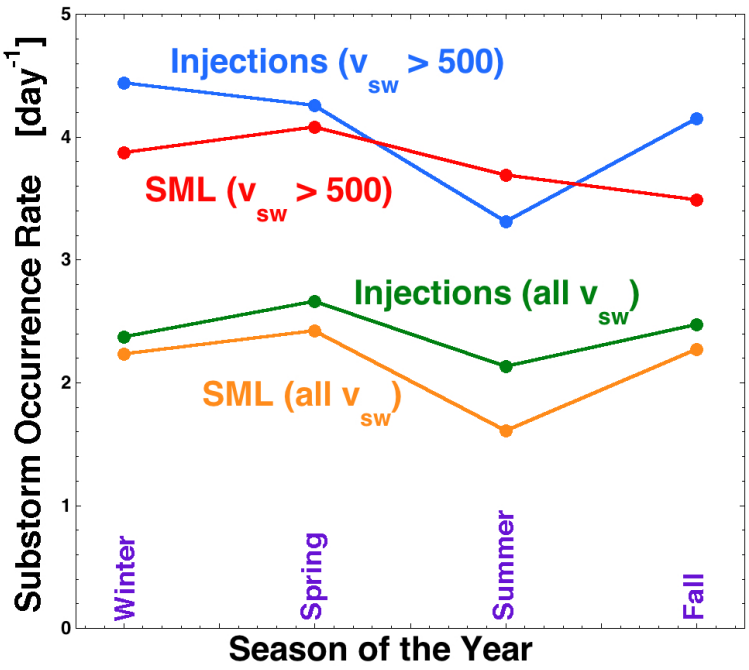

Figure 3.15: The substorm occurrence rates (substorms per day) are plotted for the four intervals around the equinoxes and solstices of the year. The lower two curves are the occurrence rates at all times, and the upper two curves are the occurrence rates when the velocity of the solar wind exceeds 500 km/s. As labeled, two curves are for substorms as determined with jumps in the SML index in 1979–2015 and two curves are for substorms determined with electron injections in 1989–2007.

using electron injections is not nearly that strong. Examining the red and blue curves of Figure 3.15, the summer minimum in the substorm occurrence rate is seen for the $v_{sw} > 500$ km/s time intervals in the injection-identified substorms but not in the SML-identified substorms.

In Figure 3.16 the analysis of Figure 3.15 is repeated separating the solar wind data into toward magnetic sectors (solid curves) and away magnetic sectors (dashed curves). The toward versus away nature of the solar wind was determined on an hourly basis by taking the dot product of the hourly averaged solar wind magnetic field vector and the hourly average velocity-dependent Parker-spiral-direction vector. The sign of the dot product determines the toward versus away nature of the solar wind interval during the occurrence of each substorm onset. Note that this method of determining toward versus away sectors is not foolproof owing to (1) large-amplitude directional variations of the solar wind magnetic field about the

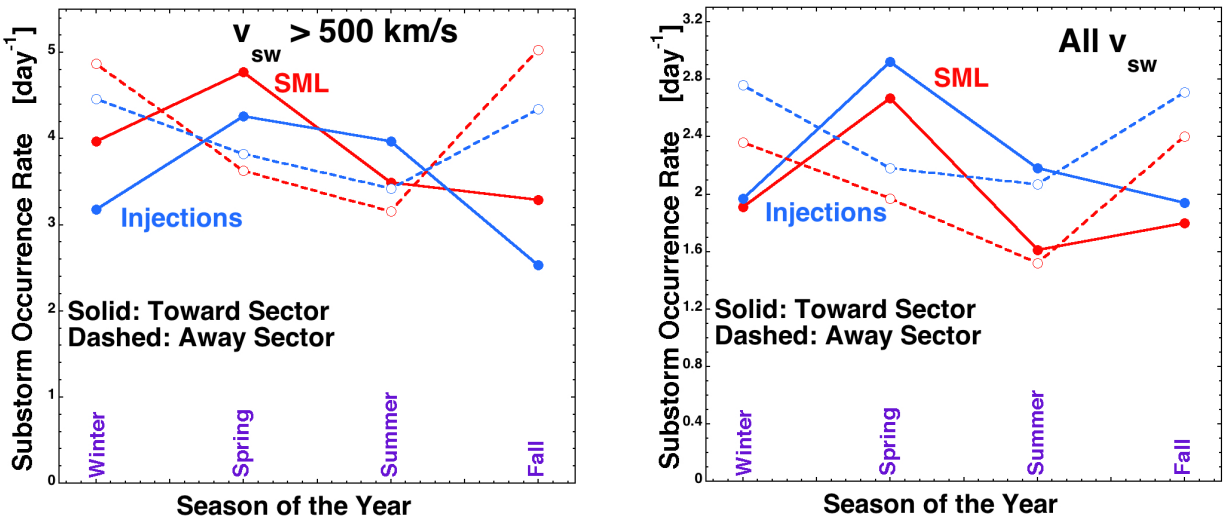

Figure 3.16: The substorm occurrence rates (substorms per day) are plotted for the four intervals around the equinoxes and solstices of the year, separating the time intervals into toward and away magnetic sectors for the solar wind at Earth. (right) The occurrence rates at all times and (left) the occurrence rates when the velocity of the solar wind exceeds 500 km/s are plotted. The red curves are for substorms as determined with jumps in the SML index in 1979-2015, the blue curves are for substorms determined by electron injections in 1989-2007, the solid curves are for toward magnetic sectors, and the dashed curves are for away magnetic sectors.

Parker-spiral direction [*Borovsky*, 2010] and to (2) ejecta which is neither toward nor away [*Bame et al.*, 1981; *Borovsky and Denton*, 2010]. A superior method for determining toward versus away magnetic orientations is to use the direction of the energetic-electron strahl [e.g., *Kahler and Lin*, 1994; *Crooker et al.*, 2004]; unfortunately, electron strahl measurements at Earth are not readily available prior to 1995. For the total substorm occurrence rates (Figure 3.16, right) and for the occurrence rates during times when $v_{sw} > 500$ km/s (Figure 3.16, left) a Russell-McPherron effect [*Russell and McPherron*, 1973] is clearly seen wherein geomagnetic activity is enhanced during toward sectors in spring and during away sectors in fall and is suppressed during away sectors in spring and during toward sectors in fall. (The values from Figure 3.16 (right) are collected in Table 3.3.) The Russell-McPherron effect in the occurrence rate of substorms has been seen before [*Borovsky and Nemzek*, 1994], where it was noted that the effect is not strong; in Figure 3.16, the Russell-McPherron effect is a tens of percent effect on the rate of substorm occurrence. For the spring and fall seasons the ratios of the Russell-McPherron-enhanced substorm-occurrence rates to the

Russell-McPherron-suppressed substorm-occurrence rates are in the range of 1.33 to 1.40.

3.7 Substorms and the type of solar wind plasma

In Table 3.4 the substorm occurrence rates (number of substorms per day) as determined by SML jumps and by electron injections are displayed for the four types of solar wind plasma. Using the *Xu and Borovsky* [2015] solar wind categorization scheme, the OMNI data set [*King and Papitashvili*, 2005] is categorized as to whether the solar wind plasma passing the Earth is of (a) coronal-hole origin, (b) streamer-belt origin, (c) sector-reversal-region origin, or (d) ejecta. (Ejecta also includes magnetic clouds.) Table 3.4 indicates that there is a great difference in the substorm occurrence rates between the different types of solar wind plasma. The occurrence rate is highest by far in coronal-hole-origin plasma, which is colloquially known as the "fast wind". The substorm occurrence rate is lower in streamer-belt-origin plasma, and the rate is very low (well below average) in sector-reversal-region plasma. The occurrence rate is about average in ejecta plasma. As noted in *Xu and Borovsky* [2015, Figure 21], coronal-hole-origin plasma is prevalent during the declining phase of the solar cycle, which according to Table 3.2 and Figure 3.13 exhibits a higher-than-normal substorm occurrence rate. Undoubtedly, the difference in the substorm occurrence rates has to do with the average levels of solar wind driving of the magnetosphere in the four types of solar wind plasma, with coronal-hole-origin plasma leading, on average, to stronger levels of driving. The distributions of substorm recurrence times in the four types of solar wind plasma are displayed in Figure 3.17, where the type of solar wind plasma is again determined with the

Table 3.4: Substorm-occurrence rates (in units of substorms per day) are collected for the four types of solar-wind plasma at Earth.

Type of Solar Wind	Occurrence Rate Using SML Jumps	Occurrence Rate Using Electron Injections
Coronal-hole-origin plasma	3.82	3.72
Streamer-belt-origin plasma	1.72	2.09
Sector-reversal-region plasma	0.91	1.26
Ejecta Plasma	1.95	2.32
All types of plasma	2.11	2.43

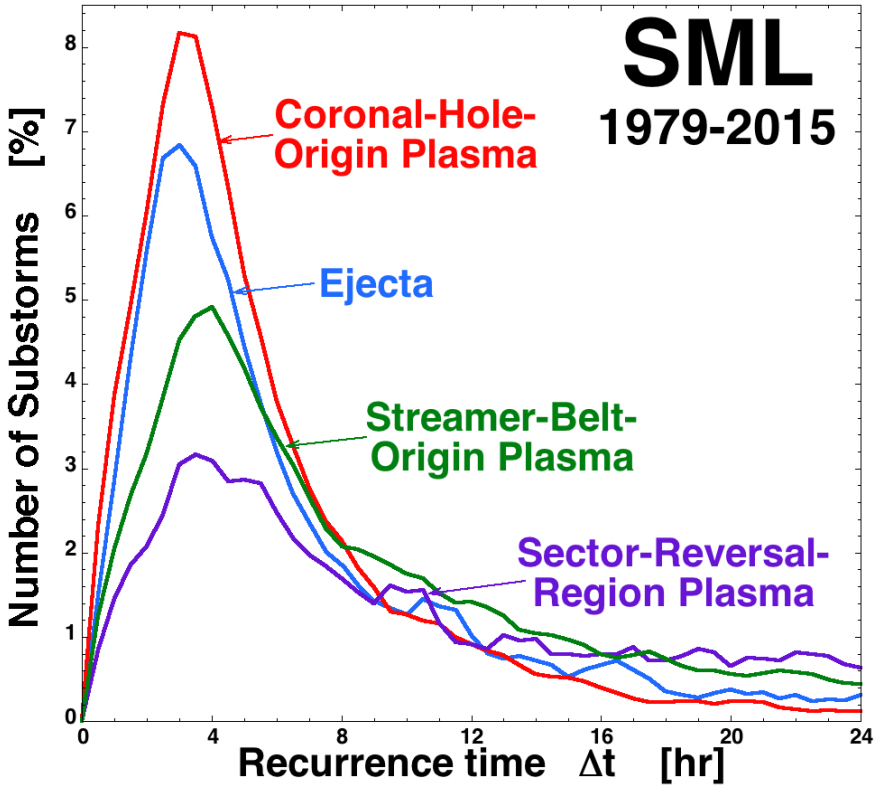

Figure 3.17: For 36 years, the recurrence-time distribution for substorms determined from jumps in the SML index is plotted separately for intervals of time when the solar wind plasma at Earth is of coronal-hole origin (red), streamer-belt origin (blue), sector-reversal-region origin (purple), and ejecta (blue).

Xu and Borovsky [2015] categorization scheme. The areas under the four curves in Figure 3.17 are all equal. Note in the red curve the dominance of the occurrence of periodically occurring substorms ($\Delta t \sim 2-4$ hr) relative to the randomly occurring substorms (Δt greater than about 6 hr) in coronal-hole-origin plasma; note the opposite trend in the purple curve for sector-reversal-region plasma where the periodically occurring substorms are sparse. The large Δt tail of the sector-reversal-region plasma (purple curve) is robust and (not shown) dominates the large Δt tails of the other curves beyond 24 hr. This indicates that long intervals of time without the occurrence of a substorm are common in sector-reversal-region plasma. For streamer-belt-origin plasma (green curve) and ejecta plasma (blue curve) periodic substorms are common, as are randomly occurring substorms.

3.8 The substorm recurrence period

The $\sim$ 3 hr periodicity of substorm (and global-sawtooth-oscillation) recurrence is well known [e.g., *Borovsky et al.*, 1993; *Prichard et al.*, 1996; *Huang et al.*, 2003a; *Borovsky*, 2004; *Henderson et al.*, 2006b; *Cai and Clauer*, 2009; *Morley and Henderson*, 2010; *Hsu and McPherron*, 2012; *Noah and Burke*, 2013]. The physical processes and controlling parameters that determine the periodicity of substorm recurrence have been a mystery for decades [e.g., *Huang et al.*, 2003a; *Borovsky*, 2004; *Freeman and Morley*, 2004; *Morley and Henderson*, 2010; *Cai and Clauer*, 2009; *Brambles et al.*, 2013; *Ouellette et al.*, 2013; *Welling et al.*, 2015]. Using the large numbers of substorms obtained from the jumps in the SML index in the years 1979–2015 and from electron injections into geosynchronous orbit in the years 1989–2007, the periodicity of substorm recurrence is investigated in this section as functions of substorm amplitude, geomagnetic activity, and solar wind conditions.

In Figure 3.18a the substorm recurrence-time distribution is examined for substorms of various amplitudes as measured by the magnitude of the jump in the SML index. In Section 3.2 the substorm-selection criteria for the SML index was chosen to be a jump of 150 nT in 15 min. If that criterion is increased to above 150 nT, fewer events are selected, with only larger-amplitude events chosen. Similarly, if the criterion is lowered below 150 nT more events are chosen and the increase is in smaller events. In Figure 3.18a the recurrence time distributions are plotted for various choices of the SML-jump criterion; the various curves in Figure 3.18a are normalized so that the area under each curve is the same. The red curve is the distribution for a 300 nT selection criterion and represents the recurrence-time distribution of larger-amplitude substorms. The yellow curve is the distribution when the criterion is 200 nT: this distribution contains the large-amplitude substorms in the 300 nT red curve plus substorms of more-modest amplitude. Likewise, the green distribution contains the orange distribution below it, which contains the red distribution. Note in Figure 3.18a that the location in Δt of the distribution of periodically occurring substorms does not shift as substorms of differing amplitudes are systematically added to the collection of substorms. This is an indication that the period of substorm recurrence is invariant to the amplitude of the substorms.

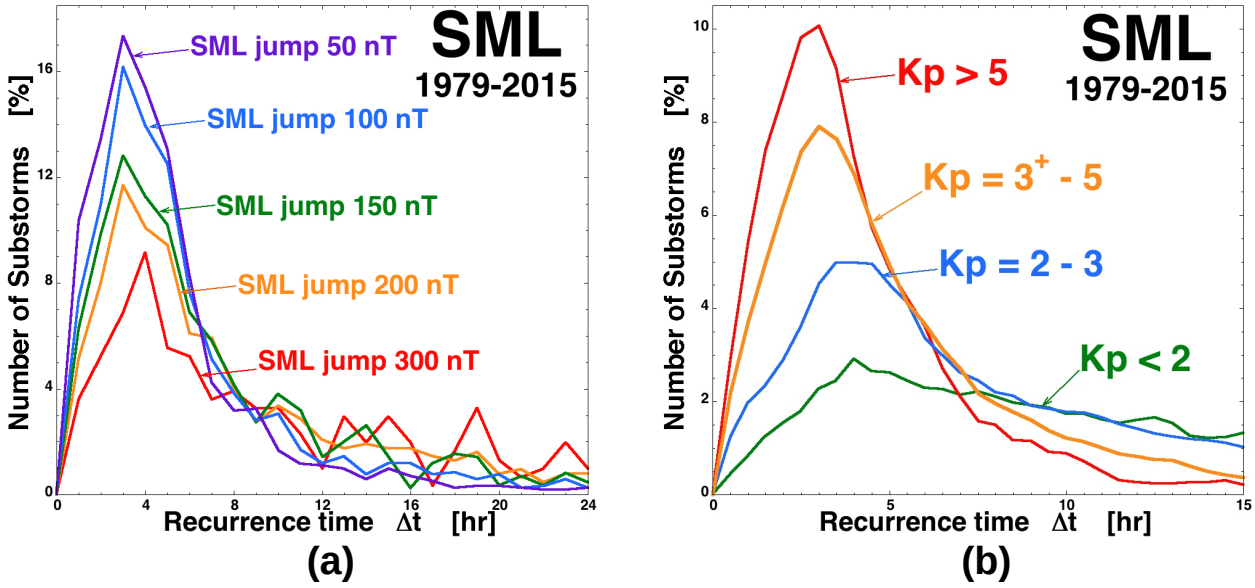

Figure 3.18: The recurrence-time distribution for SML events in 1979-2015 is plotted (a) for various amplitudes taken for the selection of events. The curves range from very small-amplitude events (purple) to large amplitude events (red). The distributions are all normalized such that the area under each curve is the same. (b) for intervals of time when the Kp index was in various ranges as labeled.

To examine the recurrence period of the periodic population of substorms versus the level of geomagnetic activity, the Kp index is used, with Kp being a good measure of the strength of convection in the magnetosphere [*Thomsen*, 2004]. Figure 3.18b displays the substorm recurrence-time distribution for various levels of geomagnetic activity, plotting the distributions for four ranges of the Kp index. At very low Kp ($Kp < 2$, green curve) the population of periodic substorms is almost absent (i.e., periodically occurring substorms are rare when geomagnetic activity is very low). At a modest range of Kp levels ($2 \leq Kp \leq 3$; blue curve) the periodic population is weak but clearly present. (Note that the median value of Kp for all times is 2, which is in the range of the blue curve.) At elevated levels of Kp ($3+ \leq Kp \leq 5$; orange curve) the periodic component dominates over the random component and periods in the range of 1.5–4.5 hr are seen with a peak in the recurrence-time distribution at about $\Delta t = 3$ hr. At high levels of Kp ($Kp > 5$; red curve) the periodic component is very dominant, periods in the range of 2-3.5 hr are seen with a peak in the recurrence-time distribution at about $\Delta t = 3$ hr. No strong trend in the recurrence time of the periodic substorms is seen with geomagnetic activity as measured by the Kp index; however, there

may be a weak trend toward shorter periods with increasing activity (comparing the orange and red curves). Note that a similar trend was not seen in Figure 3.18a when the period versus substorm amplitude was plotted.

Looking back at Figure 3.17, which displays the substorm-recurrence-time distributions in the four types of solar wind, it is seen that there is a slight shift toward shorter periods for the periodic population for ejecta (blue curve) relative to the other three types of plasma.

In the six panels of Figure 3.19 the substorm recurrence-time distribution is examined under various solar wind and solar conditions. All plots in Figure 3.19 pertain to substorms determined by jumps in the SML index. In Figures 3.19a,b the substorm recurrence times are plotted for various ranges of the solar wind velocity v_{sw} and for various ranges of the solar wind density n_{sw}; no strong variation of the period of recurrence is seen for variations in v_{sw} or n_{sw}. Figure 3.19c plots the substorm recurrence-time distribution for three ranges of the solar wind ram pressure P_{ram}; a trend is seen where the recurrence time of periodic substorms is lower when the ram pressure of the solar wind is very strong (red curve). The red curve distribution for very strong ram pressure exhibits recurrence times Δt of 1.5–4 hr. In Figure 3.19d the substorm recurrence-time distributions are plotted for three ranges of the solar wind magnetic field strength $B_{sw} = |\mathbf{B_{sw}}|$. A similar trend to that of P_{ram} in Figure 3.19c is seen, with the recurrence period of the periodic population being slightly lower for strong values of B_{sw} (red curve). In Figure 3.19c the substorm recurrence-time distributions are plotted for three ranges of the solar wind Alfvén Mach number $M_A = v_{sw}/v_A \propto v_{sw} n_{sw}^{1/2}/B_{sw}$, where v_A is the Alfvén speed in the solar wind upstream of the bow shock: a trend is seen where the period of substorm recurrence for the periodic population is slightly lower when the solar wind Mach number is low (red curve for $M_A < 4$). Low-Mach-number solar wind occurs almost exclusively when the solar wind type is ejecta [cf. *Lavraud and Borovsky*, 2008; *Xu and Borovsky*, 2015, Figure 1 and Figure 16 correspondingly], and ejecta showed hints of a slightly reduced substorm-recurrence period in Figure 3.17. In Figure 3.19f the substorm recurrence-time distribution is plotted for three ranges of the solar $F_{10.7}$ flux values, with $F_{10.7}$ being a proxy for solar EUV flux. No systematic change in the substorm recurrence period of the periodic population is seen going from low values of solar $F_{10.7}$ (green curve) to high values of solar $F_{10.7}$ (red curve). Note that ionospheric ion composition, ionospheric ion

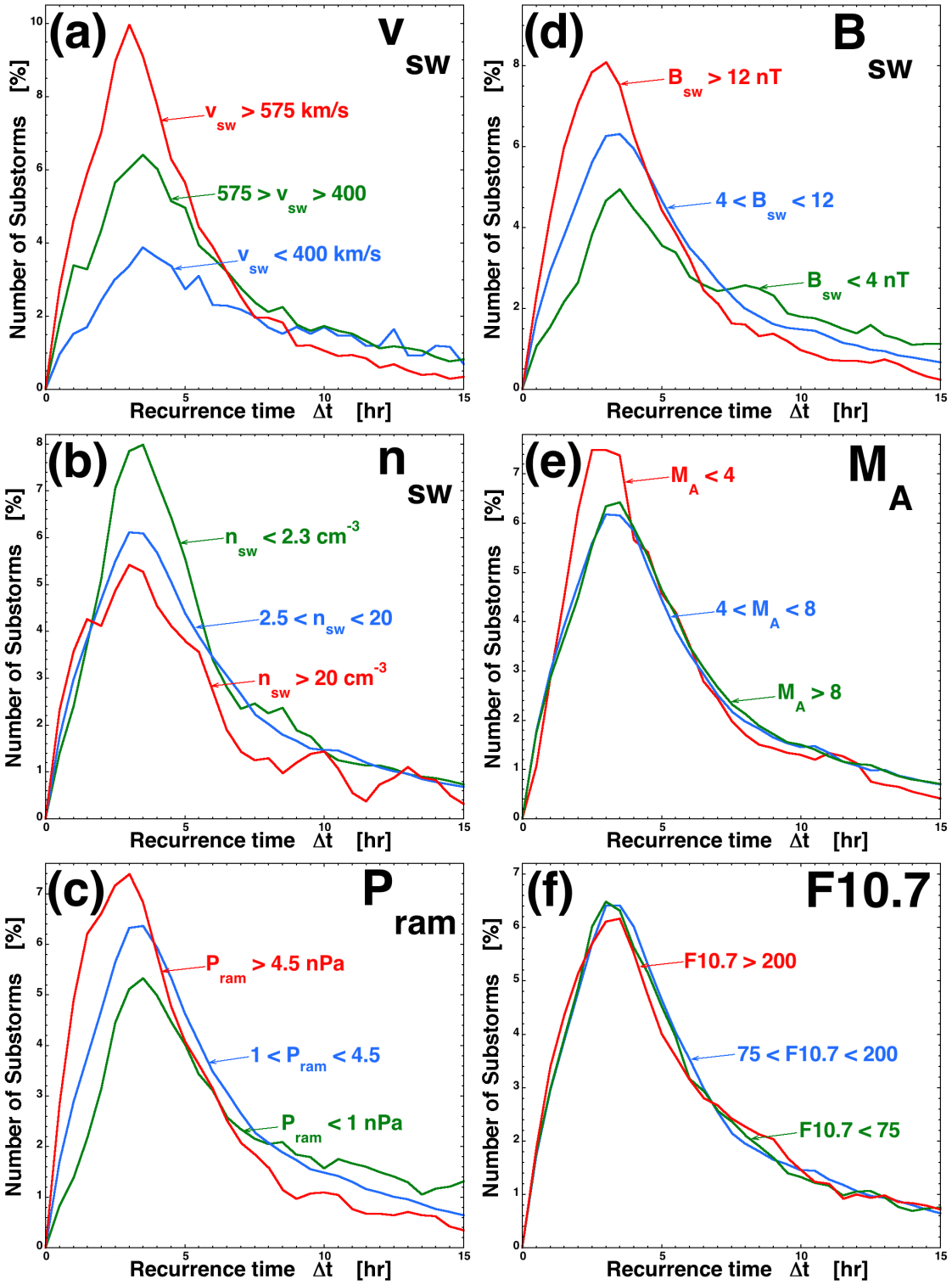

Figure 3.19: The recurrence-time distributions of substorms as determined from jumps in the SML index in 1979–1980 are plotted for various ranges of various solar and solar wind parameters. (a) The velocity v_{sw} of the solar wind. (b) The density n_{sw} of the solar wind. (c) The ram pressure P_{ram} of the solar wind. (d) The magnetic field strength B_{sw} in the solar wind. (e) The Alfvén Mach number M_A of the solar wind. (f) The solar 10.7 cm radio flux $F_{10.7}$.

outflows into the magnetosphere, and the ionic composition of the magnetosphere all vary with solar $F_{10.7}$ [e.g., *Lennartsson*, 1989; *Yau et al.*, 2011; *Welling et al.*, 2015]; this lack of change of the observed substorm period with solar $F_{10.7}$ may impact the hypothesis that ion outflow controls the periodicity of substorm occurrence [e.g., *Brambles et al.*, 2011, 2013; *Ouellette et al.*, 2013].

In the two panels of Figure 3.20 the substorm recurrence-time distribution is plotted for three ranges of values of the *Siscoe et al.* [2004] polar-cap saturation parameter $Q = \Sigma_P v_A/796$ (cf. equation (22) of *Borovsky* [2013]) where Σ_P is the height-integrated Pedersen conductivity of the Earth's polar cap (in units of mhos) and v_A is the Alfvén speed in the solar wind upstream of the Earth (in units of km/s). For an estimate of the Pedersen conductivity, the expression $\Sigma_P = 0.77F_{10.7}^{1/2}$ [*Ober et al.*, 2003] can be used, yielding $Q = F_{10.7}^{1/2} v_A/1034$. Note that $Q \propto F_{10.7}^{1/2} B_{sw}/n_{sw}^{1/2}$. The median value of Q is 0.56, and polar-cap potential saturation sets in as Q makes the transition from 1 to 2. In Figure 3.20 (left) the recurrence-time distributions of substorm onsets determined by jumps in the SML index are plotted for three ranges of the polar-cap potential saturation parameter: not saturated ($Q < 1$, green curve), in the transition to saturation ($1 \leq Q \leq 2$, blue curve), and saturated ($Q > 2$, red curve). A slight shift toward lower Δt values for the periodic substorms in the red curve is present compared with the other two curves. Figure 3.19f confirms this shift by repeating the analysis using the substorm onsets determined from electron injections. In both panels of Figure 3.20 the reduction of the average period of substorm recurrence is about 0.5 hr for the $Q > 2$ distribution.

The reaction of the substorm-recurrence period to the various properties examined in this section is summarized in Table 3.5. The recurrence time of periodic substorms is reduced slightly for high values of Q, low values of M_A, and large values of B_{sw}: these three parameters are all associated with polar-cap potential saturation of the magnetosphere. The periodic-substorm recurrence time is reduced slightly in ejecta plasma relative to the other types of solar wind plasma. Note that global sawtooth oscillations are associated with low-Mach-number solar wind, with polar-cap potential saturation, and with magnetic clouds (a subset of ejecta plasma) [*Borovsky and Steinberg*, 2006; *Lavraud and Borovsky*, 2008]. The recurrence time of periodic substorms is also reduced slightly for high values of P_{ram} and high values

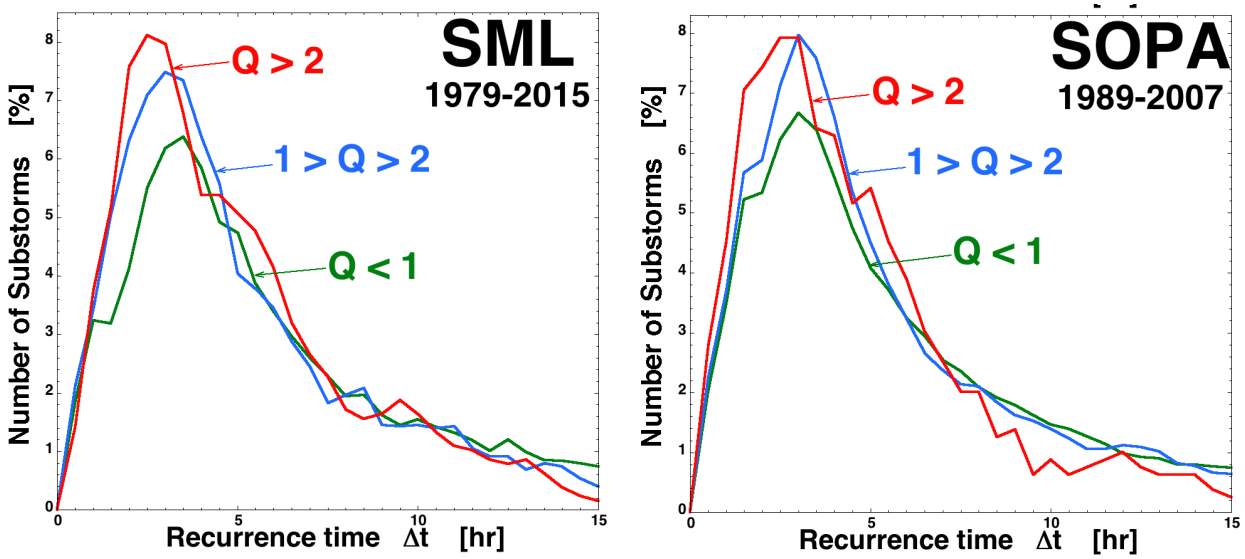

Figure 3.20: (left) For substorms as determined from jumps in the SML index in 1979–2015 and (right) for substorms as determined from electron injections in 1989–2007, the recurrence-time distribution is plotted separating the data into time intervals when the polar-cap-saturation parameter $Q = \Sigma_P v_A/796$ is in various ranges. The green curves represent times when the polar-cap potential is not saturated, the red curves represent times when the polar-cap potential is saturated, and the blue curves represent times when the potential is in transition toward saturation.

of Kp. The recurrence period of periodic substorms does not appear to be affected by the amplitude of the substorms, by n_{sw}, by v_{sw}, nor by solar $F_{10.7}$.

3.9 Summary and discussion

The findings of this study are the following:

1. Collections were made of 103,905 events identified with SOPHIE-75 algorithm in years 1982-2015, 28,464 substorms identified with jumps in the SML index in the years 1979–2015, 121,541 positive bays from the MPB index for years from 1982 to 2012 and 16,025 substorms identified with electron injections into geosynchronous orbit in the years 1989–2007.

2. Analysis of event-recurrence times (waiting times) indicates that SML events and injection events are onsets of substorm (i.e. they are the sudden beginning of an interval

Table 3.5: The effects of various properties on the recurrence period of periodic substorms.

Property	Quantity Examined	Effect on Recurrence Period Δt
Polar-cap potential saturation	Q	Period slightly less for high Q
Solar-wind Alfvén Mach number	M_A	Period slightly less for low M_A
Solar-wind magnetic field strength	B_{sw}	Period slightly less for strong B_{sw}
Solar-wind ram pressure	P_{ram}	Period slightly less for high P_{ram}
Type of solar wind plasma		Period slightly less in ejecta plasma
Geomagnetic activity	Kp	Period slightly less for high Kp
Substorm amplitude	SML	Period independent of substorm amplitude
Solar-wind velocity	v_{sw}	Period independent of v_{sw}
Solar-wind density	n_{sw}	Period independent of n_{sw}
Solar EUV flux	$F_{10.7}$	Period independent of $F_{10.7}$

of enhanced geomagnetic activity and the sudden appearance of a fresh energetic-particle population at geosynchronous orbit) and that the MPB events and SOPHIE events are dominated by substorm activations.

3. The substorm occurrence rate is higher on average when geomagnetic activity (as measured by the Kp index) is higher, however, SOPHIE and MPB event lists show different variations with Kp to SML and injection lists. They also differ from each other which implies that substorm-like intensifications in SOPHIE and MPB list are of caused by different processes.

4. Although the algorithms for finding substorm onsets detect a substorm when an interplanetary shock passes the Earth, analysis indicates that the substorm-like signatures are caused by compression of the magnetosphere rather than by the actual occurrence of a substorm.

5. The recurrence-time distributions of electron injection events and SML jumps have very similar properties.

6. The substorm recurrence-time distribution is composed of three populations: (a) quasiperiodic substorms with recurrence times of 2 to 4 hr, (b) a population of randomly occur-

ring substorms with recurrence times of about 6 to 15 hr, and (c) long intervals of time (greater than about 24 hr) wherein no substorms occur.

7. Substorm onsets are temporally associated with intervals of enhanced driving of the magnetosphere by the solar wind. This holds for both randomly occurring substorms and periodically occurring substorms.

8. Periodic substorms are associated with time intervals of stronger driving of the magnetosphere than are randomly occurring substorms.

9. The time scales of the variations of the magnetic field orientation of the solar wind do not control the ~ 3 hr periodicity of substorm occurrence.

10. It is speculated that the substorm recurrence period may be associated with the combinations of (a) an inherent periodicity of the magnetosphere and (b) a solar wind time scale for producing an interval of driving sufficient for a substorm to occur.

11. The occurrence statistics of the population of randomly occurring substorms are similar to (a) the occurrence statistics of changes in the clock angle of the solar wind magnetic field and (b) the occurrence statistics of solar wind driving intervals of above-average strength, both implying that randomly occurring substorms are associated with randomly occurring intervals of enhanced solar wind driving of the magnetosphere.

12. Substorm occurrence rates (number of substorms per day) are substantially higher during the declining phase of the solar cycle than they are during the other three phases of the solar cycle.

13. The additional substorms occurring during the declining phase are predominantly periodically occurring substorms.

14. Substorm occurrence is weaker in summer than it is in the other three seasons of the year, but not as weak as was found in prior studies.

15. There is a Russell-McPherron effect in the occurrence rate of substorms; they are more frequent in spring and in fall with increase by tens of percent depending on whether the Earth is in a toward or away solar wind magnetic sector.

16. Examining the type of solar wind plasma at Earth, substorm occurrence rates are highest in coronal-hole-origin plasma, weakest in sector-reversal-region plasma, and near average in both streamer-belt-origin plasma and ejecta plasma.

17. Much of the increase in substorm occurrence in coronal-hole-origin plasma is owed to an increase in the number of periodically occurring substorms. Periodically occurring substorms are prevalent in coronal-hole-origin plasma.

18. Periodic substorms are almost absent in sector-reversal-region plasma, and long intervals without the occurrence of substorms are prevalent.

19. The recurrence period of periodically occurring substorms is slightly shorter in ejecta plasma than it is in the other types of solar wind plasma.

20. The recurrence period of periodically occurring substorms does not depend on the amplitude of the substorms.

21. The recurrence period of periodically occurring substorms is slightly shorter when geomagnetic activity is very high.

22. The recurrence period of periodically occurring substorms is slightly shorter when (a) the ram pressure P_{ram} of the solar wind is high, (b) the magnetic field strength B_{sw} of the solar wind is strong, (c) the Mach number M_A of the solar wind is low, and (d) the polar-cap potential saturation parameter Q is high.

23. Several of the factors that reduce (slightly) the recurrence period of periodically occurring substorms are connected with polar-cap potential saturation: Q, B_{sw}, M_A, and ejecta.

24. Several quantities do not affect the recurrence period of periodically occurring substorms: (a) the solar wind speed v_{sw}, (b) the solar wind density n_{sw}, and (c) the solar EUV flux as proxied by solar $F_{10.7}$.

3.9.1 A working picture of substorm occurrence controlled by the solar wind

In this study a working picture is presented of substorms occurring in three populations (Figure 3.7b): (1) a population of periodically occurring substorms with recurrence periods of 2–4 hr (green curve in Figure 3.7b), (2) a population of randomly occurring substorms with recurrence time scales Δt in the range of about 6–15 hr (red curve in Figure 3.7b), and (3) a population of substorms occurring after long intervals wherein no substorms occurred (orange curve in Figure 3.7b).

The periodically occurring substorms

The onset of a periodic substorm is temporally associated with an interval of solar wind driving of the magnetosphere (blue curves in Figure 3.10), but no evidence was found for a recurrence time in solar wind magnetic field direction changes that might be responsible for the 2–4 hr periodicity of substorm occurrence (Figure 3.11). Hence, it is suggested that the period of substorm recurrence is set by some properties of the magnetosphere-ionosphere system independent of solar wind driving, but that a substorm will not occur until an interval of enhanced solar wind driving occurs after the magnetosphere becomes ready for substorm occurrence. Hence, it is speculated that the period of recurrence is set by the magnetosphere, but that the actual time of occurrence varies because of the random intervals of solar wind driving needed to set up the magnetosphere for a substorm. This might be expressed as the recurrence time being $\Delta t = \Delta t_{magnetosphere} + \Delta t_{driving}$ where $\Delta t_{magnetosphere}$ is a fixed time (maybe $\sim$ 2 hr) and $\Delta t_{driving}$ is a random number that varies from 0.5 to 2 hr. Note in Figure 3.9 that the solar wind driving (black curve) varies on a time scale faster than the recurrence time of periodic substorms (distances between the red points or between the blue points). Every recurrence interval Δt will vary in length owing to the random values of $\Delta t_{driving}$, turning a periodic process into a quasiperiodic process.

The randomly occurring substorms

Under weak solar wind driving, substorm occurrence becomes nonperiodic with an exponential distribution of waiting times (expression (2)) consistent with random occurrence. The time scales Δt for substorm recurrence for this population are in the range of 6–15 hr. It

makes sense that the occurrences of these substorms are caused by clock-angle variations of the IMF that are favorable enough to drive the magnetosphere strongly (if the plasma properties of the solar wind can support strong driving) so that the magnetosphere can be energized into having a substorm. These clock-angle temporal variations are caused by the advection past the Earth of mesoscale spatial structure of the vector magnetic field of the solar wind. The exponential distribution of substorm waiting times (Figure 3.7b) is similar to the exponential distribution of waiting times for the solar wind magnetic field clock angle (Figure 3.12).

The long intervals without substorms

Long time intervals in which no substorms occur are caused by the advection of plasma past the Earth that is unfavorable for driving substorms: the solar wind velocity may be too slow, the solar wind magnetic field may be too weak, etc. These properties of the solar wind plasma are slowly varying as compared with rapid variations in the direction of the solar wind magnetic field. For instance, the solar wind velocity v_{sw} has an autocorrelation time of 53 hr (Table 6 of *Borovsky* [2012]), meaning that intervals of slow solar wind can last typically $\sim$ 53 hr at Earth. It was found that the substorm recurrence-time distribution in sector-reversal-region plasma was dominated by long times Δt between substorms (Figure 3.17); intervals of sector-reversal region plasma at Earth can last for days. This suggested working picture is similar to the concept underlying the solar wind-driven "minimal substorm model" of *Freeman and Morley* [2004], which successfully reproduces the observed recurrence-time distribution of substorm onsets. The minimal substorm model assumes that the Earth's magnetosphere has an intrinsic substorm-recurrence period that is the period of substorm recurrence under steady driving by the solar wind (such as would occur during the passage of a magnetic cloud where the variations in the magnetic field direction are small). Under nonsteady driving, the recurrence times of substorm onsets in the model deviate from the intrinsic period of the magnetosphere and are governed by the temporal structure of the solar wind driving. When driving is sufficient, quasiperiodic substorms result, and when driving is sparse, randomly occurring substorms result. For the quasiperiodic substorms, most recurrence times are longer than the intrinsic magnetospheric period, but some are shorter. Using actual solar wind data as input, the model describes the quasiperiodic recurrence popula-

tion and the randomly occurring population. The period of periodically recurring substorms being slightly shorter in ejecta plasma (i.e., where there can be steady driving by magnetic clouds) and during high Kp (where driving is plentiful) agrees with this concept.

3.9.2 The period of periodic substorms

A few related quantities (high B_{sw}, high Q, low M_A, high Kp, and ejecta) were found to be associated with a slightly reduced recurrence time for the quasiperiodic substorms (Table 3.5). If, as suggested in Section 3.9.1 [cf. *Freeman and Morley*, 2004], the period of substorm recurrence is determined by a combination of (1) an intrinsic magnetospheric period $\Delta t_{magnetosphere}$ plus (2) the need for wait for an interval $\Delta t_{driving}$ of solar wind driving, then the various quantities (high B_{sw}, high Q, low M_A, high Kp, and ejecta) could be affecting either $\Delta t_{magnetosphere}$ or $\Delta t_{driving}$.

Reducing the waiting time for driving intervals $\Delta t_{driving}$ to shorten the substorm recurrence period could be related to high Kp, where driving is plentiful, and could be related to ejecta plasma, where the driving is steady because of the low levels of vector magnetic field fluctuations [cf. *Xu and Borovsky*, 2015, Figure 14e], particularly for the magnetic-cloud subset of ejecta [*Klein and Burlaga*, 1982; *Lepping et al.*, 2005].

Low-Mach-number solar wind (low M_A) and polar-cap potential saturation (high Q) are associated with morphological changes of the magnetosphere, and these morphology changes could alter the intrinsic periodicity $\Delta t_{magnetosphere}$ of the reaction of the magnetosphere to the solar wind. The morphology changes are the following. Low M_A results in a low-β magnetosheath with an altered flow pattern [*Spreiter et al.*, 1966; *Biernat et al.*, 2000] including large-scale flow jets that increase the velocity shear along the magnetopause [*Lavraud et al.*, 2007]. The anisotropic pressure of the low-β magnetosheath at low M_A results in a strongly distorted cross-sectional shape of the magnetosphere [*Lavraud and Borovsky*, 2008; *Lavraud et al.*, 2013]. Polar-cap potential saturation (high Q) results in (1) new current systems in the dayside magnetosphere [*Siscoe et al.*, 2004; *Lopez et al.*, 2008; *Borovsky and Denton*, 2009], (2) changes in the connections and communications of current systems in the dayside magnetosphere [*Siscoe et al.*, 2002; *Lopez et al.*, 2008], (3) magnetic field strengths that are weaker than the dipole value in the dayside magnetosphere [*Hill et al.*, 1976; *Siscoe et al.*,

2004; *Borovsky and Denton*, 2009], (4) magnetic field strengths that are stronger than the dipole value in the nightside magnetosphere [*Borovsky and Denton*, 2009], (5) changes in the shape of the dayside magnetopause [*Raeder et al.*, 2001; *Merkin et al.*, 2005a,b], (6) a sunward movement of the cusps [*Raeder et al.*, 2001; *Borovsky and Denton*, 2009], (7) lobe pressure acting on the dayside dipole regions [*Ober et al.*, 2006; *Lavraud and Borovsky*, 2008], and (8) a buckling of dayside dipole magnetic field into a tail-like morphology [*Lavraud and Borovsky*, 2008; *Borovsky and Denton*, 2009]. The weakening of the dayside magnetic field during polar cap saturation also leads to an earthward motion of the dayside magnetopause [*Borovsky and Denton*, 2009], shrinking the spatial volume of the dayside magnetosphere. Another solar wind parameter that was found to be associated with shorter recurrence periods of substorms is high solar wind ram pressure P_{ram}: higher ram pressure also acts to decrease the volume of the magnetosphere [*Schield*, 1969].

Data analysis [*Shue et al.*, 2001], simulations [*Lopez et al.*, 2004], and theory [*Lavraud and Borovsky*, 2008] have demonstrated that at low Mach numbers geomagnetic activity is positively correlated with the number density of the solar wind. *Borovsky and Birn* [2014] derived a low-Mach-number solar wind driving function for the magnetosphere with the functional form $\sin^2(\theta_{sw}/2) n_{sw}^{0.24} v_{sw}^{1.49} B_{sw}^{0.51}$, where n_{sw}, v_{sw}, and B_{sw} are the density, velocity, and magnetic field strength of the solar wind and θ_{sw} is the magnetic clock angle of the solar wind. Changes in any one of these four solar wind variables will result in changes in the driving of the magnetosphere. This opens the possibility that in the absence of variations of other variables, the solar wind number density could control the timing of intervals of driving and hence control the occurrence of substorms.

3.9.3 Global sawtooth oscillations

Global sawtooth oscillations are a subcategory of periodic substorms wherein the magnetic field in the dayside magnetosphere undergoes stretching and dipolarization and dispersionless particle injections can be seen in the dayside: the strict definition of global sawtooth oscillations is that magnetic field dipolarization and dispersionless particle injections are seen sunward of the dawn and dusk terminators [*Borovsky*, 2004]. In a global sawtooth oscillation, a substorm-like dipolarization of the magnetic field can even occur at local noon.

Typical substorms involve time-dependent current systems that are restricted to the nightside magnetosphere, whereas global sawtooth oscillations involve time-dependent current systems that form in the dayside magnetosphere. Global sawtooth oscillations are associated with low-Mach-number solar wind [*Borovsky*, 2004; *Borovsky and Denton*, 2006; *Pulkkinen et al.*, 2007; *Lavraud and Borovsky*, 2008; *Cai et al.*, 2011] and tend to occur during the passage of magnetic clouds [*Borovsky and Denton*, 2006; *Lavraud and Borovsky*, 2008], which are a subset of ejecta plasma. Global sawtooth oscillations are intimately related to polar-cap potential saturation [*Borovsky and Denton*, 2006; *Lavraud and Borovsky*, 2008; *Borovsky and Denton*, 2009]; polar-cap potential saturation changes the nature of currents in the dayside magnetosphere [*Siscoe et al.*, 2004; *Lopez et al.*, 2008; *Borovsky and Denton*, 2009] and changes the morphology of the dayside magnetic field [*Raeder et al.*, 2001; *Merkin et al.*, 2005a,b; *Borovsky and Denton*, 2009]. In the present study, global sawtooth oscillations were not separately identified from substorms. In examining the recurrence period of periodically occurring substorms in this study, it was noted that there was a slight decrease in the recurrence period for low Mach numbers (Figure 3.19e), for strong solar wind magnetic field (Figure 3.19d), for a large polar-cap-saturation Q parameter (Figure 3.20), and for ejecta plasma (Figure 3.17), all of which are characteristics of the times when global sawtooth oscillations have been identified. It may be that the recurrence period of global oscillations are statistically slightly less (by about 0.5 hr) than the recurrence period of ordinary substorms. This reduction in period may be related to the strong driving of the magnetosphere: during times of strong driving the magnetosphere has only a short wait for a driving interval after the intrinsic time scale of the magnetosphere is up.

Chapter 4

IMF as a driver of B_z^+ flows in the polar cap

Interaction between the solar wind and embedded in it interplanetary magnetic field with the Earth's magnetic field results in establishing certain patterns of plasma circulation in the near-Earth environment. Identifying these patterns and understanding the physics of the processes responsible for their creation would be an important contribution to a comprehensive model of the Sun-Earth connections. Although satellite measurements at numerous locations are required to establish a complete 3-D model of plasma circulation in the Earth's magnetosphere and ionosphere, a simplifying factor is that the magnetospheric plasma is highly conducting so that the large-scale plasma motions in the magnetosphere are "mapped" into the ionosphere where plasma flow patterns are possible to study with ground-based radars and low-orbiting satellites (Chapters 1 and 2). This Chapter is devoted to assessing patterns for one of the most intriguing but less investigated situation when the IMF B_z is positive and strongly dominating over the IMF B_y component. Some materials presented in this Chapter have been published in *Koustov et al.* [2017].

4.1 Introduction

High-latitude patterns of ionospheric plasma circulation are known to strongly depend on the magnitude and orientation of the IMF. This is expected theoretically [*Cowley*, 1983] and has been demonstrated by using ground-based magnetometer measurements [*Papitashvili et al.*, 1994], data from radio instruments such as incoherent scatter radars [*de la Beaujardiere et al.*, 1991; *Zhang et al.*, 2007] and ionosondes [*Smith et al.*, 1998; *Jayachandran and MacDougall*,

2001] and by using drift meters on satellites [*Heppner and Maynard*, 1987; *Rich and Hairston*, 1994; *Förster and Haaland*, 2015]. Individual instrument observations have been successful in investigating specific events in limited areas of the high-latitude ionosphere. By merging data collected over extended periods from specific instrument observations, statistical models of the flow pattern have been developed [*Rich and Hairston*, 1994; *Papitashvili and Rich*, 2002; *Haaland et al.*, 2007]. Assimilative techniques digesting data from multiple instruments have been introduced [e.g., *Lu et al.*, 1994]. Installation of the SuperDARN HF coherent radars [*Greenwald et al.*, 1995] significantly expanded capabilities in monitoring convection patterns by making simultaneous measurements over large areas with temporal resolution as good as one minute and in both hemispheres [e.g., *Ruohoniemi and Greenwald*, 2005; *Pettigrew et al.*, 2010].

Although significant advances in understanding the ionospheric plasma flow patterns and their drivers have been made, some aspects of the problem remain unsettled. One example is the variability of the flow patterns under strongly dominant positive north-south component of the IMF $B_z > 0$ (B_z^+). The initial suggestion by *Heppner and Maynard* [1987] that under these conditions the pattern consists of two distorted cells with twisted to antisunward kinks at near-noon hours has been challenged by many [e.g., *Reiff and Burch*, 1985; *Heelis et al.*, 1986; *Huang et al.*, 2000a,b] who put forward theoretical arguments and data indicating that two additional cells with sunward flow at the near-noon meridian exist instead so that the overall pattern consists of four convection cells. This is expected if the lobe magnetic reconnection becomes very effective [*Crooker and Rich*, 1993] and overpowers (in regions where they present) two other possible drivers, the viscous processes and the frontside "merging" powered by nonzero IMF component. Numerous observations [e.g., *Huang et al.*, 2000b; *Ambrosino et al.*, 2009; *Cousins and Shepherd*, 2010] are consistent with this expectation. Although the occurrence of four cells seems to be undisputed, SuperDARN observations often show more complicated patterns [*Greenwald et al.*, 1995; *Knipp et al.*, 2000, e.g.,] warranting further studies. This is of particular importance in view of a recent discovery that the lobe reconnection in one hemisphere can be affected by the lobe reconnection in the other hemisphere leading to the so-called interchange cycle [e.g., *Watanabe et al.*, 2006, 2010]. *Wilder et al.* [2011] showed simultaneous observations of four cells in each hemisphere, and in a

follow-up study by *Wilder et al.* [2013] the authors simulated the event and found that the difference in magnetic field topology can lead to the summer-winter asymmetry in the intensity of the flows consistent with the initial expectation by *Crooker and Rich* [1993] that the lobe reconnection processes are easier to initiate in the summer hemisphere because the magnetic flux lines geometry here is more suitable for merging with incoming magnetic flux lines. Although this expectation has never been questioned, supporting evidence is rather limited and often indirect. For example, *Crooker and Rich* [1993] refer to Defense Meteorological Satellite Program (DMSP) satellite statistical data by *Rich and Hairston* [1994] that showed the dawn winter cell to be less round and of a smaller electric potential magnitude than the dawn summer cell for the IMF conditions. They suggested that this seasonal difference results from addition of lobe reconnection driven flows in summer. To stress the importance of the effect, they even designated the lobe reconnection as a "summer phenomenon". However, the effect is not always seen. For example, *Ruohoniemi and Greenwald* [2005], by considering multi-year statistics of SuperDARN data, mention that the winter/summer asymmetry for condition seems to be not in accord with the lobe reconnection model. Another aspect of the issue is whether reverse flows occur in both hemispheres simultaneously. Highly averaged SuperDARN and satellite data show occurrence of reverse cells in both hemispheres [*Pettigrew et al.*, 2010; *Förster and Haaland*, 2015] although the degree of similarity yet to be quantified, for example in terms of the timing for the cells onset [*Ambrosino et al.*, 2009; *Watanabe and Sofko*, 2009].

Here we focus on SuperDARN observations of ionospheric convection in the central polar cap during northward IMF with the clock angle $\theta_{clock} < 30°$. For this condition, the plasma is expected to flow predominantly sunward along the noon-midnight meridian on the dayside. Our goal is to assess the summer/winter differences in the plasma flows.

4.2 Highly-averaged SuperDARN maps

The seasonal differences of the sunward flows can be indirectly assessed, in a statistical sense, in two ways. The first approach is to consider data in one hemisphere and compare averaged convection patterns for winter and summer seasons. A second way is to consider data accumu-

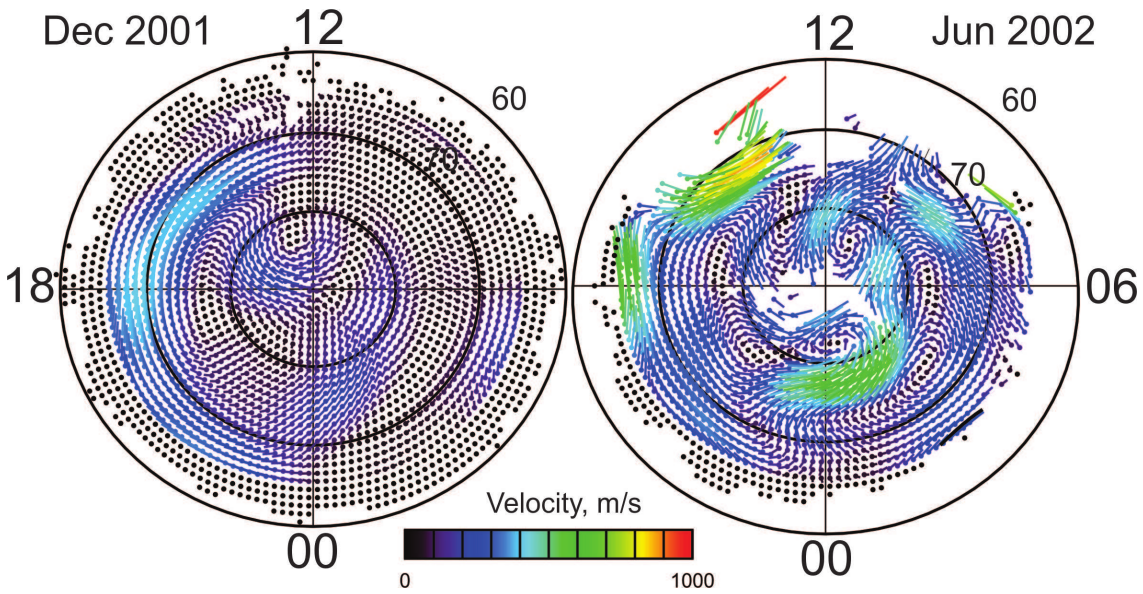

Figure 4.1: Convection pattern (plasma flow vectors) in the MLT-MLAT coordinates inferred from (a) December 2001 and (b) June 2002 SuperDARN grid velocity data for $B_z > 0$ and 6 nT< B_t <12 nT by applying the SCHA technique of *Fiori et al.* [2010]. Every dot represents the origin of a plasma velocity vector with length coded by color. (Courtesy of R. Fiori and A. Koustov.)

lated over a number of events in both hemispheres and statistically average them over the same periods, for summer/winter in either hemisphere. Although the second approach is a better way of assessing the hemispheric, and simultaneously, seasonal differences, not much data is available. Here we investigate SuperDARN data in both ways.

In the first approach, we consider monthly-averaged convection patterns in the Northern hemisphere (where the SuperDARN coverage is much better) for winter and summer months. Such an approach has been adopted by *Koustov et al.* [2015] and *Koustov and Fiori* [2016]. We considered an extensive period of 1995–2013 for periods of positive IMF B_z for three magnitudes of the IMF $B_t = \sqrt{B_z^2 + B_y^2}$: $0 < B_t \leq 4$ nT, 4 nT< $B_t \leq 6$ nT, and 6 nT< $B_t \leq 12$ nT. These bands were chosen as they are adopted by the SuperDARN high-latitude convection model developed by *Ruohoniemi and Greenwald* [1996]. Here data are presented for the case of 6 nT< B_t < 12 nT corresponding to the strongest IMF driver.

Figure 4.1 gives an example of monthly-averaged plasma convection maps for winter (December 2001) and summer (June 2002) conditions. In both plots, reverse convection cells are identifiable with clearer features in summer. The stronger magnitude of the sunward flow

at near noon hours in summer is evident. The effect of faster summer flows is seen for many other years of SuperDARN observations between 1995 and 2013.

Between MLATs of $80^\circ - 85^\circ$ (preferential latitudes for sunward flows), Figure 4.1 shows that, on average, flow is directed along the midnight-noon meridian in winter but deviates from the noon-meridian toward prenoon hours of $\sim$11 MLT in summer. We note that such an effect was not consistently observed for all other years; for some years, no deviation was observed and for some a deviation toward postnoon hours was observed.

One can argue that adopting a relatively wide range of possible B_t, without specifying the magnitudes of the IMF B_y, might not be sufficient for assessing the subtle effect under investigation. For this reason, we now present results from the *Cousins and Shepherd* [2010] SuperDARN statistical convection model (in the text to follow, it will be referred to as the CS2010 model), which does limit the IMF B_y. Again, we consider the case of dominant IMF B_z.

Figure 4.2 shows the output of the CS2010 model for strong B_z^+ driving conditions with electric field in the solar wind $E_{sw} > 4.1$ mV/m for summer and winter in the Northern hemisphere (positive and negative orientation of the Earth's magnetic dipole, respectively). In Figure 4.2 both plots show reverse convection cells on the dayside. The magnitudes of the sunward flow vectors around the midnight-noon meridian are clearly larger in summer. In terms of direction, the flow crosses the midnight-noon meridian being oriented toward prenoon MLT hours in winter and toward postnoon MLT hours in summer. The deviation of the flow from the midnight-noon direction is stronger in summer. For weaker external drivers (smaller E_{sw}), all the above features hold except the velocity magnitudes are smaller. The model gives no flow deviation from the midnight-noon meridian for equinoctial conditions so that the reverse convection cells are fairly symmetric.

Our conclusion from the above SuperDARN statistical data analysed in two ways is that while the sunward flows seem to be faster in summer, the direction of the flow deviation from the midnight-noon meridian is not certain. For this reason, we decided to continue investigation of the effects by looking at the original SuperDARN l-o-s velocities measured in individual beams and then investigate 2-D velocity maps by restricting events to clear-cut B_z^+-dominant events.

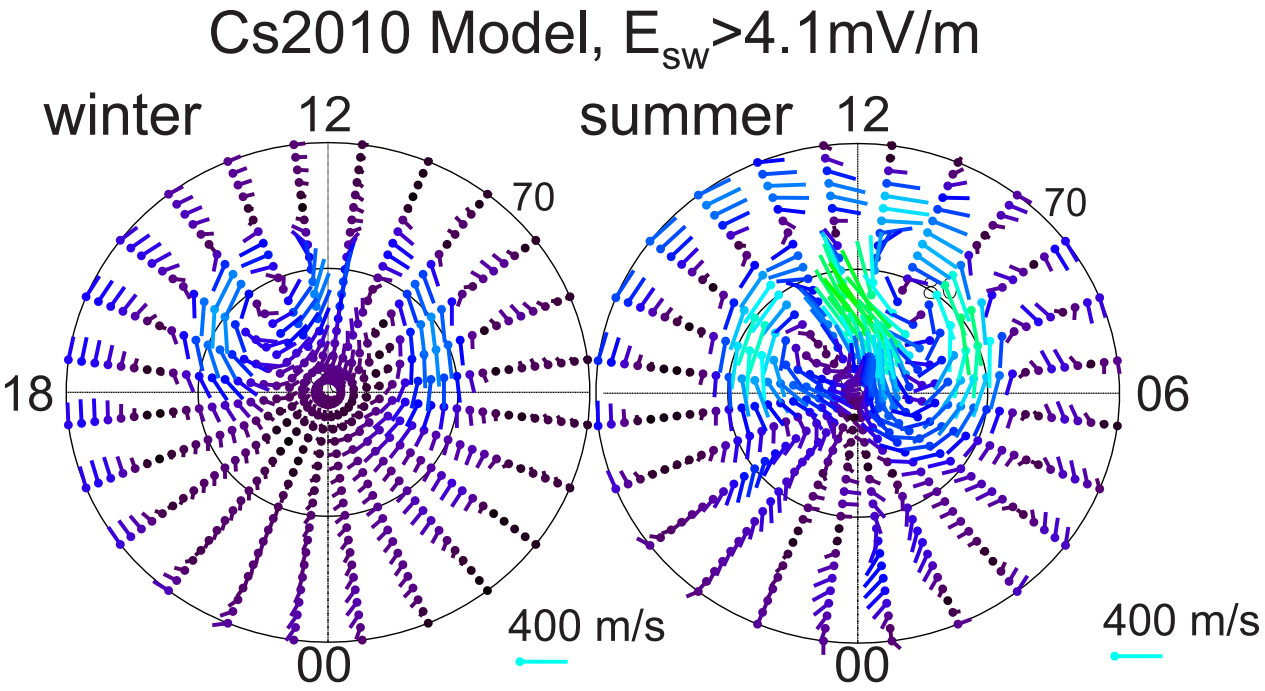

Figure 4.2: Plasma flow patterns (velocity vectors) in MLT-MLAT coordinates according to the SuperDARN statistical model by *Cousins and Shepherd* [2010] for winter and summer conditions in the Northern hemisphere with the IMF $B_z > 0$ and $E_{sw} > 4.5$ mV/m. (Courtesy of R. Fiori and A. Koustov.)

4.3 Polar cap SuperDARN radar observational conditions

Since sunward flows (the reverse convection cells) occur at magnetic latitudes above 80° (e.g., Figures 4.1,4.2), we start working with the data from three polar cap SuperDARN radars. Two radars are in the Southern hemisphere, McMurdo (MCM) and Dome-C East (DCE). These radars are well suited for monitoring meridional plasma flows over the magnetic Pole and in the central polar cap. We also consider data from the Northern hemisphere Rankin Inlet (RKN) radar that also monitors the meridional flows but at lower magnetic latitudes. The RKN radar is "conjugate" to the MCM radar in a sense that the RKN central beams being projected into the Southern hemisphere (flipping the sign of the geomagnetic latitude) have directions similar to those of the central beams for the MCM radar (although there is a difference in magnetic latitude).

Figure 4.3 shows the fields of view FoVs of (a) the MCM and DCE SuperDARN radars in the Antarctica and (b) the RKN radar in the Arctic. The FoVs are limited to range gates 9-40 where most of F-region echoes are detected. We investigate data in central beams 6, 7 and 8 whose orientation is roughly along the magnetic meridians, toward the magnetic Poles. We also bin the data from these radars according to three consecutive range gates; these are marked in Figure 4.3. There is one important difference between MCM and DCE radar observations, their direction. While the former looks toward the geomagnetic Pole, the latter looks away from it implying that the line-of-sight (l-o-s) velocity of these radars would have different polarity. In this Chapter, we discuss MCM and DCE measurements in gates 15-17 and the RKN measurements in gates 27-29, see color boxes in Figure 4.3. We note that the FoVs on the dayside for all the radars considered cover magnetic latitudes where the geomagnetic field lines are open. To illustrate this fact, we show in Figure 4.3 (dashed green line) the open-closed boundary (OCB) according to the Tsyganenko-08 model (*Tsyganenko* [1989] and `http://ampere.jhuapl.edu/code/idl_geopack.html`) for the IMF $B_z = 5$ nT and $B_y = 0$ nT. The boundary can be at slightly different locations depending on the IMF conditions [e.g., *Kabin et al.*, 2004; *Wilder et al.*, 2013], but for all typical ranges, the echo detection is confidently poleward of the OCB.

The reasons for the specific gate selection are as follows. In the Southern hemisphere, the gates selected are relatively close to each other (MLAT$\sim 87^\circ$ for MCM and MLAT$\sim 84^\circ$ for DCE) so that possible rotation of the plasma flow direction (at one latitude as compared to another latitude) should not be significant. In the Northern hemisphere, we selected maximum ranges with reasonable data coverage for all the seasons (see echo occurrence plots in Figure 3 of *Ghezelbash et al.* [2014]). In addition, the far RKN ranges are those where the radar consistently shows the summer sunward flows (not as consistently at lower latitudes). The solar wind parameters and IMF were taken from the 1-min OMNI database at `http://omniweb.gsfc.nasa.gov`. These data have been originally propagated from the satellite locations to the bow shock nose. We delayed them by an additional 8 min to allow propagation of the solar wind and IMF perturbations from the bow shock nose to the ionosphere. This selected number is somewhat arbitrary. *Jackel et al.* [2012] reported about 4–6 min delay in magnetic perturbation detection in the magnetosphere at a geosynchronous

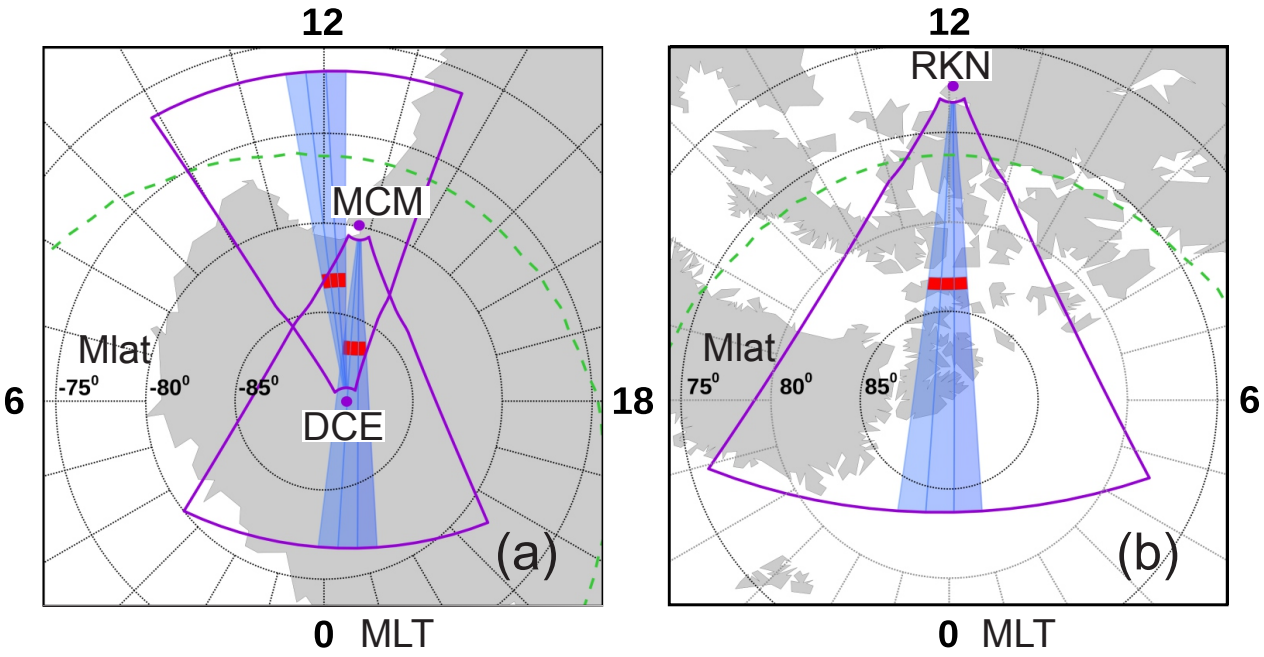

Figure 4.3: (a) Fields of view (FoVs) of the MCM and DCE SuperDARN radars up to the range gate 45 (purple line). Coordinates used are the Magnetic Local Time (MLT) - the Altitude Adjusted Corrected Geomagnetic (AACGM) latitude [*Baker and Wing*, 1989]. The FoVs are for 20:00 UT. Beam-like sectors within FoVs are orientations of beams 6, 7, and 8 whose data were considered. Red rectangles indicate range gates data from which will be presented. Dashed green curve is the location of the open-closed boundary of the geomagnetic field lines on the dayside as predicted by the Tsyganenko model [*Tsyganenko*, 1989]. (b) the same as (a) but for the RKN radar at 18:30 UT and up to the range gate 65.

orbit ($\sim 6.6\ R_E$) followed pressure pulses at the bow shock. We allowed additional 2–4 min delay for disturbance propagation to the ionosphere. These estimates are comparable with reported delays in response of the high-latitude convection to sudden changes in the IMF which can start with a short delay of ~ 1 min on the dayside [e.g., *Ruohoniemi and Baker*, 1998], but the delay can exceed 10 min on the nightside [*Fiori et al.*, 2012], and get settled in about 10 min.

To characterize the flows quantitatively, we consider hourly median values of the l-o-s velocity in the gates and bins selected, similar to *Koustov et al.* [2013]. Enlarged bins allow us to achieve reasonable data coverage for all seasons and local time sectors. Of particular concern was a significant data decrease for the winter dark southern polar cap (12–22 UT) when both the MCM and DCE radars suffer from deficiency in the F-region electron density

[*Bristow et al.*, 2011]. Our analysis covers two years of continuous radar operation, 2013 and 2014.

4.4 Typical meridional l-o-s velocity for IMF B_z^- and B_z^+.

Figure 4.4 is a series of contour plots for the median l-o-s velocity versus UT inferred for conditions with the IMF B_z^- (left column) and IMF B_z^+ (right column). The top (a, b), middle (c, d) and bottom (e, f) rows correspond to observations by the DCE, MCM and RKN radars, respectively. The vertical axes span between 0 and 24 months (2013–2014). The scale of contours is two times coarser for B_z^- the data of Figures 4.4a, 4.4c, and 4.4e.

In Figure 4.4, the DCE and MCM/RKN velocities for the same UT time are of opposite polarity. This is owing to the opposite radar look directions, as explained in Section 4.3. There are several features that are common for all panels in Figure 4.4. One is a change in the l-o-s velocity polarity at ∼12 and 24 UT, irrespective of a season. These are times when the radars look almost perpendicular to mostly azimuthal flows (for all IMF conditions) according to a 2-cell convection pattern. Another feature is fastest flows at ∼06 UT. At this time, all the radars monitor predominantly antisunward plasma flows in the midnight sector. Importantly, irrespective of the radar station and/or magnetic latitude of measurements, the maximum l-o-s velocity magnitudes are about the same, up to 300 m/s for B_z^- conditions and up to 200 m/s for B_z^+ conditions. Lower velocity magnitude for B_z^+ conditions is a well-known feature of high latitude convection [e.g., *Bristow et al.*, 2015; *Koustov et al.*, 2015]. All the radars show winter maxima for antisunward flows (months 6 and 18 for DCE and MCM in the summer hemisphere and months 12 and 24 for RKN in the winter hemisphere) for both B_z^- and B_z^+ conditions.

Patterns of the l-o-s velocity change at around 18 UT (magnetic noon is roughly at 19 UT) are less consistent between the radars. For B_z^-, DCE and MCM show about the same magnitudes up to 300 m/s with more typical maximum values of 200 m/s. The RKN l-o-s velocity magnitudes are at the same level but only in winter; the velocities are significantly decreased in other seasons. For B_z^+, DCE shows increased positive velocities up until around

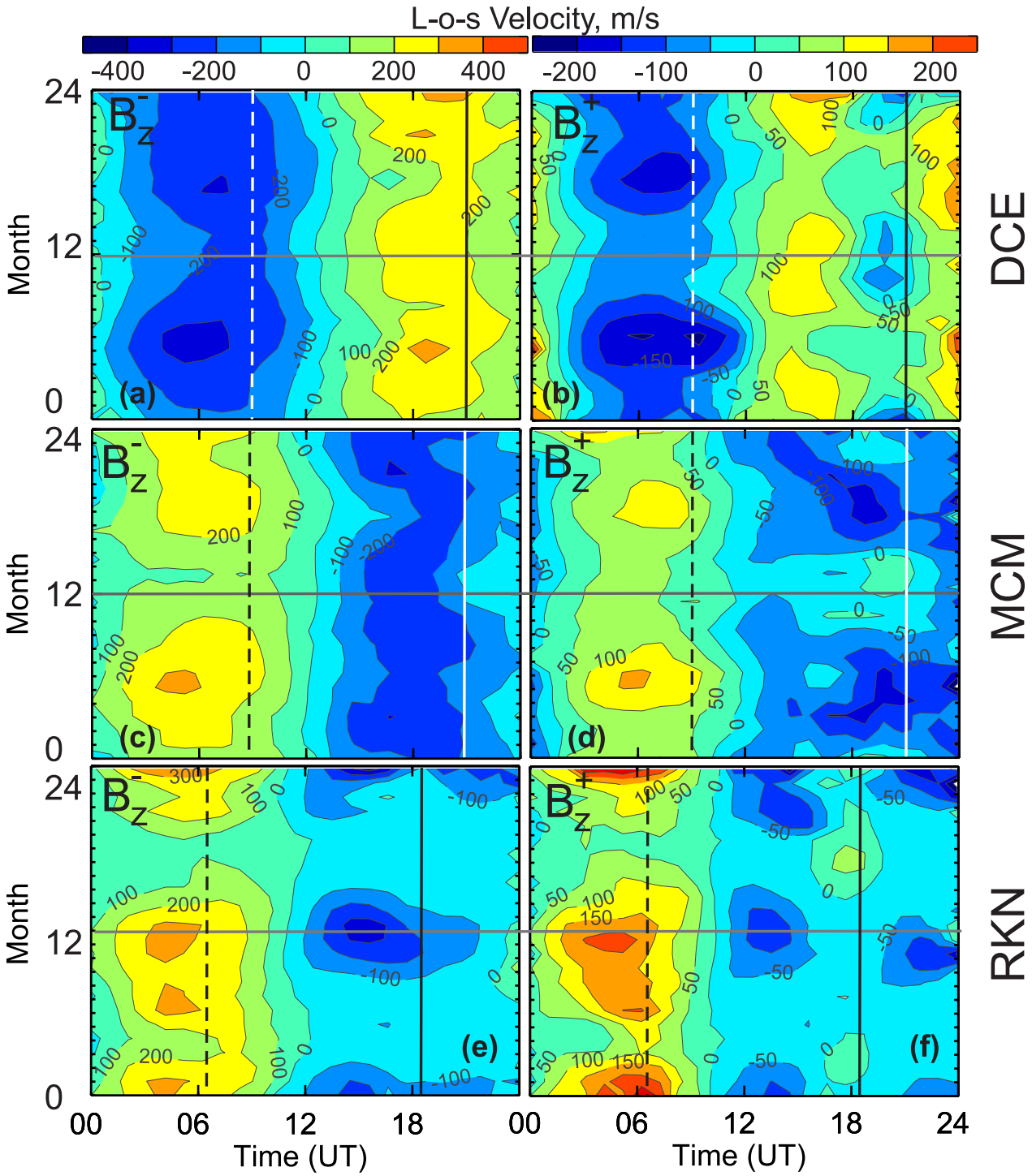

Figure 4.4: Contour plot for the hourly-median l-o-s velocity measured by the (a, b) DCE, (c, d) MCM and (e, f) RKN SuperDARN radars versus universal time. The DCE and MCM data are for beams 6, 7 and 8, gates 15-17 while the RKN data are for beams 6, 7 and 8 as well but for range gates 27-29. Plots a, c and e are for observations during the IMF $B_z < 0$ while plots b, d and f are for observations during the IMF $B_z > 0$. The scale for contour lines in plots a, c and e is doubled as compared to that for plots b, d and f. Vertical solid and dashed lines are approximate time for the magnetic noon and midnight, respectively.

18 UT (prior to the magnetic noon) in summer (months 0-3, 9-15, 22-24) and negative velocities during the same months after 18 UT (around and just after the magnetic noon). In other seasons, the DCE near noon l-o-s velocity is still positive but clearly decreased. The MCM velocities are mostly negative (antisunward flows) with smaller magnitudes in summer. The RKN data show negative l-o-s velocity enhancements at $\sim$ 16 UT in winter and "islands" of enhanced positive l-o-s velocity during summer months at $\sim$ 18 UT; the latter are sunward flows and their domination is consistent with the DCE summer negative l-o-s velocity enhancements.

An important conclusion from the data presented in Figure 4.4 is that at near noon and under B_z^+ condition, the flows are often sunward and this is more evident in summer.

4.5 Seasonal dependence for the occurrence of sunward plasma flows

Since B_z^+ dayside plasma flows are significantly affected by the IMF B_y component, we limited the B_z^+ dataset by considering only measurements with the IMF clock angle $\theta_{clock} < 30°$. Figure 4.5 shows the DCE and MCM l-o-s velocity distributions for all months of observations between 18 UT and 20 UT in 2013–2014 in a form of a contour plot. The clock-like cartoons at the bottom illustrate the position of the DCE and MCM FoVs at near magnetic noon and the sunward flow directions (expected for the IMF $B_z^+ >> |B_y|$). The plots were obtained by considering each month separately, making a histogram distribution of all the velocities with 50-m/s bins and then normalizing the distribution to 1 for each month separately. The contour procedure, while considering data for all 24 months of observations, washes out the maxima but still allows one to assess the tendencies. Figure 4.5a for the DCE radar shows that the velocities are mostly negative in summer (months 1, 12, 24) but less negative or even slightly positive in winter (months 5, 6). Figure 4.5b for the MCM radar shows that the velocities are somewhat positive in summer (months 1, 12, 24) and negative in winter (months 5, 6, 20). The summer velocities are consistent with the expected sunward flows under strongly dominant IMF. The RKN velocities (data are not presented here) observed between 18 UT and 20 UT do not show a strong seasonal effect; moreover, the l-o-s velocity

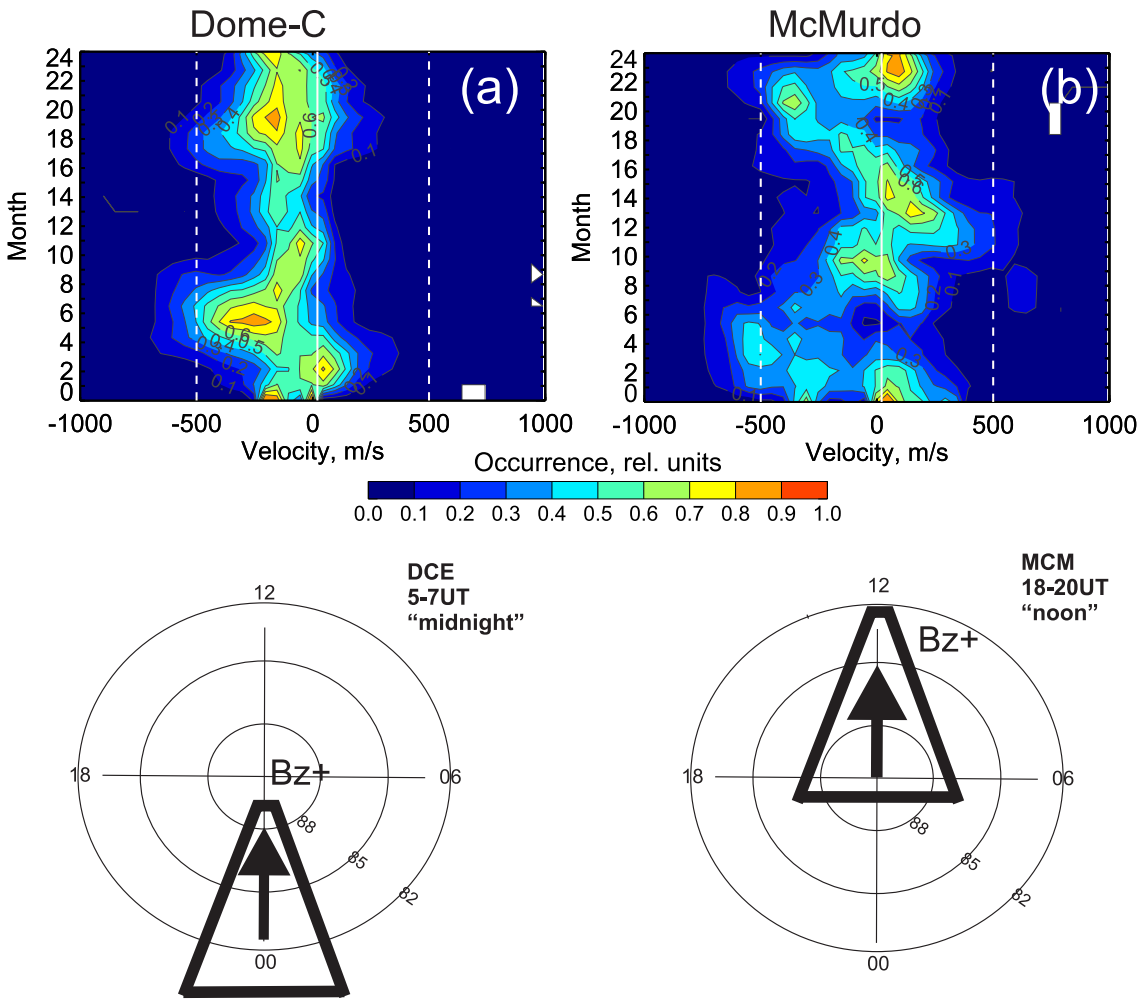

Figure 4.5: Contour plot for the l-o-s velocity occurrence on a month-velocity plane for (a) the DCE and (b) MCM SuperDARN radars. All data collected in beams 6, 7 and 8 (beam orientations are shown in Figure 4.3a) and range gates 15, 16 and 17 (red-colored rectangles in Figure 4.3a) between 18 UT and 20 UT in 2013–2014 were considered. Cartoons at the bottom illustrate sunward plasma flow vectors (arrows) in the MLT-MLAT coordinate system and approximate radar beam orientations (triangles) for the radars.

distribution indicates prevalence of antisunward flows for all seasons. The l-o-s velocity distributions become closer to zero in summer and there is an enhancement in occurrence of sunward flows in summer/fall equinox of 2014. These can be interpreted as a signature of sunward flows in summer. Part of the problem with this radar is that the data are limited on the dayside.

Plots similar to those of Figure 4.5a,b have been produced for observations between 05 UT

and 07 UT. The DCE radar shows domination of antisunward flows during winter but the distributions are centered on zero l-o-s velocity with significant presence of sunward-directed flows (positive DCE velocities) in summer. For the MCM radar, the velocities are mostly sunward although winter distributions are broader showing presence of antisunward flows. Sunward flows are not seen at lowest magnetic latitudes. The RKN radar shows sunward flows at equinoctial and summer time.

4.6 Intensity of sunward flows as a function of reverse convection electric field

To characterize the response of sunward flows to external driver variations, we consider the reverse convection electric field introduced by *Wilder et al.* [2008], Equation 1.11. Only radar measurements with $\theta_{clock} < 30^\circ$ are considered. Since the data set under this restriction is limited, we re-organised the 2013–2014 data for individual months into 3 seasons, summer (May-August), winter (November-January) and equinox (February-April, September-October). Here we present the results for the DCE radar.

Figure 4.6a is a scatter plot of the measured l-o-s DCE velocity (black dots) for equinox. Figure 4.6b presents the same data but in a form of a contour plot for a number of points in each pixel (40 m/s by 2 kV/R_E) of the plane. Both plots show that the l-o-s velocity magnitude increases with E_{RC} (more negative l-o-s velocity at larger E_{RC}) for small to moderate E_{RC} values of 0-20 kV/R_E. At larger E_{RC}, there is a saturation in the l-o-s velocity magnitude with a local decrease at ∼25-30 kV/R_E.

The saturation part of the dependence has been discussed at length by *Wilder et al.* [2010] and we will not focus on it. Rather we bin the data with 1 kV/R_E step of E_{RC} and quantify the increasing trend, Figure 4.6a. Red dots and blue vertical bars in Figure 4.6a are the median values of the l-o-s velocity and the standard deviation in each bin (each containing at least 20 points). We then make a linear fit line to the median values (red dots) by considering E_{RC} values below 20 kV/R_E. This is the range where the l-o-s velocity magnitude clearly increases. We found that the correlation coefficient for the red dots in this range of E_{RC} is high, 0.91 (although for all the black diamonds in Figure 4.6 it is only 0.32). Such a limit

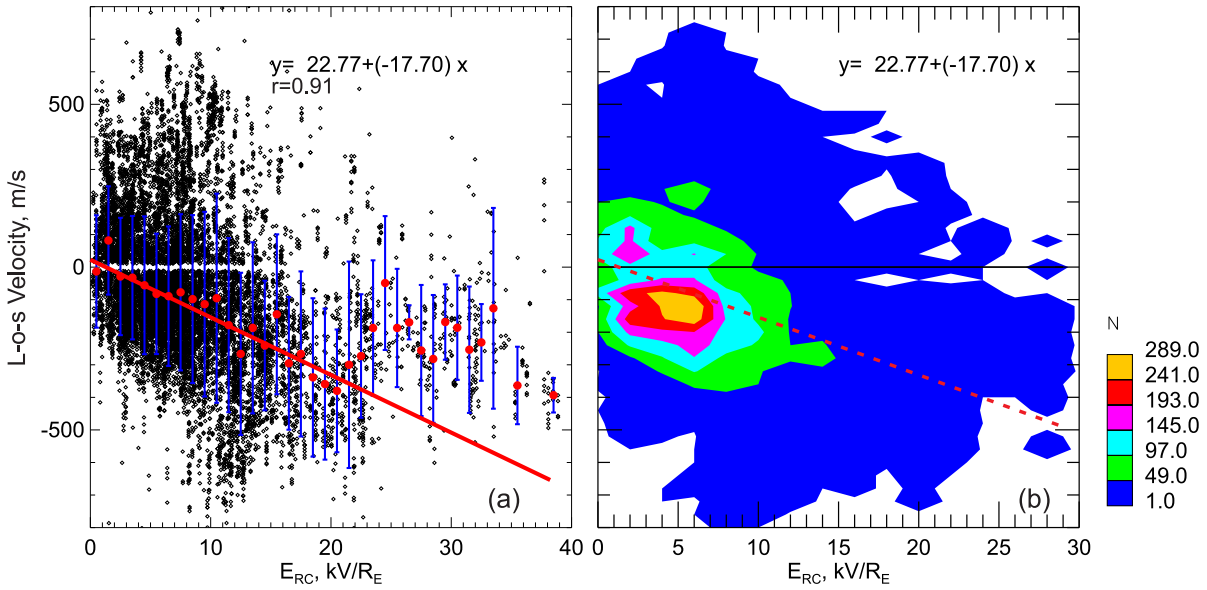

Figure 4.6: (a) Scatter plot of the l-o-s velocity measured by the DCE SuperDARN radar in beams 6, 7 and 8 and range gates 15, 16 and 17 versus reverse convection electric field [*Wilder et al.*, 2008], black dots. All equinoctial data collected between 18 UT and 21 UT and for IMF-dominated conditions (IMF clock angle $\theta_{clock} < 30°$) were only considered. Red circles with vertical blue bars are the l-o-s velocity medians for E_{RC} bins of 1-kV/R_E step. The red line is a linear fit line to the l-o-s velocity medians (red circles). The slope and y-intercept of the line as well as the correlation coefficient r are shown at the top of the plot. (b) The same data as in (a) but characterised by the contours of occurrence of the l-o-s velocity. A tendency for the l-o-s velocity magnitude to increase with E_{RC} is evident, consistent with the dashed line of the linear fit from panel (a).

was imposed because the number of large E_{RC} points vary with season dramatically [*Wilder et al.*, 2010] affecting the slope of the fit line. The slope and y-intercept of the line are shown at the top of the plot; we also place the coefficients of the fit in Table 4.1. We have done the linear fitting to the data by *Wilder et al.* [2010], scaled from their plots, and by *Abooalizadeh* [2015] in the same manner. We note that the RKN data presented by *Abooalizadeh* [2015] were erroneously plotted by using 1.3 times larger E_{RC} values, we corrected the error in our calculations. All the data in Table 4.1 consistently show largest slopes in summer, somewhat smaller values in equinox, and smallest values in winter. On the basis of the slopes, one would expect, on average, faster flows in summer (if observations over long periods are considered) and this is consistent with our results of Figures 4.5 and 4.7 where B_z^+ flows were more evident in summer.

Table 4.1: Coefficients of the linear fit on the l-o-s velocity-E_{RC} plots for various data sets. L-o-s velocity magnitudes were considered.

Data set	Season	Slope, (m/s)/ (kV/R_E)	y-Intercept, m/s
Wilder et al. [2010]	Winter	7.9	124.7
(scaled from their	Summer	10.8	208.6
Figures 5-7)	Equinox	9.15	200.4
Abooalizadeh [2015]	Winter	9.7	76.7
RKN radar,	Summer	12.7	186.9
corrected, all B_z^+ data	Equinox	11.5	322.8
DCE, 2013–2014,	Winter	5.34	38.8
B_z^+-dominated	Summer	19.9	81.3
data	Equinox	17.7	-22.8

4.7 Sunward plasma flows in both hemispheres, individual cases

Since sunward flows are particularly frequent in summer (our Figures 4.3-4.5, results by *Pettigrew et al.* [2010]) one can expect that, in a case of simultaneous observations in both hemispheres near solstice, the sunward flows would be faster in the summer hemisphere. To check this expectation, we considered simultaneous observations of DCE, MCM and RKN radars on a daily basis. We found that despite the fact that the beam meridians for the radars are not far apart in terms of MLT, finding data at about the same magnetic latitudes is problematic; this is not a surprise since the radars FoVs do not coincide in magnetic latitude. One example of successful sunward flow monitoring in both hemispheres is presented in Figure 4.7.

Figure 4.7a shows temporal variations of the IMF B_y and B_z components over 2-hour period, from 18 UT to 20 UT. At the beginning of this interval, the IMF B_z was negative and small but after about 20 min it turned positive and stayed steady at ~ 4 nT for almost 2 hours. The IMF B_y component was slightly varying around -2 nT during the first half of the period and then, after ∼18:55 UT, changed to near zero values. The IMF conditions changed after 19:35 UT when both components turned to negative values. Over this event,

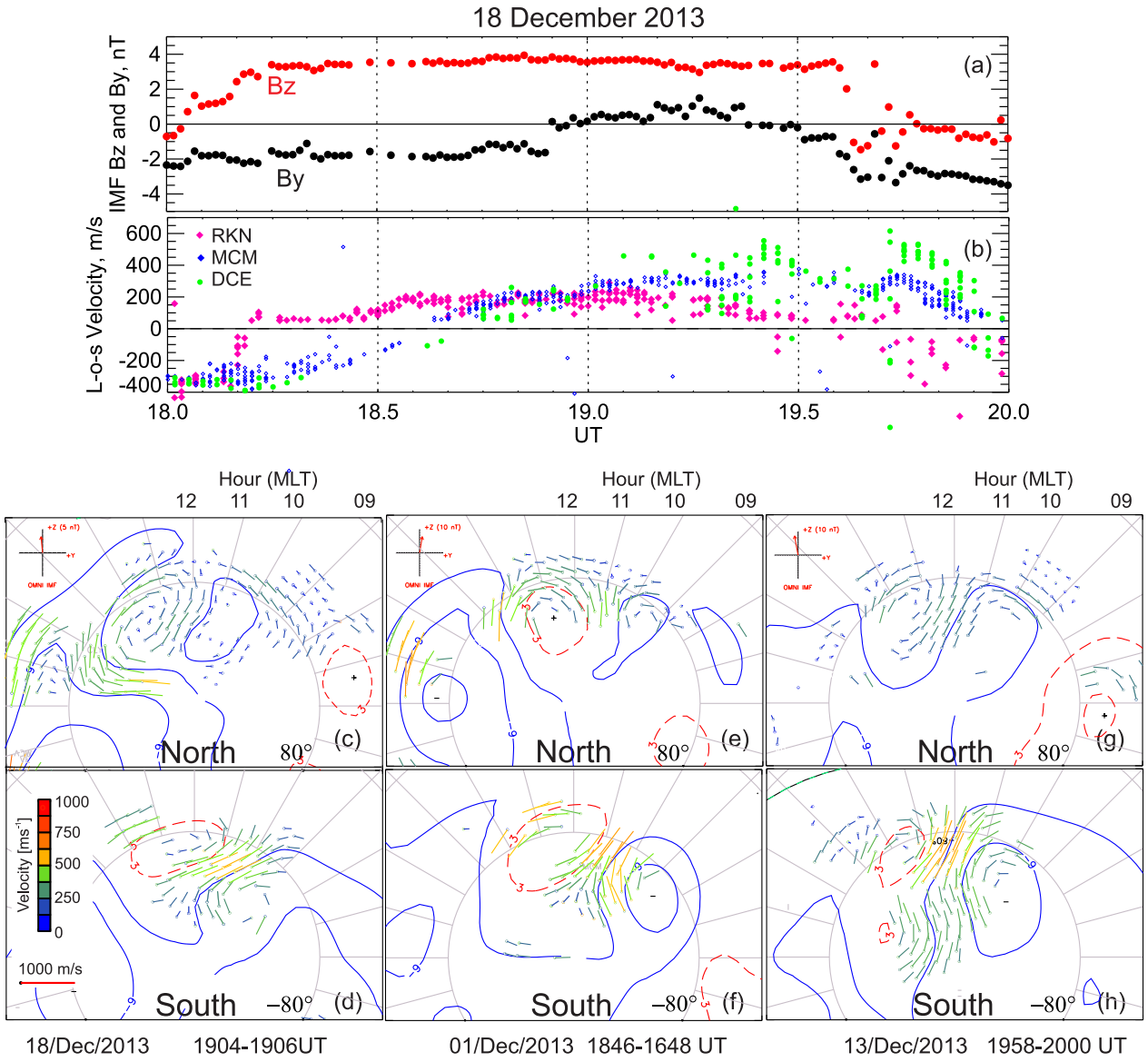

Figure 4.7: (a) Variations of the IMF B_y and B_z components on 18 December 2013 between 18 and 20 UT. Plotted are the OMNI data with an additional 8-min delay; (b) L-o-s velocity recorded by the RKN (pink diamonds), MCM (blue diamonds) and DCE (green circles) radars in their central beams 6, 7 and 8 and range gates 15-17 for MCM and DCE and range gates 27–29 for RKN. Bottom panels are plasma flow vectors at high latitudes according to all SuperDARN radar observations (by applying the potential fit technique by *Ruohoniemi and Baker* [1998]) in the (c, e, g) Northern and (d, f, h) Southern hemispheres for three 2-min intervals on 18 December 2013 (19:04–19:06 UT, panels c, d), 1 December 2013 (18:46–18:48 UT, panels e, f), and 13 December 2013 (19:58–20:00 UT, panels g, h). In the upper left corner of each upper row panels the IMF vector for the time of measurements is shown. Each panel in the bottom row has the same color bar and vector characterising the velocity scale used as shown in panel (d) Blue and red lines are contours of equal electric potential, negative and positive values, respectively. Large black circle is the magnetic latitude line of 80°. Radially-diverging straight lines are the lines of equal MLT. The lines of 09, 10, 11, and 12 MLT are marked in top-row panels.

the IMF B_z was strongly dominant during ∼18:55–19:35 UT. This is the period of our interest. Earlier, 18:15–18:55 UT, the B_y component magnitude was still significant although smaller than the B_z magnitude. Figure 4.7b shows l-o-s velocities measured by the DCE (green), MCM (blue) and RKN (pink) radars over entire 2-hour period. The beams and the gates are the same as those used for producing Figures 4.4-4.6. Here we reversed the polarity of the DCE l-o-s velocity to facilitate a direct comparison of measurements.

We first mention that the DCE and MCM velocities in Figure 4.7b agree reasonably well over the entire event with perhaps noticeable differences at the end of the event when the IMF started showing strong variations. This is despite the fact that the measurements are separated in magnetic latitude by $\sim 4°$. The RKN data, at about the same MLAT as the DCE data, show inconsistency with the Southern hemisphere radars during 18:15–18:40 UT, first of all in the polarity of the flow. We believe these differences are originated from the effect of the IMF B_y component, as described by *Huang et al.* [2000b].

However, between 18:40 UT and 19:35 UT, the l-o-s velocity polarity was consistent for all three radars. This is the time when the radars monitor the sunward flows, presumably of "matched" convection cells in the Northern and Southern hemispheres. Between 18:45 UT and 18:55 UT, the RKN l-o-s velocity was larger than that for the DCE and MCM radars. During this period, however, the IMF was not strongly dominant and we can explain the effect by influence of the IMF B_y component. After 18:55 UT, as the B_z component became dominant, the RKN l-o-s velocity is consistently smaller than the l-o-s velocity measured by the DCE and MCM radars (whose velocities are consistent). Thus for the period with dominant B_z^+ component, the sunward flow is faster in the Southern (summer) hemisphere. We mention that during this time, the Southern hemisphere radars FoVs were completely sunlit while the Northern hemisphere RKN radar FoV was completely dark.

One may argue that some l-o-s velocity differences in Figure 4.7b are owing to somewhat different direction of the plasma flow in the opposite hemispheres. Generally, this can be the case as the SuperDARN radars measure only the l-o-s flow velocity component and at least small differences can arise. To estimate the potential role of the effect, we investigated the standard maps of the plasma flow inferred by considering all SuperDARN radar data and applying the potential fit technique by *Ruohoniemi and Baker* [1998] and *Shepherd and*

Ruohoniemi [2000]. The maps obtained do show some azimuthal differences in the direction of the flow in the hemispheres, but the effect is not very strong.

In support, we show in Figures 4.7c and 4.7d plasma flow vectors in both hemispheres for 19:04–19:06 UT. The same velocity scale (see a color bar and a scale vector on the left of Figure 4.7d) is used for the plots. The IMF conditions used for the derivation of the patterns are illustrated, with an insert, in the left upper corner of Figure 4.7c. In Figures 4.7c and 4.7d, the sunward flows at $\sim$ 11 MLT and MLATs from 80° to 83° are evident. An important feature here is that the plasma flow vector magnitudes are larger in the Southern (summer, sunlit) ionosphere; this can be recognized by the color of the vectors. The effect is seen for other moments of the event. The directions of the flow, with respect to the magnetic meridians, are slightly different. The flow deviation from magnetic meridians is larger for the Southern hemisphere implying that the reported DCE and MCM velocities are only a component of full vectors meaning that the effect of faster flows in the Southern, summer hemisphere is actually even stronger than what can be inferred from Figure 4.7b.

To illustrate that the effect of faster sunward flows in the summer (Southern) hemisphere for individual events is not a unique phenomenon, we present 2-D plasma flow data for a couple of other events in 2013, 1 December and 13 December, Figures 4.7e-h. For both events, the IMF was strongly dominant. Here sunward flows can be seen at $\sim$ 11 MLT and MLATs from 80° to 83°; the Southern hemisphere data coverage is more extended toward the magnetic Pole. In both cases, Southern (summer) hemisphere flows are faster. Interestingly enough, the IMF was about 2 times larger for these two additional events and so the flow vectors are generally larger than those for the 18 December event, in the Southern hemisphere. This is an expected effect; stronger IMF driver produces faster flows, *Wilder et al.* [2010] and our data in Figure 4.6. For the Northern hemisphere, the velocity magnitudes in three events do not differ significantly.

4.8 Sunward plasma flows in both hemispheres, averaged convection maps

Although the analysis of plasma flow speed along the midnight-noon meridian, undertaken in Sections 4.4 and 4.5, gives a clear indication of the asymmetry in the plasma speed between the summer and winter conditions, analysis of 2-D maps is still needed to prove that the differences are not due to a simple change in the direction of the flows. In this sense, 2-D maps discussed in Section 4.7 give a more reliable assessment of the sunward flows. The cases presented are, however, just a set of clear-cut events and whether this is a typical situations for strongly northward IMF B_z is not clear. Now we are to investigate the asymmetry in the summer-winter sunward flows by using a statistical approach.

4.8.1 Approach to the analysis of 2-min SuperDARN maps, the event of 20 January 2015

To gain further insights into the winter-summer differences in the sunward near-noon flows, we consider here a more direct way of looking at flows by comparing simultaneous SuperDARN convection maps in both hemispheres. We note that although one can think of an interhemispheric comparison of standard 2-min SuperDARN maps, in reality this would hardly give a result. While the maps are routinely available for both hemispheres, the data are too patchy to compare interhemispherically on a point-by-point basis, at the same MLAT and the same MLT. Additional difficulty is strong variability of the flows for the IMF $B_z > 0$ even for relatively steady IMF conditions [*Walker et al.*, 1998] so that some sort of averaging is required.

To illustrate our approach to the analysis, we consider here one event, 20 January 2015, for which reasonable data coverage in both hemispheres was reached and the IMF was stable for an extended period of time. We note that to select this kind of events, the SuperDARN database for 2013–2015 was searched to find long-lasting events of ~ 2 hour duration with identifiable reverse convection cells.

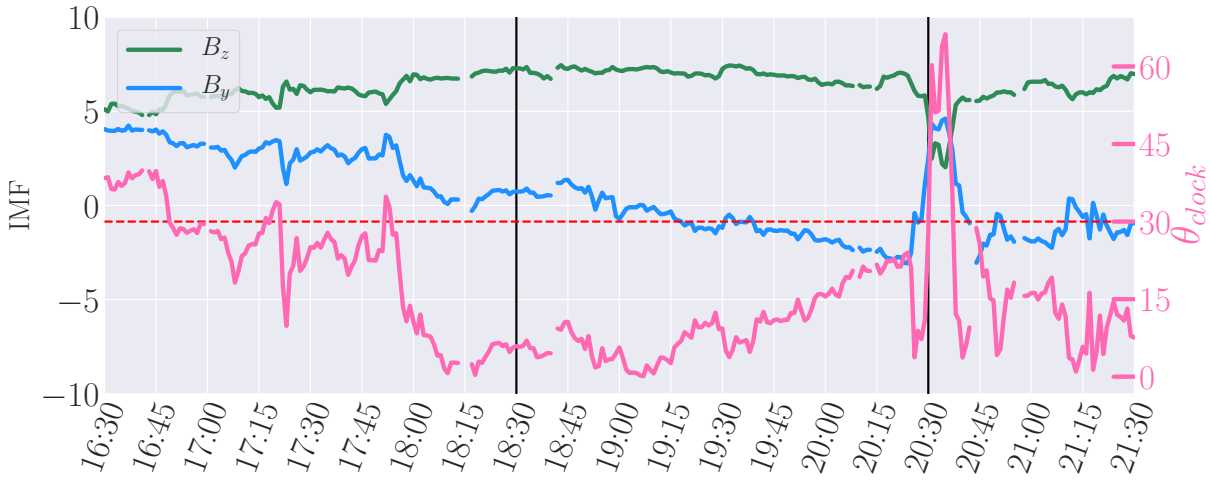

Figure 4.8: Variations of the IMF B_y and B_z components (blue and green lines, respectively) and the IMF clock angle (pink line) on 20 January 2015 between 16:30 and 21:30 UT. Plotted are the OMNI data propagated to the bow shock location. Vertical black lines indicate the beginning and end of the period over which averaging of the standard 2-min SuperDARN convection maps has been performed. Red dashed line is the line of the 30° IMF clock angle.

Figure 4.8 shows temporal variations of the IMF B_z and B_y components and clock angle between 16:30 and 21:30 UT on 20 January 2015. The IMF B_z was fairly stable at $\sim$ 7 nT while the IMF B_y was slowly decreasing from +2 nT to -2 nT. At $\sim$20:30 UT there was a quick transition of both IMF components and the SuperDARN convection patterns showed significant changes in flow configuration. To avoid the possible effect of these transitions, we decided not to consider data after 20:30 UT even though the IMF clock angle recovered to an almost pure northward orientation. We note that for other events, some variations in the IMF components did occur but for the periods selected these were not very sharp, with very few exceptions.

For each identified event, averaging of the convection maps over a B_z^+-dominated interval was performed as follows. First, standard 2-min velocity maps were produced for both hemispheres. These were done by applying the Potential Fit technique by *Ruohoniemi and Baker* [1998] in its standard version. Then individual velocity vectors at every MLT and MLAT of the grid space were averaged.

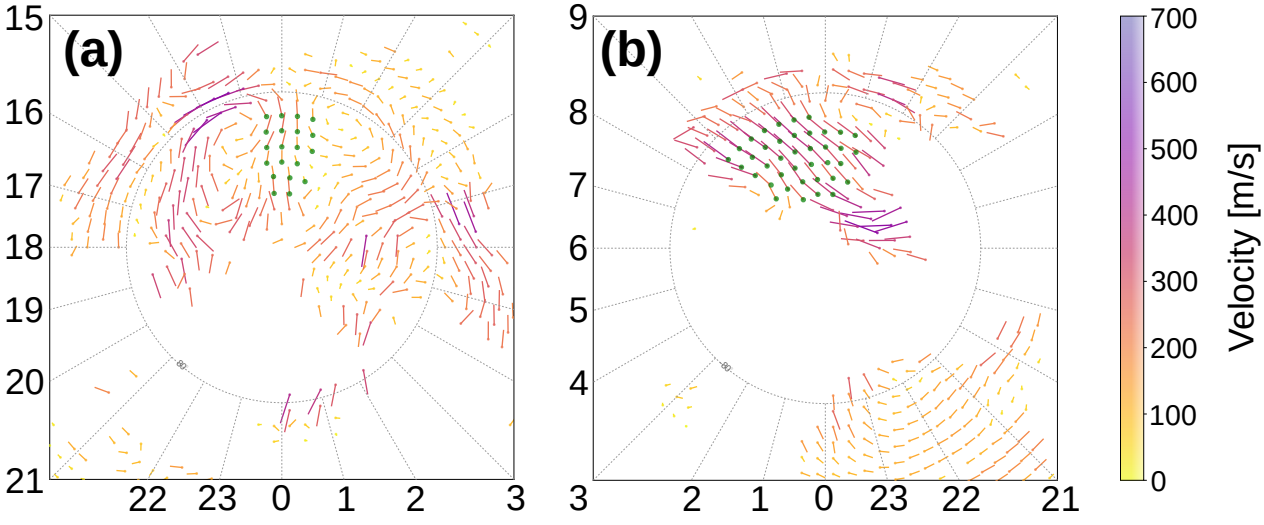

Figure 4.9: Averaged convection pattern according to SuperDARN radar measurements in the (a) Northern and (b) Southern hemispheres for the event of 20 January 2015. Averaging was performed for time interval from 18:30 to 20:30 UT. Vectors marked by green dots at their origin were selected for the averaging as vectors representing sunward flows.

Figure 4.9 shows averaged convection maps in both hemispheres, in MLT-MLAT coordinates, for the entire duration of the event. One can recognize two reverse convection cells in the Northern hemisphere data, Figure 4.9a, at near noon hours and MLAT=80°-85°. For the Southern hemisphere, Figure 4.9b, the sunward transpolar flow is well seen. It stretches from the South Pole to latitudes of MLAT=80° and some signatures of the "curving" of the cells can be recognised. The Northern hemisphere near-noon velocity flow magnitudes in the ∼12 MLT time sector and MLAT=80° − 85° seem to be slower than that in the Southern hemisphere as color the Northern hemisphere vectors seems to be, on average, more yellow. In terms of direction, the Northern hemisphere flow is almost along the midnight-noon meridian while the Southern hemisphere flow is directed toward early prenoon hours of ∼ 09 − 10 MLT.

To characterise the near-noon flows quantitatively we selected a number of vectors on each map and computed the average value for the velocity magnitude and the velocity direction. The selection of vectors on a map was somewhat subjective: we first identified, by eye, a general tendency of the flow and the center line of the flow "stream" and then selected a group of vectors representing this flow. For the event of 20 January 2015, the points selected are shown by green solid circles at the origin of individual vectors.

The flow direction was characterised by its deviation (in degrees) from the midnight-noon meridian; the flow toward prenoon and postnoon hours of MLT was assigned positive and negative values, respectively. The direction of 90° corresponds to the flow parallel to the dusk-dawn line. For the data of Figure 4.9, the velocity magnitudes and angles with the noon-midnight meridian were found to be 184 m/s and −3.9° for the Northern hemisphere map (Figure 4.9a) and 347 m/s and 49.7° (toward prenoon) for the Southern hemisphere map (Figure 4.9b).

4.8.2 Analysis of averaged SuperDARN 2-min maps, all events

We identified 12 events in 2013–2015 when the IMF B_z was strongly dominating for extended periods of typically $\sim$ 2 hours and reasonable SuperDARN coverage was in effect in both hemispheres. The list of such events is given in Table 4.2. In Table 4.2 we also present median values of the IMF B_z and B_y components, over respective periods of measurements. Two events had very strong IMF B_z exceeding 10 nT while for others it was moderate, in a range of 5–8 nT. For 5 events, the IMF B_y was negative while for 7 other events it was positive.

The average convection maps were produced and assessed in the same way as the above event of 20 January 2015. Results of the analysis are presented as a scatter plot in Figure 4.10. Here we also present information on the variability of the near-noon velocity for each map by vertical and horizontal bars corresponding to the standard deviation of respective parameters in each event.

Figure 4.10a shows that the majority of the points are located below the bisector corresponding to equal flow speeds in the hemispheres. This implies occurrence of faster flows in the Southern hemisphere. We remind the reader that the data selected are for winter conditions in the Northern hemisphere and summer conditions in the Southern hemisphere. There is one anomalous point in Figure 4.10a lying well above the bisector. It is for observations on 06 January 2015. We investigated the individual SuperDARN maps for this event and did not find anything unusual except of strong variability of the velocity. However, we noticed that the convection vectors used in averaging of the Southern hemisphere data were based

Table 4.2: Coefficients of the linear fit on the l-o-s velocity-E_{RC} plots for various data sets. L-o-s velocity magnitudes were considered.

Event number	Day	Start–end (UT)	$< B_z >$	$< B_y >$
1	01 Dec 2013	18:00–20:00	6.71	0.52
2	13 Dec 2013	17:30–19:30	8.06	2.39
3	27 Nov 2013	17:00–19:00	5.79	0.78
4	26 Dec 2013	18:40–20:10	4.51	-0.39
5	24 Jan 2014	18:30–21:00	5.02	-1.03
6	05 Nov 2014	19:40–20:20	4.33	-1.17
7	27 Nov 2014	17:20–19:00	6.72	0.94
8	06 Jan 2015	18:00–19:40	11.52	0.77
9	07 Jan 2015	17:30–19:30	15.15	8.68
10	10 Jan 2015	19:10–21:00	5.04	1.6
11	20 Jan 2015	18:30–20:30	7.0	-0.9
12	15 Dec 2015	18:10–19:40	6.76	-1.3

mostly on DCE radar observations. For this specific event, this radar was detecting echoes from the E region. E-region SuperDARN velocities are known to be up to 2 times smaller than the true $\mathbf{E} \times \mathbf{B}$ drift of the F region plasma [*Koustov et al.*, 2005]. This explains the anomalous point in Figure 4.10a. Data of Figure 4.10a indicate that the difference in the flow speed between the hemispheres is somewhat stronger for IMF $B_y < 0$ as red points tend to be at the bottom of the cloud of points.

The interhemispheric/seasonal difference in the directions of the flow is well seen in Figure 4.10b. Here the points are shifted toward positive values in the Southern, summer hemisphere. Positive directions imply plasma flow deviation toward prenoon hours of MLT. Quantitatively, if the flow goes over the magnetic pole to lower latitudes, its direction of 30° would mean a direction toward 10 MLT. We can estimate that, overall, the "deviation" of the flow in the Southern hemisphere is on the order of 2 hours. There is no such a tendency for the Northern hemisphere flows; the directions here are almost evenly distributed between positive and negative values with typical values below 20°. We estimate that in the Northern hemisphere, the flows are roughly along the midnight-noon meridian with deviations on the order of 1 hour to prenoon or postnoon hours. In the Southern hemisphere, the flow "deviates" toward $\sim$ 10 MLT meridian.

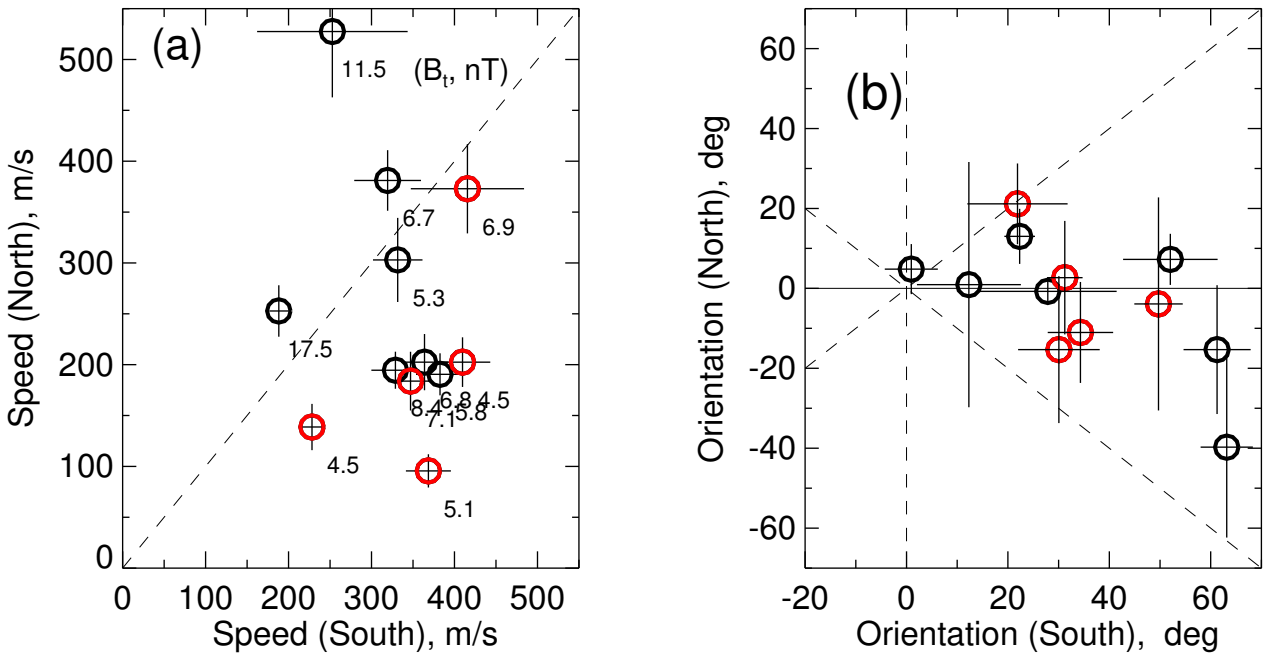

Figure 4.10: (a) The Northern hemisphere throat flow speed versus the southern hemisphere throat flow speed for 12 events selected for analysis. All events are under strongly-dominating IMF B_z; the number by each individual point is the ratio of the IMF transverse components, B_z/B_y. (b) The orientation of the throat flow with respect to the noon-midnight meridian for the Northern hemisphere versus the orientation of the flow in the Southern hemispheres for the same events as in (a). Red-colored points in both (a) and (b) are for the events with the IMF $B_y < 0$. Vertical and horizontal bars are the standard deviation of the velocity for speed (panel (a)) and orientation (panel (b)) at the near-noon flows in each hemisphere.

4.9 Discussion

The direction and intensity of the sunward flows for northward-oriented IMF during various seasons is not easy to ascertain from data published so far. One possibility is to look at statistical models of the high-latitude convection. However, such models, from various instruments, are usually formulated in terms of the electric potential and estimates of the average flow velocity from maps of the potential are imprecise although some models exist in digital format and perhaps answers can be found. We presented in Section 4.2 (Figures 4.1 and 4.2) the output for the CS2010 SuperDARN model and monthly map analysis using the *Fiori et al.* [2010] approach and showed that although both techniques predict faster flows

in the summer hemisphere and non-alignment of the flows with the midnight-noon meridian, the preferential direction of the flow is not consistent between the approaches. One of the reasons is probably the difference in the databases used for building the statistical convection maps. The CS2010 maps are based on a larger statistics (many years of measurements), but binning according to the intensity of the convection driver and season diminishes the advantage and analysis of monthly-averaged velocity vectors could be a reasonable alternative. The fact that the flow directions are different between the considered models suggests that the effect is rather weak and probably very sensitive to the external driving conditions. For this reason, we undertook two additional ways to study sunward flows: by considering l-o-s velocities of the polar cap radars looking along the magnetic meridian (Section 4.4-4.6) and by averaging 2-D SuperDARN maps over periods of strongly dominating B_z^+ obtained for both hemispheres simultaneously (Sections 4.7-4.8). Several aspects of sunward flows are of general interest: 1) overall frequency of occurrence, 2) their spatial extent, and 3) seasonal dependence.

Wilder et al. [2010] reported that for near-noon SuperDARN observations in the Northern hemisphere with relatively stable IMF B_z^+, in more than 85% of cases one would see a sunward flow. The authors considered the so-called gridded velocities, i.e. l-o-s velocities median-filtered over space and time [*Ruohoniemi and Baker*, 1998]. For general purposes, however, the above percentage is somewhat misleading. If one removes the condition for the IMF B_z^+ to be stable (adopted by the authors) the percentage of sunward flows under the IMF B_z^+ is smaller. Our data presented in Figure 4.7 show as both the DCE and MCM radars detect antisunward flow under settled B_z^+ conditions for as long as 40 min. Statistical data of Figure 4.6 are even more revealing; there is significant amount of points with antisunward flows for relatively weak E_{RC}. We estimated that for the 2-year period of DCE measurements in gates 15-17 and beams 6-8, the percentage of expected sunward flows for B_z^+ is at a level of $\sim 60\%$ and often less than that. A comparable number was obtained for the RKN radar. The sunward flows are particularly difficult to see whenever the B_z^+ driving is weak (the IMF B_z^+ values are low), see Figure 4.6a. These conclusions are consistent with ionosonde observations by *Jayachandran and MacDougall* [2001] who stated that sunward flows are only seen in the polar cap if the IMF $B_z > +2$ nT.

With respect to the sunward flows extent, we note that reverse convection cells on SuperDARN convection maps are usually seen as circles of a smaller size than the regular large-scale convection cells, see examples presented in *Huang et al.* [2000a,b]. However, the reverse convection cell size is typically difficult to determine because the data coverage is very limited around the magnetic Pole. Examples in *Huang et al.* [2000b] are rather unique cases. This is one of the reasons why we selected in this study two (relatively new) SuperDARN radars at DCE and MCM that have ample data in the central polar cap. The only problematic period for the flow monitoring is winter darkness time [*Bristow et al.*, 2011, 2015]. The SuperDARN radars in the Northern hemisphere hardly detect echoes in the near magnetic Pole area [e.g., *Ghezelbash et al.*, 2014] although they provide useful information at magnetic latitudes equatorward of $\sim 83^\circ$.

Our analysis showed (actual data are not presented here) that signatures of the summer sunward flows become weaker and disappear for DCE observations at MLAT$< 80^\circ$ (range gates above 21). On the other hand, the near-noon MCM data of Figure 4.4d, for largest considered MLAT, show the effect less clearly than at lower latitude of 83°, indicating that the sunward flows are frequently not spread beyond the magnetic pole toward the nightside. Thus, from statistical analysis of l-o-s velocities, the reverse convection cells are confined to the noon sector and MLATs$= 83^\circ - 87^\circ$.

Recently, *Förster and Haaland* [2015] reported that, according to CLUSTER statistics, the reverse convection cells are less prominent in the southern hemisphere. Our data show otherwise; the DCE radar shows sunward flow signatures at MLAT$= 80^\circ - 85^\circ$, including relatively low latitudes of $80^\circ - 83^\circ$ where the RKN radar (as well as the INV radar whose data were investigated but not presented here) does not have clear indications of sunward flows. The MCM radar shows sunward flows at MLAT$= 86^\circ - 90^\circ$; these latitudes are not covered by the other two radars.

Our analysis showed a clear increase of the sunward flow speed with intensification of the lobe reconnection driver E_{RC} (specified by *Wilder et al.* [2008]). The increasing part of the dependence was found to be fastest for summer and slowest for winter, in agreement with *Wilder et al.* [2010]. The only difference with *Wilder et al.* [2010] is that the slopes are larger in our case. This is, perhaps, because we selected periods with dominant B_z^+ while *Wilder*

et al. [2010] included data with relatively large IMF as well. Thus our observations further support the original suggestion by *Crooker and Rich* [1993].

The fact that sunward flows are stronger in a summer hemisphere where the ionospheric conductance is larger implies that FACs have to be stronger in the summer hemisphere for the IMF B_z^+. Some observations support this expectation [e.g., *Stauning*, 2002].

Another effect reported by *Förster and Haaland* [2015] is that the average direction of the sunward flow, crossing the central polar cap, is rotated toward prenoon hours in the summer hemisphere while it aligns with the noon-midnight line in the winter hemisphere. This effect is well seen in our plots of Figure 4.7c–4.7h for individual events, and our more extensive analysis in Section 4.8 (Figures 4.9 and 4.10) fully supports the original suggestion by *Förster and Haaland* [2015]. We note that individual SuperDARN convection maps for the summer (Southern) hemisphere, however, did show occasional average flow deviation to the postnoon MLT hours. We think that this might be associated with the effect of the IMF B_y component.

It has always been expected that reconnection processes associated with the IMF B_y component might contribute to the flow pattern at high latitudes [e.g., *Reiff and Burch*, 1985]. Recently, *Maimaiti et al.* [2017] clearly articulated the fact that, even for strongly northward IMF, the frontside reconnection can be significant and develop independently of the lobe reconnection processes and affect the resultant convection pattern. In our events, the IMF B_y was not necessarily small all the time; the condition for the IMF clock angle has been satisfied but the magnitude of the IMF B_y was more than 2–3 nT in many instances. Splitting the averaged velocity data according to positive and negative average IMF B_y did not give a clear answer (Figure 4.10 data). In the summer hemisphere, the flow deviations were all positive but moderate for $B_y < 0$, (Figure 4.10b, red circles) with no preferential values within the entire dataset. In the winter hemisphere, no clear tendency can be identified even in the sign of deviation: 2 events had the flow deviation toward prenoon MLT hours and 2 events had deviation toward postnoon MLT hours while in 1 event the flow was almost along the midnight-noon meridian.

Although the DCE, MCM and RKN data seem to support the hypothesis by *Crooker and Rich* [1993], we noticed that, for some periods, the l-o-s velocity does not respond to

intensification of external driver of the lobe reconnection E_{RC}. *Bristow et al.* [2015] reported the same result with respect to B_z^- convection driver. Their opinion is that the central polar cap plasma flows are affected by substorm processes. However, because substorms are not frequent for B_z^+ conditions we think that there are other sources of the ionospheric flow variability. We are not aware of known mechanisms of this variability. One can hypothesize that there is an electric linkage to the conducting polar cap ionosphere while the lobe reconnection processes and interchange cycle (dominant B_z^+) occur. In this case, the efficiency of reconnection in the sunlit (high conducting) hemisphere might be hindered by not so efficient reconnection in the dark (low conducting) hemisphere while the interchange cycle is in progress. Another viable option, as mentioned earlier, is significant contribution from the front side reconnection due to non-zero IMF B_y.

4.10 Summary

We can summarise the result obtained in this chapter as follows:

1. For strongly dominant IMF B_z^+ conditions ($\theta_{clock} < 30°$), the plasma flow along magnetic meridian in the central polar cap is predominantly toward the Sun in a broad range of latitudes, $80° - 90°$. The flows are more frequent and faster in summer; this supports the original theoretical suggestion by *Crooker and Rich* [1993] based on preferential conditions for the lobe reconnection processes in the summer hemisphere.

2. For observations in the Southern hemisphere, the l-o-s velocity increase with intensification of the external driver, the reverse convection electric field, is faster in summer, slightly slower in equinoxes and slowest in winter. The rates of the increase are slightly faster than those inferred from the analysis of SuperDARN data in the Northern hemisphere.

3. Sunward plasma flows in the summer hemisphere are not aligned with the magnetic midnight-noon line but rather rotated toward prenoon hours, supporting original finding by *Förster and Haaland* [2015]. The deviations can be as large as 50°. In the summer (Southern) hemisphere, the deviation is mostly towards prenoon MLT hours

while it can deviate to either prenoon or postnoon MLT hours in the winter (Northern) hemisphere. The winter hemisphere flow deviations to prenoon or postnoon MLT hours has no clear relation to the polarity of the average IMF B_y component.

Chapter 5

Ionospheric plasma convection associated with polar cap arcs

It is well established that auroral displays observed from the ground and space are affected by solar wind driving conditions. When the IMF B_z is negative, the auroral oval is the major region of luminosity and, not surprisingly, the auroral oval features have been a target of extensive research. One of the major focuses is auroral arcs and their relationship to the substorm onsets. When the IMF B_z is positive, the auroral oval is usually dimmer, and other auroral features become more recognizable. One of these is a special class of auroral arcs often observed in the region poleward to the auroral oval. These arcs are referred to in the literature as polar cap arcs, sun-aligned arcs, transpolar arcs, theta aurora, and extreme high-latitude arcs.

This Chapter focuses on a detailed investigation of electrodynamics of individual polar cap arcs observed by the OMTI all-sky camera at Resolute Bay (RB) in combination with the PolarDARN radars and Swarm and DMSP satellites. We attempt to characterize 1)the ionospheric plasma flow in the vicinity of the polar cap arcs, 2)the flow intensity within the arc structure, 3)modification of the global-scale high-latitude convection pattern by individual polar cap arcs, and 4)association of the arc-related plasma flows with plasma convection in the magnetotail.

5.1 Introduction

First documented observations of very high-latitude aurora are dated back to the early twentieth century [*Mawson*, 1916, 1925]. Systematic study of morphology of polar cap arcs started

during the International Geophysical Year (IGY, 1957–1958) with introduction of a new tool, the all-sky camera. Global imaging of the polar cap and the auroral oval in both dark and sunlit conditions became possible by means of visible and ultraviolet imagers onboard of the high-orbiting DE 1 satellite [*Frank et al.*, 1982]. The global images led to the discovery of a very large-scale polar cap aurora, which crossed the entire polar cap, connecting the nightside oval with the dayside oval [*Frank et al.*, 1982, 1986]. Such auroral configuration was named "transpolar arc" or "theta aurora" for its resemblance to the Greek letter "theta" Θ. Both names are frequently used in the literature even for cases when an arc does not necessarily crosses the center of the polar cap or is connected to the both sides of the auroral oval.

Polar cap arcs vary significantly in their shape, size, brightness, location within the polar cap, motion, spatial and temporal intensity variations. The most comprehensive and systematic review of various properties of polar cap arcs can be found in *Zhu et al.* [1997]. Despite the great variability of polar cap arcs, they all have several common characteristics. One of the first firmly established properties of polar cap arcs is their near alignment with the Sun-Earth direction [*Denholm*, 1961; *Gustafsson*, 1967; *Lassen and Danielsen*, 1978; *Valladares et al.*, 1994; *Maggiolo et al.*, 2011] (the name "sun-aligned arcs" comes from this property).

Another property known since early studies is negative correlation with geomagnetic activity [*Akasofu*, 1963; *Davis*, 1963]. It has been established that occurrence of polar cap arcs is related to the northward orientation of the IMF [*Berkey et al.*, 1976; *Ismail et al.*, 1977]. Although majority of polar cap arcs are observed under positive B_z conditions, there is a fraction of arcs observed for negative B_z [*Lassen and Danielsen*, 1978; *Rairden and Mende*, 1989; *Valladares et al.*, 1994; *Hosokawa et al.*, 2011]. This was explained by a delay between the southward turning of the IMF and disappearance of polar cap arcs rather than by actual appearance of a polar cap arc under negative B_z conditions. There is also a delay associated with the northward B_z turning and appearance of polar cap arcs. It was shown that B_z stays northward for 1–2 hours before the advent of polar cap arcs [*Troshichev et al.*, 1988; *Kullen et al.*, 2002]. Dawn-dusk motion of polar cap arcs also depends on the orientation of the IMF; motion in the dusk-to-dawn direction appears preferably for $B_y < 0$ and dawn-dusk motion for $B_y > 0$ in the Northern Hemisphere [*Craven et al.*, 1991; *Valladares et al.*, 1994; *Hosokawa et al.*, 2011]. The motion of polar cap arcs in the Southern hemisphere is in

opposite direction to the motion of polar cap arcs in the Northern hemisphere [*Rairden and Mende*, 1989].

Polar cap arcs are associated with a shear in convection; however, great variety of convection signatures is reported for polar cap arcs. Summarizing experimental data described in the literature, there is a shear associated with polar cap arcs which is characterised by a strong antisunward flow on the dawnward flank of an arc which is decreasing toward dusk with either significantly reduced antisunward flow or with sunward flow on the dusk side of the arc [*Nielsen et al.*, 1990; *Marklund et al.*, 1991; *Weber et al.*, 1991]. Different studies report flow within the arcs convecting sunward, antisunward, sunward for one end and antisunward for the other, or being very irregular. Antisunward flow within polar cap arcs was reported by a number of researchers [*Robinson et al.*, 1987; *Mende et al.*, 1988; *Marklund et al.*, 1991]. Sunward flow within polar cap arcs has also been reported [*Frank et al.*, 1986; *Weber et al.*, 1989; *Chang et al.*, 1998; *Blomberg and Cumnock*, 2005]. *Liou et al.* [2005], studying flows within a theta aurora, found that the dayside part of the aurora at different time instances was associated with sunward, antisunward, and zonal flow, while the nightside part of the theta aurora was consistently antisunward convecting. The question of the plasma convection within the region of auroral precipitation is an important one as it can help us to shed a light on the source region for polar cap arcs. It is not clear if the contradictory observations indicate that there are different types of sun-aligned arcs which originate from different magnetospheric source regions or that some instruments cannot resolve convection within thin arc structure and thus reported observations are not strictly from within polar cap arcs.

Tangential to sun-aligned arcs plasma drift (or perpendicular horizontal electric field) is usually much larger than perpendicular plasma drift (tangential electric field) [*Robinson et al.*, 1987; *Gallaher*, 1997].

Many researchers made attempts to relate location of polar cap cap arcs to particular gradients in the high-latitude convection pattern. The high-latitude convection for northward B_z is itself a difficult problem, which is still not fully resolved (see Chapter 4). For example, as was discussed above, sunward flow was observed within the transpolar arc in number of observations. It was suggested by *Frank et al.* [1986] and *Gusev and Troshichev* [1990] that

this sunward flow is basically the sunward flow of the four-cell convection pattern. Different observations indicate that the coherent four- or three-cell convection pattern is displaced toward sunlit part of the polar cap; at the same time, convection on the nightside could be highly irregular and turbulent [*Heelis et al.*, 1986; *Cumnock et al.*, 1995]. Transpolar arcs, however, often extend deep into the nightside part of the polar cap and this makes it difficult to relate the arcs to the lobe convection cells. Thus attempts were made to fit polar cap arcs into a distorted two-cell convection pattern [e.g., *Robinson and Mende*, 1990] where the arcs occur in the reversal region of one of the cells. It was also argued that the reversal alone could produce the arc without any magnetospheric trigger [*Zanetti et al.*, 1990]. However, polar cap arcs are not always observed in such regions of large-scale reversals, for example, *Hoffman et al.* [1985] reported a polar cap aurora embedded in a region of antisunward flow of two-cell convection pattern. All the diverse observations indicate that perhaps polar cap arcs cannot simply be related to a specific feature of large-scale convection. *Sojka et al.* [1994], using the coupled magnetosphere-ionosphere model by *Zhu et al.* [1993], showed that sun-aligned arcs can be formed for all known convection patterns observed for northward IMF conditions and different sun-aligned structures form in response to these different background convection patterns.

5.1.1 Source regions for polar cap arcs

An arc is a band of increased electron precipitation and identification of the source region of the precipitating electrons is important for development of the theory of polar cap arc formation. Theories suggesting that sun-aligned arcs originate on open magnetic field lines imply that the precipitating electrons originate from the magnetosheath. For closed field-line configuration, central plasma sheet, plasma sheet boundary layer, low-latitude boundary layer, and reconnected or bifurcated lobe magnetic field lines were proposed as source regions for particle associated with polar cap arcs.

Magnetic field lines in the polar cap are normally open to the solar wind and naturally it was assumed by a number of researches that arcs in the polar cap also lie on open magnetic field lines [e.g., *Burke et al.*, 1982]. It was argued that electrons that produce visible arcs are the magnetosheath electrons which underwent field-aligned acceleration between the iono-

sphere and magnetopause [*Hardy et al.*, 1982; *Hardy*, 1984; *Chiu*, 1989; *Gussenhoven and Mullen*, 1989].

Despite some evidence supporting the open field-line configuration and magnetosheath as the source region for polar cap arcs, it would be fair to say that majority of researchers believe that polar cap arcs are on closed field lines. *Shinohara and Kokubun* [1996] showed that localized and structured electron precipitations they considered to be associated with polar cap arcs were accompanied by ion fluxes, which are more intense and energetic than those of the solar wind. They argue that the ion fluxes are typical to the plasma sheet boundary layer and thus sun-aligned arcs occur on closed field lines. *Hoffman et al.* [1985] performed comparison of electron and ion spectra within polar cap arcs electron and ions spectra in different regions of magnetosphere. The authors concluded that both the electron and ion spectra are consistent with plasma sheet spectra. Many other observations [*Frank et al.*, 1982; *Peterson and Shelley*, 1984; *Gorney et al.*, 1986; *Menietti and Burch*, 1987] supported the evidence that particle spectra inside polar cap arcs are very similar to those of the plasma sheet or plasma sheet boundary layer.

The low-latitude boundary layer (LLBL) was also suggested as a plasma source for polar cap arcs. *Lundin et al.* [1991] argued that during periods of northward IMF, the LLBL becomes wider and topologically coupled to the plasma sheet boundary layer. Polar cap arcs, according to the authors, originate in this expanded LLBL. This is supported by observations of antisunward flows along polar cap arcs [*Nielsen et al.*, 1990]. A similar argument was put forward by *Liou et al.* [2005], who observed antisunward plasma flows in the nightside portion of a theta aurora and consequently proposed that entire arc is mapped to the LLBL. Recent observations by *Fear et al.* [2014] showed evidence that the theta aurora originate on closed fluxes of magnetic field lines trapped in the lobe region. The authors argue that this atypical to the lobe region plasma was heated by the reconnection mechanism and served as the source region for transpolar arcs.

Occurrence of closed field line fluxes containing hot plasma inside the polar cap requires magnetospheric configuration different from the standard configuration. *Frank et al.* [1982] suggested that a bifurcation of the magnetotail lobe inside the plasma sheet could be a reason for occurrence of polar cap arcs. The lobe bifurcation configuration was supported by

Huang et al. [1987]. Using plasma and magnetic field data, *Huang et al.* [1987] showed that filamentary structures consisting of relatively dense and energetic plasmas frequently exist in the distant tail lobes. The authors suggested that these structures could be related to polar cap arcs. There are two difficulties with this explanation. Firstly, *Huang et al.* [1987] observed the filaments in the lobe at all levels of geomagnetic activity, while polar cap arcs could be usually seen only for relatively quiet geomagnetic conditions. Secondly, filaments are embedded in the tenuous cold plasma of the lobe, so it is expected that the arcs will be surrounded by plasma very distinct to the plasma inside the arcs. However, quite a few observations indicate that polar cap arcs are embedded in soft precipitation regions extending continuously from the oval [e.g., *Meng*, 1981; *Feldstein et al.*, 1995]. This led to speculations that perhaps the plasma sheet has different shape during occurrence of polar cap arcs.

Meng [1981] suggested that the arcs are actually a part of discrete arcs in the auroral oval. The authors report on conjugate widening of the auroral oval in both the northern and southern polar regions. It is hypothesised that this widening is a consequence of the thickening of the central plasma sheet. *Makita et al.* [1991] supported this hypothesis with auroral images and the corresponding particle observations. The authors proposed two plasma sheet configurations of the expanding plasma sheet: one is a simple tilting of the plasma sheet and the other is more complicated asymmetrically expanded plasma sheet.

5.2 Polar cap arcs observed on 1 December 2014

In this section we consider an event of auroral activity over RB observed on 1 December 2014. Multiple polar cap arcs were observed in the morning sector of the polar cap between $\sim$ 09 and 14 UT. The IMF B_z stayed positive (with few excursions to near-zero values) during this time interval (Figure 5.1), while the IMF B_y was negative most of the time.

5.2.1 Evolution of polar cap arcs and IMF conditions

At $\sim$7:40 UT the IMF B_z turned positive and remained positive for more than 6 hours. Between 7:40 and 8:46 UT only very weak auroral luminosity was seen by the RB camera. Aurora intensification began after $\sim$8:46 UT with diffuse aurora onset at the eastern edge of

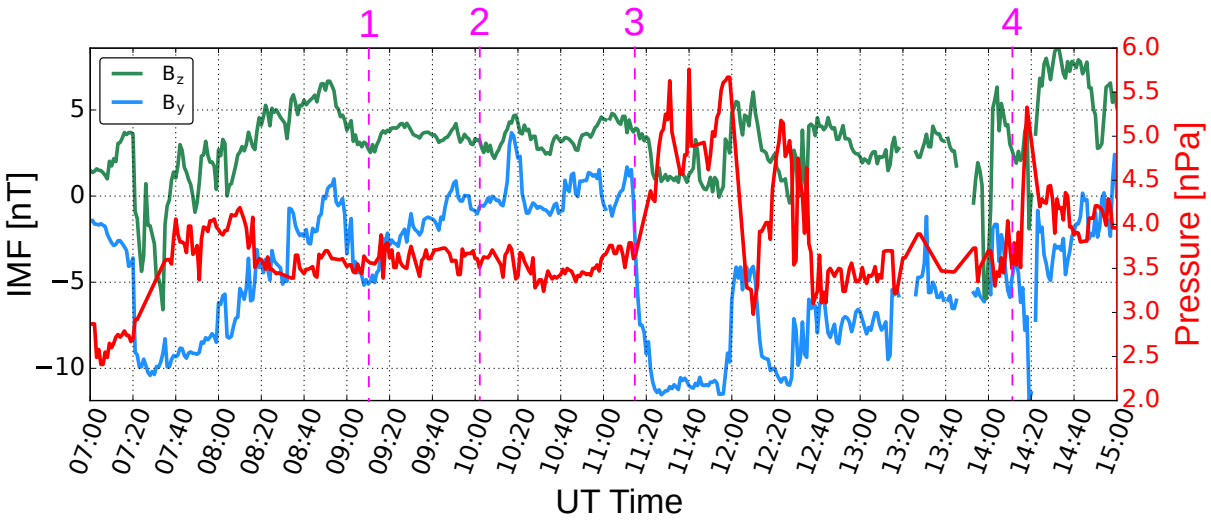

Figure 5.1: The IMF B_y (blue line) and B_z (green line) components in the GSM coordinate system and dynamic pressure (red line) according to the ACE satellite measurements on 1 December 2014 between 23:00 and 04:00 UT. Solar wind parameters were taken from the OMNI data set where the values were propagated to the bow shock location using the standard procedure. Pink vertical dashed lines indicate: 1 – occurrence of the first polar cap arc; 2 – formation of the first prominent sun-aligned arc; 3 – pressure pulse at the bow shock of the magnetosphere; 4 – the last polar cap arc vanished from the FoV of the RB camera.

the RB camera FoV (Figure 5.2a). At ∼9:10 UT, first polar cap arc appeared within the FoV of the RB all-sky camera (vertical dashed line "1" in Figure 5.1). It was a hook-shaped arc with its equatorward end connected to the morning auroral oval and the other end pointing toward the Sun (Figure 5.2b); the arc disappeared shortly after that. The first prominent sun-aligned arc over RB appeared at ∼10:12 UT (the time is marked by pink vertical line "2" in Figure 5.1). This single arc was stretched from the nightside to the dayside following very closely the auroral oval, but clearly separated from it as seen in Figure 5.2c. Note that onset of the arc has not been preceded by an IMF B_y sign change: there were only two very small and short excursions of the IMF B_y toward positive values during more than 3 hours before the arc occurrence. The arc moved slightly toward dawn and after some time multiple thin arc structures were observed over RB. This can be seen in Figure 5.2; the blue line in this figure shows trajectory of the DMSP F16 satellite which crossed the dayside portion of the polar cap at time of the observation. The data from the satellite will be discussed latter. At ∼11:14 UT dynamic pressure of the solar wind increased sharply (indicated by vertical line "3" in Figure 5.1); this was accompanied by decrease in the IMF B_y toward very low

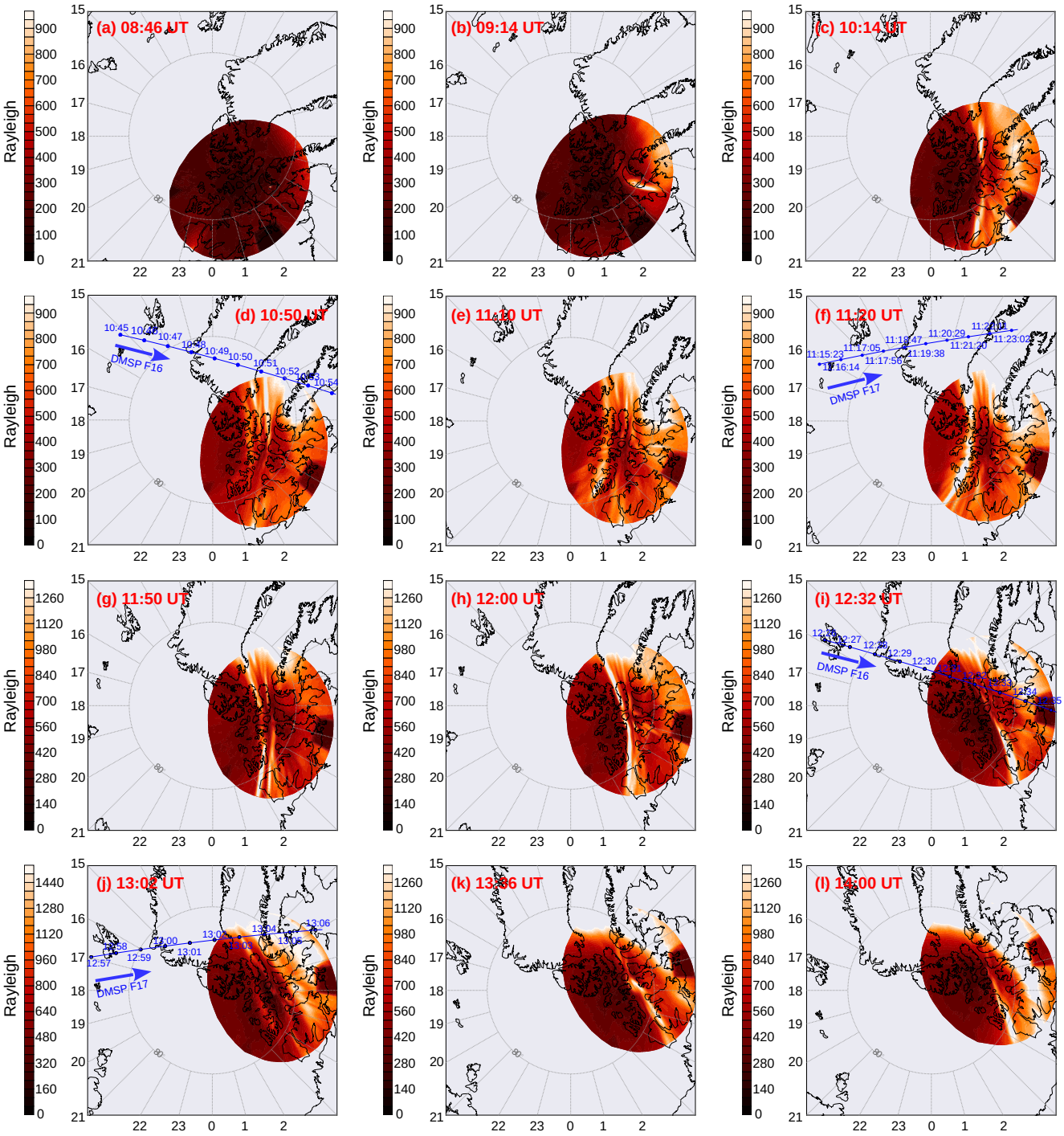

Figure 5.2: Sequence of auroral luminosity images recorded by the RB OMTI camera on 1 December 2014. The images show emission at 630 nm. The OMTI data (red) are mapped to 250-km altitude and shown in MLAT-MLT coordinate system. The circle dashed line corresponds to MLAT= 80°. A diffuse type of aurora on the dawn side of the images represents the auroral oval luminosity. Blue lines in panels d,f,i, and j represent trajectories of the DMSP satellites.

values (below -10 nT). About five minutes later, a transpolar arc over RB brightened suddenly (compare auroral images in Figures 5.2e and f). During this time, the arc moved rapidly equatorward, toward dawn, i.e. in the direction of the IMF B_y. Figure 5.2g shows a new location of the arc 30 min later. Appearance of a new arc, dawnward to the old one, can also be seen in Figure 5.2g.

Figures 5.2f–j show the arc motion in response to the negative IMF B_y: the dayside portion of the arc moved noticeably slower than its nightside part. Finally, at ∼13:10 UT the arc merged with the morning oval. At about 13:55 UT there was a brief excursion of the IMF B_z to negative values (< -5 nT) and approximately 15 minutes later the last polar cap arc faded away from the FoV of the RB all-sky camera (pink vertical line "4" in Figure 5.1).

5.2.2 DMSP observations of polar cap arcs

At ∼10:51 UT the DMSP F16 satellite flew very close to the FoV of the RB all-sky camera (Figure 5.2d). Multiple arcs were observed at this time over RB and it is expected that DMSP F16 crossed them during its pass over the polar cap. At ∼13:03 UT another DMSP satellite, F17, traversed a thin polar cap arc as can be seen in Figure 5.2j. The DMSP F16 and F17 satellites are equipped with SSJ5 spectromenters, which provide measurements of electron and ion fluxes in 19 energy channels from 30 eV to 30 keV (Chapter 2). Electron and ion spectrograms corresponding to the two DMSP crossings are shown in two top panels in Figure 5.3a (DMSP F16) and in Figure 5.3b (DMSP F17). The cross-track ion drift velocity (V) from the IDM instrument onboard DMSP satellites is shown in the middle panels of Figures 5.3a,b. Variations of plasma density measured with Langmuir probes along the satellites orbits at altitude of about 840 km are shown by blue lines in Figure 5.3. Finally, the SSM instrument flown on the DMSP satellites provides measurements of the magnetic field. The bottom panels in Figures 5.3a,b show variations of the magnetic field with the main component of the Earth's magnetic field (obtained from the IGRF model) subtracted from the measurements.

At ∼10:49:40 UT the DMSP F16 satellite entered a region where discrete bands of monoenergetic electron precipitations were observed (the regions are highlighted by semitransparent strips in Figure 5.3a). These regions correspond to the precipitations causing polar

cap arcs. Note that electron fluxes associated with these bands demonstrate different behavior to the precipitating electrons in the auroral oval or to the background electron fluxes inside the polar cap. Two broad regions of precipitating electrons between 10:44 UT and 10:47 UT and between 10:51 and 10:54 UT correspond to precipitations in the postnoon and prenoon auroral oval. Energies of electrons here reach 3 keV and enhanced fluxes observed for electrons with energies between several tens and several hundreds eV; the latter are seen as red lines in the spectrogram. In contrast, red regions inside bands of polar cap arc-associated electron precipitations increase along the satellite track from a few hundred eV to $\sim$ 1 keV, and then decline back to a few hundred eV. Electron precipitation events with such energy-time pattern are called inverted-V events [*Frank and Ackerson*, 1971]. The inverted-V events are associated with auroral arcs inside the auroral oval, primary in the nightside region [*Lin and Hoffman*, 1979]. The inverted-V electrons in the auroral oval, however, normally are much more energetic (several keV). It is believed that inverted-V electrons are accelerated by parallel electric field.

Another inverted-V event is seen in the electron spectrogram in Figure 5.3b at $\sim$13:03:25 UT, that is at the time when the DMSP F17 crossed a thin polar cap arc as seen in Figure 5.2j. However, not all the polar cap arcs are associated with inverted-V precipitating electrons. For example, from Figure 5.2j it is well seen that the DMSP F17 crossed an arc-like luminosity structure at 13:03:00 UT, this crossing is marked by a yellow semitransparent line in Figure 5.3b. A band of electron precipitation is collocating with the highlighted region, however, electron fluxes inside the band are evenly distributed for different energies. All the bands of electron precipitation associated with polar cap arcs are located poleward to the region of oval-associated ion precipitations and overall the polar cap is void of ion precipitations. However, there are enhanced fluxes of precipitating ions around the regions of the arc-associated electrons.

Location of auroral arcs is related to localized enhancements in the electron density of E and lower to middle F regions of the ionosphere [e.g., *Moen et al.*, 1998]. From Figure 5.3 it is seen that small plasma density enhancements co-located with polar cap arcs observed as high as 840 km.

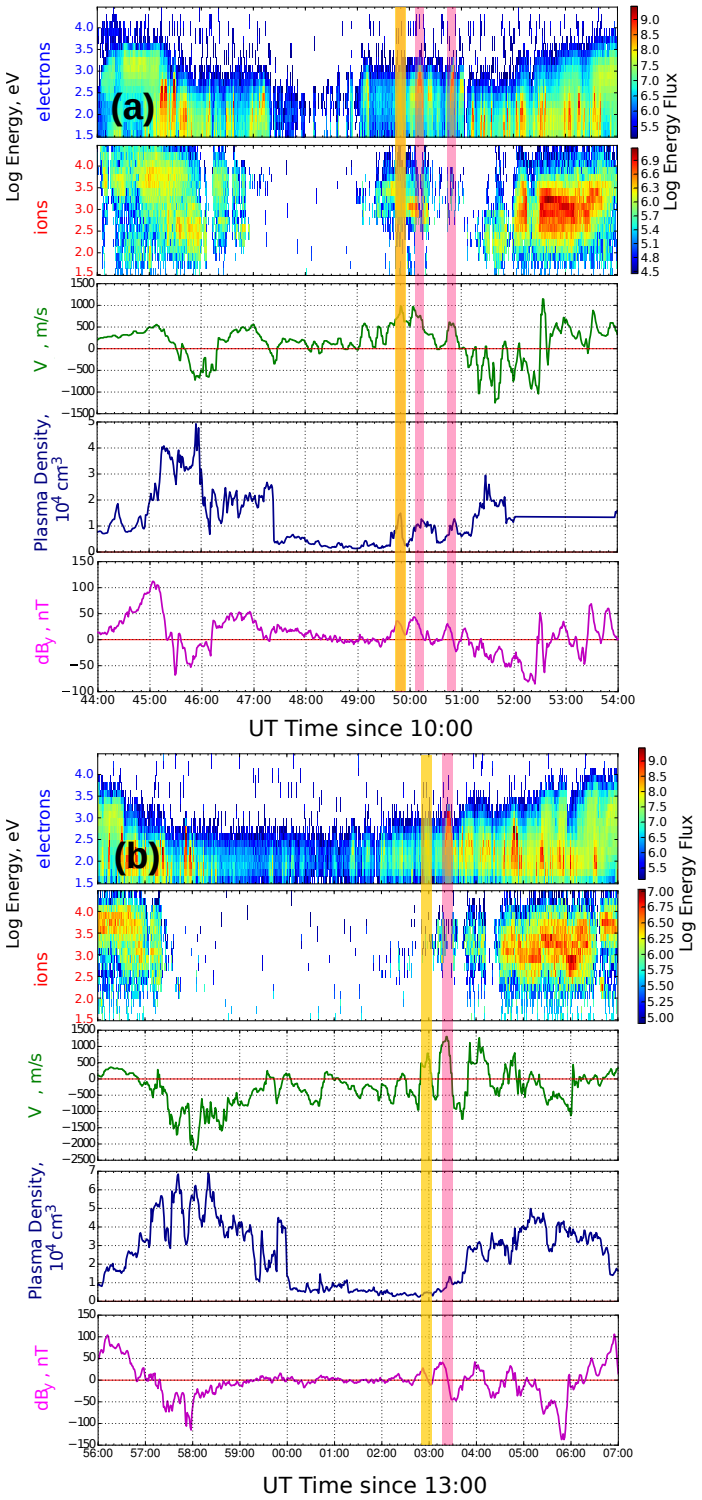

Figure 5.3: DMSP observations for the 1 December 2014 event. Figure (a) shows the observations during the F16 pass and Figure (b) shows observations during the F17 pass. Panels from top to bottom show precipitating electron spectrogram, precipitating ion spectrogram, horizontal cross-track velocity of ionospheric plasma flow, variations of plasma density and transverse magnetic field residuals. The semitransparent pink bands indicate locations of the inverted-V electron precipitations. The semitransparent yellow bands mark approximate extend of polar cap arcs not associated with the inverted-V precipitations.

To analyze magnetic field data, consider spacecraft-centered coordinate system where $+Z$ axis points vertically downward, $+X$ axis is along the satellite velocity vector and $+Y$ axis is perpendicular to $+X$ and $+Y$ in the sense of a right-hand coordinate system. Then applying Ampere's law to a satellite crossing perpendicularly an infinite FAC sheet,

$$j_{\parallel} = \frac{1}{\mu_0}\frac{\partial B_y}{\partial x}$$

where $j_{\parallel}$ is the current density along Z axis; for the polar cap region this approximately corresponds to FAC density. Downward FACs are along $+Z$ axis, thus a positive slope in plots of time variations of dB_y represents a downward FAC, while a negative slope represents an upward FAC. Therefore, Figure 5.3 indicates that polar cap arcs are co-located with an upward FACs and there are sheets of downward FACs on one or both sides of the arcs. Thus FACs associated with polar cap arcs are closed locally. The currents are small-scale. For example, it took about 10 s for the DMSP F17 to cross an upward polar cap arc-associated FAC highlighted by a pink band in Figure 5.3b. The speed of DMSP satellites is ~ 7.5 km/s, which means that spatial extend of the current sheet is about 75 km. The dB_y component decreased by about 90 nT across the extend of the upwards FAC, which gives an estimate of the current density of ~ 1 μA/m^2.

The variations of cross-track plasma flow velocity shown by green lines in Figure 5.3 indicate that there are enhancements of sunward convection within the polar cap arcs. Convection reversal is clearly seen on the equatorward boundary of the arc in Figure 5.3b. For the system of polar cap arcs in Figure 5.3a there is one convection reversal on the equatorward edge of the system. Several flow shears are observed here and convection between two separate bands of precipitation is significantly reduced.

5.2.3 SuperDARN observations of polar cap arcs

On the left panel of Figure 5.4 INV l-o-s velocities and DMSP cross-track velocities are shown. The flow reversal at the dawnward edge of the system of arcs is clearly seen in both DMSP and INV data. Another interesting feature is narrow bands of sunward flowing plasma at short radar ranges. The bands coincide very well with the arcs. Propagation conditions in

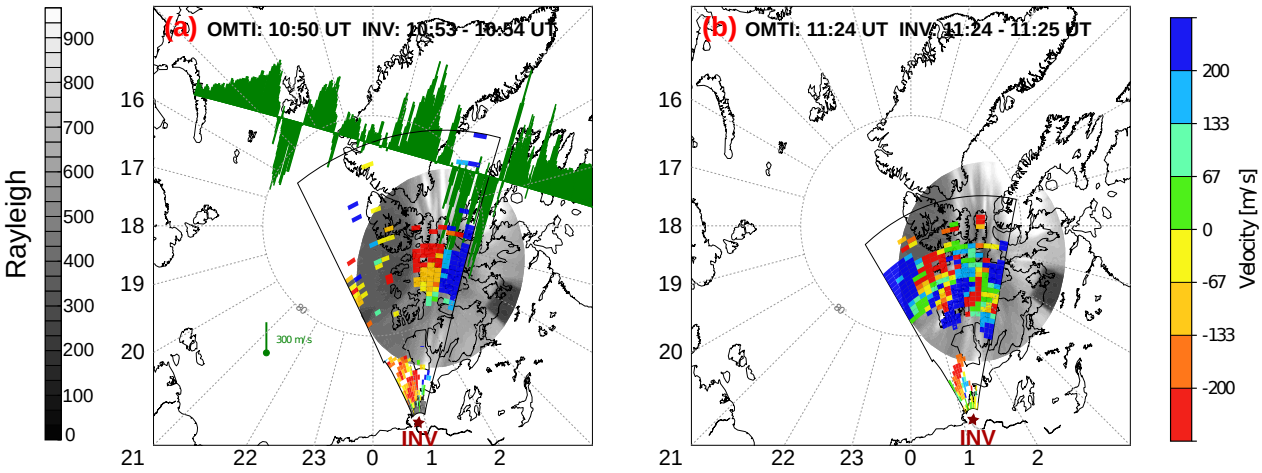

Figure 5.4: INV l-o-s velocities are shown in color superimposed on the OMTI luminosity images (black and white) showing emission at 630 nm for observations on 1 December 2014. Cross-track DMSP F16 velocities are plotted by green in panel (a). The panels are shown in MLAT-MLT coordinate system.

this region are generally not favorable for HF backscatter, however, increased densities inside an arc provide good conditions for backscatter so that we can monitor sunward flowing plasma within the arc. These radar observations are consistent with the DMSP observations which show enhanced sunward flows coinciding with the arcs. The right panel of Figure 5.4 is another example of INV l-o-s velocity map. Multiple reversals could be identified in SuperDARN data. Again, a thin band of a backscatter region aligned with the arc is seen at short ranges. The sunward flows co-locating with polar cap arcs are also seen at larger distances, but for these ranges SuperDARN resolution may be not sufficient to resolve plasma flow within thin arc structures. However, thin bands of sunward convection coinciding with polar cap arcs are consistently observed at short ranges where azimuthal resolution is better and no echo is expected from outside the arc location.

Figure 5.5 presents evolution of ionospheric convection associated with appearance of a polar cap arc on 1 December 2014. In panel (a) a background plasma convection over RB is shown for conditions before the first occurrence of the arc. Plasma flow within FoV of the RB OMTI camera poleward to the auroral oval is generally antisunward consistent with the standard two-cell convection pattern. However, several minutes before the appearance of the arc, a strong sunward flow is entering polar cap from the nightside auroral oval (Figure 5.5b). The sunward flows are very unusual in the nightside portion of polar cap. As was discussed

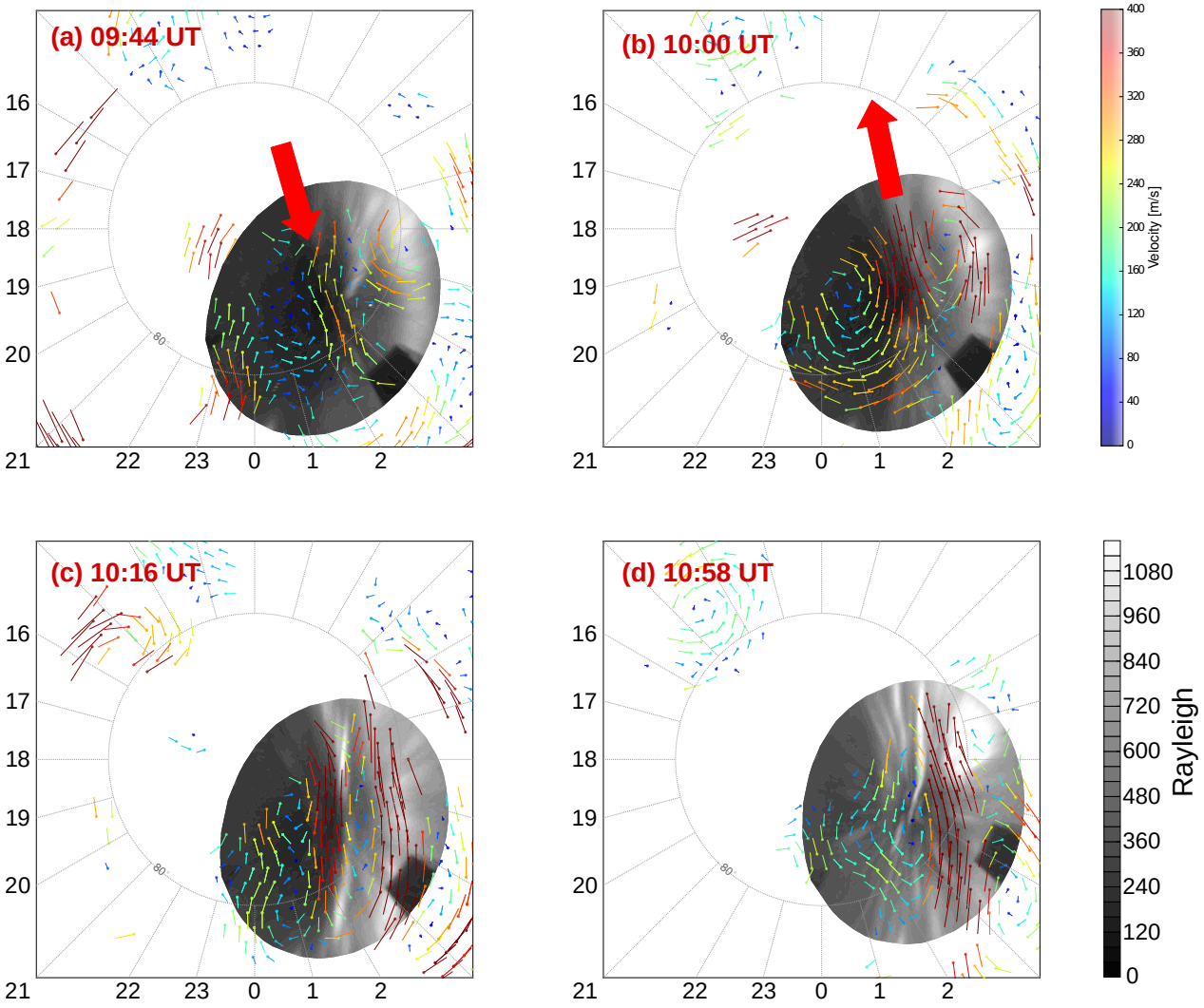

Figure 5.5: SuperDARN convection (shown by color vectors) superimposed on top of the OMTI images. Changes in convection associated with formation and evolution of a polar cap arc observed on 1 December 2014 are shown in panels (a)-(c): (a) convection before appearance of the arc; (b) sunward flow penetrating polar cap from the auroral oval; (c) appearance of the arc over RB; (d) convection around the arc after disappearance of the sunward flow.

in Chapter 4, sunward flows in polar cap for positive B_z conditions are associated with two small lobe convection cells which reside in the dayside portion of polar cap. In Figure 5.5c a prominent sun-aligned arc is formed over RB. The sunward flow is still present within the RB OMTI FoV, but it now has narrower spatial extent: it first reduces and then reverses at the equatorward edge of the arc. The sunward flow from the auroral oval finally vanishes and the convection around the sun-aligned arc becomes strongly antisunward on the equatorward

edge of the arc and weakly sunward on the poleward edge of the arc. This is typical convection pattern in the vicinity of polar cap arcs and it will be discussed in more detail in Section 5.3.

5.3 Polar cap arcs observed on 28 January 2014

In this section we consider an event of 27-28 January 2014 between 23 UT and 04 UT, respectively. This is an extended period with positive IMF B_z and B_y, Figure 5.6. Optical activity poleward of the auroral oval with several polar cap arc intensifications was seen almost during the entire interval, Figure 5.7.

5.3.1 IMF conditions and evolution of polar cap arcs

The RB all-sky camera started observations at ∼23:00 UT. Diffuse and weak luminosity in the postnoon auroral oval was seen at magnetic latitudes close to 80°. Two faint, diffuse arc-like features near the RB zenith (83°) were seen. At ∼23:30 UT, the polar cap arc-like feature closest to the oval brightened and then moved toward magnetic pole eventually "detaching" from the auroral oval luminosity band, Figure 5.7(a). It was stretched in the East-West direction of the camera FoV, but in the MLAT-MLT coordinates, it was oriented toward the Sun, Figure 5.7a,b so that the arc can be classified as a sun-aligned arc. This is the type of arcs that was observed during the entire event considered. This particular arc lasted for about 20 min ending up with as a very weak band of luminosity. The arc onset was, very likely, a response to relatively fast changes in the B_y and B_z components of the IMF that started at ∼23:20 UT, Figure 5.6. We note that the IMF records in Figure 5.6 are given for the location of the bow shock. It is expected that several more minutes (up to 6–8) are needed for a disturbance to reach the high-latitude ionosphere [e.g., *Jackel et al.*, 2012].

After about 30 min of relatively weak auroral luminosity, with 2–3 weak bands visible off the auroral oval, the oval started to intensify at 00:30 UT. In the following 10 min, the bright luminosity spot within the oval expanded toward dusk along the oval and 2 detached sun-aligned arcs appeared, Figure 5.7c. No obvious IMF changes were observed in association with these arcs onset in Figure 5.6. The arcs weakened by 01:00 UT and were seen as such up to about 01:50 UT, Figure 5.7d. During these ∼ 50 min some luminosity intensifications

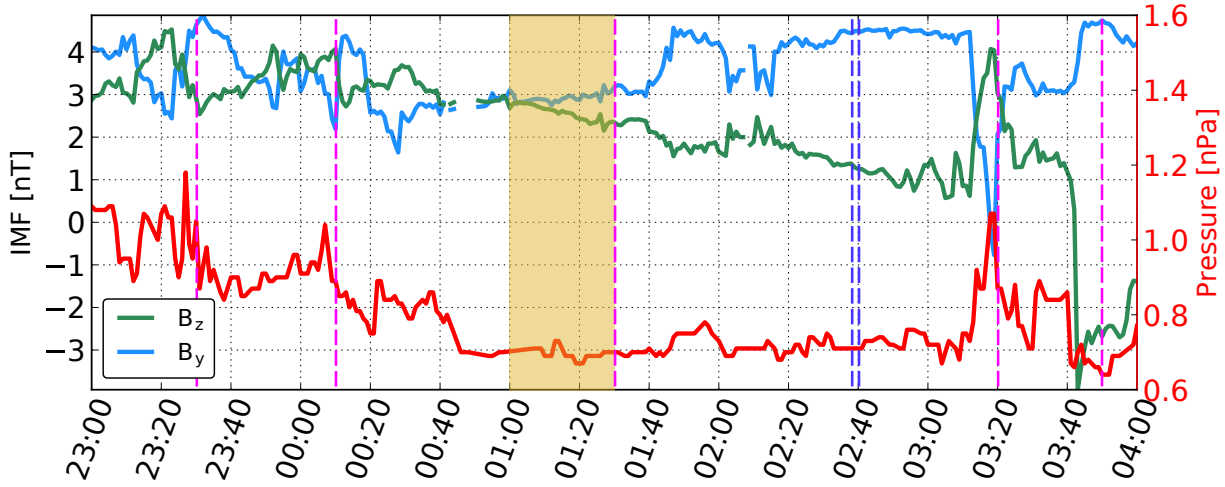

Figure 5.6: The IMF B_y (blue line) and B_z (green line) components in the GSM coordinate system and dynamic plasma flow pressure (red line) acquired from to the ACE satellite on 27-28 January 2014 between 23:00 and 04:00 UT. The Solar wind parameters were taken from the OMNI data set where the values were propagated to the bow shock location using the standard procedure. Semitransparent box corresponds to the period during which stable weak arc-like structures were observed over RB. Pink vertical dashed lines indicate moments of arcs intensifications, blue dashed lines – moments when Swarm satellites crossed a polar cap arc.

were seen within the oval but these activations were not matched with any changes in the weak arc's luminosity. At 01:30 UT, one of the arcs intensified. This intensification is very likely related to the IMF B_y upward transition, Figure 5.6. During the following hour, the arc varied in intensity and moved slightly around the RB zenith. In Figure 5.7e, an image of this arc is presented. At 02:08 UT and 02:16 UT two luminosity pulses progressed along the arc in antisunward direction. These pulses correlate with sharp B_y upward transitions, Figure 5.6. The arc weakened by 02:20 UT. By ∼03:00 UT, both the oval and the arc luminosity were subvisual.

Later on, an interesting event occurred starting from ∼03:20 UT when a very weak arc appeared in the eastern part of the camera FoV. Over the next 30 min, the arc moved toward dusk, Figure 5.7h,i, arrows. Onset of this arc correlates with a sharp downward transition of the IMF B_y to ~ 0 nT, and upward transition of the IMF B_z to $\sim +4$ nT. At the same time, a solar wind pressure increase is seen in Figure 5.6. All of these changes correlate with the arc onset. We stress that arc's motion was toward the dusk while a number of short-distance

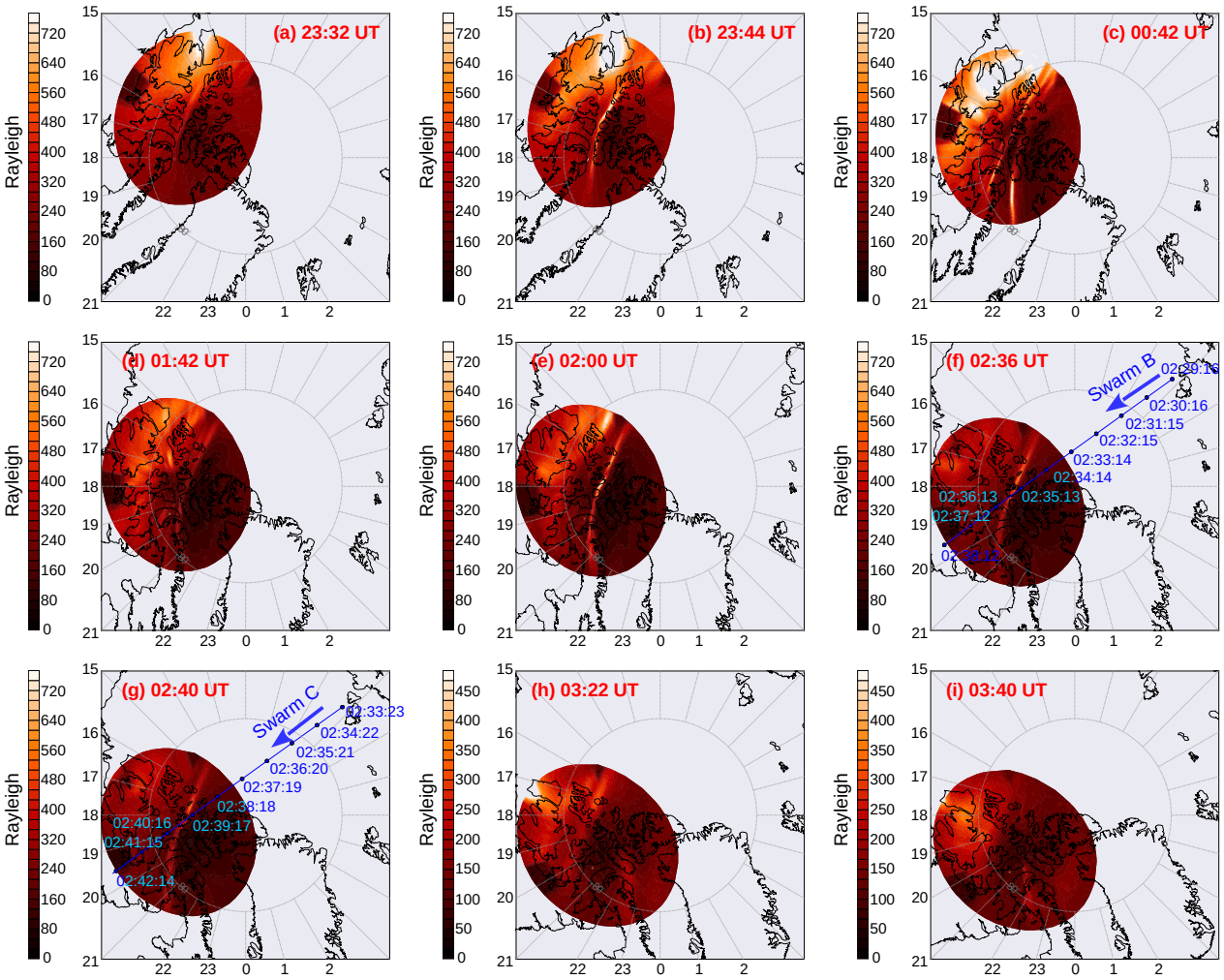

Figure 5.7: Sequence of auroral luminosity images recorded by the RB OMTI camera on 27–28 January 2014. The OMTI 630 nm emission (red) is mapped to 250 km and shown in a MLAT-MLT coordinate system. The circle dashed line corresponds to MLAT= 80°. A diffuse type of aurora on the dusk side of images represents the auroral oval luminosity. Narrow strips of luminosity located closer to the Pole (detached from the auroral oval bands) are polar cap arcs. Blue lines in panels (f) and (g) show trajectories of Swarm B and Swarm C.

displacements of the arcs during previous periods (mentioned earlier) were rather toward dawn/Pole.

The above description indicates that major changes in the luminosity pattern, such as brightening of an arc, seem to correlate with some quick and significant changes of the IMF B_z or B_y. Interestingly, the B_y transitions at 00:10 UT, Figure 5.6, correlates with the onset of additional arc while negative B_y transition at 02:20 UT is accompanied by a decline in

the luminosity intensity. However, no optical intensification was observed at 03:40 UT for a quick upward IMF B_y transition. Perhaps, this is due to the fact that the IMF B_z was negative at this time.

Auroral intensifications in the postnoon aurora have been known for quite some time [e.g., *Sandholt and Lockwood*, 1990; *Kozlovsky et al.*, 2002]. Our observations show that there is a great deal of relationship between intensification of the sun-aligned arcs at the poleward edge of the auroral oval and changes in the IMF.

5.3.2 Plasma flow velocity around polar cap arcs, l-o-s velocity

The PolarDARN radars data are extensive for this event but echoes mostly cover the latitudes of the auroral oval luminosity and its poleward boundary. Here we present some data illustrating salient features of the plasma flows around the arcs.

Figures 5.8a,b are velocity maps according to INV and CLY observations around 23:43 UT when a clear sun-aligned arc was located in the RB zenith, Figure 5.7b. One obvious feature of Figure 5.8a is a channel of sunward flow (blue channel) clearly correlating with the arc. CLY data, Figure 5.8b, are more complicated but the channel with sunward flow is well seen here as a red-colored bar in central beams. The data show presence of a second channel of sun-aligned flow located dawnward from the first one. This channel is located at the poleward edge of the auroral oval luminosity. No INV data are available for this region. Figures 5.8c,d are velocity maps according to INV and CLY observations around 00:40 UT when a double-arc structure was seen near the RB zenith, Figure 5.7c. Here INV shows a channel with antisunward flow (red stripe) at the equatorial edge of the more duskward arc 1 and sunward flows around the dawnward arc 2 so that there is a velocity shear close to arc 1. CLY shows a channel of sunward flow in a region between the arcs, presumably at the equatorward edge of the duskward arc 2. We will not discuss PolarDARN data with respect to the moment 01:40 and 02:00 UT because the flow features are very similar to those observed around 02:40 UT. Observations at that time will be discussed in the next section where the radar data are supported by high-resolution measurements on the Swarm satellites, Figures 5.7f,g.

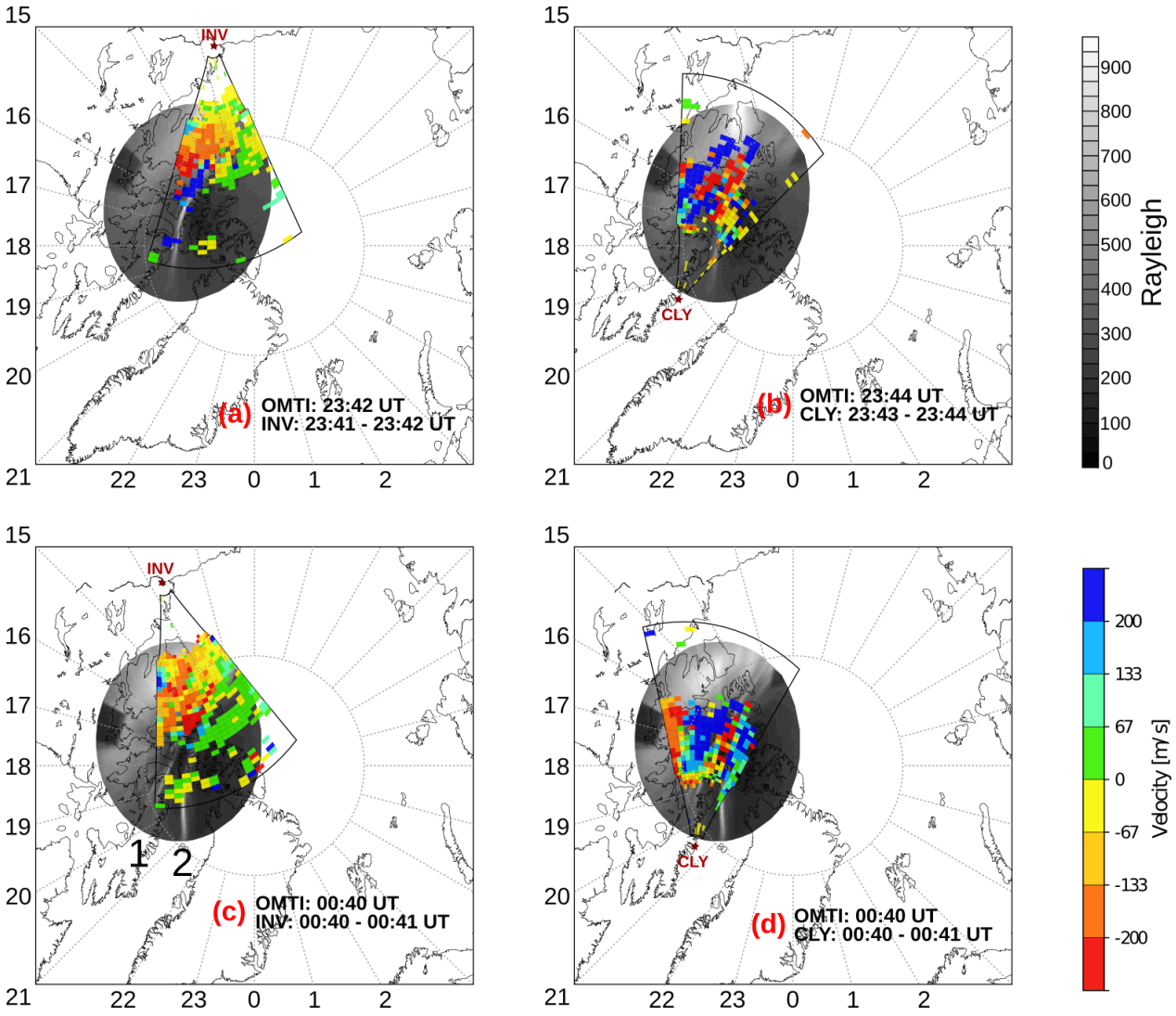

Figure 5.8: INV (panels (a) and (c)) and CLY (panels (b) and (d)) l-o-s velocity maps overlaid on top of optical luminosity images for 3 specific moments of sun-aligned arc occurrence shown in Figure 5.8, 23:40 UT on 27 January 2014 and 00:40 UT on 28 January 2014. Mapping is done in MLAT-MLT coordinates.

5.3.3 Arc-related plasma flows according to the Swarm satellite measurements

Of special interest are radar observations of polar cap arc at around 2:40 UT because at this time, two Swarm satellites, B and C, crossed the observational area as shown in Figure 5.9. Here the blue lines represent the trajectories of the Swarm B and C satellites as they cross polar cap.

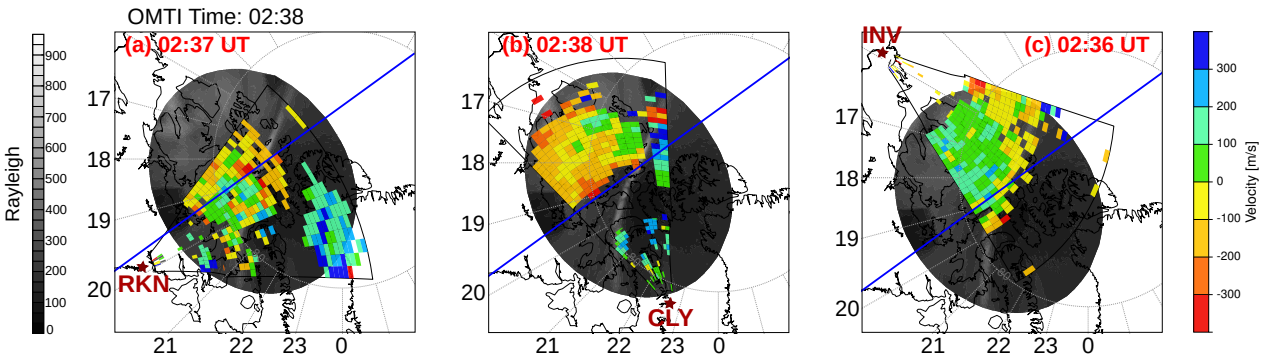

Figure 5.9: (a) RKN, (b) CLY and (c) INV l-o-s velocity maps overlaid on top of the OMTI luminosity images (black and white) for observations around 02:38 UT. The Swarm C trajectory is superimposed as a straight blue line. The data are shown in MLAT-MLT coordinate system.

Figure 5.9 shows that echo coverage was good for RKN, reasonable for INV and rather poor for CLY. CLY shows echoes at short ranges in low number beams 0–5. The l-o-s velocity is positive here implying antisunward flow on the dawn-side of the arc. CLY l-o-s velocity at far ranges and high number beams 14–15 is also positive on the dawnside, but mostly positive on the arc's dusk side implying sunward flow on that side of the arc. INV velocities are negative at farthest ranges and positive at intermediate ranges corresponding again to an antisunward flow on the dawnside and sunward flow on duskside. The RKN data are confusing, although on average, the velocities are negative on the dusk side and positive on the dawn side. One can interpret the radar data as indicative that the flow is mostly antisunward on the arc's dawn side and sunward on the arc's dusk side. This would mean a converging type of electric field distribution with the electric field pointing toward the arc on both its sides.

Figure 5.10a presents electron density data as measured by the satellites B (green) and C (blue) plotted against time but with a shift of about 4 min for C satellite (note different horizontal axis). Both satellites observed decline of the electron density by a factor of 2 in the arcs' close vicinity on its dawnside. The density depletion was observed for about 30 s of the satellite flight. Because the arc was oriented at an angle, roughly to speak, of 30 degrees

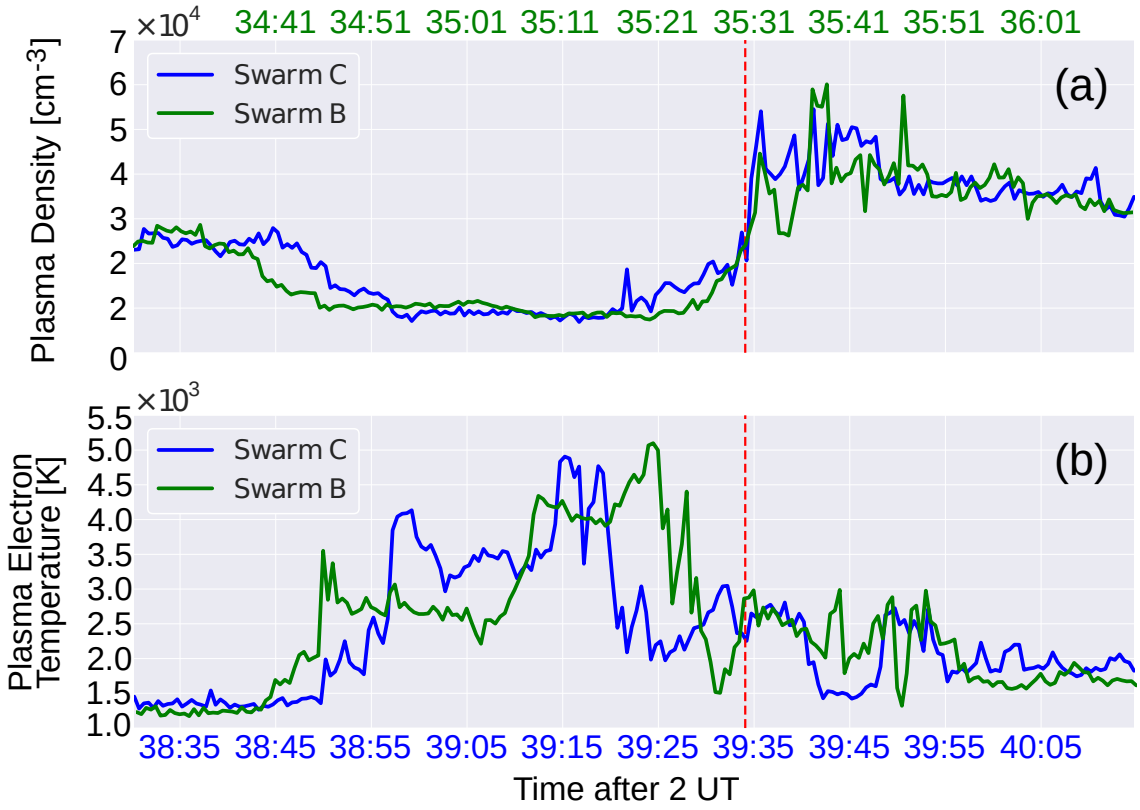

Figure 5.10: Swarm data for the 2 passes over RB on 28 January 2014. The Swarm C data (pass 1) are shown by a blue line while Swarm B data (pass 2) are shown by a green line. Vertical red dashed line is roughly the time of satellite arrival to the arc edge on the dawn side. (a) Electron density. (b) Electron temperature.

to the satellite track, we estimate that the density depletion is about 100 km in width in the direction across the arc. The maximum measured density inside the arcs was about the same for the 2 passes. However, the density distributions inside the arc are not the same. Both satellites detected a sharp density enhancement, very likely representing the dawnside edge of the arc. Later on, after a short-lived density dip, the density was enhanced again while showing irregular variations lasted for about 10 s ($\sim$ 75 km along the track, about 35 km across the arc). During this time, the satellites were crossing the arcs' body and strong density variations reflect the filament structure of the arc.

Figure 5.10b shows that significant local enhancements of the electron temperature occurred in the region with the depleted electron density on the arc's dawnside. This points at presence of strong electric fields here, significant Joule heating of the ionospheric E-region

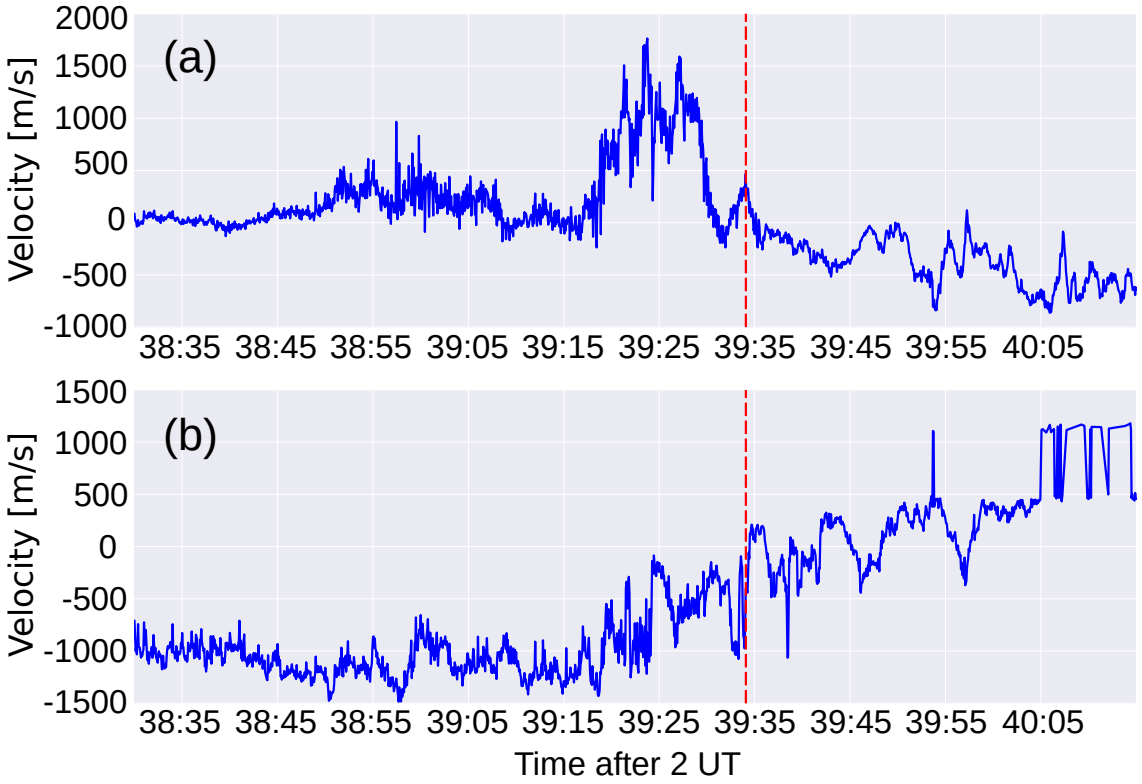

Figure 5.11: Swarm plasma drift data for the Swarm C satellite pass over RB on 28 January 2014. Panel (a) shows the cross-track component (positive velocity values are for an eastward flow) and (b) for along-the-track component (positive velocity values are for a northward flow). Vertical red dashed line is roughly the time of satellite arrival to the arc edge on the dawn side.

plasma and heat transfer to the topside ionosphere. The data on the electric field/plasma flow shown in Figure 5.11 confirm this expectation although the temperature enhancements are seen in a spatially broader region than spatial extent of the local electric field enhancement near the arc. Note that Swarm B, while crossing the arc at earlier time, detected temperature enhancements in a broader spatial region than Swarm C. Visually, the arc was somewhat more intense during the Swarm B crossing and this might be a reason for the differences. The temperature was, overall, decreased inside the arc, as the satellites were kept flying along the arc at later time. Figure 5.11 shows plasma flow velocity data as the Swarm C satellite crossed the arc. We do not present the Swarm B data because they are very noisy and we judge them as unreliable (This was confirmed by Prof. D. Knudsen, the Principal Investigator of the instrument). The vertical red line is the dawnward location of the arc, as

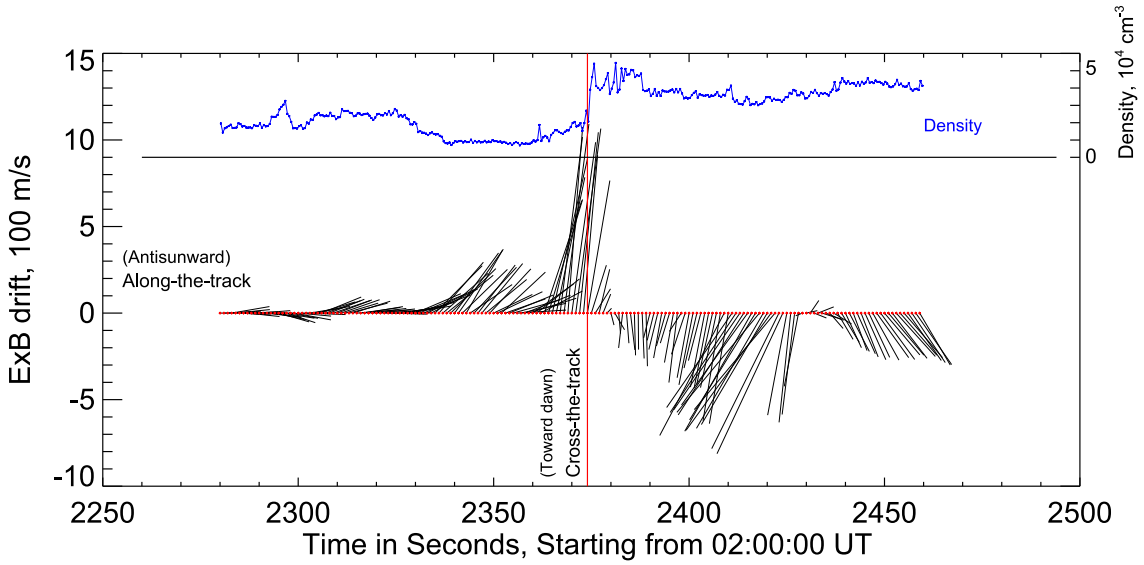

Figure 5.12: Swarm electron density (blue line) and 2-D plasma flow vectors ($\mathbf{E} \times \mathbf{B}$ drift, black line) according to Swarm C satellite measurements on 28 January 2014.

inferred from the electron density data (Figure 5.11a). The most striking feature of the data is a sharp enhancement of the velocity component perpendicular to the track, from ∼100–200 m/s away from the arc to ∼1000 m/s close to the arc. Spatially, this component is directed roughly toward early morning hours, Figures 5.7e,f. Along-the-track flow component, is fairly large at locations away from the arc, 1000 m/s, but decreased to ∼500 m/s close to the arc. As the satellite travelled inside the arc, both components decreased and along the track component showed significant variations. Figure 5.12 shows the 2-D plasma flow velocity vectors inferred by averaging the raw data of Figure 5.11 over 1-s intervals. In the immediate vicinity of the arc, on its dawn side, the velocity vectors are mostly perpendicular to the satellite track direction which corresponds to the antisunward flow in the polar cap, roughly along the 18-03 MLT line. On the dusk side of the arc, the flow is in opposite direction, and much weaker. The data indicate that the flow changes the direction within the arc thickness which we associated with a bump of enhanced electron density observed between time 2370 and 2390 s (after 02:00:00 UT). This is somewhat different from what we reported in Section 5.2.2 where the reverse in the direction of the flow was seen outside of the arc. On the other hand, observed sheared flow reminds very much the situation with the evening auroral zone arcs where the flow is significantly enhanced at the equatorward edge

of an arc [*Aikio et al.*, 1993; *Aikio et al.*, 2002]. Variations of the velocity components in Figures 5.11,5.12 within the arc reflect microstructure of the flows with filaments of 10–20 km size (5 s of flight corresponds to ∼35 km in space). Judging by length of vectors in Figure 5.12, one can conclude that the flow velocity magnitude inside the arc is decreased by a factor of 5–10.

5.3.4 Impact of polar cap arcs on global-scale plasma flow pattern

The sheared plasma flows around polar cap arcs, as shown in Figure 5.12, indicate that the arc itself would modify the global-scale convection pattern. The radar data are not suitable for discussion of small-scale features of flows around the arc. This is because of rather coarse spatial resolution of measurements, 45-km range resolution and ∼100 km resolution in the azimuthal direction due to radar beam width. However, the data can tell us about large-scale features of the convection pattern. Previous SD observations indicated that a polar cap arc is often a special feature in the overall pattern [*Koustov et al.*, 2008]. Here we demonstrate the impact of the arc onset for one period of arc intensification and motion.

A pattern in Figure 5.13a is the dawnside cell of a two-celled circulation with antisunward flow on the dawnside and return sunward flow on the dusk side. Shown by pink dots is the approximate location of the convection reversal boundary (CRB). It is located at latitudes $78^\circ - 80^\circ$, depending on the MLT sector. The CRB correlates well with the bright luminosity (strong particle precipitation) within the auroral oval. At this time, there are 2 weak polar cap arcs immersed within the antisunward flow and related to them convection flows are over-powered by the background flows. Figure 5.13b shows plasma flow pattern when the arc detached from the oval and was on a dawnward move. At this time, the arc is within a broad region of sunward flow. Figure 5.13c shows plasma flow pattern about 1 hour later when the oval luminosity decreased in intensity and the arc clearly detached from the oval. Here the flow is toward the Sun at all latitudes equatorward of the arc. Several vectors at 19–20 MLT show that the flow is in antisunward direction on the duskward side of the arc. Thus, at this time the arc is co-locating with the large-scale convection reversal boundary. The data thus show initial distortions of the overall convection pattern and setting up a new location for the CRB.

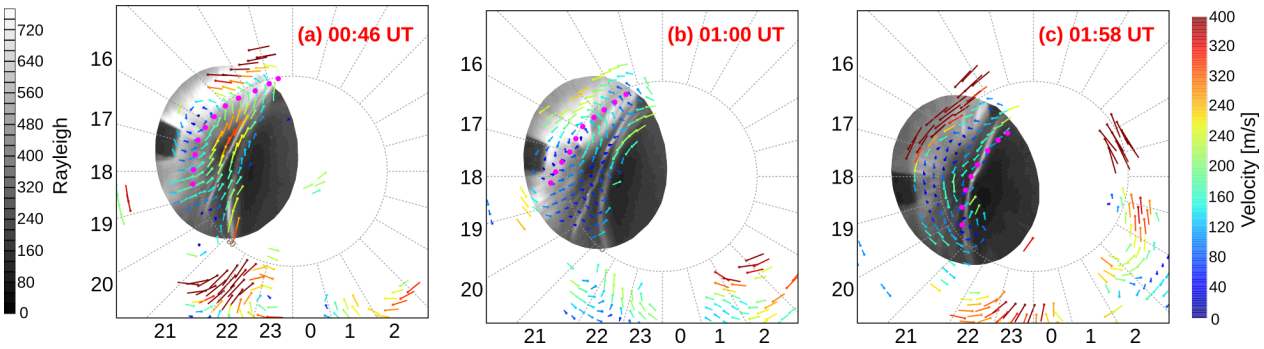

Figure 5.13: SuperDARN convection maps are superimposed on top of auroral images (black and white) for measurements at (a) 00:46 UT, (b) 01:00 UT and (c) 01:58 UT.

5.4 Decameter irregularities and HF echoes in the polar cap

Previous sections of this Chapter showed usefulness of SuperDARN/PolarDARN radar data for studying plasma flows in the vicinity of the polar cap arcs. However, for many other events, the radar coverage is not as good as in the examples considered so that the SuperDARN radars are less effective. A natural question is why the echo coverage is limited. There is a more general question as to what extent the SuperDARN radars are capable of detecting irregularities in a specific ionospheric spot. In this section we discuss this issue.

5.4.1 Echo occurrence around polar cap patches

Polar cap patches regularly crossing the polar cap in antisunward direction is a classical example of a situation where the GDI is expected to operate producing irregularities in a broad range of scales, and HF echo detection from patches is highly expected. Moreover, the expectation is very definite: preferential conditions for the GDI are on the trailing edge of the patches plasma [e.g., *Tsunoda*, 1988].

Although the SuperDARN radars have always been expected to detect echoes from polar cap patches, investigation of specific events has been very limited so far. One of the problems is identification of the patches by an independent instrument. In this section we give one example of SuperDARN echo detection in conjunction with polar cap patches which were

detected by one of the Swarm satellites, following *Spicher et al.* [2015].

We consider here one of the 14 Swarm satellites polar cap crossings on 29 December 2013. Figure 5.14a shows the footprints of Swarm A trajectory within the RKN radar FoV. The data are presented in magnetic latitude (MLAT) and magnetic local time coordinates. The satellites flight path is shown as a green dashed line over the color-coded map of the radar power observed at 17:57–17:58 UT. Poleward of a broad region of high backscatter power at the near ranges, the radar detected two regions of enhanced power (marked by two red arrows in Figure 5.14a). Subsequent SuperDARN maps show that these structures moved poleward, along the direction of plasma flow shown by blue vectors.

As the Swarm A satellite crossed these regions of strong echo power, they observed two plasma density enhancements with density up to 8 times larger than the background level inside the polar cap. These enhancements are marked by a horizontal blue line in Figure 5.14b. The second plasma density enhancement is of particular interest because it has distinguishable leading and trailing edges encountered by Swarm A between $\sim 84.1^\circ$ MLAT and $\sim 86.5^\circ$ MLAT and between 17:56:47 UT and 17:57:32 UT in time. While the leading edge was very sharp, the trailing side was significantly structured. The latter was collocated with strong backscatter power of the RKN PolarDARN radar (see Figure 5.14a). *Spicher et al.* [2015] confirmed that the GDI growth rate is indeed positive at the trailing edge of the patch in this specific event by estimating the values of the density gradient and $\mathbf{E} \times \mathbf{B}$ drift. Generation of decameter-scale irregularities (detectable by HF radars) is highly expected as well. In this case, the background propagation conditions for HF radio waves were very favorable and monitoring of the patch with the RKN radar was successful.

This example along with computer modeling of the GDI by *Gondarenko and Guzdar* [2004] and *in-situ* observations by *Basu et al.* [1994] strongly support the notion that the electron density fluctuations are more intense at the trailing edges of the moving polar cap electron density patches. We note that generally the RKN radar detects blobs of enhanced power moving toward the radar quite regularly in the midnight sector. This is consistent with expected motion of polar cap patches in antisunward direction. These are very likely the polar cap patches but whether this is true requires additional investigation in each specific case.

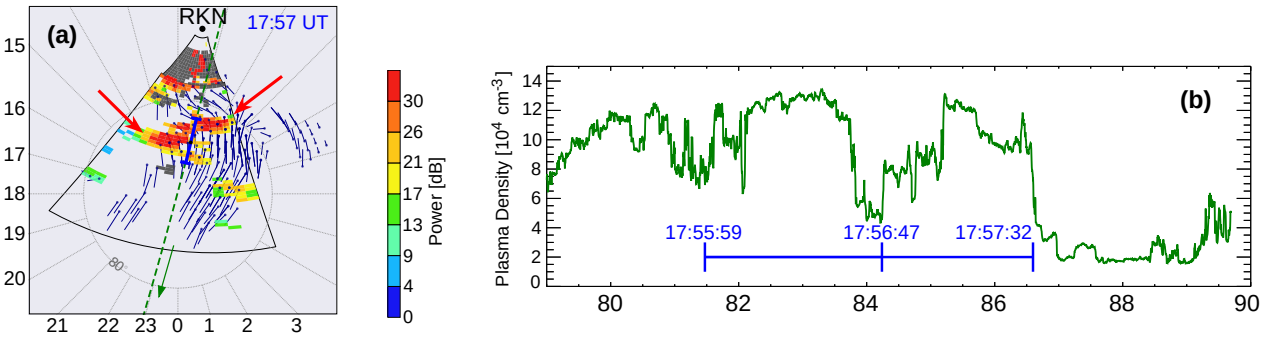

Figure 5.14: (a) Spatial distribution of the Rankin Inlet SuperDARN radar echo power for 1-min scan started at 17:57 UT. Close to this time, the Swarm A satellite travelled across the radar field of view. The satellite trajectory footprints are shown by a green dashed line and the direction of motion is represented by green arrow. The blue portion identifies the patch region recorded onboard of the satellite. Red arrows indicate the position of two regions of enhanced backscatter power. (b) Plasma density as measured by Swarm A. The extent of density enhancements in latitude is shown by a blue bar.

5.4.2 Expected echo power around polar cap arcs

Another type of plasma density enhancement in the polar cap are arcs produced by electron precipitations. One can think that a polar cap arc onset would dramatically improve the chances to get echoes with an HF radar because of improvement in propagation conditions. This is, unfortunately, not the case. The fact is that although the electron density inside polar cap arcs is enhanced, the increase is not very strong, as measured by ISRs [e.g., *Gallaher*, 1997]. In addition, the arc is a relatively narrow structure, see Section 5.2.2. Because the SuparDARN radar scattering volume is $\sim$ 45 km $\times$ 100 km, enhanced density in a fraction of the scattering volume might not be sufficient to detect echo, especially if the ionospheric irregularities present only at the arcs edges, where the background density is not strong. Echo detection is especially difficult at relatively short ranges where stronger refraction is needed to achieve orthogonality. On the other hand, tilts of the ionospheric layer in the arc vicinity might improve the propagation conditions at ranges close to the arc [*Uspensky et al.*, 1993], but low overall background density might not allow for this factor to be effective. For the auroral zone arcs, this effect seems to work [*Séran et al.*, 2009; *Uspensky et al.*, 2000].

In terms of the GDI excitation, there is a preferential side of the arc where HF echoes are expected [*Lamarche and Makarevich*, 2016; *Koustov et al.*, 2012]. Typically, the arc-

associated plasma drifts are superimposed on a generally antisunward background flow with some duskward component. If the arcs are of a converging type [*Marklund*, 1984], the arc-associated flows are away from the sun on the arcs dawn side and toward the sun on its dusk side. This implies that excitation of the GDI is favourable on the dawn side of the arc where the plasma drift and electron density gradient are oriented in the same direction, toward dusk.

Lamarche and Makarevich [2016] analyzed in detail the growth rate of the GDI for perturbations propagation along various directions with respect to arc-like structure and for various directions of the background ExB flow. General conclusion was that the GDI growth rate is largest at the trailing side of the arc. The domination is particularly strong for perturbations propagating along the arc-like structure.

5.4.3 Typical locations of HF echoes around polar cap arcs, case of 24 January 2014

As an example of a typical HF echo distribution around polar cap arcs, we consider an event on 24 January 2014. In this event, a duskward-moving arc (velocity of $\sim$ 300 m/s) was observed within the RB OMTI camera in the morning sector. The arc existed for about 1 hour. The direction of motion was consistent with the positive IMF B_y component. The arc appeared on images right after the IMF B_y started a quick transition to smaller B_y (up to $B_y = 0$). The brightness of the arc varied. The plot of Figure 5.15 gives an example of the arc for one such intensifications. Clearly, the arc is detached from the auroral oval and stretched toward noon (sun-aligned arc) slightly off the $\sim$ 02 MLT line.

All three PolarDARN radars detected echoes in this event but with different coverage. Both INV and CLY see echoes duskward of the arc, Figure 5.15a,c. The echoing region is much farther away from the arc for CLY so that here one can hardly relate the patch with the arc presence; echoes existed here prior to arc onset. Importantly for the CLY radar, there is clearly visible aurora (and thus precipitations) at short radar ranges; these precipitations could have provided significant electron density enhancement and bending of HF radio waves to orthogonality so that the echoes dawnward of the arc would be detected. No echoes,

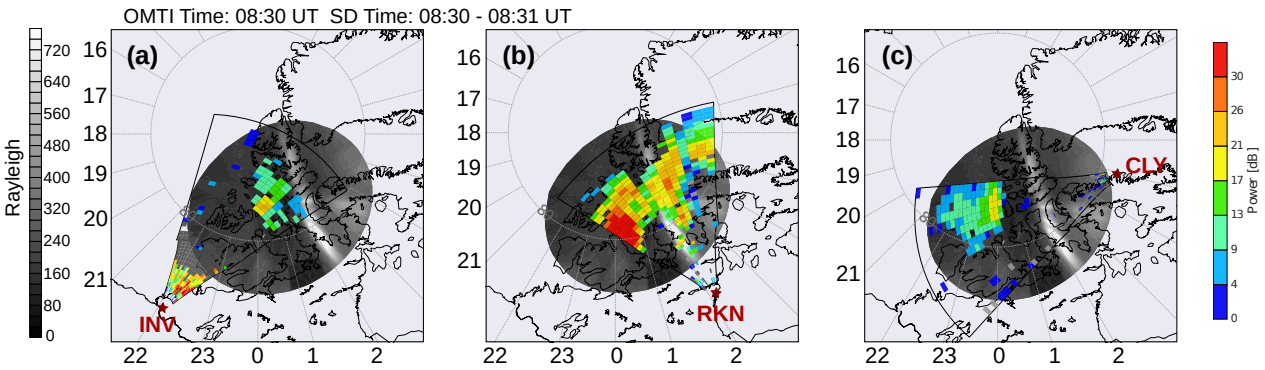

Figure 5.15: Concurrent optical data from the RB OMTI (grayscale) and PolarDARN radar data collected on 24 January 2014 at $\sim$ 0830 UT. HF radar echo power observed over azimuthal scan was overlaid on top of the auroral image. Panels (a), (b) and (c) are for INV, RKN and CLY observations, respectively. The panels are in a MLAT-MLT coordinate system.

however, are seen. One possible explanation is a relatively low electron density (dark region) very close to the arc so that radar wave bending was not sufficient for CLY. The INV radar also sees echoes with comparable coverage but from somewhat spatially-different region as compared to that of the CLY echoing region, compare Figures 5.15 a and c. The echo ranges are comparable ($\sim 1200 - 1300$ km), consistent with expected comparable densities in the observational areas (no aurora there). The beam directions do not differ much; moreover, CLY beam 5 almost coincides with beam 15 of INV (see Figure 2 in *Ghezelbash et al.* [2014]). However, the radars detect echoes in quite different directions. The CLY-INV data thus indicate that propagation conditions were somewhat different for these two radars. We note that according to ray tracings (reported in *Koustov et al.* [2014]) one would expect the echo detection for density $\sim 1.8 \times 10^5\,\mathrm{cm}^{-3}$ and $\sim 1.3 \times 10^5\,\mathrm{cm}^{-3}$ for RKN and INV at 12 and 10 MHz, respectively.

Contrary to CLY and INV, the RKN radar detects echoes in all beams. By looking at the pattern of spatial power variations, one can identify a region with enhanced power, stretched along the optical arc. It is in a wake of the moving arc and corresponds to that side of the arc where preferential GDI generation is highly expected. Indeed, the RKN l-o-s velocity was positive on the dawnside of the arc and negative on the duskside of the arc (data are not shown here). The INV l-o-s velocity was positive so that the resultant (combining/merging the RKN and INV velocities) vector was toward midnight with a dusk component so that

the flow velocity had significant component along the gradient of the electron density at the arcs dawn side. Similar examples of enhanced HF echoes in a wake of moving arcs have been reported by *Koustov et al.* [2012]. Although the RKN data indicate the irregularities presence at the dawnward side of the arc, no echoes were seen from here by the CLY and INV radars, signifying poor propagation conditions for these radars. We comment that the RKN echoes were coming from the duskside of the arc as well but they were much weaker than those coming from the dawnside of the arc. We believe these are the background echoes that would present here even in absence of the arc (echoes here were present before the arc arrival). At later time, after 8:40 UT, the arc moved closer to the INV site, and the echoes were seen at the arc location and at farther ranges, corresponding to the region of optimal GDI excitation and favorable propagation conditions (enhanced luminosity in the wake of the moving arc). At this time, propagation conditions for the INV radar improved as the arc can provide additional radio wave refraction.

To illustrate how the choice of operating radar frequency affects the echo detection of the polar cap arcs with the PolarDARN radars, we show in Figure 5.16 INV and RKN power maps for two sequential scans at ~ 10 and ~ 12 MHz. We do not present here data for CLY since no echoes were seen at 12 MHz implying that the propagation condition for this radar were below the sensitivity threshold (10 MHz echoes were still observed, e.g. in Figure 5.15c). For INV, the 12-MHz echoes in the arc vicinity are very limited and observed at azimuths of not strongest 10-MHz echoes. Echoes at much farther ranges, correlating with oval luminosity, are seen for this scan. The 10-MHz echoes are seen closer to the radar, as expected. The differences imply that in these instances the echo detectability is strongly controlled by propagation conditions and not so much by the irregularity production factors (we do not expect much difference in properties of 12-m (12 MHz radar frequency) and 15-m (10 MHz radar frequency) GDI waves).

Observations at RKN also show shorter ranges for echoes at 10 MHz and fewer echoes at 12 MHz. The echo power enhancement in central beams correlates with the auroral arc for 10 MHz scan while 12-MHz scan shows a wide echo patch in the arcs wake with no obvious maximum.

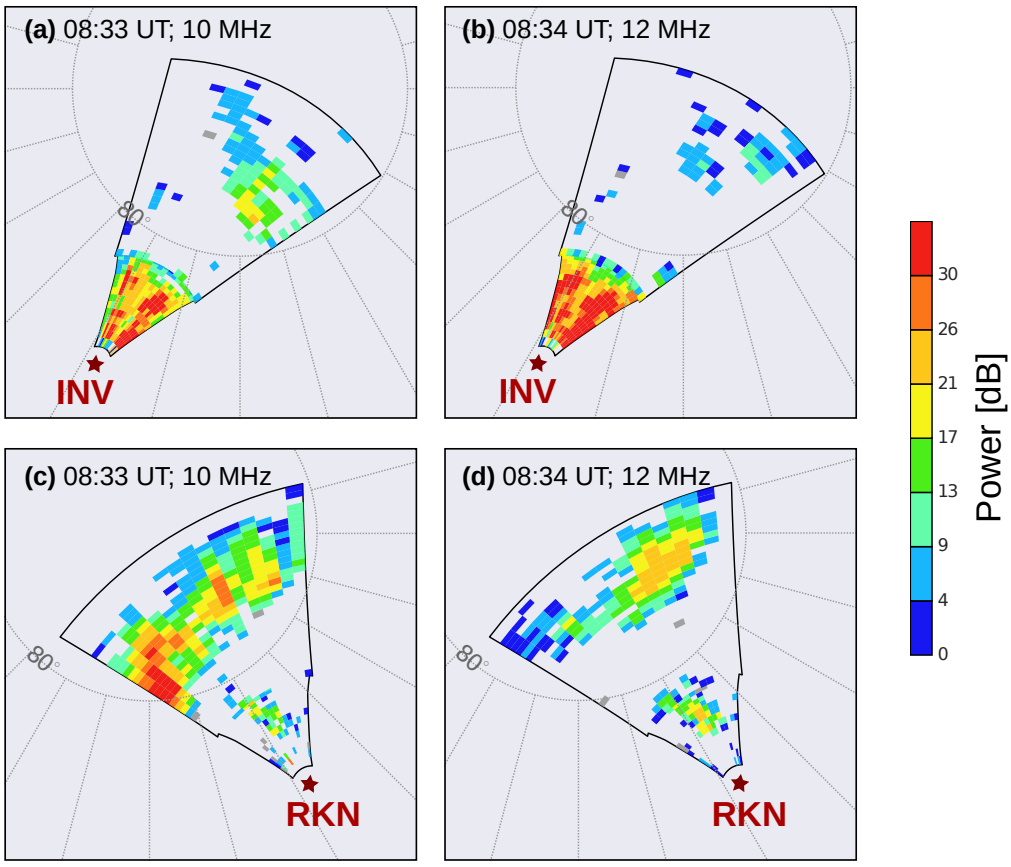

Figure 5.16: The same as in Figure 5.15 but for the observations at 08:33 UT and 08:34 UT for two sequantial scans at two different radar frequencies. Radar data are for (a,b) INV and (c,d) RKN.

5.5 Discussion

We presented data of multi-instrument observations of very high-latitude auroral arcs during prolonged periods of positive IMF B_z which support results of previous studies and give new information that might be useful in developing a comprehensive magnetosphere-ionosphere model of polar cap arcs. We selected one event in the dawn sector (1 December 2014, event 1) and one event in the dusk sector (28 January 2014, event 2) to understand possible differences between morphologically similar arcs but in different time sectors. Both arcs were simply detached from the auroral oval and remained detached for extended periods, weakening and intensifying several times. Both arcs experienced limited latitudinal motions.

5.5.1 External drivers and arc intensity variations and motions

Both events showed a certain degree of response to variations in the intensity of the external drivers of the high-latitude processes. The relationship to the IMF B_z and B_y was found to be complicated, in agreement with numerous previous studies [e.g., review by *Zhu et al.*, 1997; *Hosokawa et al.*, 2011].

We were unable to clearly identify threshold conditions for the arc onset. In terms of the IMF B_z, the arcs appeared on the RB camera images while the IMF B_z was positive for quite some time. The delay between the positive turning of the IMF B_z and onset of polar cap arcs is consistent with other observations with the imager at RB [*Koustov et al.*, 2008; *Hosokawa et al.*, 2011] as well as those reported in the literature for other locations [e.g., *Kullen et al.*, 2002]. Disappearance of the arcs in both cases seems to be linked to the IMF B_z turning to negative values. In event 1, this turning was short, just few minutes, and ~ 8 minutes later the last polar cap arc vanished from the RB camera FoV. In event 2, the IMF B_z negative turning was more obvious leading to disappearance of the last faint polar cap arc ~ 10 minutes later. The disappearance of polar cap arcs after a southward IMF B_z turning is consistent with other observations. *Troshichev et al.* [1988] reported a delay between the IMF B_z transition and disappearance of polar cap arcs of about 10-15 min, while *Valladares et al.* [1994] reported the delay of 30 min, noting that enough time have to pass to reconfigure the magnetosphere into a new topology. Our observations indicate that the arcs vanish from the OMTI images shortly after a southward transition, within about 10 min. Moreover, in event 1, the transition was short, indicating that polar cap arcs disappear before global magnetospheric reconfiguration.

In terms of the IMF B_y, the polar cap arcs at the poleward edge of the morning auroral oval (event 1) intensified in response to a quick dawnward transitions in the IMF $B_y < 0$ although the most prominent transition coincided with a sharp enhancement of the solar wind pressure, and this might be even a stronger factor, as known from previous publications [*Kozlovsky et al.*, 2005, 2007; *Meurant et al.*, 2003]. The polar cap arcs on the poleward edge of the afternoon/dusk auroral oval (event 2) typically intensified in response to quick upward transitions in the IMF B_y, whenever the IMF B_z was positive. The occurrence of polar cap

arcs was not accompanied by an IMF B_y sign change in either event, which is at variance with the notion that the change of the IMF B_y sign change triggers polar cap arcs [*Cumnock et al.*, 1997; *Kullen*, 2000].

In terms of the solar wind dynamic pressure, one can say that in both events, polar cap arcs have been more intense (more weak), temporarily for several minutes, in response to sharp increase (decrease) of the dynamic pressure. Generally, aurora intensification and appearance of additional arc structures in the polar cap in response to arrival of the solar wind pressure pulses have been reported by several authors [e.g., *Elphinstone et al.*, 1990; *Liou et al.*, 2005; *Kozlovsky et al.*, 2005].

Our data presented one surprise. In one occasion in event 2, no clear variations of the magnetospheric drivers were identified despite the arc intensified very clearly. We think that the polar cap arc intensification in this case was driven by some internal magnetospheric processes.

We also noticed that arc intensifications in some instances correlated with more intense aurora at latitudes of the auroral oval but sometimes they did not. Activations of the auroral oval aurora did not always correlate with significant changes of the intensity of detached polar cap arcs. This kind of "uncorrelated" behavior of polar cap arcs and oval aurora in the 16 MLT sector were reported by *Sandholt and Lockwood* [1990].

Considering the direction of polar cap arc motion, in both events the arcs were generally moving in the direction of the IMF B_y, as expected from previous publications [e.g., *Hosokawa et al.*, 2011]. The speeds of the motion were very typical, below 300 m/s [e.g., *Shiokawa et al.*, 1995, 1997; *Koustov et al.*, 2012]. In the event 2, several closely-located parallel arcs were moving synchronously, which is expected for a uniform background electric field. However, some motions in our events were not a simple parallel shift in the dawn-dusk-dawn directions. For example, in event 1, although one of the arcs was moving in the direction of the IMF B_y, the speed of the progression was different for the dayside and nightside ends of the arc such that it was "rotating" in MLAT-MLT coordinates.

5.5.2 Magnetospheric sources of polar cap arcs

Presented DMSP data on particle precipitation near the polar cap arcs for event 1 allow us to conclude that enhanced electron and ion precipitations correlate with polar cap arc locations. Moreover, since the spectra of precipitating electrons exhibited inverted-V signatures, we concluded that the electrons must have undergone acceleration along the magnetic field lines. Inverted-V signatures and additional acceleration associated with the polar cap arcs is similar to a case of the auroral zone arcs [*Marklund*, 1984; *Opgenoorth et al.*, 1990]. As discussed in Section 5.1, the particle data published so far indicate that the polar cap arcs are very likely formed on closed magnetic field lines. Our data are consistent with this notion although we cannot conclude where this lines are extended, for example, whether the electrons are coming from the plasma sheet/plasma sheet boundary layer or from closed lines in the far magnetotail lobes [*Fear et al.*, 2014]. We noticed that the onset of polar cap arcs can be preceded by a sunward plasma inflow into the polar cap from the auroral oval latitudes (on the nightside). This signifies the importance of instability processes in the plasma sheet or plasma sheet boundary layer. Theoretical models of such processes, as applied to polar cap arcs, have been considered in a number of publications [e.g., *Kozlovsky et al.*, 2003; *Golovchanskaya et al.*, 2006]. Another indication that polar cap arcs originate in the plasma sheet is sunward plasma flows within the polar cap arcs observed by SuperDARN and DMSP in event 1. Plasma in the plasma sheet moves in sunward direction, so that it is expected that the ionospheric footprints of magnetic field lines connected to the plasma sheet also move in sunward direction.

On the other hand, one can think that the source of precipitating electrons is on the LLBL-lobe closed (very far in the magnetotail) field lines and these lines can experience motion toward the magnetotail on their outer end and toward the Sun on their ionospheric (inner) end. We note that there is an opinion (that seems to be not shared by many researchers) that the weak polar cap arcs can actually be formed on open magnetic flux lines because particle acceleration to required energies of ~ 1 keV is achievable [*Carlson and Cowley*, 2005].

5.5.3 Ionospheric flows around polar cap arcs

Both events indicate that when a polar cap arc is formed, mesoscale convection pattern is established in the vicinity of the arc at the ionospheric level. It is characterized by a plasma flow shear or reversal such that there is a strong antisunward flow on one side of the arc and weak sunward or antisunward flow on the other side of the arc. Similar features are known from satellite measurements [e.g., *Carlson et al.*, 1988]. The flow data at the mesoscale level reported for events 1 and 2 can be represented as a superposition of two plasma flow systems: 1) background flow, for example according to the standard two-cell convection pattern (driven by quasi-viscous processes) and 2) an additional flow associated with the arc driven by a converging type of the electric field. The converging electric field will make plasma to $\mathbf{E} \times \mathbf{B}$ drift in opposite directions along opposite sides of the arc. This is schematically shown in Figure 5.17.

Our data indicate that the arc-associated flows can be sometimes more intense than the background flows. In this case, the global-scale pattern of the polar cap flow gets perturbed so that the arc, being deeper in the polar cap, can form a new convection reversal boundary at 2–3 degrees higher magnetic latitude than usual. In event 2, the postnoon polar cap arc eventually co-located with a new convection reversal of a large-scale dusk convection cell. This indicates that polar cap arcs can be involved in a global circulation processes which has always been the case of more global arcs [*Kozlovsky et al.*, 2002] and theta aurora [*Cumnock et al.*, 2009].

Our observations also show that sometimes no clear plasma flow perturbations are seen in the vicinity of polar cap arcs, and they, at least apparently, do not affect the global-scale pattern. This occurs usually when the polar cap arcs are weak in luminosity although it is evident that not every weak arc has weak arc-associated flow.

Our data for plasma flows within polar cap arcs are somewhat controversial. In event 1, PolarDARN radars and DMSP satellites consistently detect very narrow sunward plasma streams/enhancements co-locating with polar cap arcs. Similar signatures were seen in PolarDARN data for event 2, for some moments, while the Swarm satellite data show almost no flow within the arc and very fast flow just outside the arc, adjacent to its poleward/dawnside

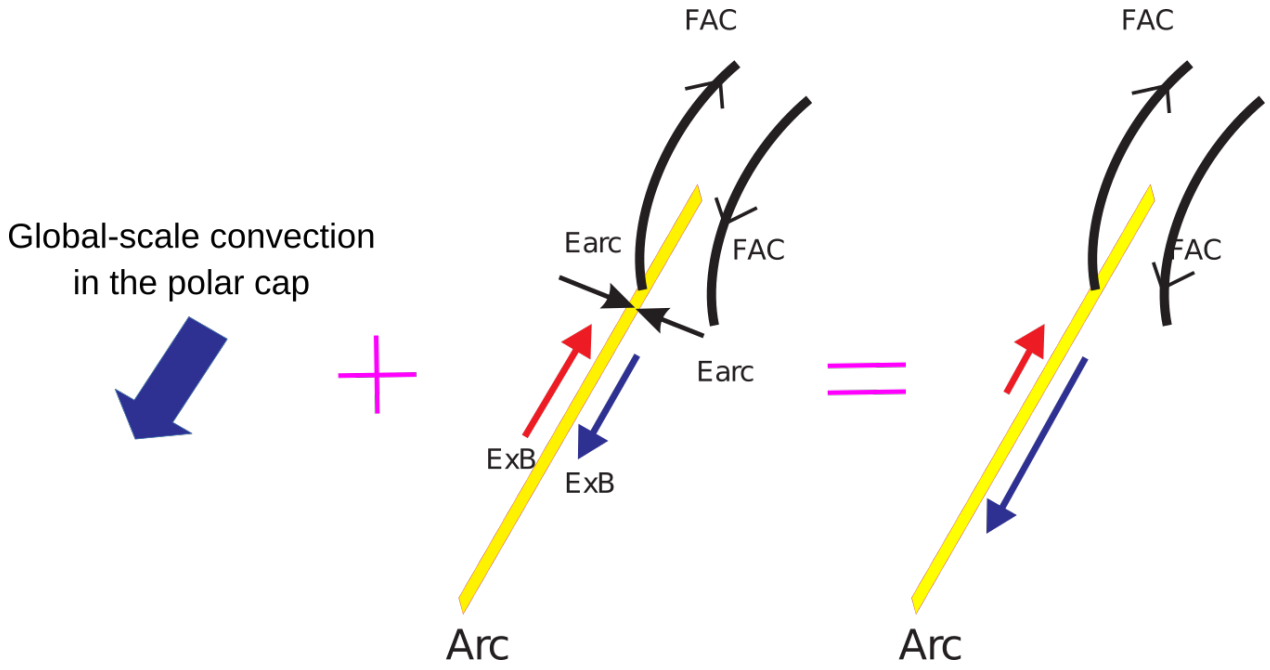

Figure 5.17: A schematic diagram explaining observations of mesoscale plasma flow pattern around a polar cap arc as a superposition of a pre-existing uniform large-scale flow and superposed flows driven by arc-associated processes.

edge. This is very similar to observations by *Perry et al.* [2015]. In many instances, however, PolarDARN data indicate antisunward flows within the arcs. We have to note that no definitive conclusion can be drawn from PolarDARN radar data because the spatial resolution of measurements is rather too coarse. It is not only because the radars have 45-km resolution in range but also because the azimuthal width of the radar beam is more than 100 km. The other exacerbating factors are uncertainties of echo mapping and a possibility of radio beam lateral refraction.

5.5.4 Field-aligned currents associated with polar cap arcs

We demonstrated (event 1) that there are upward FAC sheets coinciding with optical luminosity bands. The currents are small-scale and their density is of the order of 1 μA/m^2. The upward FACs are closed locally by downward FACs on one or both sides of polar cap arcs. The configuration of FACs and their intensity are consistent with previous measurements [*Zhu et al.*, 1997; *Kozlovsky et al.*, 2002].

5.5.5 Ionospheric irregularities and their detection with SuperDARN HF radars

Presented data on HF radar echo detection from vicinity of the polar cap patches and polar cap arcs show that the radars do see echoes in those ionospheric regions where ionospheric irregularities are expected. However, whether an echo will be actually detected in every expected region, strongly depends on the propagation condition for HF radio waves.

Every HF radar has optimal ranges of coherent echo detection. This is because to receive a coherent echo, a radar wave should propagate almost perpendicular to the ionospheric irregularities that are stretched along the magnetic field lines (the so called orthogonality condition). The geometrical aspect angles for the Northern hemisphere high latitude SuperDARN radars is on the order of 20 degrees so that the amount of refraction needed is significant. This is not problem at HF for typical electron densities in the ionosphere but the orthogonality can be achieved only at certain ranges, usually in a band of ranges of 200–500 km [e.g., *Uspensky et al.*, 1994; *Ponomarenko et al.*, 2009]. The amount of refraction and the optimal ranges depend on the electron density distribution in the ionosphere. Radar transmission frequency is important as well; lower frequency echoes are generally coming from shorter radar ranges [e.g., *Uspensky et al.*, 1994].

Within the polar cap the electron density in the dark winter F region is relatively low, especially on the nightside [*Ghezelbash et al.*, 2014; *Koustov et al.*, 2014]. This is one of the reasons for low echo detection rates during this season and local time sector. Since the orthogonality condition is easier to achieve at lower radar frequency, a general expectation is that echo detection rates are higher at lower radar frequency, for example, at 10 MHz as compared to 12 MHz observations and this is indeed generally the case if one would simply look at the two frequency PolarDARN radar data at VT SuperDARN web-site.

Our data in Section 5.4.3 indicate that indeed the PolarDARN radars detect echoes at ranges of optimal echo detection. In a case when a patch or a polar cap arc approaches this zone, the radars start getting echoes in their vicinity. Dependence of the radar viewing zone on the frequency of radar transmission has also been demonstrated. We conclude that one can hardly associate occurrence of echoing regions with regions of preferential GDI excitation

as implied by *Lamarche and Makarevich* [2016].

5.6 Summary

In this Chapter we investigated external drivers and their effects in the ionosphere while luminosity arcs occurred in the polar cap. The arc were of special type; they all have been just detached from the auroral oval, either on the dusk or dawn sides, but not very deep into the polar cap. The dawnside arc, eventually, moved back and merged with the oval luminosity. The dynamics of these arcs have been expected to be closely related to the auroral oval processes. This was not quite the case; the arc intensity was often uncorrelated with the oval luminosity variations. We tested whether intensification of these arcs and limited motions were affected by the IMF B_z and B_y as well as the dynamic pressure enhancements in the solar wind and found that, generally, the arcs responded to these factors but the character of the response varied, depending on the conditions. These responses are consistent with some existing magnetospheric models of the arc formation but contradict to others. We also attempted to draw a more definitive conclusion on the pattern of plasma flow around the detached arcs. In this aspect, our data indicate that the weak arcs are probably developed locally, without involvement of large-scale processes and they do not affect the large-scale flows in the polar cap. The stronger arcs, however, can affect the entire polar cap plasma circulation. For example, the duskside arc was established in places where large-scale convection reversal boundary was formed 5–10 min later on. We also found that formation of the detached arcs is often preceded by plasma inflow from the auroral oval into the polar cap so that the arcs are formed within large-scale sunward plasma streams that are part of large-scale circulation at the IMF $B_z > 0$. Close relation of sunward flows to the oval flows implies that the arcs could be formed as consequence of plasma instabilities at the outer edge of the plasma sheet boundary layer. Our observations of precipitating electron energies and field-aligned currents associated with detached arcs are consistent with previous publication referred to generic arcs in the polar cap.

Chapter 6

Conclusions and suggestions for future research

6.1 Conclusions

The primary objective of this thesis was to investigate several aspects of the magnetosphere-ionosphere system's response to the solar wind driving. For southward IMF conditions, the magnetosphere-ionosphere system reacts to the solar wind driving by sporadically releasing bursts of energy from the magnetotail into the entire system during substorms. The occurrence of substorms looks unpredictable and chaotic and there are ongoing debates about what triggers them. One aspect of the problem is the role of the solar driving in substorm occurrence. During northward IMF conditions, the character of the solar wind-magnetosphere interaction changes, and a transition to a new state happens. Onset of sunward ionospheric flows on the dayside and occurrence of auroral arcs deep inside the polar cap are two manifestations of this new state. In this thesis, we focused on these three phenomena, substorms, sunward plasma flows and polar cap arcs. Now we summarise our main conclusions.

6.1.1 Substorm occurrence rates, substorm recurrence times, and solar wind driving

1. Substorm signatures could be seen in various data sets. Depending on a data set used and the way one defines a substorm in this data set, very different lists of substorm events can be produced. This was demonstrated in Section 3.3 where substorm lists from four data sets, created with 5 different algorithms, were compared. All but two

lists have very different properties, more specifically:

(a) The most widely used substorm list is obtained from the IMAGE and Polar spacecrafts. The list has an advantage of including only clear substorm onsets, but it cannot be used in a statistical study on substorm occurrence. The reason for this is that the list is dominated by substorms occurring during intervals of relatively quiet geomagnetic conditions. During disturbed conditions, visual identification of a clear auroral breakup becomes difficult and any "unclear" events are disregarded in this list. In addition, continuous data coverage is crucial for making an accurate statistics and specifics of the IMAGE and Polar spacecraft's orbits did not allow continuous monitoring of the auroral oval. In contrast, ground-based dense network of magnetometer stations and LANL GEO satellites provide this kind of continuous monitoring necessary to a good substorm statistics.

(b) The MPB list, which includes all positive bays identified in the time records of the MPB index, has the largest number of events. It was found that the list is contaminated by many substorm intensifications and, possibly, SAPS-related flows. Simple requirement of including only isolated events results in missing many substorm events as substorms often are preceded by pseudobreakups and accompanied by intensifications.

(c) The SOPHIE list, although also contaminated by substorm intensifications, is different from the MPB list. We found that by asking the SOPHIE events to follow a period defined as a growth phase as suggested by *Forsyth et al.* [2015], the list would miss many substorm events occurring during periods of disturbed geomagnetic conditions.

(d) The events determined by jumps in the SML index (SML list) and by injections of energetic particles into geosynchronous orbit were found to have very similar properties and probably are the most reliable lists. For further investigation of substorm occurrence, we focused on the SML list as it has higher temporal resolution.

(e) Substorm-like signatures are sometimes produced by compression of the magne-

tosphere when interplanetary shock arrives at Earth.

2. Mathematical analysis of substorm recurrence-times distribution revealed that there are three types of substorm occurrence pattern: quasiperiodically occurring substorms, randomly occurring substorms, and long intervals without substorms. Quasiperiodic substorms occur during intervals of the strongest solar wind driving and have recurrence period of 2–4 hours. We found no $\sim$ 3-hour periodicity in the solar wind that might cause the $\sim$ 3-hour periodicity of substorm occurrence. Our interpretation is that the period is set by the magnetosphere, but an interval of enhanced solar wind driving is required to trigger a substorm. Randomly occurring substorms with recurrence times in the range of 6–15 hours are associated with randomly occurring intervals of enhanced solar wind driving. Long intervals without substorms of 24 hours or more occur when the solar wind driving is very weak, typically during intervals of sector-reversal region plasma at Earth.

3. Using much larger statistics than in previous studies, we confirmed that substorm occurrence rates are significantly higher during the declining phase of the solar cycle. It is also confirmed that the substorm occurrence varies with season. We found that substorm occurrence rates are smallest in summer (but higher than reported in previous studies) and highest around equinoxes depending on whether the Earth is in a toward or away sector, consistent with the Russel-McPherron effect. The occurrence rates also vary depending on the type of solar wind plasma at Earth: they are highest in coronal-hole-origin plasma and weakest in sector-reversal-region plasma.

6.1.2 Sunward flows in the polar cap for the IMF B_z^+ conditions

Although the mere fact that the plasma flow at near noon hours reverses to the sunward direction has been known for years, we attempted in this thesis to characterize the flows on a more extensive statistical basis with a focus on differences in the intensity and direction of the flows during summer and winter conditions for strongly dominant IMF B_z^+.

1. We confirmed statistically, by looking at the Northern hemisphere SuperDARN data including recent observations during the solar cycle 24 maximum, that the sunward

plasma flows during winter months are smaller in magnitude than during summer months. This is consistent with previous SuperDARN publications where older data have been involved and where the amount of plasma vectors deep in the polar cap were limited. No clear threshold in terms of the IMF B_z^+ magnitude for the onset of flows was found although the data demonstrate that the sunward flows are persistent for reverse electric field of larger than ~ 10 kV/R_E.

2. We found that the seasonal difference in the speed of the sunward flows is also seen while simultaneous flow data in both hemispheres are considered. This has been shown by looking at statistically averaged line-of-site velocities, by considering convection maps and by looking at individual events where direct and simultaneous SuperDARN radar measurements in the polar caps are performed.

3. The directions of the sunward flows were found to be not exactly along the noon-midnight meridian as anticipated from most of previous publications. The SuperDARN data show that while in the winter hemisphere, the flow can deviate from this meridian by $\pm 20^\circ$, both toward prenoon and postnoon hours, in the summer hemisphere, the flows are systematically rotated by $\sim 30^\circ$ toward prenoon hours of ~ 10 MLT. This is irrespective of the IMF B_y polarity eliminating this potential source of the flow direction change. The winter/summer differences in the flow direction in hemispheres might explain our finding that the onset of sunward flows, as detected by meridionally-looking SuperDARN radars, is not simultaneous with delay in one hemisphere on the order of ~ 10 min.

6.1.3 Electrodynamics of polar cap arcs

Most of previous publications in this area are based on observations of theta aurora which is a relatively strong luminosity band easily identifiable with a satellite-based imagery. We focused here on rather weak and limited in space polar cap auroral arcs/forms that were seen just detached from the auroral oval. Both cases of dusk and dawn arcs have been considered.

1. We showed that appearance (disappearance) of polar cap arcs was linked to northward (southward) transition of the IMF B_z (but no transition of the IMF B_y was observed)

with a delay consistent with previous studies. Our observations indicate that polar cap arcs intensify temporally in response to sharp enhancements of solar wind dynamic pressure. Direction of polar cap arc motion was found to be consistent with the IMF B_y polarity, in line with previous reports. We additionally found that the dayside and nightside parts of polar cap arcs generally have quite different speeds with the nightside parts moving faster.

2. We found that the onset of polar cap arcs detached from the auroral oval can be preceded by intrusion of sunward moving plasma from the auroral oval into the polar cap. Sunward plasma flows in the polar cap usually occur in the dayside portion of the polar cap where they are associated with the lobe reconnection. Such flows are rarely extend past the magnetic pole toward the night side and one would not expect sunward flows associated with the lobe reconnection in the nightside portion of the polar cap. Thus we hypothesise that this sunward inflow is associated with the appearance of polar cap arcs and can be interpreted as plasma intrusions from the plasma sheet into the magnetotail lobes due to an instability process occurring in the plasma sheet. Another hint that polar cap arcs have the plasma sheet as their source region is narrow sunward plasma streams collocating with the arcs as observed by DMSP and the SuperDARN.

3. The polar cap arcs, while detaching from the auroral oval, can profoundly change the global-scale plasma flow pattern in the polar cap. While they appear often within a large-scale sunward stream, eventually, they can become the center of the convection reversal boundary of a large-scale cell.

4. Detection of polar cap arcs with SuperDARN radars strongly depends on propagation conditions. The location and shape of regions from where HF echoes are observed depend on the radar look direction and radar frequency and not necessary appear as bands aligned with the arc's side where conditions for GDI excitation are favorable.

6.2 Suggestions for future work

6.2.1 Substorms

Our work in Chapter 3 indicated, once again, that particle injections into geosynchronous orbit are one of the most reliable indicators of a substorm onset. The research undertaken in Chapter 3 is based on LANL data with resolution of 30 min. This is what was available to us at the time of work. The LANL geosynchronous satellites energetic particle database spans over ~ 40 years and actually has higher temporal resolution: 60-s resolution for years 1977–1989 and 10-s resolution for data from 1989 to present day. We plan to create a list of substorms for all the years of observations with 1-min resolution by looking for dispersionless injections in the data. For case when all the satellites detected dispersed injections, an algorithm will be developed to trace the measured injections back to the original injection site. We believe that a substorm list created in this way would benefit the space physics community. Presently, the most widely used substorm lists are based on IMAGE and Polar satellite aurora imagery. As discussed in Chapter 3, both lists include a large number of small-amplitude events occurring mostly during relatively quiet conditions. The new list would be less biased and would cover more years of observations.

The created list of substorms can be used for a statistical study of the response of the outer electron radiation belts to substorms. One expects to see incremental heating of electrons in the radiation belt after substorm onset caused, for instance, by chorus waves generated by the injected electrons or directly amplified by the substorm-related induction electric field. However, there are complications to seeing these subtle single-substorm effects; there is a substorm distortion of the Earth's magnetic field caused by stretching, collapse, and the diamagnetism of the injected plasma sheet that impacts the spacecraft observations of the electron radiation belt. Additionally, substorms typically occur amidst of ongoing geomagnetic activity. To properly perform the study of the substorm impact on the radiation belt, the substorm onsets will need to be separately analyzed according to substorm amplitude, according to stormtime substorms versus non-stormtime substorms, and according to temporally isolated substorms versus periodic substorms.

The list of substorms based on particle injection data would be a useful contribution to more general studies of the Sun-Earth system. For example, in studies of the solar wind driving effects on various magnetospheric processes, there is a demand for "indices" that describe the various aspects of the state of the magnetosphere. An index that describes the ongoing substorm-occurrence rate made from various measures of substorm occurrences will be valuable for such studies. This new index can be added to ongoing canonical correlation analysis (CCA) studies of the reaction of the magnetosphere-ionosphere system to the solar wind variations [*Borovsky et al.*, 2014; *Borovsky and Denton*, 2014]. These CCA studies digest multi-variable time-dependent information about the solar wind (number density, mass density, speed, ram pressure, Mach number, magnetic field strength, clock angle, turbulence amplitude [*King and Papitashvili*, 2005]), geomagnetic activity (Kp, MBI, AU, AL, PCI, MPB, Dst), ULF amplitudes [*Romanova et al.*, 2007; *Kozyreva et al.*, 2007], the Pi-2 wave power [*Nosé et al.*, 2012], and the hemispheric power of precipitating electrons and protons [*Emery et al.*, 2009]. CCA is capable of identifying multiple "modes of reaction" of the magnetosphere-ionosphere system to the solar wind driving and it allowed to infer the solar wind properties related to each mode. With the highly intercorrelated variables, CCA is also making progress in resolving the issue on causal connections (in terms of physics) versus coincidental correlation (in terms of mathematics) between the solar wind and the magnetosphere.

The 1-min resolution list of substorm events can be used for studies of plasma convection restructuring in relation to substorms. Of special interest are convection changes prior to substorms. These are important to identify for the development of a comprehensive model of the substorm development. One can also think about their use for predictions of substorms as one of the signatures of incoming onset, along with a host of other already known signatures.

Classical understanding of processes leading to a substorm is the IMF B_z turning to negative values and enhancement of the ionospheric plasma flow through the central polar cap lasting for periods on the order of 30 min and culminating in the onset [*Rostoker et al.*, 1980]. SuperDARN data show this effect on a statistical basis [*Provan et al.*, 2004]. However, some substorms are accompanied by a convection velocity decrease [e.g., *Lyons et al.*, 2003; *Jayachandran et al.*, 2003]. *Lyons et al.* [2003] noticed relatively short-lived ($\sim$ 10 min)

and patchy reductions of the dayside plasma flows and related the effect to a sharp IMF B_z transition to positive values that, according to these authors, triggers many substorms. This explanation implies weakening of the solar wind driver(s) supplying energy to the magnetotail. *Jayachandran et al.* [2003] noticed a rather large-scale (although not demonstrated) flow reduction effect in the polar cap. It was seen as a steady velocity decrease lasting for tens of minutes and occurring only for substorms initiated after a long period of steady, strongly negative IMF B_z. Such events are not frequent but do occur. These authors related the effect with changes in the linkage between the Region 1 currents and the cross-tail currents implying internal magnetospheric processes. Work on further investigation of these two effects has been stopped despite of obviously quite different visions as to what happens with the flow at the very last minutes prior to substorm onset.

One difficulty in investigating substorm-related changes of the large-scale convection is the fact that the IMF is seldom in a quasi-steady state. Variations of the IMF imply changes in the intensity of external drivers. We are planning to isolate events with relatively stable IMF. We intend to consider the entire SuperDARN data base which now covers more than 20 years of operation. Having a list of all reliably identified substorms will be very helpful in this work.

6.2.2 Dayside plasma flows at the IMF B_z^+

Global-scale SuperDARN convection maps are only reliable in those parts of MLAT-MLT portions where good radar coverage is achieved. This is especially critical for the conditions with the IMF $B_z > 0$. Patchiness of the SuperDARN data did not allow us to answer on a basic question regarding to the latitudinal extent of the sunward flows seen on the dayside. One can think that in coming years, with increase in a number of operational SuperDARN radars, such an analysis could be performed. This, unfortunately, hardly would happen. Currently, the solar activity is on the decaying phase so that the number of SuperDARN echoes will be decreasing, a known effect for SuperDARN echo occurrence [*Ghezelbash et al.*, 2014]. It is unlikely that several new radars will be built and installed in high Arctic or Antarctic in coming 2–4 years; currently known plans are on the construction of midlatitude radars (Europe, China). Since next solar cycle maximum is many years ahead of us, there

are limiting chances for successful work on B_z^+ flows with SuperDARN data alone.

Fortunately, there is an incoherent scatter radar operational in the Canadian Arctic at Resolute Bay, RISR-North and recently a new radar has been constructed there, the RISR-Canada [*Gillies et al.*, 2016]. Combined observational zone of these radars cover broad range of magnetic latitudes, from about 86° to 76°. These radars, despite they are operational for limited number of days in a year, provide reliable and uninterrupted data on large-scale plasma flows. Recently, *Maimaiti et al.* [2017] demonstrated extreme usefulness of the RISR-N radar for studies of sunward flows. The authors' major conclusion is that the high-latitude and auroral zone flows might be driven independently so that statistical models of the plasma convection might not be very helpful in understanding plasma flows in individual events. This is consistent with what we discovered in Chapter 4. It is highly desirable to run experiments with these radars or consider already collected data to investigate details of the plasma flows at the IMF B_z^+ conditions.

Besides the question of spatial extent of sunward flows, an important issue is on the dynamical changes of the flow patterns as the IMF driver turns from negative to positive values. Recent SuperDARN model of *Cousins and Shepherd* [2010] is dynamical one; it is statistical in its nature but since the gates of the external drivers (such as E_{sw}) are narrow, as compared to the classical Ruohoniemi and Greenwald 1996 model [*Ruohoniemi and Greenwald*, 1996], it can predict the patterns for intermediate states as the IMF undergoes a transition. It is highly desirable to assess the CS2010 model versus measurements with the RISR radars to evaluate reliability of the model for pattern prediction. This eventually would enable more reliable nowcast of space weather.

Finally, the question on the potential and average velocity saturation at extreme solar wind and the IMF driving conditions continue to attract interest of researchers [*Clauer et al.*, 2016]. There is certainly modeling effort behind it [*Bhattarai et al.*, 2012]. Further contributions with RISR data on this aspect would be met with high interest. SuperDARN data in the Southern hemisphere can be of use, as there is a reasonable radar coverage anywhere between 80° and 90° of MLAT though in a limited time sector.

6.2.3 Sun-aligned arcs

One of the unresolved and controversial issues in this Thesis is the character of the plasma flow within the polar cap arcs. We commented that SuperDARN measurements are hardly helpful to answer this question because of their poor spatial resolution and uncertainties with mapping of echo regions. More detailed analysis of the RISR-N incoherent scatter radar data, however, looks promising. Unfortunately, the RISR data are prone to significant error in measurements with fine time resolution of ~ 3 min [*Koustov et al.*, 2017]. However, data averaged over 5-min and longer periods can be produced, these are of much better quality and would be beneficial for the analysis. This is because the polar cap arcs often show not much of a motion, staying in about the same place for many minutes and repositioning relatively slow. There are good chances to get data for such events.

The Swarm data are another possibility. Unfortunately, the quality of these data continue to be an issue [*Fiori et al.*, 2016]. Currently, general perception is that at least the spatial variations are reflected properly in the available data, but for addressing the question on the flow inside polar cap arcs, absolute values of the velocity are needed. Recently, a new attempt to correct the data has been undertaken (report by the PI, D. Knudsen). Validation work on the Swarm electric field data is in progress.

Another interesting aspect of polar cap arc formation mechanism is interhemispheric differences in polar cap arc configuration and response to the solar wind drivers. In the past [e.g., *Cumnock et al.*, 2009], DMSP measurements have been considered. Recent installation of MCM and DCE radars gives good chances to provide additional information on the nature of plasma flows around the polar cap arc, first of all with respect to what extent the arcs affect the global-scale plasma pattern.

Bibliography

Abooalizadeh, Z. (2015), Long-term variations in the high-latitude plasma flows inferred from superdarn radar data, Master's thesis, Univ. of Saskatchewan.

Aikio, A. T., H. J. Opgenoorth, M. A. L. Persson, and K. U. Kaila (1993), Ground-based measurements of an arc-associated electric field, *J. Atmos. Terr. Phys.*, *55*, 797–808.

Aikio, A. T., T. Lakkala, A. Kozlovsky, and P. J. S. Williams (2002), Electric fields and currents of stable drifting auroral arcs in the evening sector, *J. Geophys. Res.*, *107*(A12), SIA 3–1–SIA 3–14, 1424.

Akasofu, S.-I. (1963), The dynamical morphology of the aurora polaris, *J. Geophys. Res.*, *68*(6), 1667–1673.

Akasofu, S.-I. (1964), The development of the auroral substorm, *Planet. Space Sci.*, *12*, 273–282.

Akasofu, S.-I. (1968), Auroral observations by the constant local time flight, *Planet. Space Sci.*, *16*(11), 1365 – 1368.

Akasofu, S.-I. (1974), The Aurora and the magnetosphere: The Chapman memorial lecture, *Planet. Space Sci.*, *22*, 885–923.

Akasofu, S.-I. (1979), *Dynamics of the Magnetosphere*, chap. What is a magnetospheric substorm?, p. 447.

Ambrosino, D., E. Amata, M. F. Marcucci, I. Coco, W. Bristow, and P. Dyson (2009), Different responses of northern and southern high latitude ionospheric convection to IMF rotations: a case study based on SuperDARN observations, *Ann. Geophys.*, *27*(6), 2423–2438.

Amm, O., A. Grocott, M. Lester, and T. K. Yeoman (2010), Local determination of ionospheric plasma convection from coherent scatter radar data using the SECS technique, *J. Geophys. Res.*, *115*(A3), a03304.

Anderson, B. J., M. J. Engebretson, S. P. Rounds, L. J. Zanetti, and T. A. Potemra (1990), A statistical study of Pc 35 pulsations observed by the AMPTE/CCE Magnetic Fields Experiment, 1. Occurrence distributions, *J. Geophys. Res.*, *95*(A7), 10,495–10,523.

André, D., G. J. Sofko, K. Baker, and J. MacDougall (1998), SuperDARN interferometry: Meteor echoes and electron densities from groundscatter, *J. Geophys. Res.*, *103*(A4), 7003–7015.

Angelopoulos, V. (2008), The THEMIS Mission, *Space Sci. Rev.*, *141*(1), 5.

Axford, W. I., and C. O. Hines (1961), A unifying theory of high-latitude geophysical phenomena and geomagnetic storms, *Can. J. Phys.*, *39*(10), 1433–1464.

Baker, D. N., S. G. Kanekal, V. C. Hoxie, M. G. Henderson, X. Li, H. E. Spence, S. R. Elkington, R. H. W. Friedel, J. Goldstein, M. K. Hudson, G. D. Reeves, R. M. Thorne, C. A. Kletzing, and S. G. Claudepierre (2013), A Long-Lived Relativistic Electron Storage Ring Embedded in Earth's Outer Van Allen Belt, *Science*, *340*, 186–190.

Baker, K. B., and S. Wing (1989), A new magnetic coordinate system for conjugate studies at high latitudes, *J. Geophys. Res.*, *94*(A7), 9139–9143.

Bame, S. J., J. R. Asbridge, W. C. Feldman, J. T. Gosling, and R. D. Zwickl (1981), Bidirectional streaming of solar wind electrons $>$ 80 eV: ISEE evidence for a closed-field structure within the driver gas of an interplanetary shock, *Geophys. Res. Lett.*, *8*(2), 173–176.

Banks, P., and G. Kockarts (2013), *Aeronomy*, Elsevier Science.

Basu, S., S. Basu, P. K. Chaturvedi, and C. M. Bryant (1994), Irregularity structures in the cusp/cleft and polar cap regions, *Radio Sci.*, *29*(1), 195–207.

Baumjohann, W., and Y. Kamide (1984), Hemispherical Joule heating and the AE indices, *J. Geophys. Res.*, *89*(A1), 383–388.

Baumjohann, W., and R. A. Treumann (1996), *Basic space plasma physics*, Imperial College Press.

Baumjohann, W., G. Paschmann, T. Nagai, and H. Lhr (1991), Superposed epoch analysis of the substorm plasma sheet, *J. Geophys. Res.*, *96*(A7), 11,605–11,608.

Belian, R. D., D. N. Baker, P. R. Higbie, and E. W. Hones (1978), High-resolution energetic particle measurements at 6.6 RE, 2. High-energy proton drift echoes, *J. Geophys. Res.*, *83*(A10), 4857–4862.

Belian, R. D., G. R. Gisler, T. Cayton, and R. Christensen (1992), High-Z energetic particles at geosynchronous orbit during the Great Solar Proton Event Series of October 1989, *J. Geophys. Res.*, *97*(A11), 16,897–16,906.

Belian, R. D., J. E. Borovsky, R. J. Nemzek, and S. C. W. (1994), Random and periodic substorms and their origins in the solar wind, in *Proceedings of the Second International Conference on Substorms*, p. 463, University of Alaska.

Belian, R. D., T. E. Cayton, R. A. Christensen, J. C. Ingraham, M. M. Meier, G. D. Reeves, and A. J. Lazarus (1996), Relativistic electrons in the outerzone: An 11 year cycle; Their relation to the solar wind, *AIP Conference Proceedings*, *383*(1), 13–18.

Berkey, F. T., L. L. Cogger, S. Ismail, and Y. Kamide (1976), Evidence for a correlation between sun-aligned arcs and the interplanetary magnetic field direction, *Geophys. Res. Lett.*, *3*(3), 145–147.

Bhattarai, S. K., R. E. Lopez, R. Bruntz, J. G. Lyon, and M. Wiltberger (2012), Simulation of the polar cap potential during periods with northward interplanetary magnetic field, *J. Geophys. Res.*, *117*(A4), a04219.

Biernat, H. K., N. V. Erkaev, C. J. Farrugia, D. F. Vogl, and W. Schaffenberger (2000), MHD effects of the solar wind flow around planets, *Nonlinear Processes Geophys.*, *7*(3/4), 201–210.

Bilitza, D. (2001), International Reference Ionosphere 2000, *Radio Sci.*, *36*(2), 261–275.

Birn, J., and M. Hesse (2014), The substorm current wedge: Further insights from MHD simulations, *J. Geophys. Res.*, *119*(5), 3503–3513.

Birn, J., M. F. Thomsen, J. E. Borovsky, G. D. Reeves, D. J. McComas, and R. D. Belian (1997), Characteristic plasma properties during dispersionless substorm injections at geosynchronous orbit, *J. Geophys. Res.*, *102*(A2), 2309–2324.

Birn, J., M. F. Thomsen, J. E. Borovsky, G. D. Reeves, D. J. McComas, R. D. Belian, and M. Hesse (1998), Substorm electron injections: Geosynchronous observations and test particle simulations, *J. Geophys. Res.*, *103*(A5), 9235–9248.

Birn, J., M. F. Thomsen, J. E. Borovsky, G. D. Reeves, and M. Hesse (2000), Particle acceleration in the dynamic magnetotail, *Phys. Plasmas*, *7*(5), 2149–2156.

Blomberg, L., and J. Cumnock (2005), Electrodynamics of transpolar aurorae, *Adv. Space Res.*, *36*(10), 1785 – 1790.

Borovsky, J. (2004), Global sawtooth oscillations of the magnetosphere, *Eos, Transactions American Geophysical Union*, *85*(49), 525–525.

Borovsky, J. E. (2008), Flux tube texture of the solar wind: Strands of the magnetic carpet at 1 AU?, *J. Geophys. Res.*, *113*(A8), a08110.

Borovsky, J. E. (2010), On the variations of the solar wind magnetic field about the Parker spiral direction, *J. Geophys. Res.*, *115*(A9), a09101.

Borovsky, J. E. (2012), The velocity and magnetic field fluctuations of the solar wind at 1 AU: Statistical analysis of Fourier spectra and correlations with plasma properties, *J. Geophys. Res.*, *117*(A5), a05104.

Borovsky, J. E. (2013), Physics-based solar wind driver functions for the magnetosphere: Combining the reconnection-coupled MHD generator with the viscous interaction, *J. Geophys. Res.*, *118*(11), 7119–7150.

Borovsky, J. E. (2016), *Solar Wind-Magnetophere Interaction*, chap. 4, pp. 48–70, CRC Press.

Borovsky, J. E., and J. Birn (2014), The solar wind electric field does not control the dayside reconnection rate, *J. Geophys. Res.*, *119*(2), 751–760.

Borovsky, J. E., and T. E. Cayton (2011), Entropy mapping of the outer electron radiation belt between the magnetotail and geosynchronous orbit, *J. Geophys. Res.*, (A6), 116, A06216.

Borovsky, J. E., and M. H. Denton (2006), Differences between CME-driven storms and CIR-driven storms, *J. Geophys. Res.*, *111*(A7), a07S08.

Borovsky, J. E., and M. H. Denton (2009), Relativistic-electron dropouts and recovery: A superposed epoch study of the magnetosphere and the solar wind, *J. Geophys. Res.*, *114*(A2), a02201.

Borovsky, J. E., and M. H. Denton (2010), On the heating of the outer radiation belt to produce high fluxes of relativistic electrons: Measured heating rates at geosynchronous orbit for high-speed stream-driven storms, *J. Geophys. Res.*, *115*(A12), a12206.

Borovsky, J. E., and M. H. Denton (2014), Exploring the cross correlations and autocorrelations of the ULF indices and incorporating the ULF indices into the systems science of the solar wind-driven magnetosphere, *J. Geophys. Res.*, *119*(6), 4307–4334, 2014JA019876.

Borovsky, J. E., and R. J. Nemzek (1994), Substorm statistics: Occurrences and amplitudes, in *Proceedings of the Second International Conference on Substorms*, p. 93, Univ. of Alaska.

Borovsky, J. E., and J. T. Steinberg (2006), The calm before the storm in CIR/magnetosphere interactions: Occurrence statistics, solar wind statistics, and magnetospheric preconditioning, *J. Geophys. Res.*, *111*(A7), a07S10.

Borovsky, J. E., and K. Yakymenko (2017), Substorm occurrence rates, substorm recurrence times, and solar wind structure, *J. Geophys. Res.*, 2016JA023625.

Borovsky, J. E., R. J. Nemzek, and R. D. Belian (1993), The occurrence rate of magnetospheric-substorm onsets: Random and periodic substorms, *J. Geophys. Res.*, *98*(A3), 3807–3813.

Borovsky, J. E., D. T. Welling, M. F. Thomsen, and M. H. Denton (2014), Long-lived plasmaspheric drainage plumes: Where does the plasma come from?, *J. Geophys. Res.*, *119*(8), 6496–6520, 2014JA020228.

Borovsky, J. E., T. E. Cayton, M. H. Denton, R. D. Belian, R. A. Christensen, and J. C. Ingraham (2016), The proton and electron radiation belts at geosynchronous orbit: Statistics and behavior during high-speed stream-driven storms, *J. Geophys. Res.*, *121*(6), 5449–5488, 2016JA022520.

Brambles, O. J., W. Lotko, B. Zhang, M. Wiltberger, J. Lyon, and R. J. Strangeway (2011), Magnetosphere sawtooth oscillations induced by ionospheric outflow, *Science*, *332*, 1183–1186.

Brambles, O. J., W. Lotko, B. Zhang, J. Ouellette, J. Lyon, and M. Wiltberger (2013), The effects of ionospheric outflow on ICME and SIR driven sawtoothevents, *J. Geophys. Res.*, *118*(10), 6026–6041.

Brekke, A. (2013), *The Sun and the solar wind*, pp. 1–50, Springer Berlin Heidelberg, Berlin, Heidelberg.

Bristow, W. A., J. Spaleta, and R. T. Parris (2011), First observations of ionospheric irregularities and flows over the south geomagnetic pole from the Super Dual Auroral Radar Network (SuperDARN) HF radar at McMurdo Station, Antarctica, *J. Geophys. Res.*, *116*(A12), a12325.

Bristow, W. A., E. Amata, J. Spaleta, and M. F. Marcucci (2015), Observations of the relationship between ionospheric central polar cap and dayside throat convection velocities, and solar wind/IMF driving, *J. Geophys. Res.*, *120*(6), 4684–4699, 2015JA021199.

Burke, W. J., M. S. Gussenhoven, M. C. Kelley, D. A. Hardy, and F. J. Rich (1982), Electric and magnetic field characteristics of discrete arcs in the polar cap, *J. Geophys. Res.*, *87*(A4), 2431–2443.

Caan, M. N., R. L. McPherron, and C. T. Russell (1977), Characteristics of the association between the interplanetary magnetic field and substorms, *J. Geophys. Res.*, *82*(29), 4837–4842.

Caan, M. N., R. L. McPherron, and C. T. Russell (1978), The statistical magnetic signature of magnetospheric substorms, *Planet. Space Sci.*, *26*(3), 269 – 279.

Cai, X., and C. R. Clauer (2009), Investigation of the period of sawtooth events, *J. Geophys. Res.*, *114*(A6), a06201.

Cai, X., M. G. Henderson, and C. R. Clauer (2006), A statistical study of magnetic dipolarization for sawtooth events and isolated substorms at geosynchronous orbit with GOES data, *Ann. Geophys.*, *24*(12), 3481–3490.

Cai, X., J.-C. Zhang, C. R. Clauer, and M. W. Liemohn (2011), Relationship between sawtooth events and magnetic storms, *J. Geophys. Res.*, *116*(A7), a07208.

Carlson, H. C., and S. W. H. Cowley (2005), Accelerated polar rain electrons as the source of sun-aligned arcs in the polar cap during northward interplanetary magnetic field conditions, *J. Geophys. Res.*, *110*, A05,302.

Carlson, H. C., R. A. Heelis, E. J. Weber, and J. R. Sharber (1988), Coherent mesoscale convection patterns during northward interplanetary magnetic field, *J. Geophys. Res.*, *93*(A12), 14,501–14,514.

Cassak, P. A., and M. A. Shay (2007), Scaling of asymmetric magnetic reconnection: General theory and collisional simulations, *Phys. Plasmas*, *14*(10), 102,114.

Cayton, T. E., and R. D. Belian (2007), Numerical modeling of the synchronous orbit particle analyzer (SOPA, Version 2) that flew on S/C 1990-095, LA Rep. LA-14335, Los Alamos Natl. Lab., Los Alamos, NM 87545.

Cayton, T. E., and M. Tuszewski (2005), Improved electron fluxes from the synchronous orbit particle analyzer, *Space Weather*, *3*(11), s11B05.

Cayton, T. E., R. D. Belian, S. P. Gary, T. A. Fritz, and D. N. Baker (1989), Energetic electron components at geosynchronous orbit, *Geophys. Res. Lett.*, *16*(2), 147–150.

Cerisier, J.-C., and C. Senior (1994), Merge: A fortran program, *Tech. rep.*, Centre dEtude des Environnements Terrestres et Planétaires CNRS.

Chang, S.-W., J. D. Scudder, J. B. Sigwarth, L. A. Frank, N. C. Maynard, W. J. Burke, W. K. Peterson, E. G. Shelley, R. Friedel, J. B. Blake, R. A. Greenwald, R. P. Lepping, G. J. Sofko, J.-P. Villain, and M. Lester (1998), A comparison of a model for the theta aurora with observations from Polar, Wind, and SuperDARN, *J. Geophys. Res.*, *103*(A8), 17,367–17,390.

Chapman, S. (1931), The absorption and dissociative or ionizing effect of monochromatic radiation in an atmosphere on a rotating earth part II. Grazing incidence, *Proc. Phys. Soc.*, *43*(5), 483.

Chisham, G., M. Lester, S. E. Milan, M. P. Freeman, W. A. Bristow, A. Grocott, K. A. McWilliams, J. M. Ruohoniemi, T. K. Yeoman, P. L. Dyson, R. A. Greenwald, T. Kikuchi, M. Pinnock, J. P. S. Rash, N. Sato, G. J. Sofko, J.-P. Villain, and A. D. M. Walker (2007), A decade of the Super Dual Auroral Radar Network (SuperDARN): scientific achievements, new techniques and future directions, *Surv. Geophys.*, *28*, 33–109.

Chiu, Y. T. (1989), Formation of polar cap arcs, *Geophys. Res. Lett.*, *16*(7), 743–746.

Chu, X., T.-S. Hsu, R. L. McPherron, V. Angelopoulos, Z. Pu, J. J. Weygand, K. Khurana, M. Connors, J. Kissinger, H. Zhang, and O. Amm (2014), Development and validation of inversion technique for substorm current wedge using ground magnetic field data, *J. Geophys. Res.*, *119*(3), 1909–1924, 2013JA019185.

Chu, X., R. L. McPherron, T.-S. Hsu, and V. Angelopoulos (2015), Solar cycle dependence of substorm occurrence and duration: Implications for onset, *J. Geophys. Res.*, *120*(4), 2808–2818, 2015JA021104.

Clauer, C. R., Z. Xu, M. Maimaiti, J. M. Ruohoneimi, W. Scales, M. D. Hartinger, M. J. Nicolls, S. Kaeppler, F. D. Wilder, and R. E. Lopez (2016), Investigation of a rare event where the polar ionospheric reverse convection potential does not saturate during a period of extreme northward IMF solar wind driving, *J. Geophys. Res.*, *121*(6), 5422–5435, 2016JA022557.

Cousins, E. D. P., and S. G. Shepherd (2010), A dynamical model of high-latitude convection derived from SuperDARN plasma drift measurements, *J. Geophys. Res.*, *115*(A12), a12329.

Cowley, S. W. H. (1981), Magnetospheric asymmetries associated with the y-component of the IMF, *Planet. Space Sci.*, *29*, 79–96.

Cowley, S. W. H. (1983), *Interpretation of Observed Relations between Solar Wind Characteristics and Effects at Ionospheric Altitudes*, pp. 225–249, Springer US, Boston, MA.

Cowley, S. W. H. (2013), *Evidence for the Occurrence and Importance of Reconnection Between the Earth's Magnetic Field and the Interplanetary Magnetic Field*, pp. 375–378, American Geophysical Union.

Cowley, S. W. H., and M. Lockwood (1992), Excitation and decay of solar wind-driven flows in the magnetosphere-ionosphere system, *Ann. Geophys.*, *10*, 103–115.

Craven, J. D., J. S. Murphree, L. A. Frank, and L. L. Cogger (1991), Simultaneous optical observations of transpolar arcs in the two polar caps, *Geophys. Res. Lett.*, *18*(12), 2297–2300.

Crooker, N. U., and F. J. Rich (1993), Lobe cell convection as a summer phenomenon, *J. Geophys. Res.*, *98*(A8), 13,403–13,407.

Crooker, N. U., S. W. Kahler, D. E. Larson, and R. P. Lin (2004), Large-scale magnetic field inversions at sector boundaries, *J. Geophys. Res.*, *109*(A3), a03108.

Cumnock, J. A., R. A. Heelis, M. R. Hairston, and P. T. Newell (1995), High-latitude ionospheric convection pattern during steady northward interplanetary magnetic field, *J. Geophys. Res.*, *100*(A8), 14,537–14,555.

Cumnock, J. A., J. R. Sharber, R. A. Heelis, M. R. Hairston, and J. D. Craven (1997), Evolution of the global aurora during positive IMF Bz and varying IMF By conditions, *J. Geophys. Res.*, *102*(A8), 17,489–17,497.

Cumnock, J. A., L. G. Blomberg, A. Kullen, T. Karlsson, and K. Å. T. Sundberg (2009), Small-scale characteristics of extremely high latitude aurora, *Ann. Geophys.*, *27*, 3335–3347.

Dai, L., J. R. Wygant, C. A. Cattell, S. Thaller, K. Kersten, A. Breneman, X. Tang, R. H. Friedel, S. G. Claudepierre, and X. Tao (2014), Evidence for injection of relativistic electrons into the Earth's outer radiation belt via intense substorm electric fields, *Geophys. Res. Lett.*, *41*(4), 1133–1141.

Davis, T. N. (1963), Negative correlation between polar-cap visual aurora and magnetic activity, *J. Geophys. Res.*, *68*(15), 4447–4453.

Davis, T. N., and M. Sugiura (1966), Auroral electrojet activity index AE and its universal time variations, *J. Geophys. Res.*, *71*(3), 785–801.

de la Beaujardiere, O., D. Alcayde, J. Fontanari, and C. Leger (1991), Seasonal dependence of high-latitude electric fields, *J. Geophys. Res.*, *96*(A4), 5723–5735.

DeForest, S. E., and C. E. McIlwain (1971), Plasma clouds in the magnetosphere, *J. Geophys. Res.*, *76*(16), 3587–3611.

Denholm, J. V. (1961), Some auroral observations inside the southern auroral zone, *J. Geophys. Res.*, *66*(7), 2105–2111.

Denton, M. H., J. E. Borovsky, and T. E. Cayton (2010), A density-temperature description of the outer electron radiation belt during geomagnetic storms, *J. Geophys. Res.*, *115*(A1), a01208.

Donovan, E. F., T. Trondsen, L. L. Cogger, and B. J. Jackel (2003), All-sky imaging within the Canadian CANOPUS and NORSTAR Project, *Sodankylä Geophys. Obs. Publ.*, *92*, 109–112.

Dungey, J. W. (1961), Interplanetary Magnetic Field and the Auroral Zones, *Phys. Rev. Lett.*, *6*, 47–48.

Dungey, J. W. (1963), *Geophysics, The Earth's Environment*, chap. The structure of the exosphere or adventures in velocity space, pp. 505–550, Gordon and Breach, New York.

Elphinstone, R. D., and D. J. Hearn (1993), The auroral distribution and its relation to magnetospheric processes, *Adv. Space Res.*, *13*, 17–27.

Elphinstone, R. D., K. Jankowska, J. S. Murphree, and L. L. Cogger (1990), The configuration of the auroral distribution for interplanetary magnetic field Bz northward: 1. IMF Bx and By dependencies as observed by the Viking satellite, *J. Geophys. Res.*, *95*(A5), 2156–2202.

Elvey, C. T., H. Leinbach, J. Hessler, and J. Noxon (1955), Preliminary studies of the distribution of auroras in Alaska, *Eos, Transactions American Geophysical Union*, *36*(3), 390–394.

Emery, B. A., I. G. Richardson, D. S. Evans, and F. J. Rich (2009), Solar wind structure sources and periodicities of auroral electron power over three solar cycles, *J. Atmos. Sol. Terr. Phys.*, *71*, 1157–1175.

Fairfield, D. H., and L. J. Cahill Jr (1966), Transition region magnetic field and polar magnetic disturbances, *J. Geophys. Res.*, *71*, 155–169.

Fairfield, D. H., and N. F. Ness (1970), Configuration of the geomagnetic tail during substorms, *J. Geophys. Res.*, *75*(34), 7032–7047.

Fear, R., S. Milan, R. Maggiolo, A. N. Fazakerley, I. Dandouras, and S. B. Mende (2014), Direct observation of closed magnetic flux trapped in the high-latitude magnetosphere, *Science*, *346*(6216), 1506–1510.

Fejer, B. G., and M. C. Kelley (1980), Ionospheric irregularities, *Rev. Geophys.*, *18*(2), 401–454.

Feldstein, Y. I. (1969), Polar auroras, polar substorms, and their relationships with the dynamics of the magnetosphere, *Rev. Geophys.*, *7*(1-2), 179–218.

Feldstein, Y. I., P. T. Newell, I. Sandahl, J. Woch, S. V. Leontjev, and V. G. Vorobjev (1995), Structure of auroral precipitation during a theta aurora from multisatellite observations, *J. Geophys. Res.*, *100*(A9), 17,429–17,442.

Fiori, R. A. D., D. H. Boteler, A. V. Koustov, G. V. Haines, and J. M. Ruohoniemi (2010), Spherical cap harmonic analysis of Super Dual Auroral Radar Network (SuperDARN) observations for generating maps of ionospheric convection, *J. Geophys. Res.*, *115*(A7), a07307.

Fiori, R. A. D., D. H. Boteler, and A. V. Koustov (2012), Response of ionospheric convection to sharp southward IMF turnings inferred from magnetometer and radar data, *J. Geophys. Res.*, *117*(A9), a09302.

Fiori, R. A. D., A. V. Koustov, D. H. Boteler, D. J. Knudsen, and J. K. Burchill (2016), Calibration and assessment of swarm ion drift measurements using a comparison with a statistical convection model, *Earth, Planets and Space*, *68*(1), 100.

Fok, M.-C., T. E. Moore, and W. N. Spjeldvik (2001), Rapid enhancement of radiation belt electron fluxes due to substorm dipolarization of the geomagnetic field, *J. Geophys. Res.*, *106*(A3), 3873–3881.

Förster, M., and S. Haaland (2015), Interhemispheric differences in ionospheric convection: Cluster EDI observations revisited, *J. Geophys. Res.*, *120*(7), 5805–5823, 2014JA020774.

Forsyth, C., I. J. Rae, J. C. Coxon, M. P. Freeman, C. M. Jackman, J. Gjerloev, and A. N. Fazakerley (2015), A new technique for determining Substorm Onsets and Phases from Indices of the Electrojet (SOPHIE), *J. Geophys. Res.*, *120*(12), 10,592–10,606, 2015JA021343.

Foster, J. C., and H. B. Vo (2002), Average characteristics and activity dependence of the subauroral polarization stream, *J. Geophys. Res.*, *107*(A12), SIA 16–1–SIA 16–10, 1475.

Frank, L. A., and K. L. Ackerson (1971), Observations of charged particle precipitation into the auroral zone, *J. Geophys. Res.*, *76*(16), 3612–3643.

Frank, L. A., J. D. Craven, J. L. Burch, and J. D. Winningham (1982), Polar views of the Earth's aurora with Dynamics Explorer, *Geophys. Res. Lett.*, *9*, 1001–1004.

Frank, L. A., J. D. Craven, D. A. Gurnett, S. D. Shawhan, D. R. Weimer, J. L. Burch, J. D. Winningham, C. R. Chappell, J. H. Waite, R. A. Heelis, N. C. Maynard, M. Sugiura, W. K. Peterson, and E. Shelley (1986), The theta aurora, *J. Geophys. Res.*, *91*, 3177–3224.

Freeman, M. P., and S. K. Morley (2004), A minimal substorm model that explains the observed statistical distribution of times between substorms, *Geophys. Res. Lett.*, *31*(12), l12807.

Freeman, M. P., and S. K. Morley (2009), No evidence for externally triggered substorms based on superposed epoch analysis of IMF Bz, *Geophys. Res. Lett.*, *36*(21), l21101.

Frey, H. U., and S. B. Mende (2006), Substorm onsets as observed by IMAGE-FUV, in *Proceedings of Eighth International Substorm Conference*, edited by M. Syrjsuo and E. Donovan, p. 7176, Univ. of Calgary, Banff Centre, Canada.

Frey, H. U., S. B. Mende, V. Angelopoulos, and E. F. Donovan (2004), Substorm onset observations by IMAGE-FUV, *J. Geophys. Res.*, *109*(A10), a10304.

Friedel, R. H. W., G. D. Reeves, and T. Obara (2002), Relativistic electron dynamics in the inner magnetosphere - a review, *J. Atmos. Sol. Terr. Phys.*, *64*, 265–282.

Friis-Christensen, E., H. Lhr, D. Knudsen, and R. Haagmans (2008), Swarm - An earth Observation Mission investigating Geospace, *Adv. Space Res.*, *41*(1), 210–216.

Fuselier, S. A., B. J. Anderson, and T. G. Onsager (1997), Electron and ion signatures of field line topology at the low-shear magnetopause, *J. Geophys. Res.*, *102*(A3), 4847–4863.

Gallaher, H. A. (1997), Radar and optical observations of plasma convection associated with very high-latitude auroral arcs, Ph.D. thesis, Boston Colledge.

Ghezelbash, M., A. V. Koustov, D. R. Themens, and P. T. Jayachandran (2014), Seasonal and diurnal variations of PolarDARN F region echo occurrence in the polar cap and their causes, *J. Geophys. Res.*, *119*(12), 10,426–10,439, 2014JA020726.

Gillies, R. G., A. van Eyken, E. Spanswick, M. Nicolls, J. Kelly, M. Greffen, D. Knudsen, M. Connors, M. Schutzer, T. Valentic, M. Malone, J. Buonocore, J.-P. St.-Maurice, and E. Donovan (2016), First observations from the RISR-C incoherent scatter radar, *Radio Sci.*, *51*(10), 1645–1659, 2016RS006062.

Gjerloev, J. W. (2012), The SuperMAG data processing technique, *J. Geophys. Res.*, *117*(A9), a09213.

Golovchanskaya, I. V., A. Kullen, Y. P. Maltsev, and H. Biernat (2006), Ballooning instability at the plasma sheetlobe interface and its implications for polar arc formation, *J. Geophys. Res.*, *111*(A11), a11216.

Gondarenko, N. A., and P. N. Guzdar (2004), Plasma patch structuring by the nonlinear evolution of the gradient drift instability in the high-latitude ionosphere, *J. Geophys. Res.*, *109*(A9), a09301.

Gonzalez, W. D., and F. S. Mozer (1974), A quantitative model for the potential resulting from reconnection with an arbitrary interplanetary magnetic field, *J. Geophys. Res.*, *79*(28), 4186–4194.

Gorney, D. J., D. S. Evans, M. S. Gussenhoven, and P. F. Mizera (1986), A multiple-satellite observation of the high-latitude auroral activity on January 11, 1983, *J. Geophys. Res.*, *91*(A1), 339–346.

Greenspan, M. E., P. B. Anderson, and J. M. Pelagatti (1986), Characteristics of the Thermal Plasma Monitor (SSIES) (Special Sensor for Ions, Electrons, and Scintillation) for the Defense Meteorological Satellite Program (DMSP) Spacecraft S8 through S10, *Tech. Rep. AFGL-TR-86-0227*, Air Force Geophys. Lab., Hanscom Air Force Base, Mass.

Greenwald, R. A., W. A. Bristow, G. J. Sofko, C. Senior, J.-C. Cerisier, and A. Szabo (1995), Super dual auroral radar network radar imaging of dayside high-latitude convection under northward interplanetary magnetic field: Toward resolving the distorted two-cell versus multicell controversy, *J. Geophys. Res.*, *100*(A10), 19,661–19,674.

Guo, J., T. I. Pulkkinen, E. I. Tanskanen, X. Feng, B. A. Emery, H. Liu, C. Liu, and D. Zhong (2014), Annual variations in westward auroral electrojet and substorm occurrence rate during solar cycle 23, *J. Geophys. Res.*, *119*(3), 2061–2068.

Gusev, M. G., and O. A. Troshichev (1990), Relation of sun-aligned arcs to polar cap convection and magnetic disturbances, *Planet. Space Sci.*, *38*, 1–7.

Gussenhoven, M. S., and E. G. Mullen (1989), Simultaneous relativistic electron and auroral particle access to the polar caps during interplanetary magnetic field Bz northward: A scenario for an open field line source of auroral particles, *J. Geophys. Res.*, *94*(A12), 17,121–17,132.

Gustafsson, G. (1967), On the orientation of auroral arcs, *Planet. Space Sci.*, *15*, 277–294.

Gustafsson, G., N. E. Papitashvili, and V. O. Papitashvili (1992), A revised corrected geomagnetic coordinate system for Epochs 1985 and 1990, *J. Atmos. Terr. Phys.*, *54*, 1609–1631.

Haaland, S. E., G. Paschmann, M. Förster, J. M. Quinn, R. B. Torbert, C. E. McIlwain, H. Vaith, P. A. Puhl-Quinn, and C. A. Kletzing (2007), High-latitude plasma convection from Cluster EDI measurements: method and IMF-dependence, *Ann. Geophys.*, *25*(1), 239–253.

Hardy, D. A. (1984), Intense fluxes of low-energy electrons at geomagnetic latitudes above 85°, *J. Geophys. Res.*, *89*(A6), 3883–3892.

Hardy, D. A., W. J. Burke, and M. S. Gussenhoven (1982), DMSP optical and electron measurements in the vicinity of polar cap arcs, *J. Geophys. Res.*, *87*(A4), 2413–2430.

Hargreaves, J. (1992), *The Solar-Terrestrial Environment: An Introduction to Geospace - the Science of the Terrestrial Upper Atmosphere, Ionosphere, and Magnetosphere*, Cambridge Atmospheric and Space Science Series, Cambridge University Press.

He, Z., H. Zhu, S. Liu, Q. Zong, Y. Wang, R. Lin, L. Shi, and J. Gong (2014), Correlated observations and simulations on the buildup of radiation belt electron fluxes driven by substorm injections and chorus waves, *Astrophys. Space Sci.*, *355*(2), 245–251.

Heelis, R. A., P. H. Reiff, J. D. Winningham, and W. B. Hanson (1986), Ionospheric convection signatures observed by De 2 during northward interplanetary magnetic field, *J. Geophys. Res.*, *91*(A5), 5817–5830.

Henderson, M. G. (2004), The May 23, 1986 CDAW-9C interval: A sawtooth event, *Geophys. Res. Lett.*, *31*(11), l11804.

Henderson, M. G., G. D. Reeves, R. Skoug, M. F. Thomsen, M. H. Denton, S. B. Mende, T. J. Immel, P. C. Brandt, and H. J. Singer (2006a), Magnetospheric and auroral activity during the 18 April 2002 sawtooth event, *J. Geophys. Res.*, *111*(A1), a01S90.

Henderson, M. G., R. Skoug, E. Donovan, M. F. Thomsen, G. D. Reeves, M. H. Denton, H. J. Singer, R. L. McPherron, S. B. Mende, T. J. Immel, J. B. Sigwarth, and L. Frank (2006b), Substorms during the 10-11 August 200 sawtooth event, *J. Geophys. Res.*, *111*(A06206).

Heppner, J. P., and N. C. Maynard (1987), Empirical high-latitude electric field models, *J. Geophys. Res.*, *92*(A5), 4467–4489.

Hill, T. W., A. J. Dessler, and R. A. Wolf (1976), Mercury and Mars: The role of ionospheric conductivity in the acceleration of magnetospheric particles, *Geophys. Res. Lett.*, *3*(8), 429–432.

Hoffman, R. A., R. A. Heelis, and J. S. Prasad (1985), A Sun-aligned arc observed by DMSP and AE-C, *J. Geophys. Res.*, *90*(A10), 9697–9710.

Hones, E. W. (1977), Substorm processes in the magnetotail: Comments on On hot tenuous plasmas, fireballs, and boundary layers in the Earth's magnetotail by L. A. Frank, K. L. Ackerson, and R. P. Lepping, *J. Geophys. Res.*, *82*(35), 5633–5640.

Hones, E. W., T. A. Fritz, J. Birn, J. Cooney, and S. J. Bame (1986), Detailed observations of the plasma sheet during a substorm on April 24, 1979, *J. Geophys. Res.*, *91*(A6), 6845–6859.

Hosokawa, K., J. I. Moen, K. Shiokawa, and Y. Otsuka (2011), Motion of polar cap arcs, *J. Geophys. Res.*, *116*(A1), A01305.

Hsu, T.-S., and R. L. McPherron (2002), An evaluation of the statistical significance of the association between northward turnings of the interplanetary magnetic field and substorm expansion onsets, *J. Geophys. Res.*, *107*(A11), SMP 31–1–SMP 31–15, 1398.

Hsu, T.-S., and R. L. McPherron (2009), A statistical study of the spatial structure of interplanetary magnetic field substorm triggers and their associated magnetic response, *J. Geophys. Res.*, *114*(A2), A02223.

Hsu, T.-S., and R. L. McPherron (2012), A statistical analysis of substorm associated tail activity, *Adv. Space Res.*, *50*, 1317.

Huang, C.-S., D. A. Andre, G. J. Sofko, and A. V. Kustov (2000a), Super Dual Auroral Radar Network observations of ionospheric multicell convection during northward interplanetary magnetic field, *J. Geophys. Res.*, *105*(A4), 7419–7428.

Huang, C.-S., G. J. Sofko, A. V. Koustov, D. A. Andre, J. M. Ruohoniemi, R. A. Greenwald, and M. R. Hairston (2000b), Evolution of ionospheric multicell convection during northward interplanetary magnetic field with $|B_z/B_y| > 1$, *J. Geophys. Res.*, *105*(A12), 27,095–27,107.

Huang, C.-S., G. D. Reeves, J. E. Borovsky, R. M. Skoug, Z. Y. Pu, and G. Le (2003a), Periodic magnetospheric substorms and their relationship with solar wind variations, *J. Geophys. Res.*, *108*(A6), 1255.

Huang, C.-S., J. C. Foster, G. D. Reeves, G. Le, H. U. Frey, C. J. Pollock, and J.-M. Jahn (2003b), Periodic magnetospheric substorms: Multiple space-based and ground-based instrumental observations, *J. Geophys. Res.*, *108*(A11), 1411.

Huang, C.-S., G. Le, and G. D. Reeves (2004), Periodic magnetospheric substorms during fluctuating interplanetary magnetic field Bz, *Geophys. Res. Lett.*, *31*(14), l14801.

Huang, C.-S., G. D. Reeves, G. Le, and K. Yumoto (2005), Are sawtooth oscillations of energetic plasma particle fluxes caused by periodic substorms or driven by solar wind pressure enhancements?, *J. Geophys. Res.*, *110*(A7), a07207.

Huang, C. Y., L. A. Frank, W. K. Peterson, D. J. Williams, W. Lennartsson, D. G. Mitchell, R. C. Elphic, and C. T. Russell (1987), Filamentary structures in the magnetotail lobes, *J. Geophys. Res.*, *92*(A3), 23492363.

Iijima, T., and T. A. Potemra (1976), The amplitude distribution of field-aligned currents at northern high latitudes observed by Triad, *J. Geophys. Res.*, *81*(13), 2165–2174.

Ingraham, J. C., T. E. Cayton, R. D. Belian, R. A. Christensen, R. H. W. Friedel, M. M. Meier, G. D. Reeves, and M. Tuszewski (2001), Substorm injection of relativistic electrons to geosynchronous orbit during the great magnetic storm of March 24, 1991, *J. Geophys. Res.*, *106*(A11), 25,759–25,776.

International Telegraph, and Telephone Corporation (1979), *Reference data for radio engineers*, sec.42-5, Howard Sams, Indianapolis.

Ismail, S., D. D. Wallis, and L. L. Cogger (1977), Characteristics of polar cap Sun-aligned arcs, *J. Geophys. Res.*, *82*(29), 4741–4749.

Jackel, B. J., B. McKiernan, and H. J. Singer (2012), Geostationary magnetic field response to solar wind pressure variations: Time delay and local time variation, *J. Geophys. Res.*, *117*(A5), a05203.

Jayachandran, P. T., and J. W. MacDougall (2001), Sunward polar cap convection, *J. Geophys. Res.*, *106*(A12), 29,009–29,025.

Jayachandran, P. T., J. W. MacDougall, E. F. Donovan, J. M. Ruohoniemi, K. Liou, D. R. Moorcroft, and J.-P. St-Maurice (2003), Substorm associated changes in the high-latitude ionospheric convection, *Geophys. Res. Lett.*, *30*(20), 2064.

Jonas, S., and E. D. McCarron (2016), White House Releases National Space Weather Strategy and Action Plan, *Space Weather*, *14*(2), 54–55, 2015SW001357.

Kabin, K., R. Rankin, G. Rostoker, R. Marchand, I. J. Rae, A. J. Ridley, T. I. Gombosi, C. R. Clauer, and D. L. DeZeeuw (2004), Open-closed field line boundary position: A parametric study using an MHD model, *J. Geophys. Res.*, *109*(A5), a05222.

Kahler, S., and R. P. Lin (1994), The determination of interplanetary magnetic field polarities around sector boundaries using E> 2 keV electrons, *Geophys. Res. Lett.*, *21*(15), 1575–1578.

Kamide, Y., and C. E. McIlwain (1974), The onset time of magnetospheric substorms determined from ground and synchronous satellite records, *J. Geophys. Res.*, *79*(31), 4787–4790.

Kan, J. R., and L. C. Lee (1979), Energy coupling function and solar wind-magnetosphere dynamo, *Geophys. Res. Lett.*, *6*(7), 577–580.

Kepko, L., R. L. McPherron, O. Amm, S. Apatenkov, W. Baumjohann, J. Birn, M. Lester, R. Nakamura, T. I. Pulkkinen, and V. Sergeev (2015), Substorm Current Wedge Revisited, *Space Sci. Rev.*, *190*(1), 1–46.

Keskinen, M. J., and S. L. Ossakow (1982), Nonlinear evolution of plasma enhancements in the auroral ionosphere, 1, Long wavelength irregularities, *J. Geophys. Res.*, *87*(A1), 144–150.

Khorosheva, O. V. (1967), Spatial-temporal distribution of aurorae, *Aurorae (in Russian)*, *16*, 1–84.

Kim, H.-J., A. A. Chan, R. A. Wolf, and J. Birn (2000), Can substorms produce relativistic outer belt electrons?, *J. Geophys. Res.*, *105*(A4), 7721–7735.

King, J. H., and N. E. Papitashvili (2005), Solar wind spatial scales in and comparisons of hourly Wind and ACE plasma and magnetic field data, *J. Geophys. Res.*, *110*(A2), a02104.

Kivelson, M., and C. Russell (1995), *Introduction to Space Physics*, Cambridge atmospheric and space science series, Cambridge University Press.

Klein, L. W., and L. F. Burlaga (1982), Interplanetary magnetic clouds At 1 AU, *J. Geophys. Res.*, *87*(A2), 613–624.

Knipp, D. J., C.-H. Lin, B. A. Emery, J. M. Ruohoniemi, F. J. Rich, and D. S. Evans (2000), Hemispheric asymmetries in ionospheric electrodynamics during the solar wind void of 11 May 1999, *Geophys. Res. Lett.*, *27*(24), 4013–4016.

Knudsen, D. J., J. K. Burchill, K. Berg, T. Cameron, G. A. Enno, C. G. Marcellus, E. P. King, I. Wevers, and R. A. King (2003), A low-energy charged particle distribution imager with a compact sensor for space applications, *Rev. Sci. Instrum.*, *74*(1), 202–211.

Knudsen, D. J., J. K. Burchill, S. C. Buchert, A. I. Eriksson, R. Gill, J.-E. Wahlund, L. hlen, M. Smith, and B. Moffat (2017), Thermal ion imagers and Langmuir probes in the Swarm electric field instruments, *J. Geophys. Res.*, *122*(2), 2655–2673, 2016JA022571.

Koustov, A., N. Nishitani, Y. Ebihara, T. Kikuchi, M. R. Hairston, and D. Andre (2008), Subauroral polarization streams: observations with the Hokkaido and King Salmon SuperDARN radars and modeling, *Ann. Geophys.*, *26*(11), 3317–3327.

Koustov, A. V., and R. A. D. Fiori (2016), Seasonal and solar cycle variations in the ionospheric convection reversal boundary location inferred from monthly SuperDARN data sets, *Ann. Geophys.*, *34*(2), 227–239.

Koustov, A. V., D. W. Danskin, R. A. Makarevitch, and J. D. Gorin (2005), On the relationship between the velocity of E-region HF echoes and ExB plasma drift, *Ann. Geophys.*, *23*(2), 371–378.

Koustov, A. V., K. Hosokawa, N. Nishitani, K. Shiokawa, and H. Liu (2012), Signatures of moving polar cap arcs in the F-region PolarDARN echoes, *Ann. Geophys.*, *30*(3), 441–455.

Koustov, A. V., K. Colville, R. Fiori, and M. Ghezelbash (2013), Assessing Doppler velocities of Rankin Inlet F-region echoes, *Advances in Polar Science*, *24*(1), 50–59.

Koustov, A. V., P. V. Ponomarenko, M. Ghezelbash, D. R. Themens, and P. T. Jayachandran (2014), Electron density and electric field over Resolute Bay and F region ionospheric echo detection with the Rankin Inlet and Inuvik SuperDARN radars, *Radio Sci.*, *49*(12), 1194–1205, 2014RS005579.

Koustov, A. V., R. A. D. Fiori, and Z. Abooali zadeh (2015), Long-term variations in the intensity of polar cap plasma flows inferred from SuperDARN, *J. Geophys. Res.*, *120*(11), 9722–9737, 2015JA021625.

Koustov, A. V., K. N. Yakymenko, and P. V. Ponomarenko (2017), Seasonal effect for polar cap sunward plasma flows at strongly northward IMF Bz, *J. Geophys. Res.*, *122*(2), 2530–2541, 2016JA023556.

Kozlovsky, A., A. Koustov, W. Lyatsky, J. Kangas, G. Parks, and D. Chua (2002), Ionospheric convection in the postnoon auroral oval: Super Dual Auroral Radar Network (SuperDARN) and polar ultraviolet imager (UVI) observations, *J. Geophys. Res.*, *107*(A12), SIA 6–1–SIA 6–16, 1433.

Kozlovsky, A., V. Safargaleev, N. Østgaard, T. Turunen, A. Koustov, J. Jussila, and A. Roldugin (2005), On the motion of dayside auroras caused by a solar wind pressure pulse, *Ann. Geophys.*, *23*(2), 509–521.

Kozlovsky, A., M. Meurant, and T. Turunen (2007), Changes of dayside auroral distribution caused by a solar wind pressure pulse and associated interplanetary magnetic field disturbances, *Ann. Geophys.*, *25*(4), 929–940.

Kozlovsky, A. E., V. V. Safargaleev, J. R. T. Jussila, and A. V. Koustov (2003), Pre-noon high-latitude auroral arcs as a manifestation of the interchange instability, *Ann. Geophys.*, *21*(12), 2303–2314.

Kozyreva, O., V. Pilipenko, M. J. Engebretson, K. Yumoto, J. Watermann, and N. Romanova (2007), In search of a new ULF wave index: Comparison of Pc5 power with dynamics of geostationary relativistic electrons, *Planet. Space Sci.*, *55*, 755–769.

Kullen, A. (2000), The connection between transpolar arcs and magnetotail rotation, *Geophys. Res. Lett.*, *27*(1), 73–76.

Kullen, A., M. Brittnacher, J. A. Cumnock, and L. G. Blomberg (2002), Solar wind dependence of the occurrence and motion of polar auroral arcs: A statistical study, *J. Geophys. Res.*, *107*(A11), 13–1–13–23, 1362.

Lamarche, L. J., and R. A. Makarevich (2016), A modeling study of asymmetries in plasma irregularity characteristics near gradient reversals, *Ann. Geophys.*, *34*(9), 709–723.

Lanzerotti, L. J., C. G. Maclennan, and M. F. Robbins (1971), Proton drift echoes in the magnetosphere, *J. Geophys. Res.*, *76*(1), 259–263.

Lassen, K., and C. Danielsen (1978), Quiet time pattern of auroral arcs for different directions of the interplanetary magnetic field in the Y-Z plane, *J. Geophys. Res.*, *83*(A11), 5277–5284.

Lavraud, B., and J. E. Borovsky (2008), Altered solar wind-magnetosphere interaction at low Mach numbers: Coronal mass ejections, *J. Geophys. Res.*, *113*(A9), a00B08.

Lavraud, B., J. E. Borovsky, A. J. Ridley, E. W. Pogue, M. F. Thomsen, H. Rme, A. N. Fazakerley, and E. A. Lucek (2007), Strong bulk plasma acceleration in Earth's magnetosheath: A magnetic slingshot effect?, *Geophys. Res. Lett.*, *34*(14), l14102.

Lavraud, B., E. Larroque, E. Budnik, V. Gnot, J. E. Borovsky, M. W. Dunlop, C. Foullon, H. Hasegawa, C. Jacquey, K. Nykyri, A. Ruffenach, M. G. G. T. Taylor, I. Dandouras, and H. Rme (2013), Asymmetry of magnetosheath flows and magnetopause shape during low Alfvn Mach number solar wind, *J. Geophys. Res.*, *118*(3), 1089–1100.

Lee, D.-Y., and K. W. Min (2002), Statistical features of substorm indicators during geomagnetic storms, *J. Geophys. Res.*, *107*(A11), SMP 16–1–SMP 16–12, 1371.

Lennartsson, W. (1989), Energetic (0.1- to 16-keV/e) magnetospheric ion composition at different levels of solar F10.7, *J. Geophys. Res.*, *94*(A4), 3600–3610.

Lepping, R. P., C.-C. Wu, and D. B. Berdichevsky (2005), Automatic identification of magnetic clouds and cloud-like regions at 1 AU: occurrence rate and other properties, *Ann. Geophys.*, *23*(7), 2687–2704.

Lezniak, T. W., R. L. Arnoldy, G. K. Parks, and J. R. Winckler (1968), Measurement and Intensity of Energetic Electrons at the Equator at 6.6 Re, *Radio Sci.*, *3*(7), 710–714.

Lin, C., and R. Hoffman (1979), Fluctuations of inverted V electron fluxes, *J. Geophys. Res.*, *84*(A11), 6547–6553.

Liou, K. (2010), Polar Ultraviolet Imager observation of auroral breakup, *J. Geophys. Res.*, *115*(A12), a12219.

Liou, K., J. M. Ruohoniemi, P. T. Newell, R. Greenwald, C.-I. Meng, and M. R. Hairston (2005), Observations of ionospheric plasma flows within theta auroras, *J. Geophys. Res.*, *110*(A3), a03303.

Lockwood, M., and J. Moen (1999), Reconfiguration and closure of lobe flux by reconnection during northward IMF: possible evidence for signatures in cusp/cleft auroral emissions, *Ann. Geophys.*, *17*(8), 996–1011.

Lopez, R. E., M. Wiltberger, S. Hernandez, and J. G. Lyon (2004), Solar wind density control of energy transfer to the magnetosphere, *Geophys. Res. Lett.*, *31*(8), l08804.

Lopez, R. E., K. S. Hernandez, R. Hallman, J. Valenzuela, P. C. A. Seiler, and M. R. Hairston (2008), Field-aligned currents in the polar cap during saturation of the polar cap potential, *J. Atmos. Sol. Terr. Phys.*, *70*(2), 555–563.

Lu, G., A. D. Richmond, B. A. Emery, P. H. Reiff, O. de la Beaujardire, F. J. Rich, W. F. Denig, H. W. Kroehl, L. R. Lyons, J. M. Ruohoniemi, E. Friis-Christensen, H. Opgenoorth, M. A. L. Persson, R. P. Lepping, A. S. Rodger, T. Hughes, A. McEwin, S. Dennis, R. Morris, G. Burns, and L. Tomlinson (1994), Interhemispheric asymmetry of the high-latitude ionospheric convection pattern, *J. Geophys. Res.*, *99*(A4), 6491–6510.

Lundin, R., L. Eliasson, and J. S. Murphree (1991), The quiet-time aurora and the magnetospheric configuration., in *Auroral Physics*, pp. 177–193.

Lyons, L. R., G. T. Blanchard, J. C. Samson, R. P. Lepping, T. Yamamoto, and T. Moretto (1997), Coordinated observations demonstrating external substorm triggering, *J. Geophys. Res.*, *102*(A12), 27,039–27,051.

Lyons, L. R., S. Liu, J. M. Ruohoniemi, S. I. Solovyev, and J. C. Samson (2003), Observations of dayside convection reduction leading to substorm onset, *J. Geophys. Res.*, *108*(A3), 1119.

Maggiolo, R., M. Echim, J. D. Keyser, D. Fontaine, C. Jacquey, and I. Dandouras (2011), Polar cap ion beams during periods of northward IMF: Cluster statistical results, *Ann. Geophys.*, *29*, 771–787.

Maimaiti, M., J. M. Ruohoniemi, J. B. H. Baker, C. R. Clauer, M. J. Nicolls, and M. R. Hairston (2017), RISR-N observations of the IMF By influence on reverse convection during extreme northward IMF, *J. Geophys. Res.*, *122*(3), 3707–3720, 2016JA023612.

Makita, K., C.-I. Meng, and S.-I. Akasofu (1991), Transpolar auroras, their particle precipitation, and IMF By component, *J. Geophys. Res.*, *96*(A8), 14,085–14,095.

Marklund, G. (1984), Auroral arc classification scheme based on the observed arc-associated electric field pattern, *Planet. Space Sci.*, *32*(2), 193–211.

Marklund, G. T., L. G. Blomberg, J. S. Murphree, R. D. Elphinstone, L. J. Zanetti, R. E. Erlandson, I. Sandahl, O. de la Beaujardire, H. Opgenoorth, and F. J. Rich (1991), On the electrodynamical state of the auroral ionosphere during northward interplanetary magnetic field: A Transpolar Arc Case Study, *J. Geophys. Res.*, *96*(A6), 9567–9578.

Mawson, D. (1916), Auroral observations at the Cape Royds station, Antarctica, *Proc. Roy. Soc. S. Aust.*, ***XL***, 151.

Mawson, D. (1925), Records of the Aurora Polaris, Australasian Antarctic expedition 1911-1914, *Sci. Rept.*, ***B***, 11.

McAllister, A. H., M. Dryer, P. Mclntosh, H. Singer, and L. Weiss (1996), A large polar crown coronal mass ejection and a problem goemagnetic storm: April 1423, 1994, *J. Geophys. Res.*, *101*(A6), 13,497–13,515.

McComas, D. J., S. J. Bame, B. L. Barraclough, J. R. Donart, R. C. Elphic, J. T. Gosling, M. B. Moldwin, K. R. Moore, and M. F. Thomsen (1993), Magnetospheric plasma analyzer: Initial three-spacecraft observations from geosynchronous orbit, *J. Geophys. Res.*, *98*(A8), 13,453–13,465.

McDiarmid, I. B., and J. R. Burrows (1965), On an electron source for the outer van allen radiation zone, *Can. J. Phys.*, *43*(6), 1161–1164.

McFadden, J. P., C. W. Carlson, and R. E. Ergun (1999), Microstructure of the auroral acceleration region as observed by FAST, *J. Geophys. Res.*, *104*(A7), 14,453–14,480.

McPherron, R. L., and X. Chu (2017), The Mid-Latitude Positive Bay and the MPB Index of Substorm Activity, *Space Sci. Rev.*, *206*(1), 91–122.

McPherron, R. L., C. T. Russell, and M. P. Aubry (1973a), Satellite studies of magnetospheric substorms on August 15, 1968: 9. Phenomenological model for substorms, *J. Geophys. Res.*, *78*(16), 3131–3149.

McPherron, R. L., C. T. Russell, M. G. Kivelson, and P. J. Coleman (1973b), Substorms in space: The correlation between ground and satellite observations of the magnetic field, *Radio Sci.*, *8*(11), 1059–1076.

Mcpherron, R. L., T. Terasawa, and A. Nishida (1986), Solar wind triggering of substorm expansion onset, *J. Geomagn. Geoelec.*, *38*(11).

Mende, S. B., J. H. Doolittle, R. M. Robinson, R. R. Vondrak, and F. J. Rich (1988), Plasma drifts associated with a system of Sun-aligned arcs in the polar cap, *J. Geophys. Res.*, *93*(A1), 256–264.

Mende, S. B., H. U. Frey, S. P. Geller, and J. H. Doolittle (1999), Multistation observations of auroras: Polar cap substorms, *J. Geophys. Res.*, *104*(A2), 2333–2342.

Mende, S. B., S. E. Harris, H. U. Frey, V. Angelopoulos, C. T. Russell, E. Donovan, B. Jackel, M. Greffen, and L. M. Peticolas (2009), *The THEMIS Array of Ground-based Observatories forthe Study of Auroral Substorms*, pp. 357–387, Springer New York, New York, NY.

Meng, C.-I. (1981), Polar cap arcs and the plasma sheet, *Geophys. Res. Lett.*, *8*(3), 273–276.

Menietti, J. D., and J. L. Burch (1987), DE 1 observations of theta aurora plasma source regions and Birkeland current charge carriers, *J. Geophys. Res.*, *92*(A7), 7503–7518.

Meredith, N. P., R. B. Horne, and R. R. Anderson (2001), Substorm dependence of chorus amplitudes: Implications for the acceleration of electrons to relativistic energies, *J. Geophys. Res.*, *106*(A7), 13,165–13,178.

Merkin, V. G., A. S. Sharma, K. Papadopoulos, G. Milikh, J. Lyon, and C. Goodrich (2005a), Global MHD simulations of the strongly driven magnetosphere: Modeling of the transpolar potential saturation, *J. Geophys. Res.*, *110*(A9), a09203.

Merkin, V. G., A. S. Sharma, K. Papadopoulos, G. Milikh, J. Lyon, and C. Goodrich (2005b), Relationship between the ionospheric conductance, field aligned current, and magnetopause geometry: Global MHD simulations, *Planet. Space Sci.*, *53*, 873–879.

Meurant, M., J.-C. Grard, B. Hubert, V. Coumans, C. Blockx, N. stgaard, and S. B. Mende (2003), Dynamics of global scale electron and proton precipitation induced by a solar wind pressure pulse, *Geophys. Res. Lett.*, *30*(20), 2032.

Moen, J., S. T. Berry, L. Kersley, and B. Lybekk (1998), Probing discrete auroral arcs by ionospheric tomography, *Ann. Geophys.*, *16*(5), 574–582.

Morley, S. K., and M. P. Freeman (2007), On the association between northward turnings of the interplanetary magnetic field and substorm onsets, *Geophys. Res. Lett.*, *34*(8), l08104.

Morley, S. K., and M. G. Henderson (2010), Comment on Investigation of the period of sawtooth events by X. Cai and C. R. Clauer, *J. Geophys. Res.*, *115*(A2), a02216.

Ness, N. F., and J. M. Wilcox (1965), Sector Structure of the Quiet Interplanetary Magnetic Field, *Science*, *148*(3677), 1592–1594.

Nevanlinna, H., and T. I. Pulkkinen (1998), Solar cycle correlations of substorm and auroral occurrence frequency, *Geophys. Res. Lett.*, *25*(16), 3087–3090.

Newell, P. T., and J. W. Gjerloev (2011), Evaluation of SuperMAG auroral electrojet indices as indicators of substorms and auroral power, *J. Geophys. Res.*, *116*(A12), a12211.

Newell, P. T., and K. Liou (2011), Solar wind driving and substorm triggering, *J. Geophys. Res.*, *116*(A3), a03229.

Newell, P. T., T. Sotirelis, K. Liou, C.-I. Meng, and F. J. Rich (2007), A nearly universal solar wind-magnetosphere coupling function inferred from 10 magnetospheric state variables, *J. Geophys. Res.*, *112*(A1), a01206.

Nielsen, E., J. D. Craven, L. A. Frank, and R. A. Heelis (1990), Ionospheric flows associated with a transpolar arc, *J. Geophys. Res.*, *95*(A12), 21,169–21,178.

Noah, M. A., and W. J. Burke (2013), Sawtooth-substorm connections: A closer look, *J. Geophys. Res.*, *118*(8), 5136–5148.

Nosé, M., T. Iyemori, L. Wang, A. Hitchman, J. Matzka, M. Feller, S. Egdorf, S. Gilder, N. Kumasaka, K. Koga, H. Matsumoto, H. Koshiishi, G. Cifuentes-Nava, J. J. Curto, A. Segarra, and C. elik (2012), Wp index: A new substorm index derived from high-resolution geomagnetic field data at low latitude, *Space Weather*, *10*(8), s08002.

Ober, D. M., N. C. Maynard, and W. J. Burke (2003), Testing the Hill model of transpolar potential saturation, *J. Geophys. Res.*, *108*(A12), 1467.

Ober, D. M., N. C. Maynard, W. J. Burke, G. R. Wilson, and K. D. Siebert (2006), Shoulders on the high-latitude magnetopause: Polar/GOES observations, *J. Geophys. Res.*, *111*(A10), A10213.

Opgenoorth, H. J., I. Haggstrom, P. J. S. Williams, and G. O. L. Jones (1990), Regions of strongly enhanced perpendicular electric fields adjacent to auroral arcs, *J. Atmos. Terr. Phys.*, *52*, 449–458.

Ouellette, J. E., O. J. Brambles, J. G. Lyon, W. Lotko, and B. N. Rogers (2013), Properties of outflow-driven sawtooth substorms, *J. Geophys. Res.*, *118*(6), 3223–3232.

Papitashvili, V. O., and F. J. Rich (2002), High-latitude ionospheric convection models derived from Defense Meteorological Satellite Program ion drift observations and parameterized by the interplanetary magnetic field strength and direction, *J. Geophys. Res.*, *107*(A8), SIA 17–1–SIA 17–13.

Papitashvili, V. O., B. A. Belov, D. S. Faermark, Y. I. Feldstein, S. A. Golyshev, L. I. Gromova, and A. E. Levitin (1994), Electric potential patterns in the northern and southern polar regions parameterized by the interplanetary magnetic field, *J. Geophys. Res.*, *99*(A7), 13,251–13,262.

Partamies, N., T. I. Pulkkinen, R. L. McPherron, K. McWilliams, C. R. Bryant, E. Tanskanen, H. J. Inger, G. D. Reeves, and M. F. Thomsen (2009), Statistical survey on sawtooth events, SMCs and isolated substorms, *Adv. Space Res.*, *44*, 376–384.

Perreault, P., and S.-I. Akasofu (1978), A study of geomagnetic storms, *Geophys. J. R. Astron. Soc.*, *54*(3), 547–573.

Perry, G. W., H. Dahlgren, M. J. Nicolls, M. Zettergren, J.-P. St.-Maurice, J. L. Semeter, T. Sundberg, K. Hosokawa, K. Shiokawa, and S. Chen (2015), Spatiotemporally resolved electrodynamic properties of a sun-aligned arc over resolute bay, *J. Geophys. Res.*, *120*(11), 9977–9987, 2015JA021790.

Peterson, W. K., and E. G. Shelley (1984), Origin of the plasma in a cross-polar cap auroral feature (theta aurora), *J. Geophys. Res.*, *89*(A8), 6729–6736.

Pettigrew, E. D., S. G. Shepherd, and J. M. Ruohoniemi (2010), Climatological patterns of high-latitude convection in the Northern and Southern hemispheres: Dipole tilt dependencies and interhemispheric comparisons, *J. Geophys. Res.*, *115*(A7), a07305.

Phan, T.-D., G. Paschmann, and B. U. . Sonnerup (1996), Low-latitude dayside magnetopause and boundary layer for high magnetic shear: 2. Occurrence of magnetic reconnection, *J. Geophys. Res.*, *101*(A4), 7817–7828.

Picone, J. M., A. E. Hedin, D. P. Drob, and A. C. Aikin (2002), NRLMSISE-00 empirical model of the atmosphere: Statistical comparisons and scientific issues, *J. Geophys. Res.*, *107*(A12), SIA 15–1–SIA 15–16, 1468.

Ponomarenko, P. V., J.-P. St-Maurice, C. L. Waters, R. G. Gillies, and A. V. Koustov (2009), Refractive index effects on the scatter volume location and Doppler velocity estimates of ionospheric HF backscatter echoes, *Ann. Geophys.*, *27*(11), 4207–4219.

Prichard, D., J. E. Borovsky, P. M. Lemons, and C. P. Price (1996), Time dependence of substorm recurrence: An information-theoretic analysis, *J. Geophys. Res.*, *101*(A7), 15,359–15,369.

Provan, G., M. Lester, S. B. Mende, and S. E. Milan (2004), Statistical study of high-latitude plasma flow during magnetospheric substorms, *Ann. Geophys.*, *22*(10), 3607–3624.

Pulkkinen, T. I., N. Partamies, R. L. McPherron, M. Henderson, G. D. Reeves, M. F. Thomsen, and H. J. Singer (2007), Comparative statistical analysis of storm time activations and sawtooth events, *J. Geophys. Res.*, *112*(A1), A01205.

Raeder, J., Y. Wang, T. Fuller-Rowell, and H. Singer (2001), Global Simulation of Magnetospheric Space Weather Effects of the Bastille Day Storm, *Sol. Phys.*, *204*(1), 323–337.

Rairden, R. L., and S. B. Mende (1989), Properties of 6300- auroral emissions at South Pole, *J. Geophys. Res.*, *94*(A2), 1402–1416.

Reeves, G. D., R. D. Belian, and T. A. Fritz (1991), Numerical tracing of energetic particle drifts in a model magnetosphere, *J. Geophys. Res.*, *96*(A8), 13,997–14,008.

Reeves, G. D., M. G. Henderson, P. S. McLachlan, R. D. Belian, R. H. W. Friedel, and A. Korth (1996), Radial propagation of substorm injections, in *International Conference on Substorms*, *ESA Special Publication*, vol. 389, edited by E. J. Rolfe and B. Kaldeich, p. 579.

Reiff, P. H. (1982), Sunward convection in both polar caps, *J. Geophys. Res.*, *87*(A8), 5976–5980.

Reiff, P. H., and J. L. Burch (1985), IMF By-dependent plasma flow and Birkeland currents in the dayside magnetosphere: 2. A global model for northward and southward IMF, *J. Geophys. Res.*, *90*(A2), 1595–1609.

Reiff, P. H., H. L. Collin, J. D. Craven, J. L. Burch, J. D. Winningham, E. G. Shelley, L. A. Frank, and M. A. Friedman (1988), Determination of auroral electrostatic potentials using high- and low-altitude particle distributions, *J. Geophys. Res.*, *93*(A7), 7441–7465.

Rich, F. J. (1984), Fluxgate Magnetometer (SSM) for the Defense Meteorological Satellite Program (DMSP) Block 5D-2, Flight 7, *Tech. Rep. ADA155229*, AIR FORCE GEOPHYSICS LAB HANSCOM AFB MA.

Rich, F. J., and M. Hairston (1994), Large-scale convection patterns observed by DMSP, *J. Geophys. Res.*, *99*(A3), 3827–3844.

Robinson, R. M., and S. B. Mende (1990), Ionization and electric field properties of auroral arcs during magnetic quiescence, *J. Geophys. Res.*, *95*(A12), 21,111–21,121.

Robinson, R. M., R. R. Vondrak, and E. Friis-Christensen (1987), Ionospheric currents associated with a Sun-aligned arc connected to the auroral oval, *Geophys. Res. Lett.*, *14*(6), 656–659.

Romanova, N., V. Pilipenko, O. Khabarova, and N. & Crosby (2007), Ulf wave index and its possible applications in space physics, *Bulgarian Journal of Physics*, *34*(2), 136–148.

Rostoker, G. (1983), Triggering of expansive phase intensifications of magnetospheric substorms by northward turnings of the interplanetary magnetic field, *J. Geophys. Res.*, *88*(A9), 6981–6993.

Rostoker, G., H.-L. Lam, and W. D. Hume (1972), Response time of the magnetosphere to the interplanetary electric field, *Can. J. Phys.*, *50*(6), 544–547.

Rostoker, G., S.-I. Akasofu, J. Foster, R. Greenwald, Y. Kamide, K. Kawasaki, A. Lui, R. McPherron, and C. Russell (1980), Magnetospheric substormsdefinition and signatures, *J. Geophys. Res.*, *85*(A4), 1663–1668.

Rostoker, G., A. T. Y. Lui, C. D. Anger, and J. S. Murphree (1987), North-south structures in the midnight sector auroras as viewed by the Viking imager, *Geophys. Res. Lett.*, *14*(4), 407–410.

Ruohoniemi, J. M., and K. B. Baker (1998), Large-scale imaging of high-latitude convection with Super Dual Auroral Radar Network HF radar observations, *J. Geophys. Res.*, *103*(A9), 20,797–20,811.

Ruohoniemi, J. M., and R. A. Greenwald (1996), Statistical patterns of high-latitude convection obtained from Goose Bay HF radar observations, *J. Geophys. Res.*, *101*(A10), 21,743–21,763.

Ruohoniemi, J. M., and R. A. Greenwald (2005), Dependencies of high-latitude plasma convection: Consideration of interplanetary magnetic field, seasonal, and universal time factors in statistical patterns, *J. Geophys. Res.*, *110*(A9), a09204.

Russell, C. (2004), Outer planet magnetospheres: a tutorial, *Adv. Space Res.*, *33*(11), 2004 – 2020.

Russell, C. T. (1972), The Configuration of the Magnetosphere, in *Critical Problems of Magnetospheric Physics*, edited by E. R. Dyer, p. 1.

Russell, C. T., and R. L. McPherron (1973), Semiannual variation of geomagnetic activity, *J. Geophys. Res.*, *78*(1), 92–108.

Sandholt, P. E., and M. Lockwood (1990), Periodic auroral events at the high-latitude convection reversal in the 16 MLT region, *Geophys. Res. Lett.*, *17*(11), 1877–1880.

Sauvaud, J.-A., and J. Winckler (1980), Dynamics of plasma, energetic particles, and fields near synchronous orbit in the nighttime sector during magnetospheric substorms, *J. Geophys. Res.*, *85*(A5), 2043–2056.

Schield, M. A. (1969), Pressure balance between solar wind and magnetosphere, *J. Geophys. Res.*, *74*(5), 1275–1286.

Schumaker, T. L., D. A. Hardy, S. Moran, A. Huber, and J. McGarity (1988), Precipitating Ion and Electron Detectors (SSJ/4) for the Block 5D/Flight 8 DMSP (Defense Meteorological Satellite Program) Satellite, *Tech. rep.*, AIR FORCE GEOPHYSICS LAB HANSCOM AFB MA.

Scurry, L., C. T. Russell, and J. T. Gosling (1994), A statistical study of accelerated flow events at the dayside magnetopause, *J. Geophys. Res.*, *99*(A8), 14,815–14,829.

Semenov, V. S., D. I. Kubyshkina, M. V. Kubyshkina, I. V. Kubyshkin, and N. Partamies (2015), On the correlation between the fast solar wind flow changes and substorm occurrence, *Geophys. Res. Lett.*, *42*(13), 5117–5124, 2015GL064806.

Séran, E., M. Godefroy, K. Kauristie, J.-C. Cerisier, J.-J. Berthelier, M. Lester, and L.-E. Sarri (2009), What can we learn from HF signal scattered from a discrete arc?, *Ann. Geophys.*, *27*(5), 1887–1896.

Shepherd, S. G., and J. M. Ruohoniemi (2000), Electrostatic potential patterns in the high-latitude ionosphere constrained by SuperDARN measurements, *J. Geophys. Res.*, *105*(A10), 23,005–23,014.

Shinohara, I., and S. Kokubun (1996), Statistical properties of particle precipitation in the polar cap during intervals of northward interplanetary magnetic field, *J. Geophys. Res.*, *101*(A1), 69–82.

Shiokawa, K., and H. Fukunishi (1990), Dependences of auroral 5577-Å and 6300-Å emission rates on thermospheric density variations, in *Coordinated Observations of the Ionosphere and the Magnetosphere in the Polar Regions*, vol. 3, pp. 24–31, National Institute of Polar Research, Tokyo.

Shiokawa, K., K. Yumoto, K. Hayashi, T. Oguti, and D. J. McEwen (1995), A statistical study of the motions of auroral arcs in the high-latitude morning sector, *J. Geophys. Res.*, *100*(A11), 21,979–21,985.

Shiokawa, K., T. Ogino, K. Hayashi, and D. J. McEwen (1997), Quasi-periodic poleward motions of morningside Sun-aligned arcs: A multievent study, *J. Geophys. Res.*, *102*(A11), 24,325–24,332.

Shiokawa, K., Y. Katoh, M. Satoh, M. K. Ejiri, T. Ogawa, T. Nakamura, T. Tsuda, and R. H. Wiens (1999), Development of Optical Mesosphere Thermosphere Imagers (OMTI), *Earth Planets Space*, *51*(7), 887–896.

Shiokawa, K., Y. Otsuka, and T. Ogawa (2009), Propagation characteristics of nighttime mesospheric and thermospheric waves observed by optical mesosphere thermosphere imagers at middle and low latitudes, *Earth Planets Space*, *61*(4), 479–491.

Shue, J.-H., P. T. Newell, K. Liou, and C.-I. Meng (2001), Influence of interplanetary magnetic field on global auroral patterns, *J. Geophys. Res.*, *106*(A4), 5913–5926.

Siscoe, G., J. Raeder, and A. J. Ridley (2004), Transpolar potential saturation models compared, *J. Geophys. Res.*, *109*(A9), A09203.

Siscoe, G. L., N. U. Crooker, and K. D. Siebert (2002), Transpolar potential saturation: Roles of region 1 current system and solar wind ram pressure, *J. Geophys. Res.*, *107*(A10), SMP 21–1–SMP 21–8, 1321.

Smith, C. W., N. A. Schwadron, and C. E. DeForest (2013), Decline and Recovery of the Interplanetary Magnetic Field during the Protracted Solar Minimum, *Astrophys. J*, *775*, 59.

Smith, P. R., P. L. Dyson, D. P. Monselesan, and R. J. Morris (1998), Ionospheric convection at Casey, a southern polar cap station, *J. Geophys. Res.*, *103*(A2), 2209–2218.

Sojka, J. J., L. Zhu, D. J. Crain, and R. W. Schunk (1994), Effect of high-latitude ionospheric convection on sun-aligned polar caps, *J. Geophys. Res.*, *99*(A5), 8851–8863.

Solomon, S. C., P. B. Hays, and V. J. Abreu (1988), The auroral 6300 Åemission: Observations and modeling, *J. Geophys. Res.*, *93*(A9), 9867–9882.

Song, P., and C. T. Russell (1992), Model of the formation of the low-latitude boundary layer for strongly northward interplanetary magnetic field, *J. Geophys. Res.*, *97*(A2), 1411–1420.

Southwood, D. J. (1976), A general approach to low-frequency instability in the ring current plasma, *J. Geophys. Res.*, *81*(19), 3340–3348.

Spanswick, E., G. D. Reeves, E. Donovan, and R. H. W. Friedel (2010), Injection region propagation outside of geosynchronous orbit, *J. Geophys. Res.*, *115*(A11), a11214.

Spicher, A., T. Cameron, E. M. Grono, K. N. Yakymenko, S. C. Buchert, L. B. N. Clausen, D. J. Knudsen, K. A. McWilliams, and J. I. Moen (2015), Observation of polar cap patches and calculation of gradient drift instability growth times: A Swarm case study, *Geophys. Res. Lett.*, *42*(2), 201–206, 2014GL062590.

Spiro, R. W., M. Harel, R. A. Wolf, and P. H. Reiff (1981), Quantitative simulation of a magnetospheric substorm 3. Plasmaspheric electric fields and evolution of the plasmapause, *J. Geophys. Res.*, *86*(A4), 2261–2272.

Spitzer, L. (1962), *Physics of fully ionized gases*, Interscience tracts on physics and astronomy, Interscience Publishers.

Spreiter, J. R., A. L. Summers, and A. Y. Alksne (1966), Hydromagnetic flow around the magnetosphere, *Planet. Space Sci.*, *14*, 223.

Sreenivasan, K. R., A. Prabhu, and R. Narasimha (1983), Zero-crossings in turbulent signals, *J. Fluid Mech.*, *137*, 251–272.

Stauning, P. (2002), Field-aligned ionospheric current systems observed from Magsat and Oersted satellites during northward IMF, *Geophys. Res. Lett.*, *29*(15), ORS 6–1–ORS 6–4.

Syrjäsuo, M., T. I. Pulkkinen, P. Janhunen, A. Viljanen, R. J. Pellinen, K. Kauristie, H. J. Opgenoorth, S. Wallman, P. Eglitis, P. Karlsson, O. Amm, E. Nielsen, and C. Thomas (1998), Observations of Substorm Electrodynamics Using the MIRACLE Network, in *Substorms-4*, *Astrophysics and Space Science Library*, vol. 238, edited by S. Kokubun and Y. Kamide, p. 111.

Tanskanen, E., T. I. Pulkkinen, H. E. J. Koskinen, and J. A. Slavin (2002), Substorm energy budget during low and high solar activity: 1997 and 1999 compared, *J. Geophys. Res.*, *107*(A6), SMP 15–1–SMP 15–11.

Tanskanen, E. I. (2009), A comprehensive high-throughput analysis of substorms observed by IMAGE magnetometer network: Years 19932003 examined, *J. Geophys. Res.*, *114*(A5), a05204.

Tanskanen, E. I., J. A. Slavin, D. H. Fairfield, D. G. Sibeck, J. Gjerloev, T. Mukai, A. Ieda, and T. Nagai (2005), Magnetotail response to prolonged southward IMF Bz intervals: Loading, unloading, and continuous magnetospheric dissipation, *J. Geophys. Res.*, *110*(A3), a03216.

Tanskanen, E. I., T. I. Pulkkinen, A. Viljanen, K. Mursula, N. Partamies, and J. A. Slavin (2011), From space weather toward space climate time scales: Substorm analysis from 1993 to 2008, *J. Geophys. Res.*, *116*(A5), a00I34.

Thomsen, M. F. (2004), Why Kp is such a good measure of magnetospheric convection, *Space Weather*, *2*(11), s11004.

Thomsen, M. F., J. Birn, J. E. Borovsky, K. Morzinski, D. J. McComas, and G. D. Reeves (2001), Two-satellite observations of substorm injections at geosynchronous orbit, *J. Geophys. Res.*, *106*(A5), 8405–8416.

Treumann, R., and W. Baumjohann (1997), *Advanced Space Plasma Physics*, Imperial College Press.

Troshichev, O. A., M. G. Gusev, S. V. Nikolashkin, and V. P. Samsonov (1988), Features of the polar cap aurorae in the Southern Polar Region, *Planet. Space Sci.*, *36*, 429–439.

Tsunoda, R. T. (1988), High-latitude F region irregularities: A review and synthesis, *Rev. Geophys.*, *26*(4), 719–760.

Tsyganenko, N. A. (1989), A magnetospheric magnetic field model with a warped tail current sheet, *Planet. Space Sci.*, *37*, 5–20.

Uspensky, M., A. Kustov, and P. Williams (1993), The amplitude of auroral backscatter-III. Effect of tilted ionospheric layer, *J. Atmos. Terr. Phys.*, *55*(10), 1383 – 1392.

Uspensky, M., P. Eglitis, H. Opgenoorth, G. Starkov, T. Pulkkinen, and R. Pellinen (2000), On auroral dynamics observed by HF radar: 1. Equatorward edge of the afternoon-evening diffuse luminosity belt, *Ann. Geophys.*, *18*(12), 1560–1575.

Uspensky, M. V., A. V. Kustov, G. J. Sofko, J. A. Koehler, J. P. Villain, C. Hanuise, J. M. Ruohoniemi, and P. J. S. Williams (1994), Ionospheric refraction effects in slant range profiles of auroral HF coherent echoes, *Radio Sci.*, *29*(2), 503–517.

Valladares, C. E., H. C. Carlson, and K. Fukui (1994), Interplanetary magnetic field dependency of stable sun-aligned polar cap arcs, *J. Geophys. Res.*, *99*(A4), 6247–6272.

Vasyliunas, V. M., J. R. Kan, S.-I. Akasofu, and G. L. Siscoe (1982), Scaling relations governing magnetospheric energy transfer, *Planet. Space Sci.*, *30*, 359–365.

Walker, A. D. M., M. Pinnock, K. B. Baker, J. R. Dudeney, and J. P. S. Rash (1998), Strong flow bursts in the nightside ionosphere during extremely quiet solar wind conditions, *Geophys. Res. Lett.*, *25*(6), 881–884.

Watanabe, M., and G. J. Sofko (2009), The interchange cycle: A fundamental mode of magnetic flux circulation for northward interplanetary magnetic field, *Geophys. Res. Lett.*, *36*(3), l03107.

Watanabe, M., G. J. Sofko, D. A. André, J. M. Ruohoniemi, M. R. Hairston, and K. Kabin (2006), Ionospheric signatures of internal reconnection for northward interplanetary magnetic field: Observation of reciprocal cells and magnetosheath ion precipitation, *J. Geophys. Res.*, *111*(A6), a06201.

Watanabe, M., G. J. Sofko, X. Yan, K. A. McWilliams, J.-P. St.-Maurice, A. V. Koustov, G. C. Hussey, and M. R. Hairston (2010), Ionospheric convection signatures of the interchange cycle at small interplanetary magnetic field clock angles, *J. Geophys. Res.*, *115*(A12), a12230.

Weber, E. J., M. C. Kelley, J. O. Ballenthin, S. Basu, H. C. Carlson, J. R. Fleischman, D. A. Hardy, N. C. Maynard, R. F. Pfaff, P. Rodriguez, R. E. Sheehan, and M. Smiddy (1989), Rocket measurements within a polar cap arc: Plasma, particle, and electric circuit parameters, *J. Geophys. Res.*, *94*(A6), 6692–6712.

Weber, E. J., J. F. Vickrey, H. Gallagher, L. Weiss, C. J. Heinselman, R. A. Heelis, and M. C. Kelley (1991), Coordinated radar and optical measurements of stable auroral arcs at the polar cap boundary, *J. Geophys. Res.*, *96*(A10), 17,847–17,863.

Welling, D. T., M. André, I. Dandouras, D. Delcourt, A. Fazakerley, D. Fontaine, J. Foster, R. Ilie, L. Kistler, J. H. Lee, M. W. Liemohn, J. A. Slavin, C.-P. Wang, M. Wiltberger, and A. Yau (2015), The Earth: Plasma Sources, Losses, and Transport Processes, *Space Sci. Rev.*, *192*(1), 145–208.

Weygand, J. M., R. L. McPherron, K. Kauristie, H. U. Frey, and H. T.-S. (2008), Relation of auroral substorm onset to local AL index and dispersionless particle injections, *J. Atmos. Solar-Terr. Phys.*, *70*, 2336–2345.

Wild, J. A., E. E. Woodfield, and S. K. Morley (2009), On the triggering of auroral substorms by northward turnings of the interplanetary magnetic field, *Ann. Geophys.*, *27*(9), 3559–3570.

Wilder, F. D., C. R. Clauer, and J. B. H. Baker (2008), Reverse convection potential saturation during northward IMF, *Geophys. Res. Lett.*, *35*(12), l12103.

Wilder, F. D., C. R. Clauer, and J. B. H. Baker (2010), Polar cap electric field saturation during interplanetary magnetic field B_z north and south conditions, *J. Geophys. Res.*, *115*(A10), a10230.

Wilder, F. D., C. R. Clauer, J. B. H. Baker, and P. T. Newell (2011), Interhemispheric observations of dayside convection under northward IMF, *J. Geophys. Res.*, *116*(A10), a10230.

Wilder, F. D., S. Eriksson, and M. Wiltberger (2013), Investigation of the interhemispheric asymmetry in reverse convection near solstice during northward interplanetary magnetic field conditions using MHD simulations, *J. Geophys. Res.*, *118*(7), 4289–4297.

Wygant, J. R., R. B. Torbert, and F. S. Mozer (1983), Comparison of S3-3 polar cap potential drops with the interplanetary magnetic field and models of magnetopause reconnection, *J. Geophys. Res.*, *88*(A7), 5727–5735.

Xu, F., and J. E. Borovsky (2015), A new four-plasma categorization scheme for the solar wind, *J. Geophys. Res.*, *120*(1), 70–100, 2014JA020412.

Yau, A. W., W. Peterson, and T. Abe (2011), *Influences of the Ionosphere, Thermosphere and Magnetosphere on Ion Outflows*, pp. 283–314, Springer Netherlands, Dordrecht.

Yeoman, T. K., M. P. Freeman, G. D. Reeves, M. Lester, and D. Orr (1994), A comparison of midlatitude Pi 2 pulsations and geostationary orbit particle injections as substorm indicators, *J. Geophys. Res.*, *99*(A3), 4085–4093.

Ylvisaker, N. D. (1965), The expected number of zeros of a stationary Gaussian process, *Ann. Math. Stat*, *36*(3), 1043–1046.

Zanetti, L. J., T. A. Potemra, R. E. Erlandson, P. F. Bythrow, B. J. Anderson, J. S. Murphree, and G. T. Marklund (1990), Polar region Birkeland current, convection, and aurora for northward interplanetary magnetic field, *J. Geophys. Res.*, *95*(A5), 5825–5833.

Zerbo, J.-L., and J. D. Richardson (2015), The solar wind during current and past solar minima and maxima, *J. Geophys. Res.*, *120*(12), 10,250–10,256, 2015JA021407.

Zhang, S.-R., J. M. Holt, and M. McCready (2007), High latitude convection based on long-term incoherent scatter radar observations in North America, *J. Atmos. Sol. Terr. Phys.*, *69*, 1273–1291.

Zhu, L., J. J. Sojka, R. W. Schunk, and D. J. Crain (1993), A time-dependent model of polar cap arcs, *J. Geophys. Res.*, *98*(A4), 6139–6150.

Zhu, L., R. W. Schunk, and J. J. Sojka (1997), Polar cap arcs: a review, *J. Atmos. Sol. Terr. Phys.*, *59*, 1087–1126.

Zolotukhina, N. A., P. N. Mager, and D. Y. Klimushkin (2008), Pc5 waves generated by substorm injection: a case study, *Ann. Geophys.*, *26*(7), 2053–2059.